

Structure and Bonding 159

Series Editor: D.M.P. Mingos

Jean-François Nierengarten *Editor*

Fullerenes and Other Carbon-Rich Nanostructures

 Springer

159

Structure and Bonding

Series Editor:

D.M.P. Mingos, Oxford, United Kingdom

Editorial Board:

F.A. Armstrong, Oxford, United Kingdom

X. Duan, Beijing, China

L.H. Gade, Heidelberg, Germany

K.R. Poeppelmeier, Evanston, IL, USA

G. Parkin, New York, USA

M. Takano, Kyoto, Japan

For further volumes:

<http://www.springer.com/series/430>

Aims and Scope

The series *Structure and Bonding* publishes critical reviews on topics of research concerned with chemical structure and bonding. The scope of the series spans the entire Periodic Table and addresses structure and bonding issues associated with all of the elements. It also focuses attention on new and developing areas of modern structural and theoretical chemistry such as nanostructures, molecular electronics, designed molecular solids, surfaces, metal clusters and supramolecular structures. Physical and spectroscopic techniques used to determine, examine and model structures fall within the purview of *Structure and Bonding* to the extent that the focus is on the scientific results obtained and not on specialist information concerning the techniques themselves. Issues associated with the development of bonding models and generalizations that illuminate the reactivity pathways and rates of chemical processes are also relevant

The individual volumes in the series are thematic. The goal of each volume is to give the reader, whether at a university or in industry, a comprehensive overview of an area where new insights are emerging that are of interest to a larger scientific audience. Thus each review within the volume critically surveys one aspect of that topic and places it within the context of the volume as a whole. The most significant developments of the last 5 to 10 years should be presented using selected examples to illustrate the principles discussed. A description of the physical basis of the experimental techniques that have been used to provide the primary data may also be appropriate, if it has not been covered in detail elsewhere. The coverage need not be exhaustive in data, but should rather be conceptual, concentrating on the new principles being developed that will allow the reader, who is not a specialist in the area covered, to understand the data presented. Discussion of possible future research directions in the area is welcomed.

Review articles for the individual volumes are invited by the volume editors.

In references *Structure and Bonding* is abbreviated *Struct Bond* and is cited as a journal.

Jean-François Nierengarten
Editor

Fullerenes and Other Carbon-Rich Nanostructures

With contributions by

D. Bonifazi • G. Chen • A. Escosura • D. Felder-Flesch •
S. Frankenbergler • D. Giust • D.M. Guldi •
J.A. Januszewski • R. Marega • T. Nakanishi • V. Sgobba •
Y. Shen • T. Torres • A. Troeger • O. Trukhina •
R.R. Tykwinski • Y. Zhao •

 Springer

Editor

Jean-François Nierengarten
Université de Strasbourg et CNRS
Ecole Européenne de Chimie
Polymères et Matériaux (ECPM)
Strasbourg Cedex 2
France

ISSN 0081-5993

ISSN 1616-8550 (electronic)

ISBN 978-3-642-54853-6

ISBN 978-3-642-54854-3 (eBook)

DOI 10.1007/978-3-642-54854-3

Springer Heidelberg New York Dordrecht London

Library of Congress Control Number: 2014937894

© Springer-Verlag Berlin Heidelberg 2014

This work is subject to copyright. All rights are reserved by the Publisher, whether the whole or part of the material is concerned, specifically the rights of translation, reprinting, reuse of illustrations, recitation, broadcasting, reproduction on microfilms or in any other physical way, and transmission or information storage and retrieval, electronic adaptation, computer software, or by similar or dissimilar methodology now known or hereafter developed. Exempted from this legal reservation are brief excerpts in connection with reviews or scholarly analysis or material supplied specifically for the purpose of being entered and executed on a computer system, for exclusive use by the purchaser of the work. Duplication of this publication or parts thereof is permitted only under the provisions of the Copyright Law of the Publisher's location, in its current version, and permission for use must always be obtained from Springer. Permissions for use may be obtained through RightsLink at the Copyright Clearance Center. Violations are liable to prosecution under the respective Copyright Law.

The use of general descriptive names, registered names, trademarks, service marks, etc. in this publication does not imply, even in the absence of a specific statement, that such names are exempt from the relevant protective laws and regulations and therefore free for general use.

While the advice and information in this book are believed to be true and accurate at the date of publication, neither the authors nor the editors nor the publisher can accept any legal responsibility for any errors or omissions that may be made. The publisher makes no warranty, express or implied, with respect to the material contained herein.

Printed on acid-free paper

Springer is part of Springer Science+Business Media (www.springer.com)

Preface

Following the discovery of fullerenes by Kroto, Curl and Smalley, the development of the macroscopic scale fullerene synthesis by Krätschmer and Huffman in 1990 represents a major breakthrough in carbon science. Indeed, the availability of these caged molecules exclusively constituted by carbon atoms has generated an unprecedented interest in the scientific community and research on carbon nanomaterials became a major hot topic in science. Among the most spectacular findings, fullerenes were found to behave like electronegative molecules able to reversibly accept several electrons, to become a supraconductor in M_3C_{60} species (M=alkali metals) or to be an interesting material for solar energy conversion. Since the incorporation of fullerenes into thin films is required for the preparation of many optoelectronic devices, the past several years have seen a considerable growth in the use of fullerene-based derivatives at surfaces and interfaces. On the other hand, the self-assembly of fullerene materials and the preparation of fullerene-containing liquid crystals have also been extensively investigated. The different aspects of this research are nicely summarized in the chapters written by Nakanishi, Zhao, Guldi and Felder-Flesch.

In recent years, the unique electronic properties of fullerenes have also generated significant research activities focused on their use as electron and/or energy acceptors in photochemical molecular devices. The combination of the carbon sphere with all kinds of donors is of particular interest. On one hand, such hybrid systems have shown excited state interactions making them excellent candidates for fundamental photophysical studies. On the other hand, such derivatives have been used for photovoltaic applications. This specific aspect of fullerene chemistry is illustrated with phthalocyanines/fullerene hybrid materials in the chapter prepared by Torres and co-workers.

The tremendous scientific interest initially generated by the discovery of fullerenes has been rapidly extended to other forms of carbon nanomaterials. Important breakthroughs in carbon science occurred rapidly with the discovery of carbon nanotubes by Iijima in 1991 and the isolation of hexagonal carbon sheets from graphite (graphene) by Geim and Novoselov in 2004. Bonifazi et al. in their chapter

describe supramolecular approaches aimed at the functionalization of such carbon-based nanostructures focusing on their properties and applicative uses as self-organized materials at interfaces.

Whereas the most common carbon allotropes are based on sp^3 - or sp^2 -carbon atoms, little is known about the allotrope constructed from sp -hybridized C atoms, a material commonly called carbyne. Without a defined sample of carbyne to study, synthetic chemists have attempted to model the properties of carbyne through the formation of defined length oligomers based on a cumulene or polyynes skeleton. In the last chapter, Tykwinski et al. summarize the most recent advances towards the preparation and the properties of sp -hybridized carbon nanomaterials.

Contributions from laboratories from all over the world are collected in this special issue and illustrate major aspects of the current state of the art of carbon nanoscience. All the chapters contained in this issue have been prepared by leading scientists, and I would like to warmly thank all of them for their contributions and their enthusiasm to participate in this volume. I further thank Springer DE for its support in this enterprise and in particular J. Bhaskar and T. Jäger for the efficient handling of all the chapters.

Strasbourg, France

Jean-François Nierengarten

Contents

Exotic Self-Organized Fullerene Materials Based on Uncommon Hydrophobic–Amphiphilic Approach	1
Yanfei Shen and Takashi Nakanishi	
C₆₀ Fullerene Amphiphiles as Supramolecular Building Blocks for Organized and Well-Defined Nanoscale Objects	23
Yuming Zhao and Guang Chen	
Multilayer Assembly for Solar Energy Conversion	55
Anna Troeger, Vito Sgobba, and Dirk M. Guldi	
Self- or Induced Organization of [60]Fullerene Hexakisadducts	101
Delphine Felder-Flesch	
Dual Role of Phthalocyanines in Carbon Nanostructure-Based Organic Photovoltaics	145
Andrés de la Escosura, Olga Trukhina, and Tomás Torres	
Supramolecular Chemistry of Carbon Nanotubes at Interfaces: Toward Applications	193
Riccardo Marega, Davide Giust, and Davide Bonifazi	
Oligomers from sp-Hybridized Carbon: Cumulenes and Polyynes	219
Stephanie Frankenberger, Johanna A. Januszewski, and Rik R. Tykwinski	
Index	257

Exotic Self-Organized Fullerene Materials Based on Uncommon Hydrophobic–Amphiphilic Approach

Yanfei Shen and Takashi Nakanishi

Abstract This review documents the recent developments of supramolecular materials composed of alkylated fullerenes (C_{60}) which have a unique hydrophobic amphiphilicity. Unlike the conventional amphiphiles composed of hydrophilic and hydrophobic units, the alkyl-conjugated C_{60} derivatives presented here contain two hydrophobic moieties, C_{60} and alkyl tails. Slightly different hydrophobicity and chemical nature make them arranged into microphase-segregated mesostructures with lamella units in nanometer scale, which mainly relies on the relatively weak interactions, π – π in neighboring C_{60} molecules, and van der Waals between alkyl chains. These molecular assemblies and supramolecular arrays feature distinct dimensionality and morphologies, namely exotic assemblies, as a consequence of the presence of different assembly environment, and different number and length of the alkyl chains, as well as the position of the substitutions. The systematic exploration of the molecular design and preparative methodologies for new versatile supramolecular materials will be reviewed in details.

Keywords Self-assembly · Supramolecular materials · Fullerenes · Hydrophobic amphiphilicity

Contents

1	Introduction	2
2	Self-Assemblies of Pristine C_{60}	3
2.1	Controlled Assembly of C_{60}	3
2.2	Supramolecular Coassembly	4
3	Exotic Assemblies of Uncommon Hydrophobic C_{60} Amphiphiles	6
3.1	Morphology Control	6
3.2	Morphology-Related Functions	10
3.3	Supramolecular Composites	12

4	Soft to Hard: Plasticization and Metallization	13
5	Exotic Fluid Materials	15
	5.1 Liquid Crystalline Assemblies	15
	5.2 Room Temperature Liquid Fullerenes	16
6	Conclusion	16
	References	17

Abbreviations

2D	Two-dimensional
AFM	Atomic force microscopy
DSC	Differential scanning calorimetry
ex-TTF	π -extended tetrathiafulvalene
FET	Field emission transistors
FFT	Fast Fourier transform
HOPG	Highly oriented pyrolytic graphite
HR-cryo-TEM	High-resolution cryogenic transmission electron microscopy
HRTEM	High-resolution transmission electron microscopy
<i>it</i> -PMMA	<i>Isotactic</i> -PMMA
LC	Liquid crystal
LLIP	Liquid–liquid interfacial precipitation
NIR	Near-infrared
OLED	Organic light-emitting diodes
PEO	Poly(ethylene oxide)
SERS	Surface-enhanced Raman scattering
STM	Scanning tunneling microscopy
<i>st</i> -PMMA	<i>Syndiotactic</i> -poly(methyl methacrylate)
SWNT	Single-wall carbon nanotubes
SXAS	Small-angle X-ray scattering
XRD	X-ray diffraction

1 Introduction

Supramolecular assembly, in which molecular building blocks are organized into high-order functional structures via comparatively weak forces, offers attractive features in chemistry, materials science, and nanotechnology [1]. One of the great challenges for materials science is the development of supramolecular materials in which the constituent units are highly regular molecular nanostructures. By controlling the surface morphology, the precisely defined molecular materials are expected to exhibit promising properties and specific functions such as controllable surface wettability [2, 3], chemical sensing [4–7], enhanced mechanical properties [8], electrical conductivity [9, 10], and promoted optoelectronic features [11–13]. Therefore, self-assembly based on supramolecular chemistry has become crucial processes and techniques for the construction of exotic soft materials, having

unique shape and morphology, with flexible properties from functional molecules. Among various functional molecules [14], conductive or semiconductive organic molecules or polymers have received intense interest because of many possible future applications such as field emission transistors (FET) and organic light-emitting diodes (OLED); organic solar cells are desired by tuning intermolecular and intramolecular interactions [15–17]. Therefore, fully understanding the characteristic of these assemblies and their optoelectronic and thermal functions is highly important for the development of exotic supramolecular soft materials.

Fullerenes are a unique class of nanocarbon molecule and therefore interesting building blocks for supramolecular architectures. With the increasing interest since the discovery of fullerenes in 1990, a great deal of effort was devoted to materials science applications such as ultimate superconductors [18], ferromagnets [19, 20], lubricants [21], and photoconductors [22]. Transferring the properties of the fullerene to bulk materials which exhibit the original features of C_{60} has been a common task in the field. However, the low solubility of pristine C_{60} somehow prohibits its large-scale productions and applications. As a result, the chemical functionalization of C_{60} has partially surmounted the problem.

In this chapter, we discuss recent developments of fullerenes in supramolecular materials, with particular emphasis to one series of uncommon C_{60} derivatives. We introduce a new concept of amphiphilicity and demonstrate different degrees of hydrophobicities by alkylation of C_{60} and control of their exotic assembly phenomena in organic solvents. It should be pointed out that the derivatives offer various number of opportunities for the development of novel materials and applications, as compared to pristine C_{60} .

2 Self-Assemblies of Pristine C_{60}

2.1 *Controlled Assembly of C_{60}*

Pristine C_{60} forms various crystals and assemblies, from different solvents, with dissimilar structure and diverse shapes. The nature of the solvent plays a major role in the cluster structure. The solution-driven assemblies such as liquid–liquid interfacial precipitation (LLIP) [23, 24] and drop drying [25, 26] processes have been developed for the assembly of C_{60} . To understand the formation of the close-packed C_{60} assemblies is quite important when one can consider their optoelectronic functions.

As a typical example of assemblies from pristine C_{60} , Miyazawa and co-workers have developed a methodology to prepare crystalline C_{60} materials as nanowhiskers, nanotubes, and hexagonal nanosheets via LLIP method [23, 27, 28]. For example, very thin hexagonal crystalline C_{60} nanosheets were prepared at the carbon tetrachloride (CCl_4)/alcohol interface, and the size of the hexagonal nanosheets could be tailored merely by changing the alcohol [27]. At CCl_4 /2-propanol interface,

a large (~ 7.5 μm diameter) hexagonal nanosheet was observed, whereas the diameter of the hexagonal nanosheets decreased to about 2.5 μm and 500 nm at the CCl_4 /ethanol and CCl_4 /methanol interface, respectively. The X-ray diffraction (XRD) pattern of the hexagonal nanosheets prepared at the CCl_4 and alcohol interfaces revealed the existence of hexagonal C_{60} crystalline arrangement.

Via a similar way, other C_{60} crystalline assemblies with various morphologies have been prepared. For instance, Curry et al. developed a rapid synthesis route to prepare single crystalline C_{60} rods by controlled dropwise addition of a toluene solution of C_{60} into 2-propanol solvent [25]. Masuhara et al. established a facile solvent-induced reprecipitation method using *m*-xylene and 2-propanol as good and poor solvents [29, 30]. By quickly injecting an *m*-xylene solution of C_{60} into vigorously stirred 2-propanol and followed by keeping at room temperature for several hours, “monodispersed” C_{60} nano/microcrystals with unique morphology can be prepared. The resulting nano/microcrystals had a hexagonal crystalline ordering with various morphologies such as rodlike, cubic, branched rods, and six-faced prism structures.

Liu and co-workers synthesized thin, rectangular C_{60} nanorods in face-centered cubic structure by evaporating an *m*-xylene solution of C_{60} on silicon or glass substrates [26]. In the initial production stage, the solvent is trapped into the crystal to form hexagonal solvated C_{60} nanorods during evaporation at temperatures below 55°C . The trapped solvent is then easily removed by heat treatment at 61°C under vacuum, resulting in a transformation of the hexagonal structure of the solvated C_{60} nanorods into the fcc structure. The length-to-diameter ratio of the rods can be controlled by the evaporation rate. As the evaporation rate increases, the aspect ratio of the length to the diameter gradually increases in the range from ≈ 10 to over 10^3 .

2.2 *Supramolecular Coassembly*

For the assembly of C_{60} , another alternative is the template-directed assembly. As an early example, Zhu et al. reported the synthesis of C_{60} nanotubes with uniform orientation from toluene solution of C_{60} by using porous alumina template [31]. Surfactants [32] and polymer matrix [33, 34] can also assist C_{60} to assemble into nano/microcrystals with various morphologies. The matrix-assisted assembly mechanism of C_{60} crystalline materials was suggested to be based on a concentration profile controlled growth. For example, during the process of the porphyrin polymer-assisted C_{60} assembly, sphere formation is initiated by nanoparticle growth followed by assembly of micrometer-sized disks (Fig. 1) [33]. A principle of “biomineralization” was supposed to be the formation mechanism, where the porphyrin unit in the polymer plays multiple roles in preorganizing and assisting the self-assembly of C_{60} into micrometer-sized fcc crystalline spheres.

Molecules possess hydrophobic property; π -conjugated structure and electron-donating feature have the possibility to provide host cavities for the encapsulation of C_{60} molecules [35–38]. The multi-encapsulation of C_{60} in the host environments

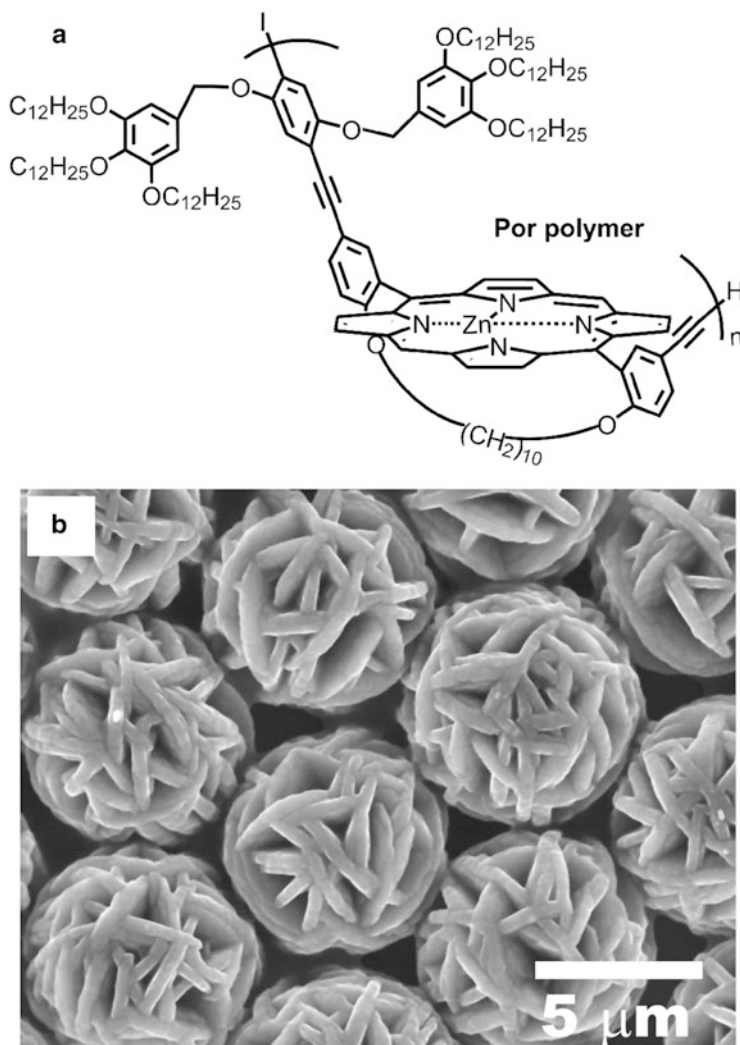
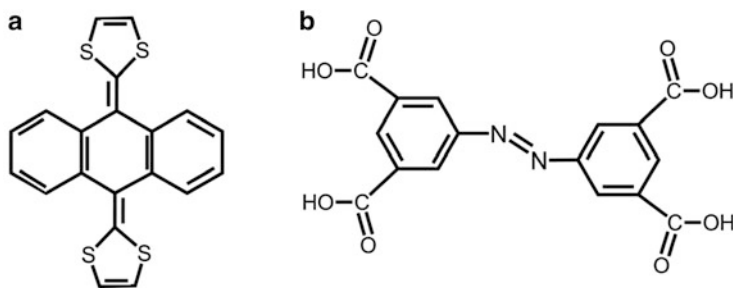


Fig. 1 (a) Chemical structure of the porphyrin polymer used for the assembly; (b) SEM image of C₆₀ microspheres of nanoplates formed by slow evaporation of a toluene solution of C₆₀ and porphyrin polymer [33]. The SEM image was provided by courtesy of Dr. M. Takeuchi and Dr. X. Zhang, NIMS

was expected to maintain the original morphologies of the host architectures with possible enhancement of electronic properties. Martín et al. reported that large π -extended tetrathiafulvalene (ex-TTF, Scheme 1a)-based dendrimers hosting a number of C₆₀ molecules form segregated arrays of donor and acceptor units which could benefit for the preparation of optoelectronic devices [35]. The hydrophobic environment inside polymers or assembled organic objects can also act as



Scheme 1 Chemical structures of (a) ex-TTF and (b) NN4A

good host environment for the encapsulation of C_{60} molecules. For instance, optically active stereocomplexes syndiotactic-poly(methyl methacrylate) (*st*-PMMA) can encapsulate C_{60} molecules to mimic to some extent the behavior of carbon nanotubes [36]. The *st*-PMMA folded into a preferred-handed helical conformation for the encapsulation of C_{60} , forming an optically active supramolecular peapod-like complex gel. The C_{60} -encapsulated *st*-PMMA is easy to prepare, inexpensive, and processable. Interestingly, the preferred-handed helical *st*-PMMA/ C_{60} could serve as a template to further encapsulate the complementary *isotactic*-PMMA (*it*-PMMA) through replacement of the encapsulated C_{60} molecules, forming optically active PMMA stereocomplexes [37]. Another example for the template-directed fabrication of C_{60} assembly is using the assembled network formed from small molecules [39, 40]. By forming hydrogen bonding, a tetraacidic azobenzene molecule NN4A (Scheme 1b) forms a 2D network when deposited onto a graphite surface [39]. STM analysis indicated that there are two different types of cavities with different sizes. Larger one is composed of six benzene rings which contain two types of cavities, while smaller one is from three NN4A molecules in a triangular shape. The network can serve as an organic template for the accommodation of C_{60} . The attractive photosensitive properties of azobenzene group in NN4A can be utilized as photoswitching units to control the structure and function of the resulted supramolecular system.

3 Exotic Assemblies of Uncommon Hydrophobic C_{60} Amphiphiles

3.1 Morphology Control

In order to prevent C_{60} aggregation, lots of efforts have been devoted to the chemical modification of C_{60} to be amphiphilic molecules for their self-organization on surfaces and in solution. Various amphiphilic (hydrophobic–hydrophilic) C_{60} derivatives, such as poly(ethylene oxide) (PEO) [41], acetylcarnitine [42], and

Scheme 2 Chemical structures of alkyl-conjugated C_{60} derivatives **1–6**



polar dendrimer [43] modified C_{60} , have been reported to self-assembled into micelles, vesicles, and rods in water. In contrast to these conventional amphiphilic assemblies, the amphiphilicity in organic solvents by combining π - π (C_{60}) and van der Waals (alkyl chain) interactions is expected to have the ability to control the polymorphic C_{60} assemblies for various applications such as surface engineer and optoelectronics. We have proposed a series of *N*-methyl fulleropyrrolidines carrying a phenyl substituent with multiple alkyloxy chains (Scheme 2). The alkylated C_{60} derivatives form a highly ordered mesophase and dimensionally controlled architectures by tuning the alkyl chain volume and varying the nature of solvent systems [44, 45].

Fine-tuning of interfacial and intermolecular interactions can result in well-defined and ordered molecular architectures, which are important for material properties and the development of molecular devices [46, 47]. The two-dimensional (2D) arrangement of C_{60} and its derivatives on surfaces is well established via covalent linking or supramolecular recognition [48–52]. However, the one-dimensional (1D) assembly of C_{60} is far less investigated [51, 53–55]. As we know, molecules that bear long alkyl chains can form perfectly aligned lamellar structures on highly oriented pyrolytic graphite (HOPG) [56–61]. We therefore modified C_{60} with three hexadecyloxy (**1**) or eicosyloxy (**2**) chains in the 3,4,5-position at the phenyl substituent, which induced epitaxial assembly of the C_{60} derivatives on HOPG upon spin coating from chloroform solution [62, 63]. Lamellar domain structures and 1D C_{60} alignment were revealed by atomic force microscopy (AFM) and scanning tunneling microscopy (STM) (Fig. 2a, b). The lamellar space for C_{60} derivatives **1** and **2** is twice the molecular length, indicating that molecules are adsorbed in a head-to-head bilayer structure motif with zigzag-type C_{60} arrangement (Fig. 2c).

Except the supramolecular alignment on solid surface, the alkyl-conjugated C_{60} showed unique ability for exotic supramolecular polymorphism relying on weak van der Waals forces of alkyl chains and π - π interactions of C_{60} moieties. With a very simple preparation, various well-defined self-organized superstructures formed by **1** in solvents including 2-propanol/toluene mixtures, 1-propanol, H_2O/THF mixture, 1,4-dioxane, and 2-(*R*)- or (*S*)-butanol (Fig. 3) [64–67]. Self-assembled objects were prepared by evaporation of 1 mL chloroform solution of **1** ($[1] = 1.0$ mM) followed by addition of 1 mL respective solvents [65]. Subsequently, heating at 60–70°C for

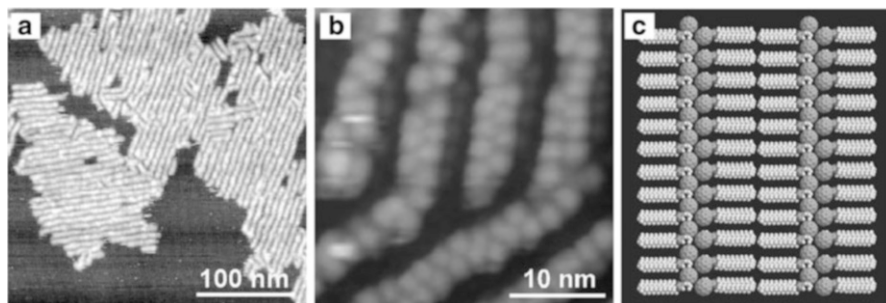


Fig. 2 (a) AFM image of **1** on HOPG spin coated from CHCl_3 solution; (b) high-resolution STM image of **1** on HOPG; (c) schematic illustration showing the molecular organization of **1** in the lamellae. Reprint with permission from [62]

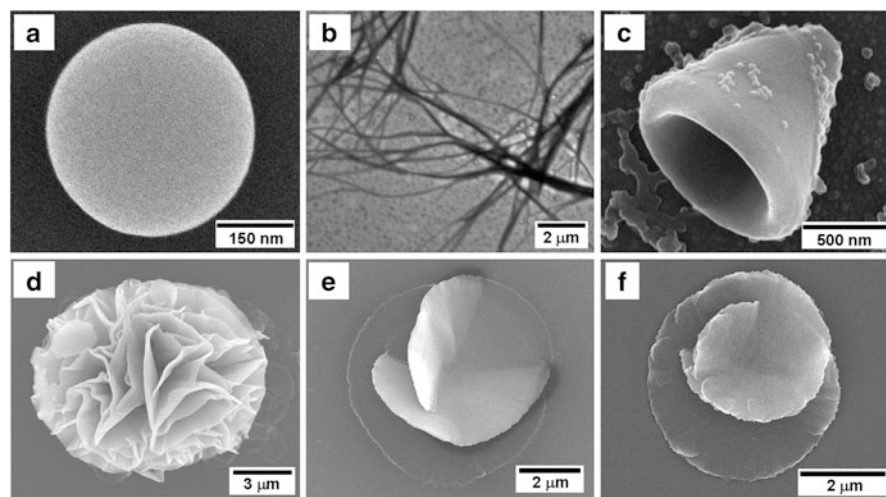


Fig. 3 SEM images of **1** formed from (a) 1:1 2-propanol/toluene mixture, (b) 1-propanol, (c) 1:1 THF/ H_2O mixture, (d) 1,4-dioxane solution, (e) 2-(*R*)-butanol, and (f) 2-(*S*)-butanol. Reprint with permission from [65] and [66]

2 h resulted in light brown mixtures. Vesicles with an average diameter of 250 nm were formed in the solvent of 1:1 2-propanol/toluene (Fig. 3a). High-resolution transmission electron microscopy (HRTEM) analysis reveals an empty core with 8–9 nm wall thickness. In 1-propanol, partially twisted tapes with length over than 20 μm were observed (Fig. 3b). Conical objects, shell thickness of around 150 nm, were developed from an equimolar mixture of $\text{H}_2\text{O}/\text{THF}$ (Fig. 3c). A flower-shaped supramolecular assembly was observed by heating **1** in 1,4-dioxane at 60°C for 2 h and then cooled at 20°C for 24 h and 5°C for half a day (Fig. 3d) [66]. By using chiral solvents such as 2-(*R*)-butanol and 2-(*S*)-butanol, chirality was introduced into the assemblies, where left- and right-handed microstructures formed, respectively (Fig. 4e, f) [66].

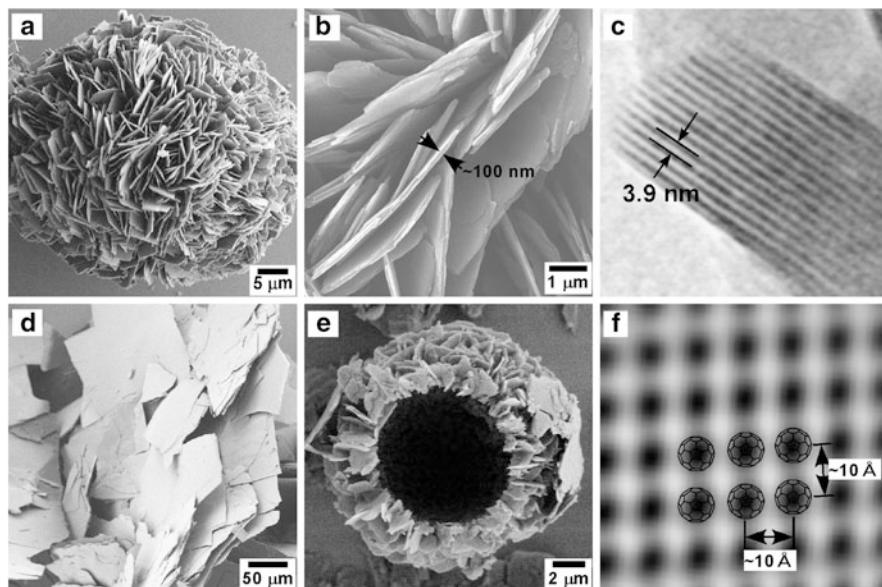


Fig. 4 (a, b) SEM images of **3** prepared from 1,4-dioxane at 20°C; (c) an HR-cryo-TEM image of the edge of (b); SEM images of **4** prepared from 1,4-dioxane at 20°C (d) and at 5°C (e); (f) the Fourier filtered image of an ED pattern of (d). Reprint with permission from [68]

Slight differences of the aliphatic chain length and number of the derivatives greatly influence the morphologies of their supramolecular assemblies. A globular particle of bis-alkylated derivative (**3**) from 1,4-dioxane solution was observed [68]. By cooling to around 20°C after solubilization, the molecules assembled into large particles with a diameter of a few tens of micrometers, which are composed of many plate structures with a thickness of around 100 nm (Fig. 4a, b). High-resolution cryogenic transmission electron microscopy (HR-cryo-TEM) on the edge of these plate structures revealed multilayer nanostructure composed of lamellar units with interdigitated alkyl chains (Fig. 4c). Further reducing the chain number but keeping the same chain length led to the formation of large sheet structures (Fig. 4d) and hierarchical organizations (Fig. 4e) of the mono-alkylated derivative **4** in 1,4-dioxane at 20°C and 5°C, respectively. Different with above lamellar assemblies in multialkylated C₆₀ derivatives **1–3**, the C₆₀ is in crystalline state with a 2D oblique lattice (Fig. 4f) while alkyl chains are in a noncrystalline state. Therefore, the assemblies of **4** have disordered alkyl tails in the lamellar arrangement at room temperature, which is ascribed to the significant mismatch of the cross section width between the C₆₀ moiety and the single alkyl tail.

Similar with the alkylated-C₆₀, the fulleropyrrolidines without alkyl chains (Fig. 5a) also featured interesting assembly. As shown in Fig. 5b, fulleropyrrolidine attached with a small pyridine group (**7**) formed flowerlike supramolecular architectures in micrometer size by a drop-casting method [69]. The X-ray

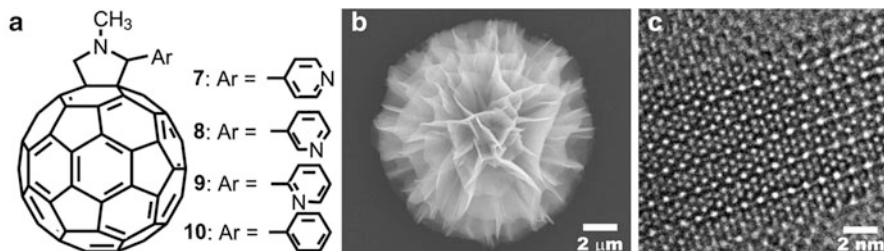


Fig. 5 (a) Chemical structures of fulleropyrrolidine derivatives 7–10; (b) SEM and (c) HR-cryo-TEM images of 7 formed by a drop-casting method. Reprint with permission from [69]

diffraction (XRD), small-angle X-ray scattering (SXAS), and HR-cryo-TEM (Fig. 5c) revealed a bilayer subunit in the flowerlike assemblies, with face-to-face conformation of the substituent of C₆₀ and an interdigitation of the bare C₆₀ side. The morphology can be facily tuned from flowerlike shape (7) to sphere of plates (8) and rod (9 and 10) by adjusting the pyridine's nitrogen position (Fig. 5a). UV–vis spectra indicated the charge transfer interaction between electron donor pyridine and electron acceptor C₆₀, which might contribute to the flowerlike organization with nanometer-scale lamellar conformation. Moreover, the flowerlike assemblies show photoinduced carrier-transporting properties comparable with pristine C₆₀. The resulted assemblies with high C₆₀ content (84 %) and photoconductive feature may provide a useful molecular design concept for further optoelectronic applications [70].

3.2 Morphology-Related Functions

Similar with lotus leaf in nature, the materials surface with low surface energy and a rough fractal interfacial morphology may display superhydrophobicity [2, 71, 72]. Such surface exhibits a water contact angle above 150°, with air trapped within the rough surface. The well-defined supramolecular object of alkylated-C₆₀ exhibits great potential to be the superhydrophobic materials.

An alkylated C₆₀ derivative (2) in 1,4-dioxane by heating and then cooling to around 20°C, assembled into microparticles with wrinkled, nanoflaked structures at the outer surface (Fig. 6a) [73]. As imaged by HR-cryo-TEM at 4 K, the edges of the flakes are multilayer nanostructures comprised of lamellar bilayer assemblies (Fig. 6b). Fast Fourier transform (FFT) analysis shows a lamellar region with a periodicity value of 4.4 nm, corresponding to the length of a bilayer of interdigitated eicosyloxy chains. The assembled objects have high potential to be useful supramolecular materials because of their high quantitative yields from the molecule and their ease of fabrication onto a substrate. Thin films of these globular objects have a lotus leaflike fractal surface morphology, possessing two-tier roughness on nano/micrometer length scales. The hydrophobic feature and the two-tier roughness resulted in an

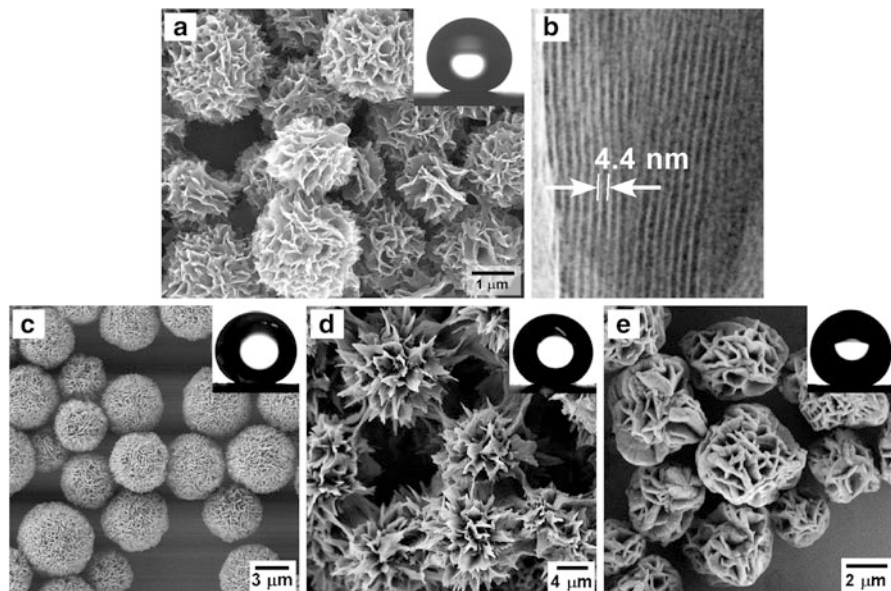


Fig. 6 SEM images of **2** from (a) 1,4-dioxane, (c) *n*-decane, (d) *n*-dodecane, and (e) **5** from diethoxyethane. The insets show water droplets with static water contact angles: (a) 152°, (c) 163°, (d) 164°, and (e) 148°, respectively; (b) HR-cryo-TEM image of a flake edge of (a). Reprint with permission from [68] and [73]

improved water-repellent ability. Thus, a superhydrophobic surface with a water contact angle of 152° was achieved from the thin film of the global objects, while a simple spin-coated film exhibits a water contact angle of only 103°.

It is interesting to explore whether C₆₀ or the alkyl chain part in self-assembled particles is exposed at the outer surface in the superhydrophobic films. Therefore, nonpolar solvents such as *n*-decane (*n*-C₁₀H₂₂) or *n*-dodecane (*n*-C₁₂H₂₆) were chosen for the assembly of C₆₀ derivative **2** [68]. In both solvents, microparticles in 5–10 μm in diameter with nanoflaked outer surfaces were obtained as precipitates which showed water contact angles of 163° and 164°, respectively (Fig. 6c, d). The higher contact angle values for the assemblies from nonpolar solvents could be attributed to the presence of more hydrophobic hydrocarbon tails compared to the moderately hydrophobic C₆₀ on the outer surface of the objects [45, 74, 75]. Therefore, it is speculated that the C₆₀ part is exposed to the outer surface in polar solvents such as 1,4-dioxane, while hydrocarbon tails exposed to the outer surface in nonpolar solvents.

The replacement of the hydrocarbon chains with more hydrophobic fluorinated tails with low surface free energy gives more evidence for the above speculation. The self-assembly of the C₆₀ derivative (**5**) with three semiperfluoroalkyl chains in diethoxyethane resulted in the formation of several micrometer (2–5 μm) sized particles with nanoflaked outer morphology (Fig. 6e) and lamellar arrangement at the molecular level [68]. The assembled structures exhibited a water contact angle

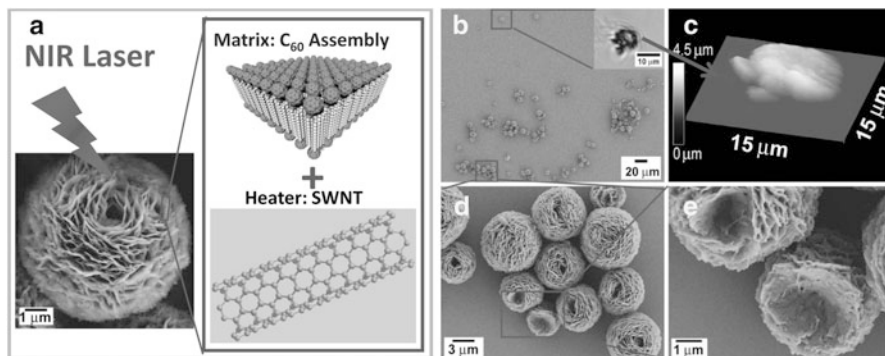


Fig. 7 (a) Schematic illustration of 1-SWNT assembly; (b) SEM image of 1-SWNT assembly. *Inset* shows the optical image of an assembly illuminated by an NIR laser (90 mW); (c) AFM image of the same 1-SWNT assembly as in the inset to (b); (d) SEM image of zoomed-in area of (b) selectively illuminated by an NIR laser (50 mW) and (e) the enlarged area of (d). Reprint with permission from [80]

of 148° , which is comparable to that of assemblies formed by the hydrocarbon derivative (2) in 1,4-dioxane. Moreover, the assembly does not have an oil-repellent performance. These results indicate that similar to the hydrocarbon derivatives, in assemblies obtained from polar solvents, the C_{60} moieties are exposed to the outer surface of the nanoflake-structured microparticles, contributing to the water-repellent surface features.

3.3 *Supramolecular Composites*

Except the water-repellent features, the assembly of C_{60} derivatives also provides a model for some photophysics studies. Single-wall carbon nanotubes (SWNT) can absorb near-infrared (NIR) light, rapidly transferring electronic excitations into molecular vibration energies which induce heat [76, 77]. This photothermal phenomenon has great potential for a wide range of applications such as drug delivery systems and cancer therapies [78, 79]. In practical applications, a proper temperature range is required for each case. The temperature change generated by laser-induced heating of SWNT is generally considered to be on the order of several tens of degrees centigrade, but it has not been clear whether it can reach even higher temperatures. In this context, the microparticles or microplates containing C_{60} derivatives (1–3) and SWNT have been developed as a temperature indicator [80]. In these microparticles or microplates, SWNT is used as a light antenna and C_{60} derivatives as a matrix (Fig. 7a). The concept is based upon the notion that temperature rise can be confirmed via the melt-induced morphological change of “nanocarbons” assembly.

The microparticles of C₆₀ derivative **2** and SWNT (Fig. 7a) prepared from 1,4-dioxane have the similar morphology with those of only **2** (Fig. 7a) [73]. HR-cryo-TEM, FTIR, and XRD studies confirmed that the assembled molecular structures are also similar to those of **2** from 1,4-dioxane. Upon NIR laser illumination at 50 mW, the flake-shaped surfaces of **2**-SWNT assemblies started to “deform” (Fig. 7d, e). When increasing the laser power to 90 mW, the microparticles were destroyed immediately (Fig. 7b, c). In contrast, the microparticles that only composed of **2** did not respond to the laser illumination. It indicates that the heating due to the photothermal conversion of SWNT reaches the melting point of **2** (around 190°C, revealed by differential scanning calorimetry (DSC)).

The investigation with coassemblies comprising SWNT and other C₆₀ derivatives (**1** and **3**), possessing higher melting points, indicated that the NIR irradiation of a fullerene–SWNT assembly can reach a local temperature in excess of around 220°C. The deformation of the micrometer-scale fullerene–SWNT assembly can easily be visualized by optical microscopy, thus providing great convenience in monitoring temperature in situ during photothermal conversion. Moreover, the assembly melting point can be tuned to a desired range by selecting an appropriate C₆₀ derivative alkyl chain length or number of alkyl chains (**1–3**). Thus, fullerene–SWNT assembly provides an unambiguous way to confirm the temperature rise upon NIR light irradiation.

4 Soft to Hard: Plasticization and Metallization

In spite of various interesting and fascinating organizations and functions, the fragileness of supramolecular objects, due to weak noncovalent interactions within assemblies, limits their potential applications. Therefore, in general, it is crucial to seek a solution for such issue in organic self-organized materials. As a result, photo-cross-linking was proposed as one of the effective approaches to improve the stability of the assemblies without changing the assembled nanostructure, surface morphology, and properties [81]. The molecular design is based on an alkyl-conjugated C₆₀ with diacetylene functional groups in long alkyl chains (**6**). The self-assembly of the C₆₀ derivative from THF–methanol mixture exhibited flake-shaped microparticles in 1 μm size with a bilayer subunit structure. Applying UV light led to the polymerization of diacetylene and C₆₀ moieties, but maintained the assembly morphology (Fig. 8). Remarkably, the cross-linked flake-shaped microparticles exhibited a significantly enhanced chemical and mechanical robustness against acidic, basic aqueous media or polar, good organic solvents for the monomer, as well as heat (up to 200°C). Moreover, the stiffness was enhanced about 25-fold as confirmed by AFM force spectroscopy. The water contact angle measurement shows that the film of flaked microparticles exhibited water-repellent property with a value around 146° [81]. The highly durable surface of cross-linked flake-shaped microparticles satisfies some of the requirements for water-repellent materials, such as substrate-independent production, high durability, and enhanced mechanical stiffness, which is promising for coating technologies in micro- or nano-electromechanical systems.

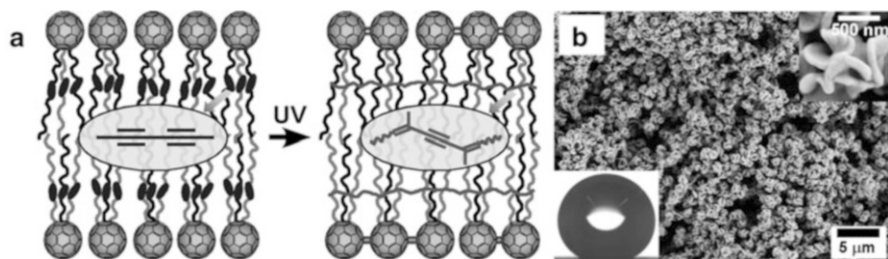
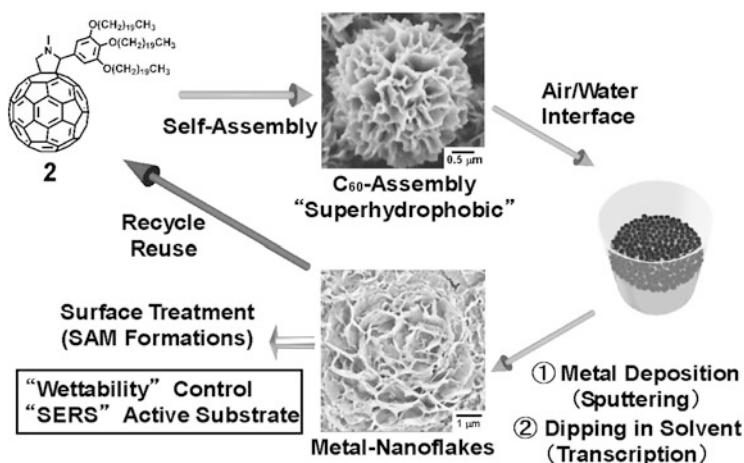


Fig. 8 (a) Scheme of the photo-cross-linking process in the bilayer structural subunit of **6**; (b) SEM image of **6** prepared from THF/MeOH solution. The inset shows an enlarged particle image and a water droplet with static water contact angle around 146° . Reprint with permission from [81]



Scheme 3 Schematic representation of the key steps for the synthesis of Au nanoflake surfaces by using supramolecular architectures of fullerene derivative **2** as templates. Reprint with permission from [83]

Another alternative to transform the supramolecular soft mater into hard mater is metallization. Supramolecular architectures with structural diversity offer a generic path towards a broad range of high-definition templates for the design and synthesis of functional metallic nanostructures. C_{60} -based microparticles with 3D nanoflake outer surface structure of **2** were used as template to transform into various metals (Scheme 3). By sputtering desired metal (e.g., Au, Pt, Ti, Ni, Ag) onto the film of supramolecular objects, the metallic nanoflaked surface was obtained by subsequently removing the template [82, 83]. The whole process is sustainable since the template can be recovered by dissolving in good solvents such as $CHCl_3$. The resulting nanoflaked Au surface exhibits enhanced plasmonic effect, where the enhancement factor was on an order of 10^5 for surface-enhanced Raman scattering (SERS). Moreover, the wettability of the resulting metal nano/macrometric surface is tunable from superhydrophilic to superhydrophobic by modifying molecules with different surface free energy [83].

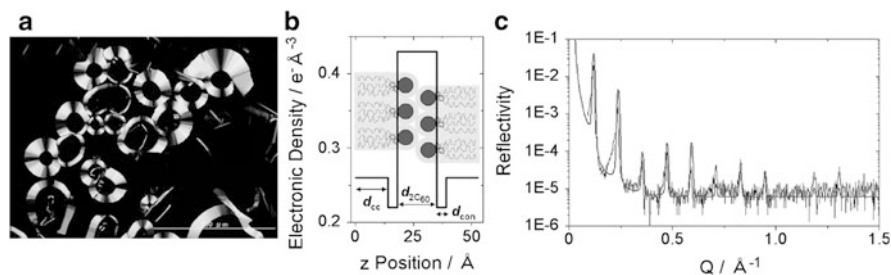


Fig. 9 (a) Polarizing optical micrographic texture of mesophase of **2** at 190°C; (b) three-box electronic density profile and (c) comparison between the corresponding model and the experimental X-ray diffraction pattern of **2** in the mesophase. Reprint with permission from [90] and [91]

5 Exotic Fluid Materials

5.1 Liquid Crystalline Assemblies

Liquid crystal (LC) is a state of matter that has properties between those of a conventional liquid and a solid crystal within a proper temperature range. C_{60} is one kind of promising electron transport materials as an *n*-type semiconductor [84, 85]. Recently, C_{60} -based LCs have been found applications in various areas such as photovoltaics because of the self-organization at molecular level in a predetermined and controllable fashion [86–89].

To achieve high carrier mobility is one of the basic requirements in LCs and is of fundamental importance in optoelectronic device applications, where the main factors may include close molecular packing, highly ordered structures, and extended π conjugation. The recent work from our group revealed that the alkyl-conjugated C_{60} derivatives (**1–3**) with high C_{60} content (up to 50 %) satisfy the requirements for high carrier mobility in the highly ordered mesophase [90]. Polarized optical microscopic (POM) studies of **2** show fluid and birefringent optical texture in the wide temperature range between 62°C and 193°C (Fig. 9a). The XRD pattern at 185°C shows a large number of diffraction peaks assigned from (0 0 1) up to (0 0 14). In order to explain the change of the relative intensity of the Bragg peaks in the XRD pattern, simple boxlike electronic density profile models were proposed [91]. The molecules arrange themselves in an unusually long-range ordered lamellar mesophase, where their long axis oriented and on average perpendicular to the plane of the layers and C_{60} moieties in a head-to-head configuration (Fig. 9b, c). The mesomorphic C_{60} derivative of **2** exhibits reversible redox activity as cast films on a glassy carbon electrode above the solid/mesomorphic phase transition temperatures, e.g., at 70°C. The electron mobility of **2** was found to be $\sim 3 \times 10^{-3} \text{ cm}^2 \text{ V}^{-1} \text{ s}^{-1}$ from a time-of-flight (ToF) measurement, indicating that dense-packed C_{60} molecules carried charges. This mobility value is comparable to those of smectic liquid crystalline phase of organic semiconductor oligomers and columnar LCs [92, 93]. The simple

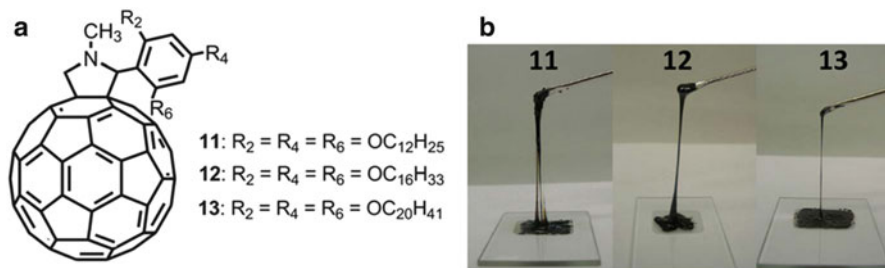


Fig. 10 (a) Chemical structures of liquid C_{60} derivatives **11–13**; (b) photos of liquid C_{60} derivatives **11–13**. Reprint with permission from [94]

modification of C_{60} by long alkyl chains permits a high C_{60} content in the mesomorphic materials, resulting in so far the largest electron mobility value for C_{60} -containing liquid crystals.

5.2 Room Temperature Liquid Fullerenes

Adjusting the position of the alkyl chains on the alkylated C_{60} can influence the intermolecular interaction between C_{60} derivatives and the resulting properties. For example, the fulleropyrrolidines substituted with a 2,4,6-tris(alkyloxy)phenyl group (**11**, **12**, **13**) were fluids at room temperature (Fig. 10) [94]. By such a substitution, alkyl chains can spread independently to prevent the aggregation of the C_{60} moieties. By a systematic investigation of the fluid behavior of liquid fullerenes and their functions, it is found that the viscosity of the liquids can be controlled by changing the length of the introduced alkyl chain. Interestingly, the greater alkyl chain length reduces efficiently the viscosity, which is completely an opposite trend of a phenomenon of viscosity in normal alkane molecules. The rheology studies show that the viscosity decreases with the increase of the alkyl chain length ($\sim 1.2 \times 10^5$, 1.3×10^4 , and 1.1×10^3 Pa·s for **11**, **12**, and **13**, respectively). The reason might be that the longer alkyl chains more effectively disturb the π - π interaction in neighboring C_{60} molecules, increasing the fluidity. In addition, the redox properties of C_{60} and their relatively high hole mobility (e.g., $3 \times 10^{-2} \text{ cm}^2 \text{ V}^{-1} \text{ s}^{-1}$ for **13**) make them attractive as exotic fluid nanocarbon materials for future electronic applications.

6 Conclusion

The novel concept of “amphiphilicity” for the design of C_{60} derivatives, by combining π - π interaction from C_{60} moieties and van der Waals interaction from long alkyl chains, allows the fabrication of various long-range ordered

superstructures. Even though both C_{60} and long alkyl chains are hydrophobic, C_{60} is relatively less hydrophobic than alkyl chains [45], which featured the alkylated C_{60} amphiphilicity. These alkyl-conjugated C_{60} derivatives exhibited supramolecular polymorphism upon slightly varying the assembly environment or molecular design (the number or length of the alkyl chains or the type of the alkyl chains on the phenyl group of the C_{60} derivative). Based on the unique properties and morphologies, various exotic organic soft materials such as superhydrophobic surfaces, photoconductive liquid crystals, room temperature liquids, and temperature indicators for CNT local heating were constructed. The methodology described here could be adopted for the development of other organic materials with controlled dimensionality and desired functions. In fact, some fullerene derivatives [95, 96], emissive extended π -conjugated molecules [97, 98], and others [99, 100] have followed similar alkylation strategy onto π -conjugated functional units and contributed great progress in the applications of supramorphological exotic organic materials.

Acknowledgements This work was supported, in part, by KAKENHI from MEXT and “PRESTO,” JST, Japan. We also thank the support of Kato Foundation, Japan. Y.S. gratefully acknowledges JSPS for the Postdoctoral Fellowships for Foreign Researchers. The authors are grateful to their co-workers and colleagues who kindly provided original photos and images illustrated here.

References

1. Ariga K, Hill JP, Lee MV et al (2008) Challenges and breakthroughs in recent research on self-assembly. *Sci Technol Adv Mater* 9:014109
2. Li XM, Reinhoudt D, Crego-Calama M (2007) What do we need for a superhydrophobic surface? A review on the recent progress in the preparation of superhydrophobic surfaces. *Chem Soc Rev* 36:1350–1368
3. Liu KS, Yao X, Jiang L (2010) Recent developments in bio-inspired special wettability. *Chem Soc Rev* 39:3240–3255
4. Anzenbacher P, Lubal P, Bucek P et al (2010) A practical approach to optical cross-reactive sensor arrays. *Chem Soc Rev* 39:3954–3979
5. Tran HD, Li D, Kaner RB (2009) One-dimensional conducting polymer nanostructures: bulk synthesis and applications. *Adv Mater* 21:1487–1499
6. Vijayakumar C, Tobin G, Schmitt W et al (2010) Detection of explosive vapors with a charge transfer molecule: self-assembly assisted morphology tuning and enhancement in sensing efficiency. *Chem Commun* 46:874–876
7. Kim HS, Jeon EK, Kim JJ et al (2008) Air-stable n-type operation of Gd-contacted carbon nanotube field effect transistors. *Appl Phys Lett* 93:123106
8. Zhang YJ, Shen YF, Han DX et al (2006) Reinforcement of silica with single-walled carbon nanotubes through covalent functionalization. *J Mater Chem* 16:4592–4597
9. Liu G, Ling Q-D, Teo EYH et al (2009) Electrical conductance tuning and bistable switching in poly(N-vinylcarbazole)–carbon nanotube composite films. *ACS Nano* 3:1929–1937
10. Hasegawa M, Iyoda M (2010) Conducting supramolecular nanofibers and nanorods. *Chem Soc Rev* 39:2420–2427

11. Babu SS, Möhwald H, Nakanishi T (2010) Recent progress in morphology control of supramolecular fullerene assemblies and its applications. *Chem Soc Rev* 39:4021–4035
12. Sergeev S, Pisula W, Geerts YH (2007) Discotic liquid crystals: a new generation of organic semiconductors. *Chem Soc Rev* 36:1902–1929
13. Fan J, Boettcher SW, Tsung CK et al (2008) Field-directed and confined molecular assembly of mesostructured materials: basic principles and new opportunities. *Chem Mater* 20:909–921
14. Harada A, Kobayashi R, Takashima Y et al (2011) Macroscopic self-assembly through molecular recognition. *Nat Chem* 3:34–37
15. Virkar AA, Mannsfeld S, Bao ZA et al (2010) Organic semiconductor growth and morphology considerations for organic thin-film transistors. *Adv Mater* 22:3857–3875
16. Guldi DM, Illescas BM, Atienza CM et al (2009) Fullerene for organic electronics. *Chem Soc Rev* 38:1587–1597
17. Wu WP, Liu YQ, Zhu DB (2010) pi-Conjugated molecules with fused rings for organic field-effect transistors: design, synthesis and applications. *Chem Soc Rev* 39:1489–1502
18. Diederich F, Whetten RL (1991) C₆₀-from soot to superconductors. *Angew Chem Int Ed* 30:678–680
19. Allemand PM, Khemani KC, Koch A et al (1991) Organic molecular soft ferromagnetism in a fullerene-C₆₀. *Science* 253:301–303
20. Stephens PW, Cox D, Lauher JW et al (1992) Lattice structure of the fullerene ferromagnet TDAE-C₆₀. *Nature* 355:331–332
21. Bhushan B, Gupta BK, Vancleef GW et al (1993) Fullerene (C₆₀) films for solid lubrication. *Tribol T* 36:573–580
22. Giacalone F, Martin N (2010) New concepts and applications in the macromolecular chemistry of fullerenes. *Adv Mater* 22:4220–4248
23. Miyazawa K, Kuwasaki Y, Obayashi A et al (2002) C₆₀ nanowhiskers formed by the liquid-liquid interfacial precipitation method. *J Mater Res* 17:83–88
24. Miyazawa K (2009) Synthesis and properties of fullerene nanowhiskers and fullerene nanotubes. *J Nanosci Nanotechnol* 9:41–50
25. Jin YZ, Curry RJ, Sloan J et al (2006) Structural and optoelectronic properties of C-60 rods obtained via a rapid synthesis route. *J Mater Chem* 16:3715–3720
26. Wang L, Liu B, Liu D et al (2006) Synthesis of thin, rectangular C₆₀ nanorods using *m*-xylene as a shape controller. *Adv Mater* 18:1883–1888
27. Sathish M, Miyazawa K (2007) Size-tunable hexagonal fullerene (C₆₀) nanosheets at the liquid-liquid interface. *J Am Chem Soc* 129:13816–13817
28. Sathish M, Miyazawa K, Sasaki T (2007) Nanoporous fullerene nanowhiskers. *Chem Mater* 19:2398–2400
29. Tan ZQ, Masuhara A, Kasai H et al (2007) Multibranching C₆₀ micro/nanocrystals fabricated by reprecipitation method. *Jpn J Appl Phys* 47:1426–1428
30. Masuhara A, Tan ZQ, Kasai H et al (2009) Fullerene fine crystals with unique shapes and controlled size. *Jpn J Appl Phys* 48:050206–050209
31. Liu H, Li Y, Jiang L et al (2002) Imaging as-grown [60]fullerene nanotubes by template technique. *J Am Chem Soc* 124:13370–13371
32. Ji HX, Hu JS, Tang QX et al (2007) Controllable preparation of submicrometer single-crystal C₆₀ rods and tubes through concentration depletion at the surfaces of seeds. *J Phys Chem C* 111:10498–10502
33. Zhang X, Takeuchi M (2009) Controlled fabrication of fullerene C₆₀ into microspheres of nanoplates through porphyrin-polymer-assisted self-assembly. *Angew Chem Int Ed* 48:9646–9651
34. Nurmawati MH, Ajikumar PK, Renu R et al (2008) Amphiphilic poly(*p*-phenylene)-driven multiscale assembly of fullerenes to nanowhiskers. *ACS Nano* 2:1429–1436

35. Fernández G, Sánchez L, Pérez EM et al (2008) Large exTTF-Based dendrimers. self-assembly and peripheral cooperative multienapsulation of C₆₀. *J Am Chem Soc* 130:10674–10683
36. Kawauchi T, Kumaki J, Kitaura A et al (2008) Encapsulation of fullerenes in a helical PMMA cavity leading to a robust processable complex with a macromolecular helicity memory. *Angew Chem Int Ed* 47:515–519
37. Kawauchi T, Kitaura A, Kumaki J et al (2008) Helix-sense-controlled synthesis of optically active poly(methyl methacrylate) stereocomplexes. *J Am Chem Soc* 130:11889–11891
38. Nielsen KA, Cho W-S, Sarova GH et al (2006) Supramolecular receptor design: anion-triggered binding of C₆₀. *Angew Chem Int Ed* 45:6848–6853
39. Li M, Deng K, Lei S-B et al (2008) Site-selective fabrication of two-dimensional fullerene arrays by using a supramolecular template at the liquid–solid interface. *Angew Chem Int Ed* 47:6717–6721
40. Bonifazi D, Spillmann H, Kiebele A et al (2004) Supramolecular patterned surfaces driven by cooperative assembly of C₆₀ and porphyrins on metal substrates. *Angew Chem Int Ed* 43:4759–4763
41. Song T, Dai S, Tam KC et al (2003) Aggregation behavior of C₆₀-end-capped poly(ethylene oxide)s. *Langmuir* 19:4798–4803
42. Angelini G, De Maria P, Fontana A et al (2001) Study of the aggregation properties of a novel amphiphilic C₆₀ fullerene derivative. *Langmuir* 17:6404–6407
43. Schade B, Ludwig K, Böttcher C et al (2007) Supramolecular structure of 5-nm spherical micelles with D₃ symmetry assembled from amphiphilic [3:3]-hexakis adducts of C₆₀. *Angew Chem Int Ed* 46:4393–4396
44. Nakanishi T (2010) Supramolecular soft and hard materials based on self-assembly algorithms of alkyl-conjugated fullerenes. *Chem Commun* 46:3425–3436
45. Asanuma H, Li HG, Nakanishi T et al (2010) Fullerene derivatives that bear aliphatic chains as unusual surfactants: hierarchical self-organization, diverse morphologies, and functions. *Chem Eur J* 16:9330–9338
46. Kudernac T, Lei S, Elemans JAAW et al (2009) Two-dimensional supramolecular self-assembly: nanoporous networks on surfaces. *Chem Soc Rev* 38:402–421
47. Yang YL, Wang C (2009) Hierarchical construction of self-assembled low-dimensional molecular architectures observed by using scanning tunneling microscopy. *Chem Soc Rev* 38:2576–2589
48. Sanchez L, Otero R, Gallego JM et al (2009) Ordering fullerenes at the nanometer scale on solid surfaces. *Chem Rev* 109:2081–2091
49. Sánchez L, Otero R, Gallego JMA et al (2009) Ordering fullerenes at the nanometer scale on solid surfaces. *Chem Rev* 109:2081–2091
50. Wei Y, Robey SW, Reutt-Robey JE (2009) TiOPc molecular dislocation networks as nanotemplates for C₆₀ cluster arrays. *J Am Chem Soc* 131:12026–12027
51. Écija D, Otero R, Sánchez L et al (2007) Crossover site-selectivity in the adsorption of the fullerene derivative PCBM on Au(111). *Angew Chem Int Ed* 46:7874–7877
52. Uemura S, Sakata M, Taniguchi I et al (2001) Novel “Wet process” technique based on electrochemical replacement for the preparation of fullerene epitaxial adlayers. *Langmuir* 17:5–7
53. Tsunashima R, Noro S, Akutagawa T et al (2008) Fullerene nanowires: self-assembled structures of a low-molecular-weight organogelator fabricated by the Langmuir–Blodgett method. *Chem Eur J* 14:8169–8176
54. Bottari G, Olea D, Gómez-Navarro C et al (2008) Highly conductive supramolecular nanostructures of a covalently linked phthalocyanine-C₆₀ fullerene conjugate. *Angew Chem Int Ed* 47:2026–2031
55. Chen L, Chen W, Huang H et al (2008) Tunable arrays of C₆₀ molecular chains. *Adv Mater* 20:484–488

56. Qiu X, Wang C, Zeng Q et al (2000) Alkane-assisted adsorption and assembly of phthalocyanines and porphyrins. *J Am Chem Soc* 122:5550–5556
57. Rabe JP, Buchholz S (1991) Commensurability and mobility in 2-dimensional molecular-patterns on graphite. *Science* 253:424–427
58. Spada GP, Lena S, Masiero S et al (2008) Guanosine-based hydrogen-bonded scaffolds: controlling the assembly of oligothiophenes. *Adv Mater* 20:2433–2438
59. Wei Y, Tong W, Zimmt MB (2008) Self-assembly of patterned monolayers with nanometer features: molecular selection based on dipole interactions and chain length. *J Am Chem Soc* 130:3399–3405
60. Severin N, Rabe JP, Kurth DG (2004) Fully extended polyelectrolyte-amphiphile complexes adsorbed on graphite. *J Am Chem Soc* 126:3696–3697
61. Lei SB, Tahara K, De Schryver FC et al (2008) One building block, two different supramolecular surface-confined patterns: concentration in control at the solid–liquid interface. *Angew Chem Int Ed* 47:2964–2968
62. Nakanishi T, Miyashita N, Michinobu T et al (2006) Perfectly straight nanowires of fullerenes bearing long alkyl chains on graphite. *J Am Chem Soc* 128:6328–6329
63. Nakanishi T, Takahashi H, Michinobu T et al (2008) Fullerene nanowires on graphite: epitaxial self-organizations of a fullerene bearing double long-aliphatic chains. *Colloids Surf A* 321:99–105
64. Nakanishi T, Takahashi H, Michinobu T et al (2008) Fine-tuning supramolecular assemblies of fullerenes bearing long alkyl chains. *Thin Solid Films* 516:2401–2406
65. Nakanishi T, Schmitt W, Michinobu T et al (2005) Hierarchical supramolecular fullerene architectures with controlled dimensionality. *Chem Commun* 5982–5984
66. Nakanishi T, Ariga K, Michinobu T et al (2007) Flower-shaped supramolecular assemblies: hierarchical organization of a fullerene bearing long aliphatic chains. *Small* 3:2019–2023
67. Nakanishi T, Wang JB, Mohwald H et al (2009) Supramolecular shape shifter: polymorphs of self-organized fullerene assemblies. *J Nanosci Nanotechnol* 9:550–556
68. Nakanishi T, Shen YF, Wang JB et al (2010) Superstructures and superhydrophobic property in hierarchical organized architectures of fullerenes bearing long alkyl tails. *J Mater Chem* 20:1253–1260
69. Zhang X, Nakanishi T, Ogawa T et al (2010) Flowerlike supramolecular architectures assembled from C₆₀ equipped with a pyridine substituent. *Chem Commun* 46:8752–8754
70. Babu SS, Saeki A, Seki S et al (2011) Millimeter-sized flat crystalline sheet architectures of fullerene assemblies with anisotropic photoconductivity. *Phys Chem Chem Phys* 13:4830–4834
71. Srinivasan S, Praveen VK, Philip R et al (2008) Bioinspired superhydrophobic coatings of carbon nanotubes and linear pi systems based on the "bottom-up" self-assembly approach. *Angew Chem Int Ed* 47:5750–5754
72. Feng XJ, Jiang L (2006) Design and creation of superwetting/antiwetting surfaces. *Adv Mater* 18:3063–3078
73. Nakanishi T, Michinobu T, Yoshida K et al (2008) Nanocarbon superhydrophobic surfaces created from fullerene-based hierarchical supramolecular assemblies. *Adv Mater* 20:443–446
74. Yang L, Shirahata N, Saini G et al (2009) Effect of surface free energy on PDMS transfer in microcontact printing and its application to ToF-SIMS to probe surface energies. *Langmuir* 25:5674–5683
75. Mouri E, Nakanishi T, Nakashima N et al (2002) Nanostructure of fullerene-bearing artificial lipid monolayer on water surface by in situ X-ray reflectometry. *Langmuir* 18:10042–10045
76. Miyako E, Nagata H, Hirano K et al (2008) Carbon nanotube-polymer composite for light-driven microthermal control. *Angew Chem Int Ed* 47:3610–3613
77. Singh P, Campidelli S, Giordani S et al (2009) Organic functionalisation and characterisation of single-walled carbon nanotubes. *Chem Soc Rev* 38:2214–2230
78. Kam NWS, O'Connell M, Wisdom JA et al (2005) Carbon nanotubes as multifunctional biological transporters and near-infrared agents for selective cancer cell destruction. *Proc Natl Acad Sci U S A* 102:11600–11605

79. Ghosh S, Dutta S, Gomes E et al (2009) Increased heating efficiency and selective thermal ablation of malignant tissue with DNA-encased multiwalled carbon nanotubes. *ACS Nano* 3:2667–2673
80. Shen Y, Skirtach AG, Seki T et al (2010) Assembly of fullerene-carbon nanotubes: temperature indicator for photothermal conversion. *J Am Chem Soc* 132:8566–8568
81. Wang J, Shen Y, Kessel S et al (2009) Self-assembly made durable: water-repellent materials formed by cross-linking fullerene derivatives. *Angew Chem Int Ed* 48:2166–2170
82. Sezer M, Feng JJ, Ly HK et al (2010) Multi-layer electron transfer across nanostructured Ag-SAM-Au-SAM junctions probed by surface enhanced Raman spectroscopy. *Phys Chem Chem Phys* 12:9822–9829
83. Shen Y, Wang J, Kuhlmann U et al (2009) Supramolecular templates for nanoflake-metal surfaces. *Chem Eur J* 15:2763–2767
84. Sariciftci NS, Braun D, Zhang C et al (1993) Semiconducting polymer-buckminsterfullerene heterojunctions-diodes, photodiodes and photovoltaic cells. *Appl Phys Lett* 62:585–587
85. Morana M, Wegscheider M, Bonanni A et al (2008) Bipolar charge transport in PCPDTBT-PCBM bulk-heterojunctions for photovoltaic applications. *Adv Funct Mater* 18:1757–1766
86. Li WS, Yamamoto Y, Fukushima T et al (2008) Amphiphilic molecular design as a rational strategy for tailoring bicontinuous electron donor and acceptor arrays: photoconductive liquid crystalline oligothiophene-C₆₀ dyads. *J Am Chem Soc* 130:8886–8887
87. Li C-Z, Matsuo Y, Nakamura E (2009) Luminescent bow-tie-shaped decaaryl[60]fullerene mesogens. *J Am Chem Soc* 131:17058–17059
88. Lenoble J, Campidelli S, Maringa N et al (2007) Liquid–crystalline Janus-type fullerodendrimers displaying tunable smectic–columnar mesomorphism. *J Am Chem Soc* 129:9941–9952
89. Sp C, Bourgun P, Guintchin B et al (2010) Diastereoisomerically pure fulleropyrrolidines as chiral platforms for the design of optically active liquid crystals. *J Am Chem Soc* 132:3574–3581
90. Nakanishi T, Shen Y, Wang J et al (2008) Electron transport and electrochemistry of mesomorphic fullerenes with long-range ordered lamellae. *J Am Chem Soc* 130:9236–9237
91. Fernandes PAL, Yagai S, Möhwald H et al (2009) Molecular arrangement of alkylated fullerenes in the liquid crystalline phase studied with X-ray diffraction. *Langmuir* 26:4339–4345
92. Funahashi M, Hanna JI (2005) High carrier mobility up to 0.1 cm² V⁻¹ s⁻¹ at ambient temperatures in thiophene-based smectic liquid crystals. *Adv Mater* 17:594–598
93. Tuladhar SM, Poplavskyy D, Choulis SA et al (2005) Ambipolar charge transport in films of methanofullerene and poly(phenylenevinylene)/methanofullerene blends. *Adv Funct Mater* 15:1171–1182
94. Michinobu T, Nakanishi T, Hill J et al (2006) Room temperature liquid fullerenes: an uncommon morphology of C₆₀ derivatives. *J Am Chem Soc* 128:10384–10385
95. Li C-Z, Matsuo Y, Nakamura E (2010) Octupole-like supramolecular aggregates of conical iron fullerene complexes into a three-dimensional liquid crystalline lattice. *J Am Chem Soc* 132:15514–15515
96. Gayathri SS, Patnaik A (2007) Aggregation of a C₆₀–didodecyloxybenzene dyad: structure, dynamics, and mechanism of vesicle growth. *Langmuir* 23:4800–4808
97. Yagai S, Kinoshita T, Higashi M et al (2007) Diversification of self-organized architectures in supramolecular dye assemblies. *J Am Chem Soc* 129:13277–13287
98. Wang J-Y, Yan J, Ding L et al (2009) One-dimensional microwires formed by the co-assembly of complementary aromatic donors and acceptors. *Adv Funct Mater* 19:1746–1752
99. Maeda H, Haketa Y, Nakanishi T (2007) Aryl-substituted C₃-bridged oligopyrroles as anion receptors for formation of supramolecular organogels. *J Am Chem Soc* 129:13661–13674
100. Yamamoto Y, Zhang G, Jin W et al (2009) Ambipolar-transporting coaxial nanotubes with a tailored molecular graphene–fullerene heterojunction. *Proc Natl Acad Sci U S A* 106:21051–21056

C₆₀ Fullerene Amphiphiles as Supramolecular Building Blocks for Organized and Well-Defined Nanoscale Objects

Yuming Zhao and Guang Chen

Abstract Fullerene-based nanomaterials have attracted extensive interest owing to their wide-ranging applications in materials science, nanotechnology, and biomedical research. This chapter gives an updated review of the recent advance in the design and characterization of fullerene derivatives as supramolecular building blocks for ordered and well-defined nanostructures and objects. The discussions are specially concentrated on the structural and morphological properties of discrete nano-aggregates by various amphiphilic fullerene derivatives formed in solution or at interfaces. Rationalization of the aggregation structure and morphology is attempted on the basis of amphiphilic molecular packing theories so as to shed light on the interplay between molecular factors (e.g., shape, polarity, non-covalent forces, and amphiphilicity) and self-assembly outcomes. Overall, this literature survey is aimed at mapping out applicable “bottom-up” strategies to control and preprogram the nanoscopic ordering of fullerene-based nanomaterials.

Keywords Amphiphile · Fullerene · Molecular packing · Nanomaterials · Self-assembly

Contents

1	Introduction	24
2	Molecular Packing of Amphiphiles	25
3	Nano-Aggregates Assembled by C ₆₀ Amphiphiles Bearing Chain-Like Polar Appendages	27
4	Nano-Aggregates Assembled by C ₆₀ Amphiphiles Bearing Branched or Dendritic Polar Appendages	34

5 Nano-Aggregates Assembled by Amphiphilic Hexakis Adducts of C_{60}	45
6 Summary and Outlook	48
References	49

1 Introduction

Fullerenes constitute a fascinating class of molecular building blocks for the synthesis and fabrication of advanced nanoscale materials and devices [1–3]. In particular, C_{60} buckminsterfullerene has found a wide range of applications in various fields of modern nano-science and technology, owing to its extremely small size (0.498 nm in radius), highly symmetrical (I_h) molecular shape, and very rich electronic properties in both the ground and excited states [4]. Prominent examples of utilizing fullerene-based materials in cutting-edge research and applications include plastic solar cells, artificial photosynthetic mimicking, photodynamic therapy, gene delivery, molecular electronics, and nanomachinery, to name a few.

Over the past two decades, the covalent chemistry of C_{60} has evolved enormously, empowering synthetic chemists nowadays to flexibly modify the C_{60} structure with a vast array of molecular attachments ranging from organic and inorganic functional groups to macromolecular (e.g., polymers and dendrimers) moieties [5, 6]. In the current literature of fullerene chemistry, the synthesis of new fullerene derivatives is still a continuous and mainstream undertaking [7]. Beyond the molecular level, the supramolecular chemistry of C_{60} has also captured considerable attention due to the preponderance of such knowledge in material, biological, and medicinal applications [8–11]. For instance, the microscopic phase segregation of C_{60} acceptor domains in the active layer of bulk heterojunction (BHJ) organic solar cells has been known to exert a key influence on the efficiency of solar energy conversion [12–18]. Water-soluble fullerene derivatives bearing cationic side chains aggregate to form supramolecular self-assemblies with DNA which effectively promote gene transfection in mammalian cells [19, 20]. Nano-aggregates of pristine C_{60} (nC_{60}) have found to exert a negative (cytotoxic) effect on cell viability and antibacterial activity [21–23] while some water-soluble C_{60} derivatives on the contrary show greatly reduced cytotoxicity or non-cytotoxicity [24].

This chapter summarizes the recent studies of well-defined C_{60} nanostructures and objects resulting from supramolecular self-assembly in solution or at interfaces. It should be noted that by no means the review herein is intended to be comprehensive and thorough due to the vastness of pertinent literature. Rather, the discussions will be specifically focused on experimentally observed supramolecular aggregation behaviors of various C_{60} derivatives and relevant theoretical rationalizations. Collectively, this literature survey provides an updated overview to facilitate

the fundamental understanding of sophisticated supramolecular self-assemblies of C₆₀-containing molecules and to guide further exploration in the preparation of controllable and preprogrammable C₆₀-based nanomaterials and nano-devices.

2 Molecular Packing of Amphiphiles

Structurally buckminsterfullerene (C₆₀) is made up of sixty sp² hybridized carbons in a rigid spherical (soccer ball) shape [5]. The extensive π -electron delocalization over the C₆₀ cage renders it chemical reactivities resembling electron-deficient arenes or alkenes [6]. In terms of physical characteristics, C₆₀ has a very large cohesive force and is prone to aggregate significantly in solutions or at interfaces through non-covalent interactions such as π -stacking and van der Waals attraction [25]. As such, the C₆₀ cage is strongly hydrophobic and virtually immiscible in water (2×10^{-24} mol/L) and many polar organic solvents (e.g., 1×10^{-6} mol/L in acetone) [25, 26]. By some special means (e.g., solvent exchange, sonication, extended mixing, or some combination of these techniques) C₆₀ can be effectively suspended in water forming stable colloids (*n*C₆₀), as the clustering of C₆₀ minimizes the thermodynamically disfavored C₆₀-solvent contact [27, 28]. A quantitative understanding of the aggregation behavior and deposition kinetics of C₆₀ particles in aqueous media was recently established by Chen and Elimelech [29]. On the other hand, the solubility of C₆₀ in water or common organic solvents can be dramatically improved when it is functionalized with soluble organic moieties.

Generally speaking, for synthetic fullerene derivatives with well-defined molecular structures, the molecular attachments show better solubility in common solvents than the C₆₀ core as a result of the practical requirements for synthesis, purification, and characterization. As such, many C₆₀ derivatives in the literature can be viewed as *amphiphiles* in which the C₆₀ cage is solvophobic, whereas the pendant organic group(s) is solvophilic in nature. The aggregation behavior of such kind of C₆₀ derivatives is therefore, to a large extent, regulated by the rules of amphiphilic molecular packing. Mother Nature often uses amphiphilic molecules or macromolecules as the building blocks to construct complex superstructures with various shapes and functionality, such as bones, tissues, and cell membranes. The self-organization of natural materials that eventually make life possible is actually dictated by the “codes” inherent in each individual building components, such as molecular shape, covalent bonding structure, and various non-covalent interactions effected by different functional groups the molecule bears. Inspired by Mother Nature, a large variety of supramolecular structures with unique properties and functionality have been designed and synthesized by chemists using synthetic compounds mimicking those amphiphiles observed in the natural world [30–32]. Indeed, understanding of supramolecular self-assembling behavior and mechanisms has become the centerpiece of current nano-science and technology.

Table 1 Relationship between amphiphile shape and predicted aggregate morphology

Shape of amphiphile	Packing parameter (P)	Aggregate morphology
Cone	$<1/3$	Spherical micelles
Truncated cone	$1/3-1/2$	Wormlike micelles
Cylinder	$1/2-1$	Bilayer vesicles
Inverted cone	>1	Inverted micelles

A major driving force for the self-assembly of amphiphilic molecules in the solution phase is the *solvophobic* effect [33]. For instance, it has been long discovered that natural or synthetic surfactants at the so-called critical aggregation concentration in water tend to organize themselves into regular micelles driven by the hydrophobic effect. Depending on the nature of the amphiphiles and experimental conditions, the aggregation morphologies vary substantially from simple spheres and tubes to complex helices, twisted ribbons, braids, and so on. Investigations on these self-assembled structures hence paved a rational way for the design and synthesis of functional materials and devices with precise control and regulation on the nanometer scale. To this end, however, development of theoretical models with strong predictive power in terms of the shape-structure relationship for amphiphile packing is highly valued. The past few decades have witnessed an evolution of theoretical methods accounting for amphiphilic molecular packing outcomes. Based on the principles of statistical thermodynamics, Israelachvili et al. devised a “critical packing parameter” (CPC) approach to predict the aggregate morphologies resulting from amphiphilic surfactant packing at equilibrium. In this model, the packing parameter (P) is defined as:

$$P = V/(l \times a) \quad (1)$$

where V is the volume of molecule, l is the length of molecule, and a is the mean cross-sectional surface of head group. Table 1 gives the correlation between the shape of amphiphile monomer and the predicted aggregate morphology according to the Israelachvili model.

Simple and straightforward as it is, the Israelachvili’s method offers both qualitative insights and prediction in agreement with a wide range of experimental results, giving a long-lasting impact in the amphiphilic packing literature. Nevertheless, this packing rule still has limitations to be addressed. Tsonchev et al. in 2003 came out with an approach of geometric packing analysis in which amphiphiles when treated as “hard” cones or truncated cones are predicted to always favor packing into spherical micelles because of the higher packing fraction [34]. The Tsonchev’s model cast a new light on amphiphilic molecular packing and is in contrast to the commonly held belief that truncated cones will form cylindrical micelles. Most recently, more computationally expensive methods utilizing molecular dynamics (MD) simulation have been exploited by several groups in order to satisfactorily rationalize the clustering of amphiphiles in small numbers as well

as to reveal atomistical details driven by directional interactions other than hydrophobicity, such as electrostatic interactions [35–37], and hydrogen bonding [38].

Although it is reasonable to state that material chemists have now been adequately armed with theoretical guides for preparation of defined and well-organized nanosystems through controllable amphiphilic molecular packing, the exploration and rationalization of fullerene-based amphiphiles within this context is still kind of lagging behind other types of amphiphiles. Previously, there have been several review articles dedicated to related topics [30, 39]. However, the detailed interplay between molecular factors (structure, shape, and non-covalent forces) and supramolecular aggregation properties appeared to be random and evasive from being unequivocally debunked, mainly due to the limited capability of experimental measurements. In the past few years, a significant progress in the synthesis of new amphiphilic C₆₀ derivatives and study of their self-assembling behavior has been made, broadening the literature database for a revisit of this topic. It is therefore our intention that the present review would serve an updated roadmap for the current pursuit of “bottom-up” controlled supramolecular synthesis of fullerene-based nanomaterials.

3 Nano-Aggregates Assembled by C₆₀ Amphiphiles Bearing Chain-Like Polar Appendages

To prepare C₆₀-based amphiphiles, a straightforward approach is to tether a highly polar and water-soluble (hydrophilic) group such as ammonium to the C₆₀ cage via a molecular chain (e.g., alkyl, oligoethylene glycol). In 1999, Tour and coworkers investigated the supramolecular assembling properties of a C₆₀-*N,N*-dimethylpyrrolidinium iodide (**1**, Fig. 1a) [40]. After adding benzene to a solution of **1** in dimethyl sulfoxide (DMSO) and water, the mixture was agitated to yield a fluorescent and hair-like material in the organic (benzene) layer. The microscopic structures of the aggregates of **1** obtained under these conditions were characterized by transmission electron microscopy (TEM) to show an ordered rod-like morphology with diameters of 14–120 nm and lengths of over 70 μm (Fig. 1b). The nanorods formation was found to be solvent and counterion dependent. On the other hand, treatment of the aqueous solution of **1** with sonication followed by filtration through a 0.45 μm filter resulted in the formation of vesicles (Fig. 1c). TEM study showed that the vesicles had diameters of 10–70 nm and wall thickness of 3–6 nm. The simply modified C₆₀-derivative **1** gave a facile way for preparation and manipulation of C₆₀ nano-assemblies. In the molecular structure of **1**, the hydrophilic pyrrolidinium moiety closely positioned to the hydrophobic C₆₀ cage only partially reduces the C₆₀–C₆₀ aggregation. It is obvious that π-stacking together with ionic interactions form the driving forces for the nanoscopic ordering. In a simple approximation, the molecular shape of **1** can be treated as an ellipsoid. According to the simple amphiphile packing rule, it is a case that favors packing

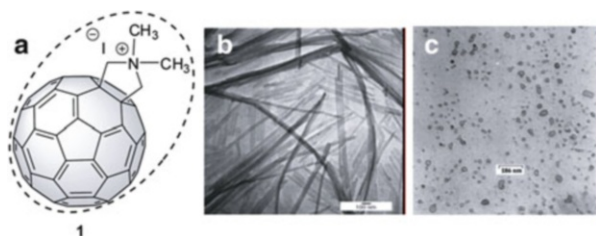


Fig. 1 (a) Structure of C_{60} - N,N -dimethylpyrrolidinium iodide **1**. (b) TEM image of nanorods of **1**. (c) TEM image of vesicular aggregates of **1** obtained after sonication and filtration. Adapted from [40] with permission. Copyright Wiley

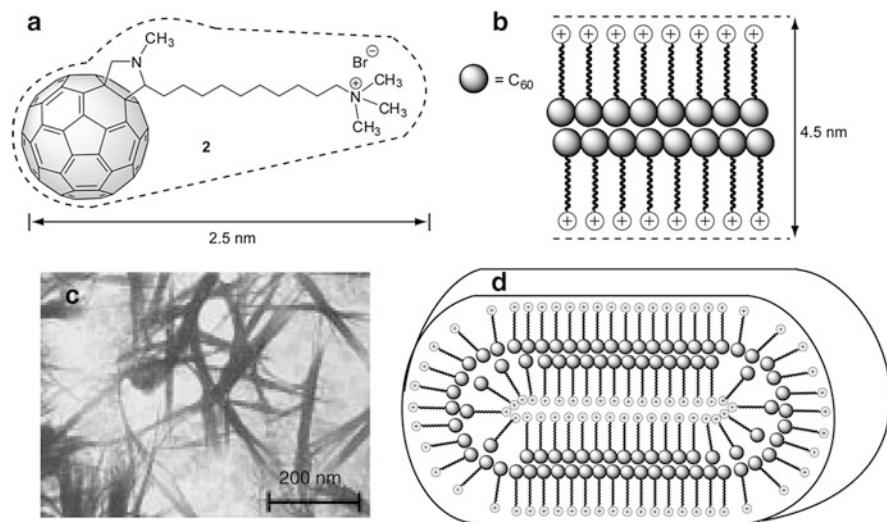


Fig. 2 (a) Structure of pyrrolidino- C_{60} amphiphile **2**. (b) Schematic drawing of molecular bilayer structure of **2**. (c) TEM image for an aqueous solution of **2**. (d) Schematic model for the disk-like aggregates of **2**. Adapted from [41] with permission. Copyright Wiley

into bilayer vesicles ($0.5 < P < 1$). Both of the observed morphologies, rods and vesicles, are kind of in line with the packing rule. However, a conclusive rationalization cannot be made in this case due to the lack of structural details in experimental measurements. Moreover, the two different assembling outcomes arising from different experimental conditions suggest that the aggregation of **1** is dependent on both thermodynamic and kinetic factors.

Nakashima and coworkers in 2002 prepared a similar pyrrolidino- C_{60} amphiphile **2** (Fig. 2a), in which a polar ammonium group was linked to C_{60} cage via a n -decylpyrrolidine chain [41]. Dispersed in an aqueous solution, C_{60} -amphiphile **2** was found to aggregate into fibrous and disk-like microstructures as evidenced by TEM imaging. X-ray diffraction analysis on the cast film of **2** revealed a d spacing from the Bragg's equation to be 4.33 and 4.46 nm before and after hot-water

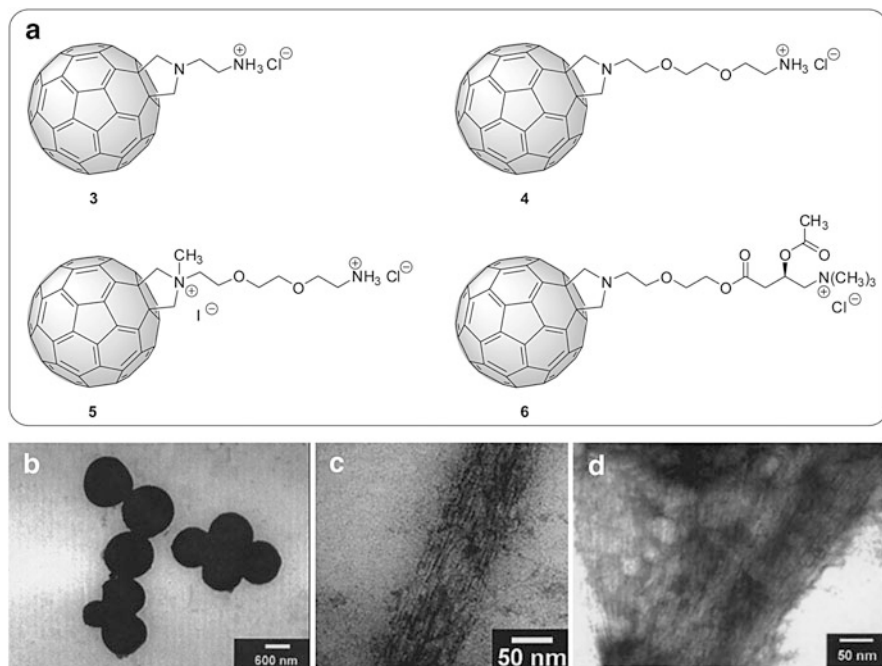


Fig. 3 (a) Structures of pyrrolidinofullerene amphiphiles **3–6**. (b) TEM image of spherical vesicles of **3**. (c) TEM image of a bundle of nanorods of **4**. (d) TEM image of a bundle of nanorods of **5**. Adapted from [42] with permission. Copyright PNAS

treatment. This result substantiated a hypothesis that the assembly was in a bilayer structure as illustrated in Fig. 2b. Furthermore, dynamic light scattering (DLS) study indicated that the particle size of the aggregates were in the range of 150–400 nm. A bilayer packing model (Fig. 2d) was proposed by the authors to account for the disk-like aggregation morphology. It is worth noting that sonication was also found to lead to molecular aggregates with smaller particle sizes (150–400 nm) in their experiments. Similar to Tour's C₆₀-amphiphile **1**, the molecular packing outcomes disclosed by Nakashima and coworkers present a case in accordance with the general amphiphile packing theory; that is, the rod-shaped amphiphile **2**, which can be viewed as a “cylinder,” favors a bilayer packing structure at equilibrium (see Table 1). Nevertheless, the experimentally observed morphology showed a disk-like microstructure rather than vesicular assemblies is beyond the predictive scope of simple amphiphilic packing rules.

A series of pyrrolidinofullerene amphiphiles **3–5** (Fig. 3a) was investigated by Georgakilas and coworkers [42]. These amphiphiles are similar to the motif of **2** in that their structures are composed of a hydrophobic C₆₀ head and a hydrophilic quaternary ammonium tail. The tether groups connecting the two amphiphilic units in **3–5** were varied in both chain length and polarity (i.e., alkyl and oligoethylene glycol) to allow the effects of molecular structure to be probed. After dispersion in

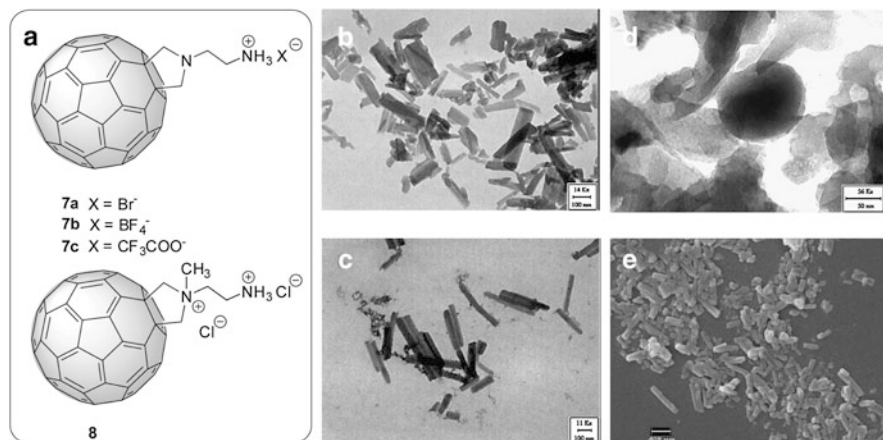


Fig. 4 (a) Structures of ammonium-attached pyrrolidinofullerenes **7a–c** and a doubly charged C₆₀ amphiphile **8**. TEM images of nanorods of (b) **7a**, (c) **7b**, and (d) **7c**. (e) SEM image of **8** deposited on silicon substrate by spin-coating. Adapted from [44] with permission. Copyright Elsevier

water followed by sonication treatment, the relatively short and less polar amphiphile **3** was found to self-assemble into spherical vesicles with a dimension of 0.5–1.2 μm (Fig. 3b) as revealed by TEM study. When the tethering chain length was further elongated, however, a dramatic change in self-aggregation morphology was observed. As shown in Fig. 3c, d, long polar amphiphiles **4** and **5** exhibited a similar tendency to aggregate into long bundles of nanorods. Close inspection by TEM revealed that these bundled nanorods were uniformly aligned in a parallel manner. Computational modeling study suggested that a plausible molecular structure of the nanorods in which the hydrophobic C₆₀ heads stacked inwardly in a fashion similar to C₆₀–C₆₀ interactions occurring in the solid state. De Maria and coworkers prepared pyrrolidone–fullerene amphiphile **6** containing a chiral L-acetyl carnitine appendage (Fig. 3a) [43]. The molecule was found to form stable aggregates in water, and static light scattering analysis indicated that the sizes of the aggregated particles were in the range of 40–300 nm with an average size of 121 ± 44 nm. Due to the lack of microscopic investigation, the detailed structure and morphological properties of these nano-aggregates are still unclear, leaving the self-assembling behavior of chiral chain-like C₆₀ amphiphiles an attractive topic awaiting further exploration.

In a general sense, the supramolecular assembling properties of chain-like C₆₀ amphiphiles with ionic appendages are dictated by two major non-covalent forces, C₆₀–C₆₀ π-stacking (attracting) and ionic interaction (repelling), while the exact morphological consequences appear to be primarily controlled by the delicate balance of these two interactions. Nevertheless, there are also other molecular and experimental factors that should not be overlooked. Prato and coworkers in 2006 demonstrated that the counterion plays a significant role in the self-organization of ammonium-attached pyrrolidinofullerenes **7** (Fig. 4) [44]. From

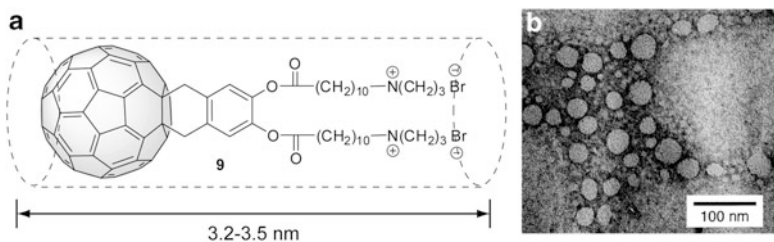


Fig. 5 (a) Structure of C₆₀ bolophile **9**. (b) TEM image of dispersed vesicles of **9**. Adapted from [46] with permission. Copyright ACS

TEM imaging (Fig. 2b, c), C₆₀ amphiphiles associated with bromide (Br⁻) and tetrafluoroborate (BF₄⁻) anions were found, after sonication in water, to aggregate into ordered nanorods with lengths of hundreds of nanometers (80–500 nm for **7a** and 100–900 nm for **7b**) and widths of tens of nanometers (20–90 nm for **7a** and 50–70 nm for **7b**). Close-up examination of these nanorods revealed tube-like microstructures. When the counterion was switched to trifluoroacetate (CF₃COO⁻), however, the resulting nano-agglomerates showed amorphous characteristics, clearly manifesting a prominent counterion effect. Scanning electron microscopic (SEM) and atomic force microscopic (AFM) characterizations were also performed on these C₆₀ aggregates, the results of which gave morphological properties in agreement with the TEM study. Moreover, a doubly charged C₆₀ amphiphile **8** was investigated, and it was found that the aggregates of **8** were structurally similar to those of **7a**, suggesting that the pyrroldinium moiety had little influence on the aggregation process. It should be noted that similar observation was also reported in the study of analogous amphiphiles (**4** and **5**) by Georgakilas [42].

Bola-amphiphiles or bolaphiles are molecules featuring a hydrophobic skeleton and two hydrophilic ends and have found appealing interfacial self-assembly properties mimicking the membranes of many organisms [45]. Sano and coworker reported a C₆₀ bolophile **9** in 2000 (Fig. 5) [46]. With two water-soluble ammonium groups at the ends, this bolophile self-assembled into spherical vesicles with diameters of 20–50 nm after sonication in water. Given the length of the molecule (ca. 3.2–3.5 nm) calculated by molecular modeling, the microstructure of these vesicles was proposed to be made of bilayers in which C₆₀ cores were packed in a head-to-head orientation. Such a bilayered vesicular assembling architecture is clearly in line with the general amphiphilic packing rules (Table 1) if one simply treats the molecular shape of C₆₀ bolophile **9** as a “cylinder.”

Self-organization of chain-like C₆₀ amphiphiles can be enhanced by introducing planar extended π -systems as ordering elements. For example, C₆₀ amphiphile **10** grafted with a porphyrin moiety was found to aggregate into uniform nanotubes with lengths of 500 nm and diameters of 30 nm (Fig. 6) [42]. Of note is that the nanotubular self-assemblies could only be obtained under the condition of sonication in water, implying that the process is kind of kinetically controlled. In principle, the molecular packing of **10** should be governed by three key π -stacking

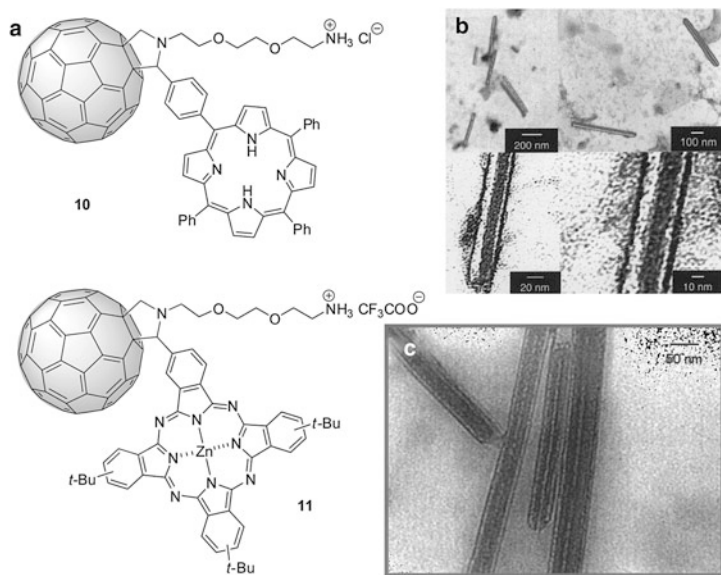


Fig. 6 (a) Structures of C_{60} amphiphiles **10** bearing a porphyrin appendage and **11** bearing a phthalocyanine appendage. (b) TEM images of nanotubes of **10** observed at different scales. (c) TEM image of nanotubes of **11**. Adapted from [42, 47] with permission. Copyright PNAS and ACS

driving forces: C_{60} - C_{60} , C_{60} -porphyrin, and porphyrin-porphyrin interactions. Modeling study suggested that porphyrin-porphyrin stacking gave the most significant contribution to stabilizing the nanoscopic organization. An analogous C_{60} -amphiphile bearing a phthalocyanine (Pc) appendage (**11**, Fig. 6) was reported by Guldi and coworkers in 2005 [47]. Similar to **10**, amphiphile **11** also showed a strong tendency to form uniform nanotubes after dispersion in water by sonication. Photophysical studies indicated that nanostructured C_{60} -Pc assembly underwent ultrafast charge separation and ultraslow charge recombination, leading to an impressively long-lived charge-separation species [47]. These results suggested intriguing application of hybrid systems containing amphiphilic C_{60} skeletons and planar π -donors in organic photovoltaic devices. Given that π -stacking instead of geometric factors plays a dominant role in the supramolecular assemblies of **10** and **11**, simple amphiphilic packing rules do not provide any instructive insight into the morphological properties of their nano-aggregates. Obviously, more sophisticated theoretical modeling is required for better rationalization.

Recently, the aggregation behaviors of a series of pyrrolidino- C_{60} derivatives **12**–**16** (Fig. 7) carrying side chains with increasing hydrophobicity (from polar nonionic to polyionic) have been studied by De Maria and coworkers [48]. The hydrophobicity vs. hydrophilicity balance was evaluated by descriptors derived from aggregation measurements in aqueous/organic mixtures, partition measurements between *n*-octanol and water, and retention factors in reverse-

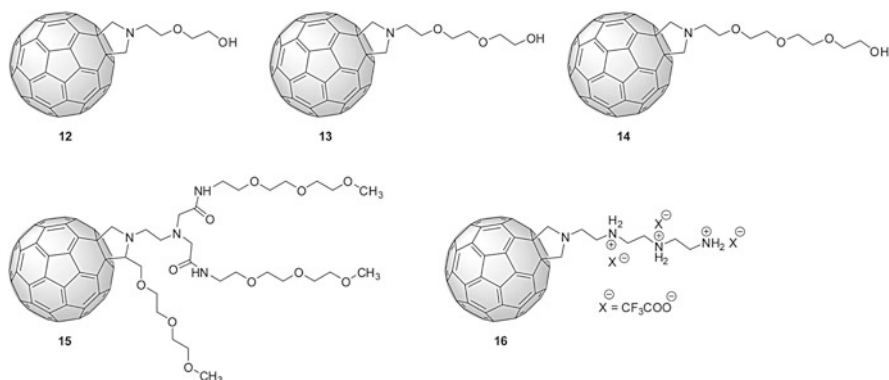


Fig. 7 Structures of pyrrolidino-C₆₀ derivatives **12–16**

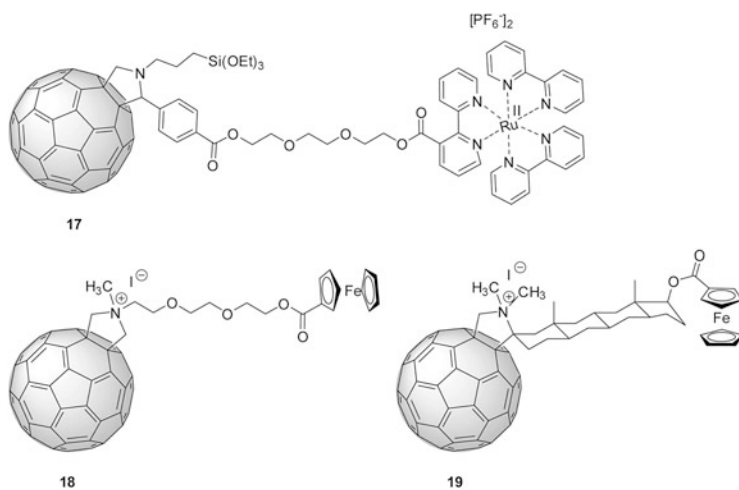


Fig. 8 Structures of C₆₀-Ru[bpy]₃²⁺ hybrid **17** and fulleropyrrolidinium-ferrocene amphiphiles **18** and **19**

phase chromatography. TEM studies of the evaporation-induced aggregates of these C₆₀-amphiphiles showed nanometer-scale clusters with different sizes, and the detailed morphologies and structures were not so well defined to be rationalized or interpreted according to the general molecular packing theories.

Chain-like C₆₀ amphiphiles containing organometallic moieties have also been found to show ordered microscopic aggregating properties. For instance, the aggregates of C₆₀-Ru[bpy]₃²⁺ hybrid **17** (Fig. 8) transferred from water to quartz surface formed microfibers made of nanosized clusters with diameters of ca. 100 nm [49]. Substitution of the hydrophilic Ru[bpy]₃²⁺ moiety of **17** with nonionic aromatic groups such as coumarin and fluorescein chromophores did not result in similar microstructures, underscoring the crucial role of Ru[bpy]₃²⁺ in assembling

ordered supramolecular structures. Guldi and coworkers successfully used two fulleropyrrolidinium-ferrocene amphiphiles **18** and **19** to construct layer-by-layer (LBL) thin films, which assembled into linear nanowires [50]. The highly organized superstructures were believed to arise from complicated interplay between short- and long-range intermolecular interactions.

4 Nano-Aggregates Assembled by C₆₀ Amphiphiles Bearing Branched or Dendritic Polar Appendages

Fullerene derivatives functionalized with multiple long side chains are usually very soluble in common organic solvents and even in water if water-soluble groups are embedded in the side chains. As such the supramolecular self-assembling properties are considerably altered in comparison to those relatively small and less soluble C₆₀ amphiphiles. It was discovered in the late 1990s by several groups that attachment of multiple mesogenic units to the C₆₀ core could give rise to interesting mesomorphic properties. For example, in 1996 Deschenaux and coworkers synthesized a C₆₀ derivative **19** (Fig. 9), the structure of which contains two cholesterol moieties [51]. Compound **19** was the first example of C₆₀-based thermotropic liquid crystals. In the same year, Nakashima and coworkers reported an artificial fullerene lipid **20**, in which the side attachment is composed of three long alkyl chains (Fig. 9) [52]. Compound **20** shows solubility in common organic solvents, but is not water-soluble. Thin films of **20** were characterized by differential scanning calorimetric (DSC) analysis to show phase transition from crystalline to liquid crystalline phases. X-ray diffraction study suggested that **20** aggregated in a multilayered microstructure in the thin film. A large array of C₆₀ derivatives in which a C₆₀ core was linked to multiple mesogenic branches was prepared later, and their liquid crystalline properties were well summarized in a previous review [53]. Nevertheless, this class of C₆₀ derivatives shows tendency to form good quality thin films rather than discrete particle-like aggregates. Such supramolecular assembling properties have been employed in the design of advanced C₆₀-based liquid crystalline materials in recent years [54–56].

A pyrrolidinofullerene **21** carrying a trialkoxybenzene appendage was synthesized by Nakanishi and coworkers in 2005 using the Prato method (Fig. 10) [57]. The supramolecular self-assemblies of **21** obtained after heating and aging in various solvents were examined by electron microscopy (SEM and TEM). It was found that the aggregate morphologies of **21** were solvent-dependent. In 2-propanol/toluene, spherical vesicles were formed with an average diameter of 250 nm (Fig. 10b). HR-TEM revealed that the vesicles take a two lamellae bilayer arrangement and the wall thickness was 8–9 nm. In 1-propanol, however, **21** aggregated into fiber-like microstructures and bundles of fibers with lengths greater than 20 μm (Fig. 10c). When 1,4-dioxane was employed as the solvent, the self-assemblies of **21** took the form of single bilayer discs (Fig. 10d). AFM imaging

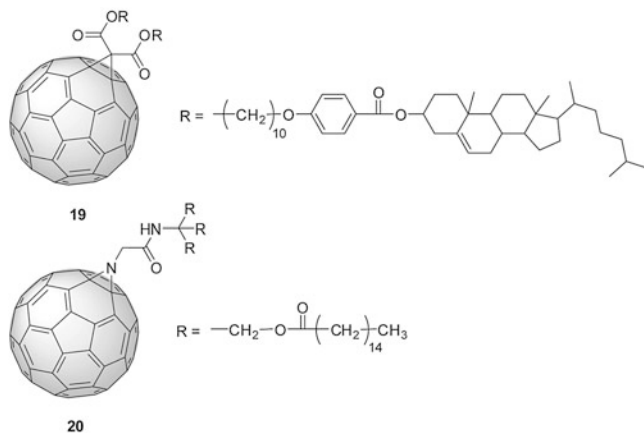


Fig. 9 Structures of C₆₀ derivative **19** with two cholesterol moieties and fullerene lipid **20** with three long alkyl chains

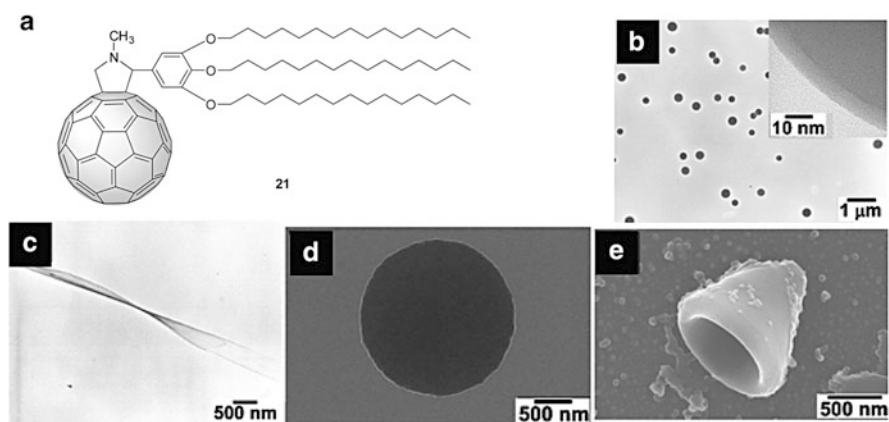


Fig. 10 (a) Structure of pyrrolidinofullerene **21** with a trialkoxybenzene appendage. (b) TEM and HR-TEM (*inset*) images of vesicles of **21** formed in 2-propanol/toluene. (c) SEM image of fiber-like aggregates of **21** formed in 1-propanol. (d) SEM image of single bilayer nanodisk of **21** formed in 1,4-dioxane. (e) SEM image of conical aggregate of **21** formed in 1:1 THF/H₂O. Adapted from [57] with permission. Copyright RSC

indicated that the discs had diameters of 0.2–1.5 μm and thickness of 4.4 nm. In 1:1 H₂O/THF, cone-shaped objects of submicron size together with disc-like structures were observed. The conical aggregate shown in Fig. 10e has a hole with a diameter of 60 nm, while the thickness of the shell is ca. 150 nm which corresponds to multilayer films. Thin films of **21** prepared by casting method were examined by XRD analysis to reveal an inter-fullerene distance of ca. 4.3 nm, suggesting the molecules were packed in an interdigitated bilayer architecture in the solid state.

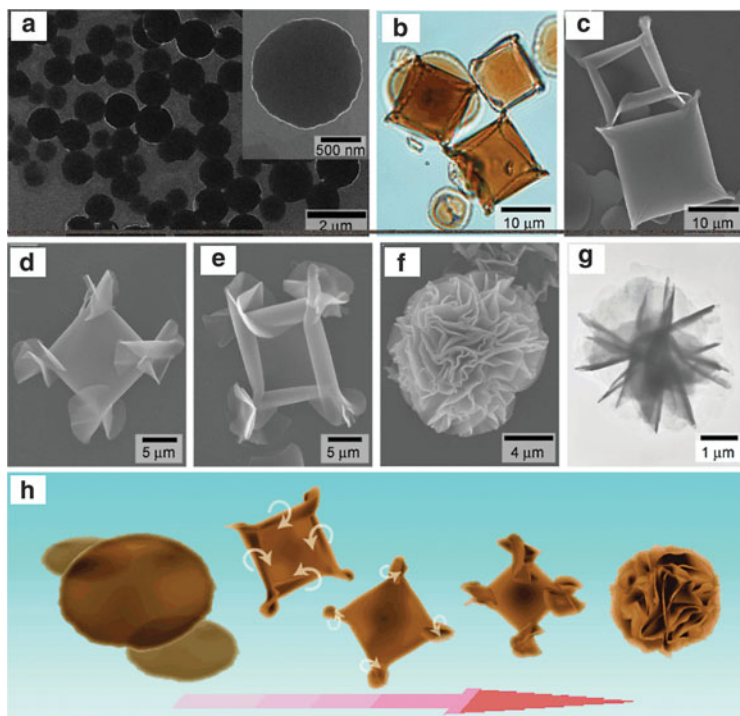


Fig. 11 Proposed mechanism for the formation of flower-shaped supramolecular assemblies of **21**. (a) SEM images of disk-shaped assemblies of **21** formed in 1,4-dioxane at 20°C as a precursor for the flower formation. (b) Optical microscopy and (c) SEM images of square-shaped objects loosely rolled up in every corner formed by rapid cooling of 1,4-dioxane solution of **21** from 60 to 5°C. (d), (e) SEM images of the further rolled-up objects of crumpled structures at the four corners. (f) SEM and (g) TEM images of the final flower-shaped objects formed by slow aging at 5°C. (h) Schematic representation of the formation mechanism of the flower-shaped supramolecular assembly. Reprinted from [58] with permission. Copyright Wiley

In 2007 Nakanish and coworkers prepared flower-shaped hierarchical supramolecular assemblies of **21** (Fig. 11f) under a sequence of preparation conditions: (1) heating in 1,4-dioxane to 60°C for 2 h; (2) aging at 20°C for 24 h; and (3) cooling to 5°C for at least 12 h [58]. The flower-like morphology had a dimension of 3–10 μm and was composed of sheet or flake-like nanostructures according to SEM and cryo-TEM studies. Variation of the preparation conditions allowed the intermediary morphologies to be observed, disclosing a transformation mechanism from flat bilayer disks, rolled up disks, to crumpled disks (Fig. 11). Moreover, spiral assemblies of **21** were prepared in different chiral butanols. The handedness of the spiral structure appeared to be originated from the hydrogen bonding interaction between **21** and the solvent molecules.

The supramolecular assemblies of a similar trialkoxybenzene-appended pyrrolidinofullerene **22** (Fig. 12a) was prepared by Nakanishi et al. in 2008

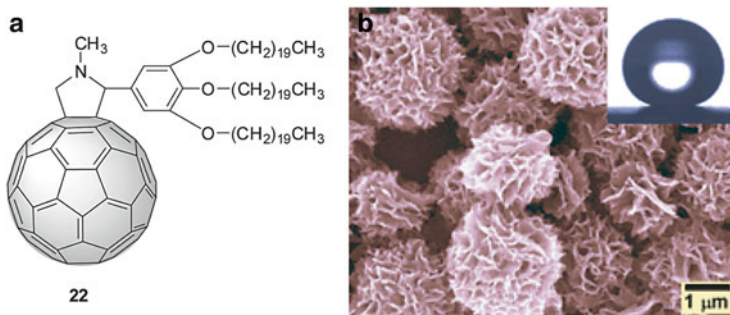


Fig. 12 (a) Structure of trialkoxybenzene-appended pyrrolidinofullerene **22**. (b) SEM image of globular objects of **22** deposited from a dilute 1,4-dioxane dispersion. Adapted [59] with permission. Copyright Wiley

[59]. The preparation conditions were as follows: heating the solution of **22** in 1,4-dioxane to 70°C and then cooling to 20°C. The resulting precipitates were analyzed by SEM and optical microscopy to show globular-shaped aggregates with diameters of a few microns and hierarchical organization of winkled flake-like submicron structures (Fig. 12b). HR-cryo-TEM analysis indicated these microstructures were assembled in the form of lamellar bilayer with a lamellar periodicity value of 4.4 nm. XRD analysis revealed a *d*-spacing value of 4.85 nm, which together with the TEM results suggested **22** packed in bilayer with the eicosyloxy chains interdigitated, given that **22** is about 3.6 nm in size. Of great interest is that thin films of **22** prepared on various substrates by slow evaporation method exhibited water-repellent superhydrophobicity with a water contact angle of ca. 152° (inset of Fig. 12b). SEM indicated that the thin films were ca. 20 nm in thickness and composed of densely packed globular aggregates (Fig. 12b). The superhydrophobicity arose from the fractal morphology of the two-tier roughness of both micro- and nanometer scale that mimics the leaf's surface of lotus.

In 2010, Nakanishi and coworkers continued to prepare some supramolecular assemblies of trialkoxybenzene-pyrrolidinofullerenes associated with carbon nanotubes. It was discovered that the morphological changes of the aggregates of alkylated fullerenes could be used as a “temperature indicator” for photothermal conversion of carbon nanotubes (both single-walled and multiple-walled) in air upon near-infrared (NIR) laser irradiation [60]. This finding provided a useful approach to explore the photothermal properties of carbon nanotubes.

Dendrimers and dendrons are an appealing subclass of dendritic polymers and are commonly used as well-defined nano-building blocks owing to their predictable and controllable hierarchical structures and shapes [61–64]. In fullerene chemistry, the hybridization of C₆₀ and various dendrimers has evolved into a fully fledged subtopic over the past decade [65, 66]. Arai and coworkers in 2006 reported a water-soluble C₆₀ derivative **23** bearing a L-lysine dendrimer and two porphyrin units [67]. It was proposed that such a large molecule would show a globular-like structure in the solution phase. Dispersed in water, the molecules self-assembled

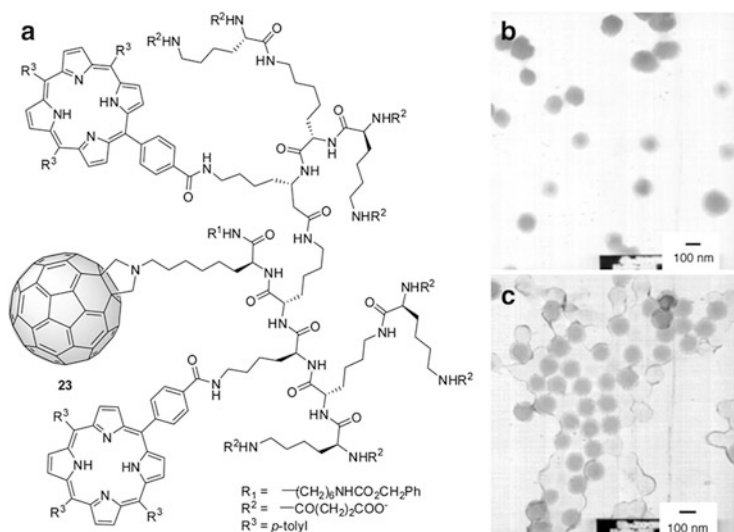


Fig. 13 (a) Structure of a water-soluble C_{60} derivative **23** bearing an L-lysine dendrimer and two porphyrin units. TEM image of samples cast from a solution of **23** in (b) H_2O ($\times 43,000$, 250 kV) and (c) 10 wt% 2-hydroxypropyl- β -cyclodextrin in H_2O ($\times 47,000$, 300 kV). Adapted from [67] with permission. Copyright ACS

into ordered nanospheres with the shape slightly distorted as revealed by TEM analysis (Fig. 13). The amphiphilicity and π - π interactions between fullerene and porphyrin units provided the driving forces for such an interesting supramolecular assembling behavior. The sizes of the aggregates of **23** in water were 90–170 nm determined by TEM. AFM study of the cast films of **23** on surfaces showed egg-shaped particles with sizes of 100–300 nm. Of particular interest is that when **23** was dispersed in water together with 2-hydroxypropyl- β -cyclodextrin (10%, wt), uniform spherical aggregates were observed by TEM, and the size distribution appeared to be much narrower (100–110 nm) compared with the case without cyclodextrin (Fig. 13c). It was reasoned by the authors that the addition of cyclodextrin tended to produce more homogeneous dispersion rather than causing de-aggregation. The spherical assemblies of **23** are in contrast to the regular nanotubes assembled by porphyrin-fullerene hybrids **11**. The extremely large globular molecular shape along with the complex hydrophilicity/hydrophobicity balance of **23** could be the reasons accounting for its unique self-aggregation properties in water.

In 2008, Martín and coworkers designed and synthesized a fullerene-dendrimer hybrid (dendrofullerene **24**, Fig. 14a), the structure of which consisted of a C_{60} core linked to a first-generation dendron and four π -extended tetrathiafulvalene (exTTF) peripheral groups [68]. Because of the favorable π - π interactions between convex C_{60} cage and the concave faces of exTTFs, dendrofullerene **24** was predicted to self-organize to form tree-like supramolecular assemblies (Fig. 14b). In a CHCl_3 solution of **24** (2.0×10^{-4} M), two sets of hydrodynamic radii were found by DLS

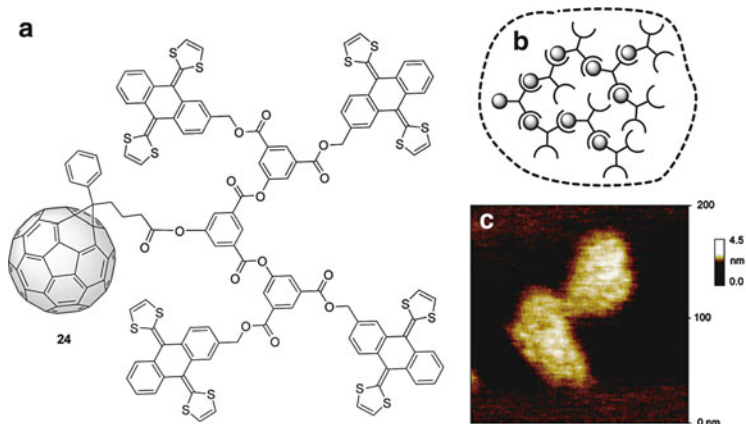
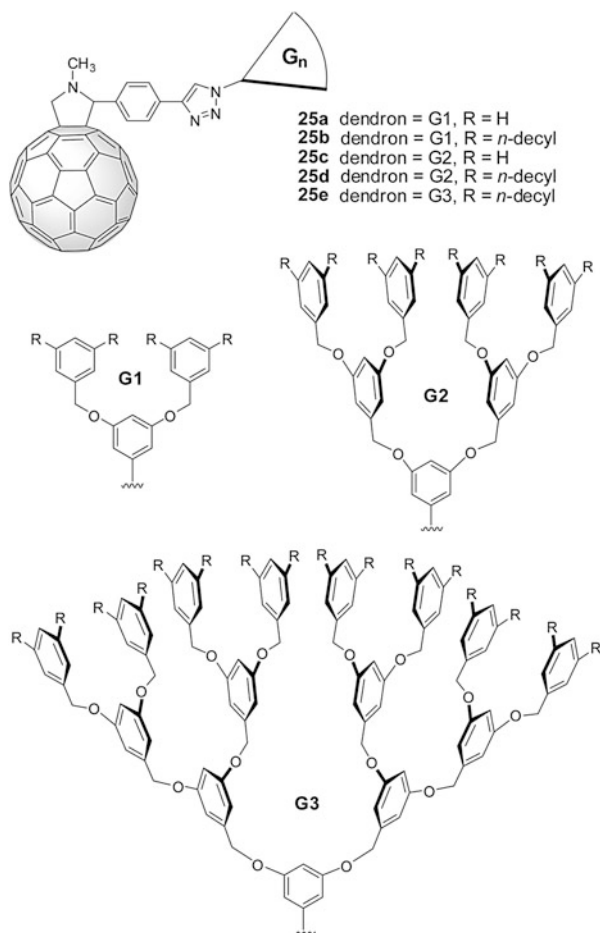


Fig. 14 (a) Structure of dendrofullerene **24** with four π -extended tetrathiafulvalene (exTTF) peripheral groups. (b) Self-assembly of **24** to form supramolecular dendrimer. (c) AFM image of a drop-cast of a CHCl₃ solution of **24** (10 μ M) on mica. Adapted from [68] with permission. Copyright ACS

analysis, showing molecular clusters in the ranges of 5–15 nm and 0.78–1.0 μ m, corresponding to monomeric to trimeric aggregates and multimetric associates, respectively. Aggregates prepared by drop casting on mica were imaged by AFM to show grape-like nanoparticles with uniform heights of 0.9–1.1 nm (Fig. 14c). A close inspection of the AFM image hints to that the large clusters were made up of small spherical aggregates grouped together by non-covalent π – π interactions. Although not conclusive about the details of the microstructure, the aggregation of **24**, if treated as a truncated cone in shape, seems to behave in line with the geometric packing model proposed by Tsonchev and coworkers [34].

Our group recently prepared a series of dendrofullerenes **25a–e** (Fig. 15) in which well-defined Fréchet-type dendrons ranging from the first to the third generations (G1 to G3) were connected to a pyrrolidinofullerene core through a Cu-catalyzed alkyne-azide cycloaddition (click reaction) [69]. The controllable molecular shapes of the dendron attachments render the dendrofullerenes a truncated cone-like structure, which accordingly would lead to spherical aggregates in amphiphilic molecular packing as schematically illustrated in Fig. 16a. Solvent (CHCl₃) evaporation-driven self-assemblies on exfoliated surfaces of mica were prepared by spin-coating method. AFM analysis revealed that the dendrofullerenes did not assemble into discrete nanoparticles with regular shapes but cross-linked worm-like aggregates or amorphous films. Such random interfacial self-assembly morphologies contradicted the amphiphilic packing rules and were ascribed to the weak amphiphilicity of dendrofullerenes **25**. To induce ordered supramolecular packing, acidification of the solution by trifluoroacetic acid (TFA) was conducted prior to spin-coating, as the protonation of the *N*-containing groups in dendrofullerenes **25** was expected to further enhance amphiphilicity. Indeed, this approach has been proven effective. Spherical nano-aggregates were observed in the thin

Fig. 15 Structures of click-synthesized dendrofullerenes **25a–e**



films of **25** as evidenced by AFM imaging. Interestingly, the nature of the peripheral group appears to exert a significant control over the size of the nanospheres. In the case where phenyl groups constitute the outer surface of the dendron, very wide size distributions were found by statistical analysis of 100 nanoparticles in a selected region (4–44 nm for **25a** and 3–30 nm **25c**). Given the molecular spans of the two dendrofullerenes (ca. 2–3 nm according to CPK models), a significant portion of the nano-aggregates was believed to take multilayer micellar forms assembled through a C_{60} -phenyl stacking motif similar to that observed in the solid state [70].

Dendrofullerenes with *n*-decyl peripheral groups (**25b**, **25d**, and **25e**) were found to form uniform spherical nano-aggregates closely packed across the surface (Fig. 16d, e). Of great interest is the statistical analysis of the vertical height of nanoparticles revealed much narrower size distributions (Fig. 16b). From Table 2 it can be clearly seen that the theoretically predicted sizes of the monolayer nanospheres are consistent with the heights of particles measured by AFM, when

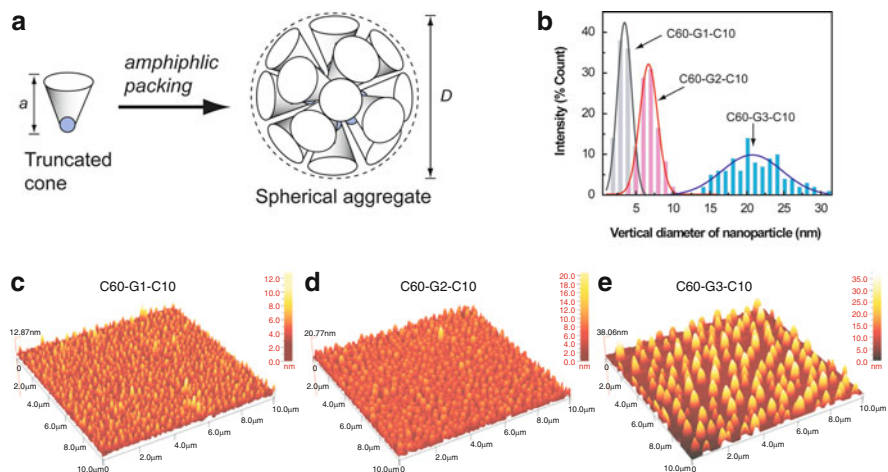


Fig. 16 (a) Spherical aggregation from truncated cones. (b) Statistical analysis of vertical diameters distribution for the spherical nano-assemblies of **25b**, **25d**, and **25e** prepared from spin-coating their dilute CHCl₃ solution on mica. AFM images of interfacial self-assemblies for (c) **25b**, (d) **25d**, and (e) **25e** under acidic conditions

Table 2 Relationship between amphiphile shape and predicted aggregated morphology

Entry	Length of amphiphile by CPK models (nm)	Predicted diameter of monolayer nanosphere (nm)	Average height of particles determined by AFM (nm)
25b	2	4	4.0
25d	4	8	7.2
25e	6	12	20.5

the dendrofullerene building blocks contained first- and second-generation dendrons. This result indicates that the *n*-decyl groups provide an effective insulating layer to prevent the monolayer nanospheres from further agglomeration. When the building blocks carried a third-generation dendron (**25e**), however, the predicted size of nanosphere is much smaller than the experimentally measured particle height. The discrepancy arises likely from the increased conformational flexibility of the larger dendron structure. Nevertheless, the use of dendrofullerenes bearing long alkyl peripheral groups has been demonstrated as an effective “bottom-up” means to attain uniform C₆₀ nanospheres. As revealed by the analysis in Fig. 16b, narrowly distributed nanospheres can be produced via interfacial molecular packing. This work clearly shows that the shape and size of the nano-aggregates of C₆₀ amphiphiles can be precisely controlled by systematically tuning the molecular structure as a dominating factor.

The Hirsch group recently reported the synthesis of a highly water-soluble dendrofullerene amphiphile **26**, the structure of which carries six nonionic, hydrophilic α -D-mannopyranosyl units as the peripheral groups (Fig. 17) [71]. This dendritic C₆₀-glycoconjugate showed a water solubility of >40 mg/mL and aggregated into small micellar sugar balls (nanospheres) in water of ca. 4 nm as

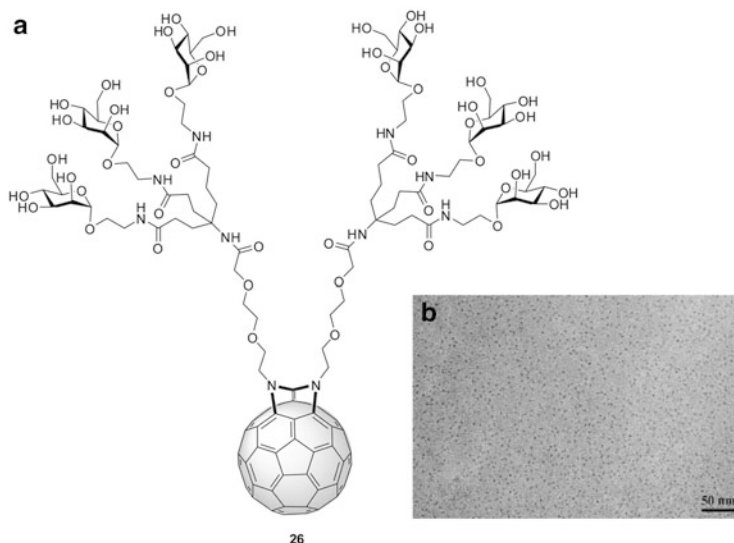


Fig. 17 (a) Structure of water-soluble dendrofullerene amphiphile **26** with six nonionic, hydrophilic α -D-mannopyranosyl units. (b) TEM image of the micellar sugar balls composed of **26**. Adapted from [71] with permission. Copyright Wiley

revealed by diffusion-ordered NMR and TEM studies. Given the truncated cone-like molecular shape of amphiphile **26**, the aggregation morphology is accountable based on the geometric packing theory as outlined by Tsonchev et al. [34].

Wang and coworkers reported the synthesis and supramolecular assembly of dendrofullerene **27** in 2010 [72]. The structure of this dendrofullerene consists of a hydrophobic C_{60} head, a hydrophilic poly(urethane amide) dendron (g_3 -PUA), and a layer of hydrophobic n -hexadecyl peripheral groups (Fig. 18). The hydrogen bonding interaction within the g_3 -PUA moiety renders the compound a flat plate-like molecular shape. In THF/ H_2O (7:3, v/v) solution, dendrofullerene **27** self-assembled in an anisotropic manner to form ribbon-like aggregates as revealed by TEM imaging (Fig. 19b). AFM studies showed that the ribbons had thickness of 12.0 and 22.7 nm (Fig. 19a), corresponding to single- and double-layered structures as proposed in Fig. 19c, d. Moreover, small-angle X-ray scattering (SAXS) analysis of the ribbon-like aggregates suggested a lamellar structure with a d spacing of 9.24 nm. The value is smaller than the thickness found by AFM, suggesting an arrangement of interdigitated alkyl chains (Fig. 19d).

In addition to the dendrofullerenes, a class of “shuttle-coke” like penta-substituted fullerenes **28** (Fig. 20) is worthy of special remarks. This type of fullerene derivatives can be readily prepared through a fivefold organocopper addition to C_{60} developed by Nakamura and coworkers [70, 73–75]. Treatment of the compounds with a strong base, KO^tBu , would lead to the formation of potassium fullerenide $[R_5C_{60}]^-K^+$ (R = aryl or alkyl) which can be solubilized in water with good stability. In contrast to many water-soluble fullerene derivatives, the

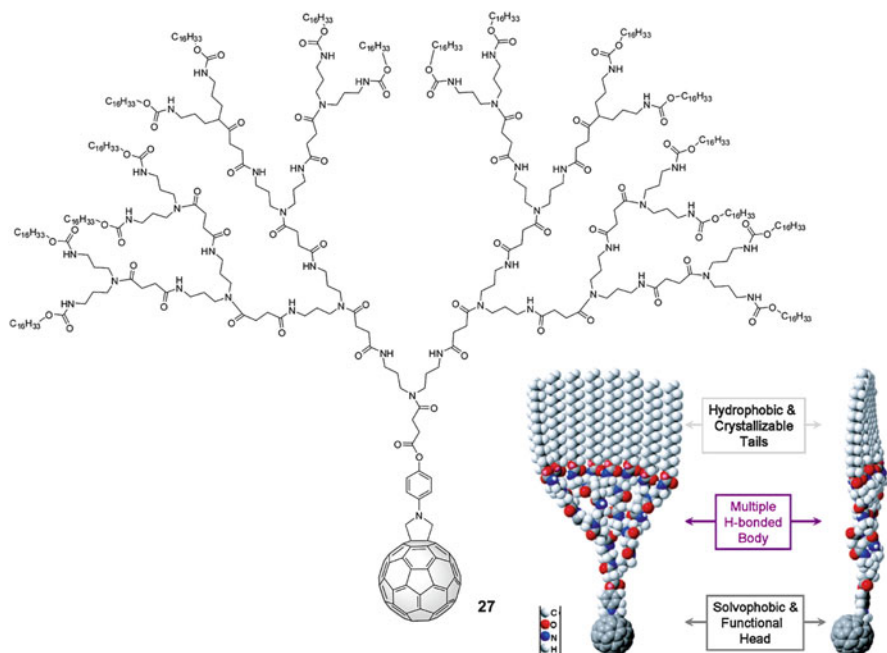


Fig. 18 Structure and molecular model of dendrofullerene **27**. Adapted from [72] with permission. Copyright ACS

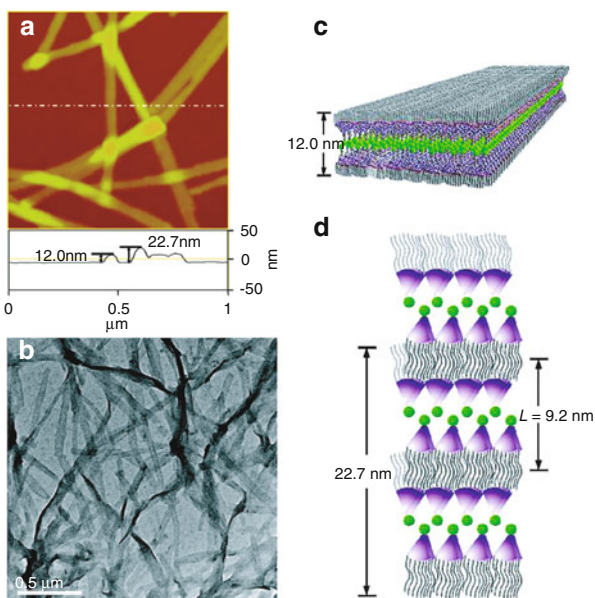


Fig. 19 (a) Tapping mode AFM image of aggregates of **27** formed in THF/H₂O (7:3, v/v) solution after spread on a silicon surface. (b) TEM image of ribbon-like aggregates of **27** formed in THF/H₂O (7:3, v/v) solution. Adapted from [72] with permission. Copyright ACS

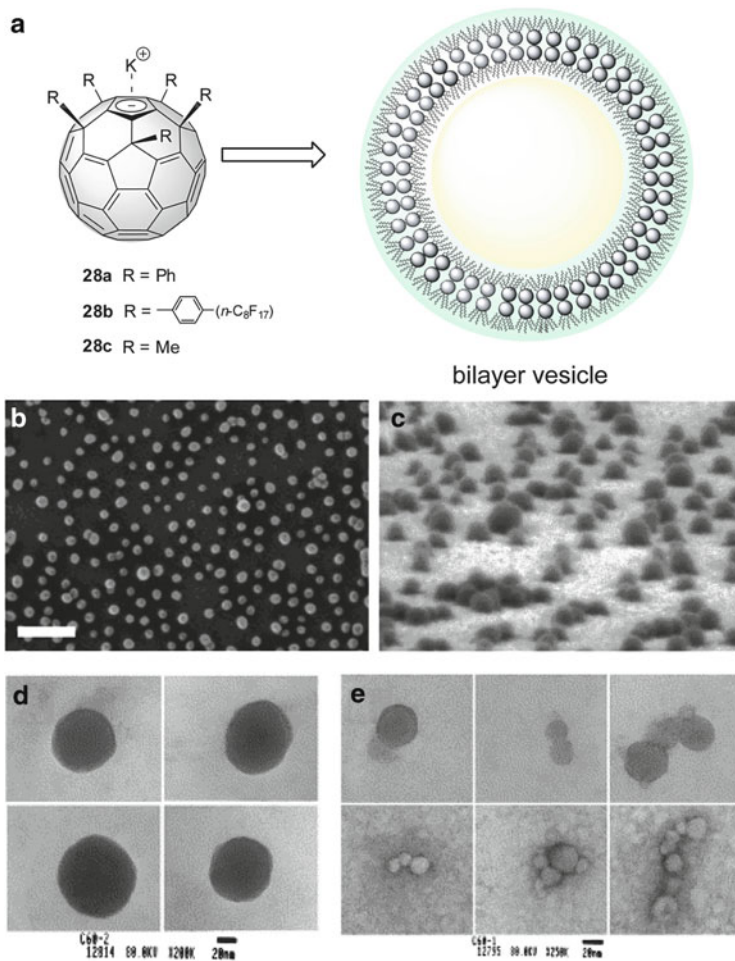


Fig. 20 (a) Structures of the penta-substituted fullerene potassium salts **28a–c** and their bilayer vesicle formation. (b) SEM image of vesicular **28b**-covered ITO surface. The scale bar represents 100 nm. (c) SEM image of a different area of the same vesicular **28b**-covered ITO sample viewed with 80° tilting of the sample stage. (d) TEM images of isolated vesicles of **28c**. (e) TEM images of isolated clusters of **28c**. Adapted from [78, 79] with permission. Copyright Wiley and Elsevier

$[\text{R}_5\text{C}_{60}]^- \text{K}^+$ type of compounds shows a reverse amphiphilic nature; that is, the hydrophilicity comes from the negatively charged C_{60} core, while the side-chain substituents are water repelling. Deposition of a dilute aqueous solution of the pentaphenyl fullerene anion (**28a**) on mica resulted in globular particles as evidenced by AFM analysis [76]. The heights of the particles were 5–16 nm, which is in accordance to the results of DLS analysis (averaged apparent hydrodynamic radius 16.8 nm, polydispersity 0.18 ± 0.02) [76]. LLS analysis revealed that the self-assembled nanospheres of **28a** in water assumed a bilayer vesicular form as schematically illustrated in Fig. 20a [77]. The vesicles featured an average

hydrodynamic radius and radius of gyration of ca. 17 nm at a very low critical aggregation concentration ($<10^{-7}$ M). The average aggregation number of the associated particles was estimated to be about 12,000.

Recently, Nakamura and coworkers demonstrated that the pentaphenyl fullerene anion bearing fluorinated tails can give rise to organized supramolecular assemblies in water and on solid surfaces [78]. DSL analysis of **28b** in water indicated that stable bilayer vesicles were formed with a narrow size distribution and an average radius of 18.1 ± 0.1 nm. Spin-coating of **28b** on the indium tin oxide (ITO) substrate led to the formation of uniform vesicles. SEM studies showed that the vesicles were assembled on the ITO surface with a density of 228 ± 14 vesicles/ μm^2 and an average radius of 17.8 ± 0.2 nm. It is also remarkable that unlike other lipid vesicles, the vesicles of **28b** assembled on surfaces showed very good structural integrity under vacuum. For instance, even at 10^{-5} Pa, spherical shape was retained for the nano-aggregates on ITO (Fig. 20b, c). Pentamethyl fullerene anion **28c** under dilute conditions self-assembled into similar bilayer vesicles (Fig. 20d); however, the sizes of the vesicles (radius 27 nm and aggregation number 21,000) appeared to be considerably larger than those of **28a** and **28b**. The aggregates of **28c** formed above the critical reaggregation concentration (CRC) were clusters made of spherical vesicles in various sizes and geometries (Fig. 20e), suggesting a significant rearrangement of the anion surfactants and counterions [79].

5 Nano-Aggregates Assembled by Amphiphilic Hexakis Adducts of C₆₀

From the aforementioned examples, the strong π - π attraction between C₆₀ cages appears to be a major driving force dictating the aggregation of C₆₀ amphiphiles into a small-sized nanoparticle. In the case of heavily functionalized C₆₀ derivatives, however, the C₆₀ spheres are usually well shielded or encapsulated by the addend groups. As such, the C₆₀ inter-cage interactions can be substantially reduced and its contribution to the aggregation behavior is negligible. Actually, such an effect has provided a useful approach for the preparation of ordered and reversible C₆₀-containing Langmuir or Langmuir-Blodgett (LB) thin films at the air-water interface [66, 80-85].

In 2005 the Hirsch group synthesized an amphiphilic [5:1]-hexakis adduct of C₆₀ **29** (Fig. 21), in which two water-soluble dendrons were connected to the C₆₀ core by amide linkers [86]. This amphiphile was found to show aggregation properties dependent on the pH of media. In neutral water (pH 7.2), compound **29** aggregated into mostly cylinders with a diameter of ca. 65 nm as revealed by cryogenic TEM studies (Fig. 22a). The tubular aggregates were reconstructed based on dimensions and density profile, suggesting a double-layered self-assembly motif in which roughly eight molecules occupied in the circular cross-section area (Fig. 22b).

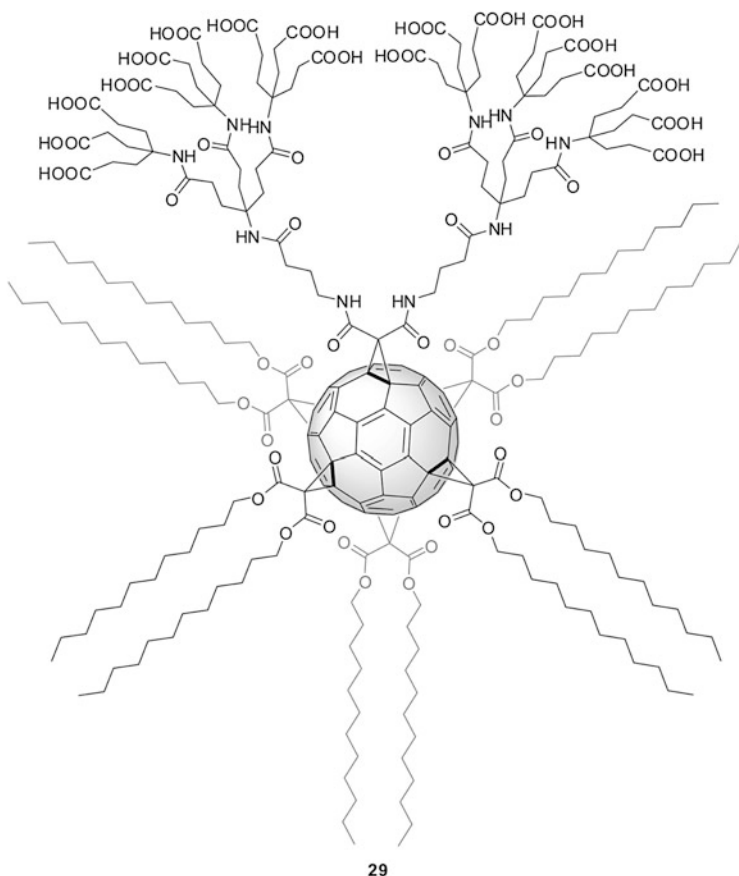


Fig. 21 Structure of amphiphilic [5:1]-hexakis adduct of C₆₀ **29** with two water-soluble dendrons

When the pH of the solution was increased to 9.2, exclusive formation of structurally defined micellar spheres was observed (Fig. 22c) with a diameter of ca. 8.5 nm. The 3D organization of these spherical aggregates was determined by a simulation method to possess a C₂-symmetrical cubic arrangement composed of eight molecules oriented in such a way that all the hydrophobic parts of the molecules were efficiently shielded by the hydrophilic groups from the aqueous environment (Fig. 22d). The pH-dependent aggregation behavior was attributed to the different degree of protonation that altered the repulsion and the size of hydration shell. Also of note is that when the amide linker groups of **29** were switched to esters, the aggregation morphologies differed dramatically; bilayer sheets or liposomes became the predominant structures [87]. An explanation for this is that the dendritic amide moieties in **29** have more pronounced rigidity that favors aggregation with a high degree of curvature rather than a planar alignment [86].

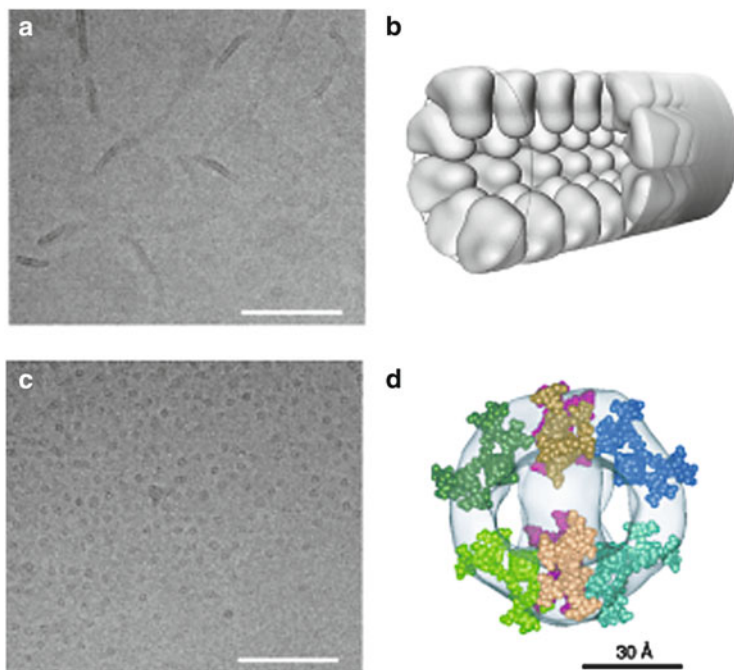


Fig. 22 (a) TEM image of rod-shaped double-layer aggregation of **29** at pH 7.2. (b) Proposed model of a molecular arrangement of **29** in micellar rods at neutral pH. The employed head-group volume is based on the partly protonated form. Hydrophobic alkyl chains, which should reside at the center of the micelle, are not shown for clarity. (c) TEM image of globular micelles formation of **29** at pH 9.2. (d) Eight head groups of the dendritic fullerene molecule may be fitted in a C₂-symmetrical mode into the reconstructed electron-density map. Reprinted from [86] with permission. Copyright Wiley

To understand the factors that dictate the structural persistence, Hirsch and coworkers further designed and investigated a [3:3]-hexakis C₆₀ adduct **30** in 2007 (Fig. 23a) [88]. Unlike amphiphile **29**, compound **30** carries three hydrophilic G-1 dendrons, with each dendritic branch ended with nine carboxyl groups. Although the total number of carboxyl functionalities was identical to that of amphiphile **29**, the space occupied by the hydrophobic moieties was much reduced. TEM analysis of the aggregates of **30** in water by a negative-staining technique disclosed the formation of uniform nanospheres with a diameter of ca. 5 nm (Fig. 23b). 3D reconstruction based on molecular modeling and TEM imaging indicated that these spherical micelles were made of three identical S-shaped motifs in the D₃ symmetry (Fig. 23c). It was also found that each S-shaped segment consists of two molecules of **30**. Overall, the spheres were assembled to minimize the contact of the hydrophobic cores with the water surrounding. The hexakis adducts of C₆₀ demonstrated by Hirsch and coworkers have not only provided insight into the precise nanoscopic organization of the supramolecular

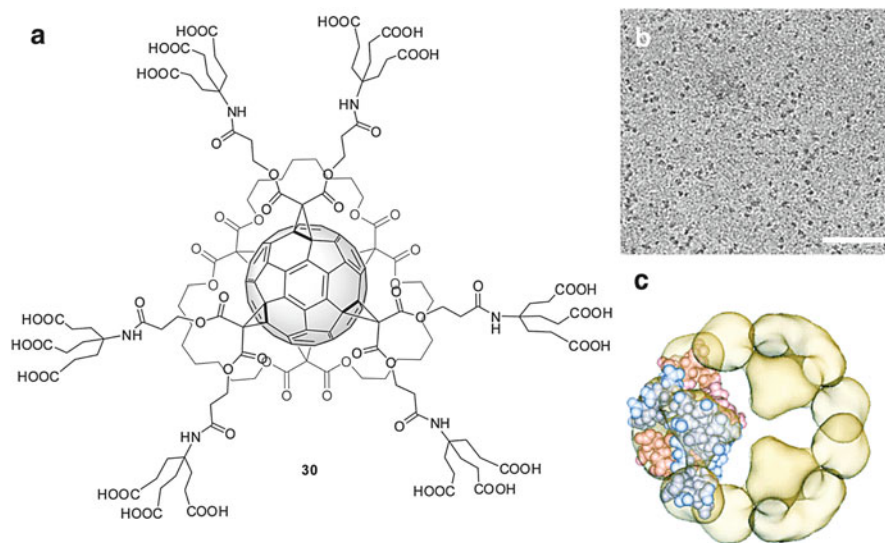


Fig. 23 (a) Structure of [3:3]-hexakis C₆₀ adduct **30**. (b) TEM image of aggregates of **30** using negative-staining technique. The scale bar represents 50 nm. (c) 3D reconstruction of the micelle and molecular fitting. Adapted from [86] with permission. Copyright Wiley

self-assemblies of C₆₀ amphiphiles but also opened the way for making shape-persistent C₆₀-based micellar superstructures [89]. These results manifested the power of using the “bottom-up” approach to construct controllable and tunable supramolecular structures and nano-devices, such as “nano-containers.”

6 Summary and Outlook

The widespread interest in nano-science and technology over the past few decades has greatly inspired and spurred synthetic and material chemists to continually refine their tools to prepare new functional materials with well-defined and controllable nanoscopic structures. Investigation and exploitation of controlled supramolecular self-organization of various C₆₀ fullerene derivatives will pave the way for a wide range of applications. However, such undertakings are still facing a number of challenging barriers. The review in this chapter highlights recent progress towards overcoming these challenges. Aggregation of C₆₀ amphiphiles tends to take a variety of forms depending on both the properties of the packing molecules and experimental conditions. It is evident that functionalization of C₆₀ with rationally designed pendant groups offers an effective approach to avert the random aggregation inherent in spherical C₆₀ cage and hence delivers controllability over the microstructure of self-assembly and organization. Yet, the ability to make a priori

prediction on aggregation behaviors and morphological outcomes for various amphiphilic C₆₀ building blocks has not been realized. To reach this end, continued efforts to design and synthesize new C₆₀ amphiphiles with controlled self-assembly properties and the use of high-resolution analytical techniques to well characterize the nanoscopic details of C₆₀ nano-aggregates are imperative and indispensable. Additionally, it is worth noting that a difficulty in applying amphiphilic packing theories to rationalize aggregation outcomes lies in *how to properly describe the molecular shapes of complex C₆₀ derivatives*. This appears to be an overlooked territory in the recent literature. In this sense, employment of consistent and reliable modeling methods [90–92] rather than empirical estimation to evaluate the shape of molecule will be of great value for facilitating better understanding of the relationship between molecular structure and aggregation properties.

References

1. Kroto HW, Walton DRM (1993) The fullerenes: new horizons for the chemistry, physics and astrophysics of carbon. Cambridge University Press, Cambridge
2. Guldi DM, Martin N (2002) Fullerenes: from synthesis to optoelectronic properties. Kluwer Academic Publishers, Dordrecht
3. Osawa E (2002) Perspectives of fullerene nanotechnology. Kluwer Academic Publishers, Dordrecht
4. Langa F, Nierengarten JF (2007) Fullerenes: principles and applications. Royal Society of Chemistry, Cambridge
5. Taylor R (1999) Lecture notes on fullerene chemistry: a handbook for chemists. Imperial College Press, London
6. Hirsch A, Brettreich M (2005) Fullerenes: chemistry and reactions. Wiley-VCH, Weinheim
7. Martin N, Altable M, Filippone S, Martin-Domenech A (2007) New reactions in fullerene chemistry. *Synlett* 20:3077–3095
8. Diederich F, Gomez-Lopez M (1999) Supramolecular fullerene chemistry. *Chem Soc Rev* 28 (5):263–277
9. Bonifazi D, Enger O, Diederich F (2007) Supramolecular [60]fullerene chemistry on surfaces. *Chem Soc Rev* 36(2):390–414
10. Hahn U, Cardinali F, Nierengarten JF (2007) Supramolecular chemistry for the self-assembly of fullerene-rich dendrimers. *New J Chem* 31(7):1128–1138
11. Nakamura E, Isobe H (2003) Functionalized fullerenes in water. The first 10 years of their chemistry, biology, and nanoscience. *Acc Chem Res* 36(11):807–815
12. Gebeyehu D, Brabec CJ, Padinger F, Fromherz T, Hummelen JC, Badt D, Schindler H, Sariciftci NS (2001) The interplay of efficiency and morphology in photovoltaic devices based on interpenetrating networks of conjugated polymers with fullerenes. *Synth Met* 118 (1–3):1–9
13. Brabec CJ, Zerza G, Cerullo G, De Silvestri S, Luzzati S, Hummelen JC, Sariciftci NS (2001) Tracing photoinduced electron transfer process in conjugated polymer/fullerene bulk heterojunctions in real time. *Chem Phys Lett* 340(3–4):232–236
14. Park LY, Munro AM, Ginger DS (2008) Controlling film morphology in conjugated polymer: fullerene blends with surface patterning. *J Am Chem Soc* 130(47):15916–15926
15. Sivula K, Ball ZT, Watanabe N, Fréchet MJM (2006) Amphiphilic diblock copolymer compatibilizers and their effect on the morphology and performance of polythiophene: fullerene solar cells. *Adv Mater* 18(2):206–210

16. Campoy-Quiles M, Ferenczi T, Agostinelli T, Etchegoin PG, Kim Y, Anthopoulos TD, Stavrinou PN, Bradley DDC, Nelson J (2008) Morphology evolution via self-organization and lateral and vertical diffusion in polymer: fullerene solar cell blends. *Nat Mater* 7(2):158–164
17. Hoppe H, Sariciftci NS (2006) Morphology of polymer/fullerene bulk heterojunction solar cells. *J Mater Chem* 16(1):45–61
18. Hoppe H, Niggemann M, Winder C, Kraut J, Hiesgen R, Hinsch A, Meissner D, Sariciftci NS (2004) Nanoscale morphology of conjugated polymer/fullerene-based bulk-heterojunction solar cells. *Adv Funct Mater* 14(10):1005–1011
19. Isobe H, Nakanishi W, Tomita N, Jinno S, Okayama H, Nakamura E (2005) Nonviral gene delivery by tetraamino fullerene. *Mol Pharm* 3(2):124–134
20. Maeda-Mamiya R, Noiri E, Isobe H, Nakanishi W, Okamoto K, Doi K, Sugaya T, Izumi T, Homma T, Nakamura E (2010) In vivo gene delivery by cationic tetraamino fullerene. *Proc Natl Acad Sci USA* 107(12):5339–5344
21. Han B, Karim MN (2008) Cytotoxicity of aggregated fullerene C₆₀ particles on CHO and MDCK cells. *Scanning* 30(2):213–220
22. Lyon DY, Alvarez PJJ (2008) Fullerene water suspension (nC₆₀) exerts antibacterial effects via ros-independent protein oxidation. *Environ Sci Technol* 42(21):8127–8132
23. Lyon DY, Brunet L, Hinkal GW, Wiesner MR, Alvarez PJJ (2008) Antibacterial activity of fullerene water suspensions (nC₆₀) is not due to ros-mediated damage. *Nano Lett* 8(5):1539–1543
24. Sayes CM, Fortner JD, Guo W, Lyon D, Boyd AM, Ausman KD, Tao YJ, Sitharaman B, Wilson LJ, Hughes JB, West JL, Colvin VL (2004) The differential cytotoxicity of water-soluble fullerenes. *Nano Lett* 4(10):1881–1887
25. Kadish KM, Ruoff RS (2000) Fullerenes: chemistry, physics, and technology. Wiley, New York
26. Ruoff RS, Tse DS, Malhotra R, Lorents DC (1993) Solubility of fullerene (C₆₀) in a variety of solvents. *J Phys Chem* 97(13):3379–3383
27. Brant JA, Labille J, Bottero J-Y, Wiesner MR (2006) Characterizing the impact of preparation method on fullerene cluster structure and chemistry. *Langmuir* 22(8):3878–3885
28. Alargova RG, Deguchi S, Tsujii K (2001) Stable colloidal dispersions of fullerenes in polar organic solvents. *J Am Chem Soc* 123(43):10460–10467
29. Chen KL, Elimelech M (2006) Aggregation and deposition kinetics of fullerene (C₆₀) nanoparticles. *Langmuir* 22(26):10994–11001
30. Ariga K, Nakanishi T, Hill JP (2007) Self-assembled microstructures of functional molecules. *Curr Opin Coll Inter Sci* 12(3):106–120
31. Shimizu T, Masuda M, Minamikawa H (2005) Supramolecular nanotube architectures based on amphiphilic molecules. *Chem Rev* 105(4):1401–1444
32. Hoeben FJM, Jonkheijm P, Meijer EW, Schenning APHJ (2005) About supramolecular assemblies of π -conjugated systems. *Chem Rev* 105(4):1491–1546
33. Chandler D (2005) Interfaces and the driving force of hydrophobic assembly. *Nature* 437(7059):640–647
34. Tsonchev S, Schatz GC, Ratner MA (2003) Hydrophobically-driven self-assembly: a geometric packing analysis. *Nano Lett* 3(5):623–626
35. Tsonchev S, Troisi A, Schatz GC, Ratner MA (2004) On the structure and stability of self-assembled zwitterionic peptide amphiphiles: a theoretical study. *Nano Lett* 4(3):427–431
36. Tsonchev S, Troisi A, Schatz GC, Ratner MA (2004) All-atom numerical studies of self-assembly of zwitterionic peptide amphiphiles. *J Phys Chem B* 108(39):15278–15284
37. Tsonchev S, Schatz GC, Ratner MA (2004) Electrostatically-directed self-assembly of cylindrical peptide amphiphile nanostructures. *J Phys Chem B* 108(26):8817–8822
38. Velichko YS, Stupp SI, de la Cruz MO (2008) Molecular simulation study of peptide amphiphile self-assembly. *J Phys Chem B* 112(8):2326–2334

39. Guldi DM, Zerbetto F, Georgakilas V, Prato M (2005) Ordering fullerene materials at nanometer dimensions. *Acc Chem Res* 38(1):38–43
40. Cassell AM, Asplund CL, Tour JM (1999) Self-assembling supramolecular nanostructures from a C₆₀ derivative: nanorods and vesicles. *Angew Chem Int Ed* 38(16):2403–2405
41. Nakashima N, Ishii T, Shirakusa M, Nakanishi T, Murakami H, Sagara T (2001) Molecular bilayer-based superstructures of a fullerene-carrying ammonium amphiphile: structure and electrochemistry. *Chem Eur J* 7(8):1766–1772
42. Georgakilas V, Pellarini F, Prato M, Guldi DM, Melle-Franco M, Zerbetto F (2002) Supramolecular self-assembled fullerene nanostructures. *Proc Natl Acad Sci USA* 99(8):5075–5080
43. Angelini G, De Maria P, Fontana A, Pierini M, Maggini M, Gasparini F, Zappia G (2001) Study of the aggregation properties of a novel amphiphilic C₆₀ fullerene derivative. *Langmuir* 17(21):6404–6407
44. Brough P, Bonifazi D, Prato M (2006) Self-organization of amphiphilic [60]fullerene derivatives in nanorod-like morphologies. *Tetrahedron* 62(9):2110–2114
45. Fuhrhop J-H, Wang T (2004) Bolaamphiphiles. *Chem Rev* 104(6):2901–2938
46. Sano M, Oishi K, Ishi-i T, Shinkai S (2000) Vesicle formation and its fractal distribution by bola-amphiphilic [60]fullerene. *Langmuir* 16(8):3773–3776
47. Guldi DM, Gouloumis A, Vázquez P, Torres T, Georgakilas V, Prato M (2005) Nanoscale organization of a phthalocyanine–fullerene system: remarkable stabilization of charges in photoactive 1-d nanotubes. *J Am Chem Soc* 127(16):5811–5813
48. Angelini G, Cusan C, De Maria P, Fontana A, Maggini M, Pierini M, Prato M, Schergna S, Villani C (2005) The associative properties of some amphiphilic fullerene derivatives. *Eur J Org Chem* 2005(9):1884–1891
49. Guldi DM, Maggini M, Mondini S, Guérin F, Fendler JH (1999) Formation, characterization, and properties of nanostructured [Ru(bpy)₃]²⁺-C₆₀ langmuir–blodgett films in situ at the air–water interface and ex situ on substrates. *Langmuir* 16(3):1311–1318
50. Guldi DM, Luo C, Koktysh D, Kotov NA, Da Ros T, Bosi S, Prato M (2002) Photoactive nanowires in fullerene–ferrocene dyad polyelectrolyte multilayers. *Nano Lett* 2(7):775–780
51. Chuard T, Deschenaux R (1996) First fullerene[60]-containing thermotropic liquid crystal. Preliminary communication. *Helv Chim Acta* 79(3):736–741
52. Murakami H, Watanabe Y, Nakashima N (1996) Fullerene lipid chemistry: self-organized multibilayer films of a C₆₀-bearing lipid with main and subphase transitions. *J Am Chem Soc* 118(18):4484–4485
53. Chuard T, Deschenaux R (2002) Design, mesomorphic properties, and supramolecular organization of [60]fullerene-containing thermotropic liquid crystals *J Mater Chem* 12:1944–1951
54. Lenoble J, Campidelli S, Maringa N, Donnio B, Guillon D, Yevlampieva N, Deschenaux R (2007) Liquid–crystalline janus-type fullerodendrimers displaying tunable smectic–columnar mesomorphism. *J Am Chem Soc* 129(32):9941–9952
55. Li W-S, Yamamoto Y, Fukushima T, Saeki A, Seki S, Tagawa S, Masunaga H, Sasaki S, Takata M, Aida T (2008) Amphiphilic molecular design as a rational strategy for tailoring bicontinuous electron donor and acceptor arrays: photoconductive liquid crystalline oligothiophene–C₆₀ dyads. *J Am Chem Soc* 130(28):8886–8887
56. Campidelli S, Bourgun P, Guintchin B, Furrer J, Stoeckli-Evans H, Saez IM, Goodby JW, Deschenaux R (2010) Diastereoisomerically pure fulleropyrrolidines as chiral platforms for the design of optically active liquid crystals. *J Am Chem Soc* 132(10):3574–3581
57. Nakanishi T, Schmitt W, Michinobu T, Kurth DG, Ariga K (2005) Hierarchical supramolecular fullerene architectures with controlled dimensionality. *Chem Commun* 5982–5984
58. Nakanishi T, Ariga K, Michinobu T, Yoshida K, Takahashi H, Teranishi T, Möhwald H, Kurth DG (2007) Flower-shaped supramolecular assemblies: hierarchical organization of a fullerene bearing long aliphatic chains. *Small* 3(12):2019–2023
59. Nakanishi T, Michinobu T, Yoshida K, Shirahata N, Ariga K, Möhwald H, Kurth DG (2008) Nanocarbon superhydrophobic surfaces created from fullerene-based hierarchical supramolecular assemblies. *Adv Mater* 20(3):443–446

60. Shen Y, Skirtach AG, Seki T, Yagai S, Li H, Möhwald H, Nakanishi T (2010) Assembly of fullerene-carbon nanotubes: temperature indicator for photothermal conversion. *J Am Chem Soc* 132 (25):8566–8568
61. Tomalia DA (2010) Dendrons/dendrimers: quantized, nano-element like building blocks for soft-soft and soft-hard nano-compound synthesis. *Soft Matter* 6:456–474
62. Fréchet JMJ, Tomalia DA (2001) Dendrimers and other dendritic polymers. Wiley, Chichester
63. Newkome GR, Moorefield CN, Vögtle F (2001) Dendrimers and dendrons: concepts, syntheses, applications. Wiley-VCH, Weinheim
64. Rosen BM, Wilson CJ, Wilson DA, Peterca M, Imam MR, Percec V (2009) Dendron-mediated self-assembly, disassembly, and self-organization of complex systems. *Chem Rev* 109 (11):6275–6540
65. Nierengarten J-F (2000) Fullerodendrimers: a new class of compounds for supramolecular chemistry and materials science applications. *Chem Eur J* 6(20):3667–3670
66. Nierengarten JF (2004) Chemical modification of C₆₀ for materials science applications. *New J Chem* 28:1177–1191
67. Arai T, Ogawa J, Mouri E, Bhuiyan MPI, Nishino N (2006) Formation of submicron scale particles of narrow size distribution from a water-soluble dendrimer with links to porphyrins and a fullerene. *Macromolecules* 39(4):1607–1613
68. Fernández G, Pérez EM, Sánchez L, Martín N (2008) An electroactive dynamically polydisperse supramolecular dendrimer. *J Am Chem Soc* 130(8):2410–2411
69. Mahmud IM, Zhou N, Wang L, Zhao Y (2008) Triazole-linked dendro[60]fullerenes: modular synthesis via a “click” reaction and acidity-dependent self-assembly on the surface. *Tetrahedron* 64(50):11420–11432
70. Matsuo Y, Muramatsu A, Hamasaki R, Mizoshita N, Kato T, Nakamura E (2003) Stacking of molecules possessing a fullerene apex and a cup-shaped cavity connected by a silicon connection. *J Am Chem Soc* 126(2):432–433
71. Kato H, Böttcher C, Hirsch A (2007) Sugar balls: Synthesis and supramolecular assembly of [60]fullerene glycoconjugates. *Eur J Org Chem* 16:2659–2666
72. Liu B, Yang M, Zhang Z, Zhang G, Han Y, Xia N, Hu M, Zheng P, Wang W (2010) Ribbonlike assembly of molecules composed of fulleropyrrolidine and PUA dendron. *Langmuir* 26 (12):9403–9407
73. Sawamura M, Iikura H, Nakamura E (1996) The first pentahaptofullerene metal complexes. *J Am Chem Soc* 118(50):12850–12851
74. Zhong Y-W, Matsuo Y, Nakamura E (2006) Convergent synthesis of a polyfunctionalized fullerene by regioselective five-fold addition of a functionalized organocopper reagent to C₆₀. *Org Lett* 8(7):1463–1466
75. Sawamura M, Nagahama N, Toganoh M, Nakamura E (2002) Regioselective penta-addition of 1-alkenyl copper reagent to [60]fullerene. Synthesis of penta-alkenyl FCp ligand. *J Organomet Chem* 652(1–2):31–35
76. Sawamura M, Nagahama N, Toganoh M, Hackler UE, Isobe H, Nakamura E, Zhou S-Q, Chu B (2000) Pentaorganofullerene R₅C₆₀⁻. A water soluble hydrocarbon anion. *Chem Lett* 1098–1099
77. Zhou S, Burger C, Chu B, Sawamura M, Nagahama N, Toganoh M, Hackler UE, Isobe H, Nakamura E (2001) Spherical bilayer vesicles of fullerene-based surfactants in water: a laser light scattering study. *Science* 291(5510):1944–1947
78. Homma T, Harano K, Isobe H, Nakamura E (2010) Nanometer-sized fluorinated fullerene vesicles in water and on solid surfaces. *Angew Chem Int Ed* 49:1665–1668
79. Burger C, Hao J, Ying Q, Isobe H, Sawamura M, Nakamura E, Chu B (2004) Multilayer vesicles and vesicle clusters formed by the fullerene-based surfactant C₆₀(CH₃)₅K. *J Colloid Interface Sci* 275(2):632–641
80. Cardullo F, Diederich F, Echegoyen L, Habicher T, Jayaraman N, Leblanc RM, Stoddart JF, Wang S (1998) Stable langmuir and langmuir–blodgett films of fullerene–glycodendron conjugates. *Langmuir* 14(8):1955–1959

81. Felder D, del Pilar Carreon M, Gallani J-L, Guillon D, Nierengarten J-F, Chuard T, Deschenaux R (2001) Amphiphilic fullerene-cholesterol derivatives: synthesis and preparation of Langmuir and Langmuir–Blodgett films. *Helv Chim Acta* 84(5):1119–1132
82. Felder D, Gutierrez Nava M, del Pilar Carreon M, Eckert J-F, Luccisano M, Schall C, Masson P, Gallani J-L, Heinrich B, Guillon D, Nierengarten J-F (2002) Synthesis of amphiphilic fullerene derivatives and their incorporation in Langmuir and Langmuir–Blodgett films. *Helv Chim Acta* 85(1):288–319
83. Zhang S, Rio Y, Cardinali F, Bourgogne C, Gallani J-L, Nierengarten J-F (2003) Amphiphilic diblock dendrimers with a fullerene core. *J Org Chem* 68(25):9787–9797
84. Felder-Flesch D, Bourgogne C, Gallani J-L, Guillon D (2005) Interfacial behavior and film-forming properties of an amphiphilic hexasubstituted [60]fullerene. *Tetrahedron Lett* 46(38):6507–6510
85. Maierhofer AP, Brettreich M, Burghardt S, Vostrowsky O, Hirsch A, Langridge S, Bayerl TM (2000) Structure and electrostatic interaction properties of monolayers of amphiphilic molecules derived from C₆₀-fullerenes: a film balance, neutron-, and infrared reflection study. *Langmuir* 16(23):8884–8891
86. Burghardt S, Hirsch A, Schade B, Ludwig K, Böttcher C (2005) Switchable supramolecular organization of structurally defined micelles based on an amphiphilic fullerene. *Angew Chem Int Ed* 44(19):2976–2979
87. Brettreich M, Burghardt S, Böttcher C, Bayerl T, Bayerl S, Hirsch A (2000) Globular amphiphiles: membrane-forming hexaadducts of C₆₀. *Angew Chem Int Ed* 39(10):1845–1848
88. Schade B, Ludwig K, Böttcher C, Hartnagel U, Hirsch A (2007) Supramolecular structure of 5-nm spherical micelles with D₃ symmetry assembled from amphiphilic [3:3]-hexakis adducts of C₆₀. *Angew Chem Int Ed* 46(23):4393–4396
89. Hirsch A (2008) Amphiphilic architectures based on fullerene and calixarene platforms: from buckysome to shape-persistent micelles. *Pure Appl Chem* 80(3):571–587
90. Grant JA, Gallardo MA, Pickup BT (1996) A fast method of molecular shape comparison: a simple application of a gaussian description of molecular shape. *J Comput Chem* 17(14):1653–1666
91. Grant JA, Pickup BT, Sykes MJ, Kitchen CA, Nicholls A (2007) The gaussian generalized born model: application to small molecules. *Phys Chem Chem Phys* 9(35):4913–4922
92. Gong LD, Yang ZZ (2010) Investigation of the molecular surface area and volume: defined and calculated by the molecular face theory. *J Comput Chem* 31(11):2098–2108

Multilayer Assembly for Solar Energy Conversion

Anna Troeger, Vito Sgobba, and Dirk M. Guldi

Abstract Organizing molecular thin films of electro- and photoactive building blocks provides a versatile platform to the nanoscale control of assembled multilayers and paves the way for the design of functional electronic devices and/or efficient photoenergy conversion devices. Assembly methods, including the Langmuir–Blodgett and the layer-by-layer technique, offer elegant means to realize well-ordered multifunctional thin films on variable surfaces. In this chapter, the fundamental factors and driving forces that govern the adsorption processes of multilayered assemblies are highlighted and numerous intriguing contributions to the field of template-assisted assemblies are presented. Owing to the applicability of these concepts to carbon-based materials – fullerenes and carbon nanotubes – particular attention is paid to the integration of these exceptionally materials combined with light absorbing constituents into nanostructured thin films *en route* towards versatile electron donor–acceptor nanohybrids for photoconversion schemes.

Keywords layer by layer · self assembly · solar cells · Langmuir Blodgett · Langmuir Schaefer · carbon nanotubes · fullerenes

Contents

1	Introduction	56
2	Historical Background	58
	2.1 Langmuir/Langmuir Blodgett	58
	2.2 Layer-by-Layer	59
3	Fundamental Concepts and Mechanisms of Multilayer Formation	63

A. Troeger, V. Sgobba, and D.M. Guldi (✉)
Department of Chemistry and Pharmacy and Interdisciplinary Center for Molecular Materials,
Friedrich-Alexander-Universität Erlangen-Nürnberg, Egerlandstr., 3, 91058 Erlangen,
Germany
e-mail: Dirk.Guldi@fau.de

3.1	Deposition of Langmuir–Blodgett Films	63
3.2	Layer-by-Layer Assembly	68
4	Thin Films of Carbon Nanotubes and Fullerenes	70
4.1	Langmuir–Blodgett Films	70
4.2	Layer-by-Layer Films	78
5	Applications of Multilayer Assemblies in Photovoltaic Devices	80
5.1	Langmuir–Blodgett and Langmuir–Schaefer Film-Based Solar Cells	81
5.2	Layer-by-Layer Film-Based Solar Cells	84
6	Summary and Outlook	93
	References	93

Abbreviations

AA	Ascorbic acid
AFM	Atomic force microscopy
CNT	Carbon nanotubes
CT	Charge transfer
DCE	1,2 Dichloroethane
FF	Fill factor
IPCE	Incident photon to current efficiency
I_{SC}	Short circuit current
ITO	Indium tin oxide
LB	Langmuir–Blodgett
LbL	Layer-by-layer
LS	Langmuir–Schaefer
MV ²⁺	Dimethylviologen
MWNT	Multi wall carbon nanotubes
ODA	Octadecylamine
PAA	Poly(acrylic acid)
PDDA	Poly(diallyl dimethylammonium)
PEI	Poly(ethyleneimine)
PmPV	<i>M</i> -phenylenevinylene co-2,5-dioctoxy- <i>p</i> -phenylenevinylene
POPT	Poly(2,5-dioctyloxy-1,4-phenylene-alt-2,5-thienylene)
PSS	Polystyrene sulfonate
SDS	Sodium dodecyl sulfate
SWNT	Single wall carbon nanotubes
V_{OC}	Open circuit voltage

1 Introduction

One of the most aspiring research objectives of our times is the construction of multifunctional assemblies and their application in photoelectrochemical solar energy conversion devices. For decades, the use of inorganic semiconducting materials has dominated the market. However, the production of organic or

mixed organic/inorganic solar cells suggested a myriad of innovative technologies. Notable impact was achieved by concepts like dye-sensitized nanocrystalline solar cells [1–3], polymer/fullerene bulk-heterojunctions [4–6], small-molecule thin films [7, 8], and hybrid polymer/nanocrystal devices [9–11]. As a leading example, small-area dye-sensitized solar cells have so far reached solar power conversion efficiencies of about 11% [12], whereas efficiencies of 3.5% and 5.7% have been reported for polymer/fullerene heterojunctions and copper phthalocyanine/fullerene hybrid planar/mixed molecular heterojunctions, respectively – all under white light illumination [13]. The most frequently encountered problems in this field are interfacial diffusion of the building blocks (i.e., electron donors and acceptors) and/or lack of efficient light response of large-band-gap semiconductor materials in the visible region of the solar spectrum [14–17]. To this end, the control over small- and large-scale organization of electron donor–acceptor nanohybrids and the creation of suitable light and redox gradients are a priority in the development of photovoltaic devices. The latter is primarily meant to assist in directing photons and charges in the desired direction. To match the aforementioned needs, preparing, shaping, and improving multifunctional electron donor–acceptor hybrids at the molecular scale is of considerable interest [18–21]. Essential prerequisites concerning the basic building blocks are accessibility and tractability. Nanoscale carbon-based materials – fullerenes and carbon nanotubes (CNT) – meet these criteria and, moreover, have emerged as unique materials with tunable physicochemical properties [22–28]. Varying, for example, the size, the diameter, and the morphology of these carbon nanostructures changes band-gap energies, electronic conduction, transport features, etc. Organizing nanoscale carbon-based materials with electron-donating compounds to create nanostructured surfaces necessitates recognition, discrimination, and binding. This requires, however, the complementarity of the binding sites in terms of size, shape, and chemical functionality. In this context, the simplicity and versatility of electrostatic interactions and/or van der Waals forces provides ample opportunities for probing fundamental/mechanistic aspects and for optimizing practical/performance aspects. Motivated by these incentives, the Langmuir–Blodgett (LB) deposition method and self-assembly techniques [28–32] provide excellent options for the preparation of ultrathin films of controlled thickness and molecular arrangement. In the 1980s, the preparation of multilayer assemblies and nanostructured thin films has been widely dominated by the LB technique – a method in which monolayers are formed at the air/water interface and subsequently transferred onto solid supports [33]. In the 1990s, self-assembled films have drawn major attention, mainly due to advantages like simplified preparation and higher stability. Among the different self-assembly techniques, electrostatic layer-by-layer (LbL) deposition presents an elegant approach. The integration of complementary motifs, that is, several positively and negatively charged binding sites in combination with van der Waals or other weak interactions expands the possible scope of this technique. The approach of integrating LB and LbL multilayers of electron donor–acceptor nanohybrids based on a combination of fullerenes and CNT with light absorbing building blocks into photovoltaic devices

revealed promising characteristics for energy conversion, high photoactivity, and environmental stability. An important feature is that the photocurrents evolving from the efficient generation of charge-separated states increase with the number of deposited layers [34].

2 Historical Background

2.1 *Langmuir/Langmuir Blodgett*

The early origins of the Langmuir–Blodgett technique date back to the ancients which already have been aware of the interesting effects of oil on the water surface. Nevertheless, the first effort to place the subject of monolayers on a scientific basis was made by Franklin in the eighteenth century [28]. His original experiments on the calming influence of oil on the water surface of the Clapham ponds were recorded in his communication to the Royal Society in 1774 [35]. Later, Rayleigh estimated from his experiments on dispersions of oil on water the thickness of these films to be in the molecular range [36]. It was Pockels, at the end of the nineteenth century, who via direct measurements of molecular dimensions [37] introduced a simple experimental setup with movable barriers, which emerged later as the model for the Langmuir–Blodgett trough. Work in this field was pursued at the beginning of the twentieth century by Devaux [38], who was among the first to accomplish experiments of spreading polymers as films utilizing proteins and polymers. Hardy [39] discovered that only materials with a polar head group extend to form good monolayers. Nevertheless, his assumption of long-range cohesive forces between molecules in the film turned out to be wrong. It was Langmuir, who postulated that these forces have short-range character and are affective exclusively between neighboring molecules [40]. He accomplished a systematic study of monolayers of amphiphilic compounds at the air/water interface and laid the scientific foundation for monomolecular films. For the latter he was awarded with the Nobel Prize in Chemistry 1932 based on his experiments that have demonstrated the formation of stable adsorbed films, in which single atoms were bound to the underlying surface. Furthermore, he invented among other new techniques and devices, the surface film balance, which carries his name today [41]. In his experiments, he shed light onto the orientation of molecules at the air/water interface. In particular, the polar head groups immerse into the aqueous phase, while the non-polar chains point almost vertically from the surface and provided evidence for Rayleigh's assumption of the single molecular layer thickness of the films. In a paper mainly devoted to other topics, Langmuir also referred to the transfer of films from the air/water interface to solid substrates [42]. It was, however, not until 1935 that Blodgett provided a systematic description of multilayers of carboxylic acids deposited onto a solid surface from the air/water interface [43]. Built-up monolayer assemblies are now referred to as Langmuir–Blodgett films in contrast to Langmuir films, which

describe only the monolayers at the air/water interface. While Langmuir concentrated on protein monolayers, Blodgett focused on the optical properties of multilayer films [28]. Until the outbreak of World War II, scientific research regarding the properties of monomolecular films mushroomed. A more detailed account of work during this period is given by Gaines whose book [44] provides a comprehensive treatment of the subject up to 1966. However, few applications were found for monolayer and multilayer structures. Within the last 10 years, LB films arose once again as a subject of detailed investigation. This interest has been in part stimulated by some intriguing possibilities for the application of these films. Many of these applications are in the fields of electronics and microelectronics [45] and have only emerged with the rapid expansion of these subjects.

2.2 *Layer-by-Layer*

Even though the LB procedure is a powerful tool for handling molecular building blocks, it suffers from some inherent drawbacks, mainly due to the extensive use of mechanical manipulation in the formation and transfer of monolayer films [46]. The control of specific properties at the molecular level has been achieved for a number of supramolecular systems by means of self-organization concepts. The self-assembly of organic, layered heterostructures was pioneered by Sagiv [47], who produced stable monolayers via covalent adsorption of molecules with specific functional groups onto solid substrates. In another work, the formation of multilayer assemblies was enabled by means of bifunctional silane surfactants exhibiting both, the usual polar head group (i.e., SiCl_3 -group) necessary for covalent attachment to hydroxyl possessing surfaces and a nonpolar group (i.e., ethylenic group) chemically convertible into a polar function after the first adsorption step (i.e., via hydroboration and H_2O_2 oxidation to terminal hydroxyls) [48]. A drawback of this strategy is the limitation to covalent or coordination chemistry and, in turn, to certain classes of molecules. These problems are most likely caused by the steric demand of covalent chemistry and the few reactions with 100% yield, which is a requirement for maintaining a high density of functional groups in each layer. A more versatile approach is the LbL method, having its roots in an extraordinarily envisaging publication by Iler [49] in 1966 and by Decher [50, 51] at the beginning of the 1990s. This method is suitable for the fabrication of layered heterostructures with a prerequisite for fine control over specific properties. The LbL technique was first applied to electrostatic assemblies of oppositely charged polyelectrolytes onto charged surfaces realizing the adsorption of polymer composite multilayer films with uniform thickness. Here, the steric demand is minimized and therefore LbL seems to be a good candidate for multilayer formation. Since the early 1990s, the deposition of multicomposite films of rod-like molecules equipped with ionic groups at both ends [52], polyelectrolytes [53], or other charged materials have been investigated through LbL adsorption from aqueous solution [54, 55]. This technique was further expanded by Rubner et al. [56] who developed the molecular

self-assembly process based on alternate depositions of p-type doped electrically conductive polymers and conjugated or non-conjugated polyanions onto different substrates. Thereby, the manipulation of polymer films for the fabrication of multilayers with novel electrical and optical properties was enabled. In the following years, the LbL method involving polyelectrolytes was further extended to other systems, namely polymeric nanocrystals, [57, 58] metal and semiconductor nanoparticles, [59, 60] and dendrimers [61]. Furthermore, multilayers for light-emitting thin films [62–66], permselective gas membranes, [67, 68] non-centrosymmetric films for nonlinear optics [69, 70], selectively patterned surfaces [71], electrochromic films [72, 73], electrocatalytic surfaces [72], and sensors [74] were established.

In most of the cases adsorption in LbL films is only driven by electrostatic interactions between oppositely charged species, but secondary interactions have also been shown to be relevant. Noteworthy, regarding conventional alternative assembling methods is the hydrogen-bonded LbL deposition [75–78]. Polymers with hydrogen bond donors and acceptors can be utilized as molecular building blocks for LbL assembly. Another driving force for LbL deposition is step-by-step reactions providing an alternative for fabricating stable multilayer films [79]. Mallouk and co-workers investigated metal-phosphate/phosphonate chemistry for a multilayer synthesis based on sequential adsorption of components of zirconium 1,10-decanebisphosphonate, $Zr(O_3PC_{10}H_{20}PO_3)$ (Fig. 1).

Kunitake and co-workers have been the first who introduced the preparation of nanocomposite thin films through stepwise adsorption of alkoxides [80] by means of metal oxide gel films from a surface sol–gel process. They demonstrated this method to be applicable to a variety of alkoxides of titanium, zirconium, silicon, indium, tin, and vanadium [81]. Additionally, this method has been applied for the implementation of organic dyes, amino acids, and sugar compounds into such gel films to accomplish molecular imprinting [82]. Another mentionable driving force for the fabrication of multilayer assemblies is charge–transfer (CT) interactions between donor and acceptor polymers, resulting in periodic layers of CT complexes. Recently [83], a procedure to deposit multilayered films by sequent adsorption of two types of nonionic polymers featuring electron-accepting groups (i.e., 3,5-dinitrobenzoyl group) and electron-donating groups (i.e., carbazolyl group), respectively, at the ends of the side chains (Fig. 2) has been established. The application of those CT multilayer films as conductive or nonlinear optical materials is well received.

Further conventional multilayer assembly methods were introduced in the context of utilizing the characteristics of the stepwise stereocomplex assembly between sterically well-defined synthetic polymers in certain solvents for LbL deposition of ultrathin polymer assemblies on substrates [84–86]. The electrochemical LbL deposition, which refers to a potentiodynamic method [87], emerged as an effective procedure for multilayer deposition of electroactive species applicable in electrochemical sensing [88–90].

Besides the aforementioned approaches, where the multilayer LbL assembly is realized by means of various interactions and driving forces between adjacent

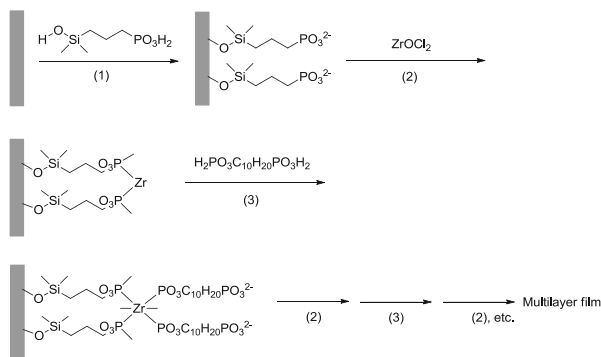


Fig. 1 Sequential adsorption of components of zirconium 1,10-decanebisphosphonate, $\text{Zr}(\text{O}_3\text{PC}_{10}\text{H}_{20}\text{PO}_3)$: First step, exposure of the substrate to an aqueous solution of a silanol resulting in a monolayer of covalently anchored phosphonate groups. Second step, exposure to aqueous ZrOCl_2 solution. Third step, exposure to an aqueous 1,10-decane bis-phosphonic acid. Multilayer adsorption by repetition of the second and third steps

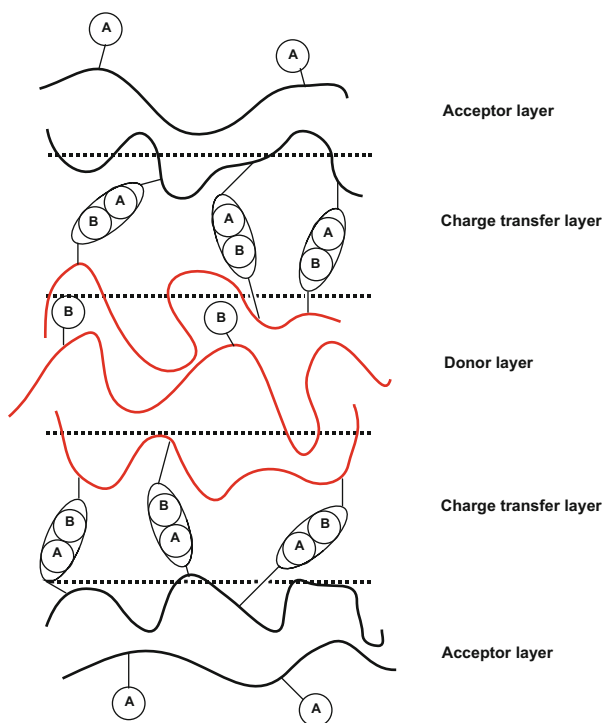


Fig. 2 Cross-sectional profile illustration of the assembled CT multilayer film. The carbazolyl and the 3,5-dinitrobenzoyl groups are simplified represented as D and A, respectively. The CT complexes formed by A and B groups are *circled*

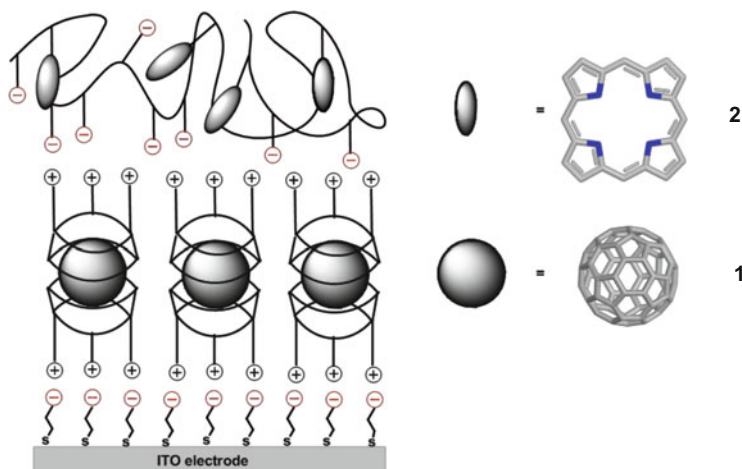


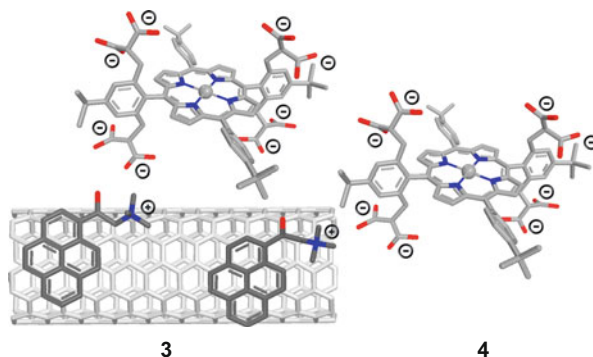
Fig. 3 Schematic representation of LbL assembled film of sodium 3-mercaptoethanesulfonate (*first layer*), inclusion complexes of fullerenes (**1**) encapsulated in cationic homooxalix[3]arenes (*second layer*), and anionic charged porphyrin (**2**) polymers (*third layer*) on ITO substrate

layers of defined molecular building blocks, several unconventional approaches describe the deposition of molecules not feasible to assemble with the aforementioned procedures (i.e., single charged, electrically neutral, or water-insoluble species). To this end, one type of supramolecular approach that renders an uncharged species charged and water-insoluble species water-soluble are inclusion complexes. In fact, the supramolecular modification secures the fabrication into multilayer thin films in a designed sequence. One of the successful examples is the assembly of pristine fullerenes (**1**) as ultrathin layers by means of encapsulation in cationic homooxalix[3]arenes [91]. Thereby, the water-insoluble fullerene becomes water-soluble and positively charged and is assembled in a second step with a negatively charged porphyrin polymer (**2**) (Fig. 3).

Another choice to render unorganizable species organizable is the non-covalent modification. A major breakthrough/refinement in depositing SWNT appeared with the supramolecular treatment of CNT with amphiphilic pyrene derivatives that carry ionic side chains (i.e., 1-(trimethylammonium acetyl)) as hydrophilic parts yielding non-covalent functionalized SWNT/pyrene⁺ nano hybrids (**3**) [92]. Noteworthy is a workup procedure that allows enrichment of SWNT in aqueous media [93]. Consequently, they were able to accomplish the electrostatically driven deposition of SWNT/pyrene⁺/Zn porphyrin⁸⁻ (**4**) associates onto polyelectrolyte surfaces (Fig. 4).

Moehwald and co-workers introduced another precursor method involving a two-step self-assembly process: first, charged metallosupramolecular coordination polyelectrolytes were formed by the reaction of metal ions with polytopic ligands, subsequently consecutive adsorption with negatively charged polyelectrolytes generated molecular films [94, 95]. In a different approach block copolymer

Fig. 4 Schematic representation of LbL assembled film of non-covalently pyrene⁺ functionalized SWNT (3)/Zn porphyrin⁸⁻ (4) associates on anionic polyelectrolyte coated ITO substrates



micelles are utilized as building blocks for LbL deposition. Small water-insoluble molecules can enter the cores of such micelles spontaneously and can be released from the micelles under special conditions. Initial reports focused on core-shell structured hydrogel thin films on surfaces by alternating deposition of poly(ethyleneglycol)-*b*-poly(D, L-lactide) micelles and poly(allylamine) [96]. However, this method bears limited potentials for applications because it involves complicated procedures. As an alternative, hydrophobic cores of block copolymer micelles have been utilized to implement water-insoluble molecules – including pyrene – into the hydrophobic micellar cores of poly(styrene-*b*-acrylic acid) for further application of the loaded block copolymer micelles as building blocks for LbL assembly [97] (Fig. 5).

In a nutshell, this field of research offers numerous possibilities for the fabrication of functional surfaces utilizing either conventional or unconventional deposition methods, which open up new vistas of surface molecular engineering. Moreover, the LbL technique is extremely versatile with regard to the applied substrates including hydrophilic and hydrophobic glass, mica, silicon, metals, quartz, and even polymers [98, 99].

3 Fundamental Concepts and Mechanisms of Multilayer Formation

3.1 Deposition of Langmuir–Blodgett Films

The study of Langmuir films, monolayers formed on the water surface, discloses an abundance of valuable information about molecular sizes and intermolecular forces. Nevertheless, the great interest in this field is based upon the fact that these monolayers can be transferred onto different substrates by means of the LB technique. In order to form LB films, a suitable substrate is normally lifted and raised vertically through the monolayer film, while maintaining a constant surface

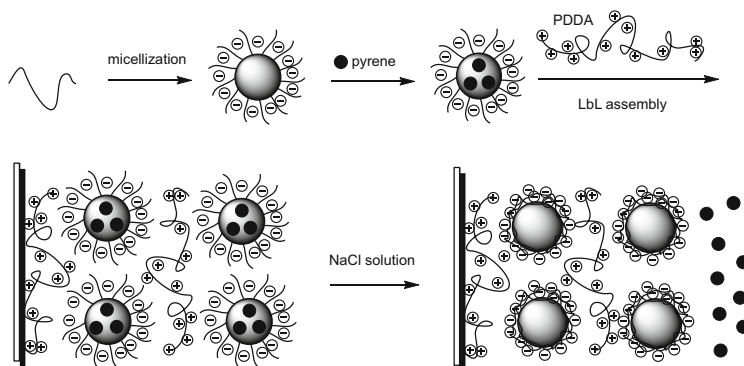


Fig. 5 Schematic representation of implementation of pyrene molecules into the cores of hydrophobic micelles, LbL assembly of PDDA and micelles, and release of pyrene molecules

pressure. There are also other transfer procedures known resulting from different interactions between the molecular monolayer, subphase, and substrate. When the adhesion on a vertically immersed substrate is rather moderate, some researchers have adopted the less satisfactory method of placing the substrate flat on the liquid surface, a technique introduced in 1938 by Langmuir and Schaefer [100]. In other examples horizontal dipping techniques are reported [101, 102].

Noteworthy, LB is one of the classical surface chemistry methods, but still the underlying transfer mechanisms of floating monolayer films onto solid substrates is not yet fully explored [103]. The materials forming monomolecular layers on water invariably consist of amphiphilic molecules featuring both water-attracting (hydrophilic) and water-repelling (hydrophobic) groups. LB films are prepared by first depositing a small quantity of the amphiphilic material, dissolved in a volatile solvent, onto the surface of carefully purified water. When the solvent has evaporated, the organic molecules may be compressed to form a floating “two-dimensional” solid. The hydrophilic and hydrophobic terminations of the molecules ensure that, during this process, the individual molecules are all aligned in the same way. In the multilayer deposition utilizing the LB technique the driving forces for the transfer of the first layer onto the solid substrate of a different material can differ from the interactions between the subsequent layers transferred onto the already existing film. Therefore, the chemical and physical structure of the first monolayer might be different from the following layers. This is the case, for instance, if the formation of the first layer occurs via chemical reactions with the substrate surface [104] resulting in a strongly linked first layer. Also, a change in the crystalline packing of the first and subsequent monolayers was monitored [105, 106] by means of infrared investigations of fatty acid films. These studies disclosed a hexagonal symmetry of the first deposited layer being followed by a transition over the next few layers resulting in an orthorhombic or monoclinic structure depending on the material used. Although there is a number of experimental evidence as well as

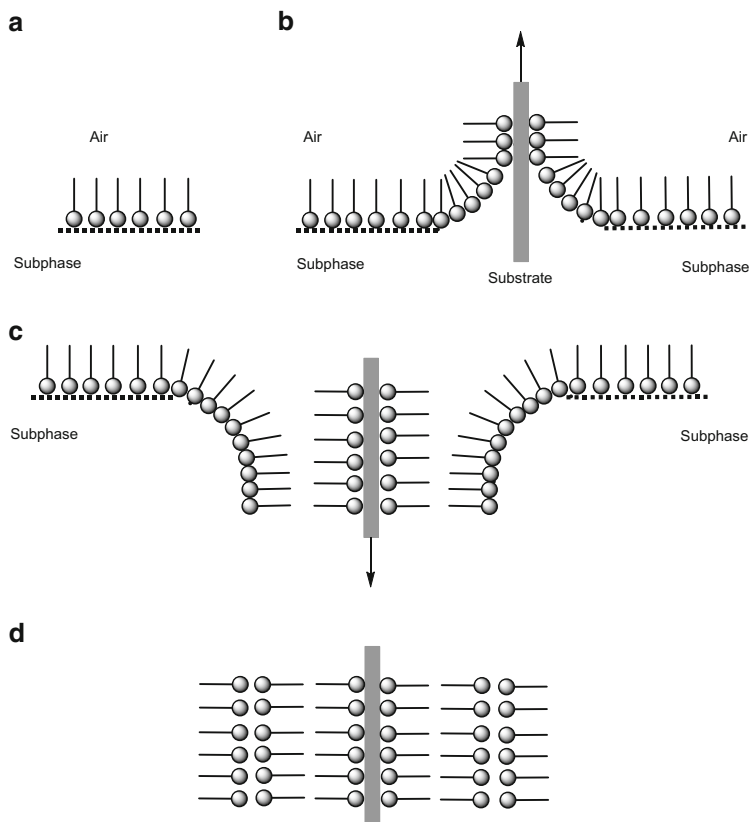


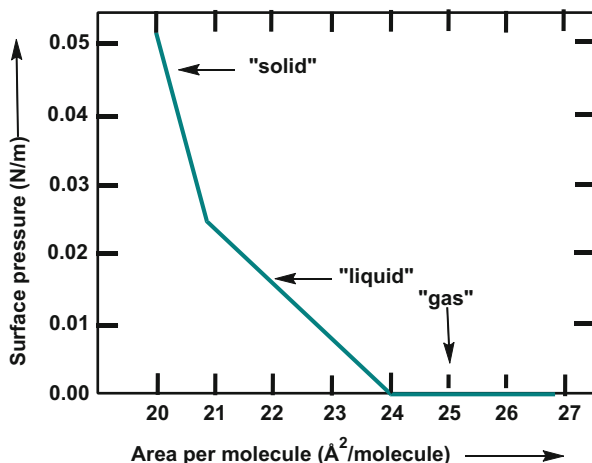
Fig. 6 Schematic representation of Y-type LB deposition of three consecutive layers onto a hydrophilic substrate, resulting in a head-to-head and tail-to-tail configuration of the monolayers

theoretical treatments [107] of LB film deposition, a complete understanding of the formation mechanisms needs further developments in both of these areas.

The most common deposition mode utilized in the LB assembly is illustrated in the schematic diagram in Fig. 6. In this process, referred to as Y-type, the immersed substrate is hydrophilic and the first monomolecular layer is deposited in both, up and down directions. The substrate is therefore either already placed into the subphase before spreading the monolayer onto the water surface or immersed into the subphase through the compressed monolayer.

During the compression process the monolayer undergoes several phase transformations. The different phases are the two-dimensional analogues of gases, liquids, and solids and can be identified by measuring the surface pressure/surface tension of the monolayer. Figure 7 depicts a plot of the surface pressure versus occupied area per molecule for stearic acid. By reducing the available area per molecule, the compressed monolayer is transformed into the condensed “solid” form, while the steep pressure area indicates low compressibility in the monolayer.

Fig. 7 Schematic diagram of surface pressure/area isotherm of stearic acid on water



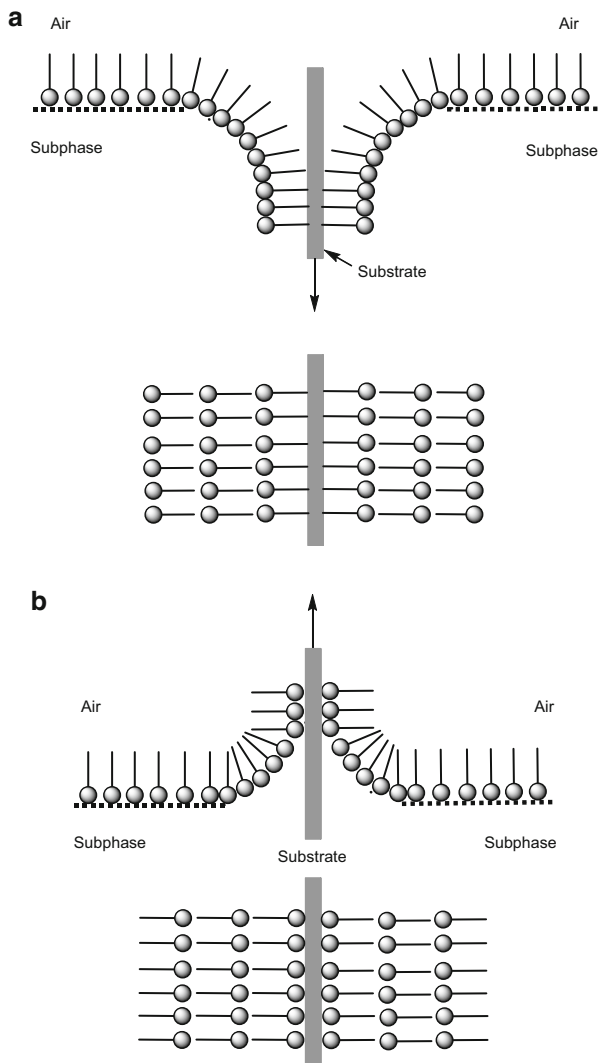
This behavior indicates the presence of strong chain–chain interactions forcing the molecules into their closest-packed arrangement, with moderate dependence on the surface pressure.

In this condensed state, monolayers may be conveniently transferred from the water surface onto a suitable substrate. During this process accurate monitoring of the surface pressure of the monolayer is essential. Although the *Y*-type deposition is the most conventional method utilized for the LB film formation, there are also procedures in which the floating monolayer is only transferred by moving the substrate in a downward direction (*X*-type) or an upward direction (*Z*-type) into or out of the water (Fig. 8).

Mixed deposition modes are also observed. Likewise, the deposition type may also be changed during the LB film is generated. It is also possible to assemble multilayers with different types of materials in the monomolecular films. The simplest case regarding this procedure is the initial immersion of the substrate through a monolayer of material A followed by lowering the substrate through a monolayer of material B. Therefore, a multilayer film containing an ABABAB... order of monolayers is obtained.

During the film transfer process the surface pressure of the floating monolayer is kept constant. The so-called *deposition* or *transfer ratio* τ refers to the ratio of the decrease in area occupied by the monolayer on the subphase to the area of substrate passed through the air–water interface. To guarantee a successful deposition, this ratio should be close to unity. Apart from the surface pressure, the temperature and acidity (pH) of the subphase are important variables that must be controlled for a successful deposition of monomolecular films. For example, at high pH of the subphase the deposition type can change from *Y*- to *X*-type in case of fatty acids or their salts. Another crucial factor is the deposition speed, which is limited by two factors. On the one hand, as the film is deposited onto the substrate, the withdrawal should be slow enough to guarantee a thorough transfer of material onto the substrate and at the same time to enable the replacement of already removed

Fig. 8 Schematic representation of *X*-type (a) and *Z*-type (b) LB deposition of three consecutive layers onto a hydrophobic (a) and hydrophilic (b) substrate, respectively



material on the water surface. Herein, the viscosity of the considered Langmuir film is the rate limiting factor. On the other hand, as the substrate is moved in the upward direction, water in contact with the hydrophilic groups of the already transferred molecules drains away from the solid to make room for the hydrophilic groups. The rate at which this process can occur is known as the drainage speed and is in the case of low viscosity materials the rate-determining process. Normally the initial layer is transferred onto the substrate with relatively slow speeds ranging from $10 \mu\text{m s}^{-1}$ to a few mm s^{-1} . Nevertheless, once the first layer is deposited, much faster deposition speeds, up to several cm s^{-1} are possible [108].

3.2 *Layer-by-Layer Assembly*

The LbL technique – a method where polyanions and polycations are alternately adsorbed onto a substrate – is a very appealing possibility for the assembly of ultrathin films and provides nm thickness control. The thickness of a single polyelectrolyte layer is in the range of several Angstroms facilitating the control of total film thickness by the number of adsorbed layers. The broad range of materials available for the incorporation into polyelectrolyte multilayers in a designed layer sequence makes this procedure peculiar when compared with other film deposition techniques. In contrast with previous methods, the LbL technique provides essentially amorphous films, which are not necessarily stratified due to interfacial overlap of adjacent layers. Importantly, this method is highly straightforward, since it involves simple equipment and preparation procedures and can be applied to diverse types of substrates without consideration of size and shape. A simple case of consecutive deposition of two monofunctional materials is represented by polyanion–polycation deposition on a positively charged surface. The charged molecules in solution are hereby assembled onto oppositely charged surfaces by means of strong electrostatic attraction. Due to the adsorption of molecules carrying more than the stoichiometric number of charges with respect to the surface, reversal of charges at the surface is achieved resulting in two important implications. On the one hand, single layer formation of one type of polyelectrolyte (i.e., polyanion) is due to repulsive interactions between equal charges and, on the other hand, adsorption of oppositely charged polyelectrolyte (polycation) on top of the other. Periodic repetition of both adsorption steps leads to the formation of multilayer structures. The fact that these films are deposited from solutions makes this concept a versatile candidate for the application on any kind of substrate with different size and topology. Multilayer film deposition onto a solid substrate is accomplished manually from ordinary beakers (Fig. 9a) or can also easily be adapted for automated fabrication within a deposition time of 20–30 min for one layer. The representation of the build-up of a multilayer film at the molecular level (Fig. 9b) shows a positively charged substrate adsorbing a polyanion and a polycation consecutively. As a leading example, two typical polyelectrolytes, poly(sodium 4-styrene sulfonate) (**5**) and poly(diallyldimethylammonium chloride) (**6**), are shown in Fig. 9c.

The charges of polyelectrolytes are highly beneficial for a strong adhesion of a monolayer to the substrate or film. In particular, they support the formation of numerous stabilizing bonds. Moreover, polymers assist in masking underlying defects. Their conformation at the substrate and film surface is mostly dependent on the considered polyelectrolytes and adsorption conditions and much less dependent on the substrate or the substrate charge density [54, 109]. As a matter of fact, substantiation for this hypothesis stems from similar linear increases of film thicknesses as the function of deposited layers even if different substrates are used. Electrostatic attractions between oppositely charged polyelectrolytes are the general driving force for the deposition cycles. Nevertheless, the amount and the conformation of adsorbed chains reveal dependence on processing parameters,

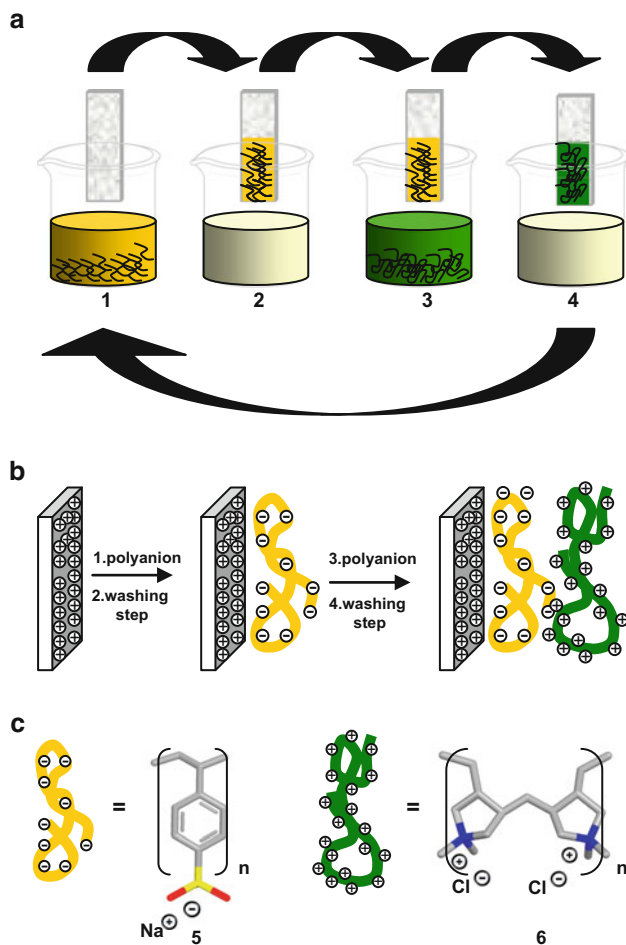


Fig. 9 (a) Schematic representation of film deposition process. The solid substrate is consecutively immersed into solutions of a polyanion (step 1) and polycation (step 3), respectively, with washing steps (2 and 4) after each layer deposition. Cyclic repetition of the four steps results in a multilayer architecture of type (A/B)_n. (b) Simplified molecular representation of a double layer formation of a polyanion and polycation on a positively charged substrate surface. (c) Chemical structures of two typical polyelectrolytes: poly(sodium 4-styrene sulfonate) (5) (left-hand side) and poly(diallyldimethylammonium chloride) (6) (right-hand side)

especially ionic strength and pH of the dipping solutions as well as on the charge densities of both the polyelectrolyte components. To this end, the effects of molecular structure, substrate, charge density, ionic strength, deposition pH, and rinsing conditions on the multilayer stability were explored and documented in several articles [110–116]. Variation of the charge density is typically achieved by changing the pH of the dipping solution when polyelectrolytes carry pH-dependent functional groups such as amines and carboxylic acids or by using copolymers

containing different ratios of ionic groups. At high ionic strengths or low polymer charge densities the electrostatic repulsion between different polyelectrolyte segments is reduced and, in turn, adsorption is promoted. Likewise, electrostatic attractions between polyelectrolytes and oppositely charged surfaces are reduced, which counteracts to polyelectrolyte adsorption. As a result, the balance between polyelectrolyte segment/segment and polyelectrolyte segment/surface interactions governs the layer growth and thickness [117]. Typically, films are transferred at concentrations as high as several milligrams per milliliter. Moreover, several rinsing steps are conducted after adsorption of each layer to prevent contaminations by liquids adhering to the substrate. Additionally, rinsing removes weakly attached molecules and, therefore, exerts a stabilizing impact [118].

4 Thin Films of Carbon Nanotubes and Fullerenes

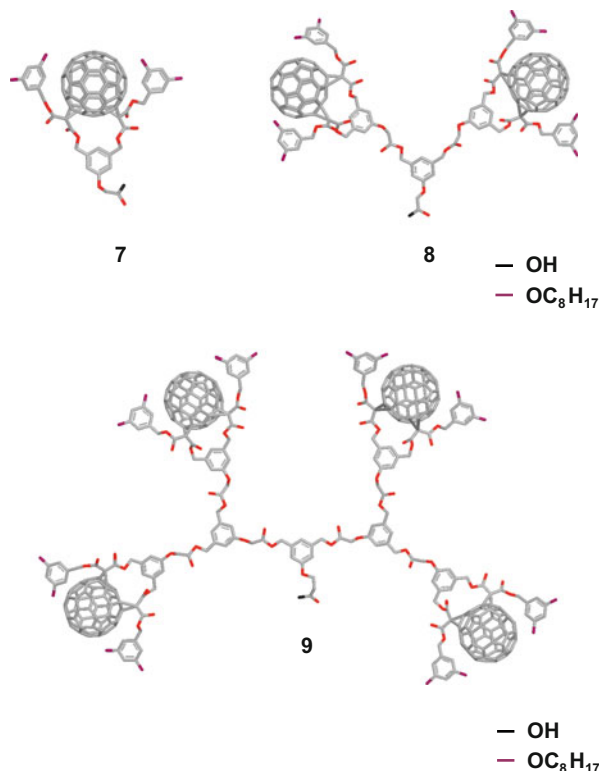
4.1 Langmuir–Blodgett Films

Development of thin film fabrication techniques constitutes a requisite section of materials science and technology. Particularly, for investigating their optical, optoelectronic, and electrical properties in a macroscopic scale, the availability of high quality, homogeneous thin films is a fundamental prerequisite. Furthermore, thin film fabrication techniques provide an important base for the development of various types of optical, electrical, and chemical devices. One set of active components considered in the nanostructured thin film fabrication are carbon allotropes, such as fullerenes [25, 27, 119–121] and CNT [23, 122].

4.1.1 Fullerenes

The large availability of macroscopic quantities of C_{60} has led to an extensive range of studies on this allotrope of carbon. In particular, thin films of C_{60} exhibit remarkable characteristics [123, 124], ranging from superconductivity [125–127] to charge-transfer behavior [128–131]. An essential requirement for the systematic investigation of these properties is the incorporation of fullerenes into organized arrays (i.e., two-dimensional) and networks (i.e., three-dimensional). There have been few reports on interfacial properties of C_{60} and its derivatives, especially in the field of floating films assembled at the air/water interface [132–148]. Moreover, the employment of the Langmuir–Blodgett technique for the deposition of highly organized C_{60} thin films was thought to lead to the discovery of applications [108]. However, C_{60} is very rigid and hydrophobic, thus exhibiting properties fundamentally different from those of rod-like self-assembling amphiphilic molecules commonly employed in LB experiments. So, the deposition of C_{60} LB films has proven to be particularly difficult and lacks reproducibility. In fact, their

Fig. 10 Fullerene-based amphiphilic dendrimers **7**, **8**, and **9**



high cohesive energy of more than 30 kcal mol^{-1} [134, 149] reflects the strong intermolecular attractive interactions and, in turn, C₆₀ aggregates spontaneously and forms very stable van der Waals crystals. As a direct consequence, C₆₀ is only sparingly soluble in most organic solvents [123, 124, 150]. Accordingly, pristine C₆₀ tends to form ill-defined films of three-dimensional aggregates at the air/water interface rather than a monomolecular layer. It appears from several studies that the aggregation of C₆₀ is circumvented by either attaching hydrophilic headgroups or blocking the contact via encapsulation. One fascinating contribution reports on the formation of stable Langmuir films of C₆₀-based amphiphilic dendrimers (**7**, **8**, **9**) (Fig. 10) and the transfer of the floating monolayers onto solid substrates, yielding high-quality LB films [151].

Although it was impossible to transfer **7** and **8** onto hydrophilic substrates, they were easily deposited onto silicon or glass substrates covered with a monolayer of octadecyltrichlorosilane. Mono- and multilayer films have been transferred with high efficiency. Films of **7** gave the best results, followed by **9**, despite the high molecular mass. A monolayer of **8** was deposited onto a hydrophilic silicon substrate by the Langmuir–Schaefer (LS) method. This approach was even enhanced by adjusting the size of the hydrophilic and hydrophobic groups of the dendrimer units [152]. **10** and **11** are composed of a dendron with peripheral long

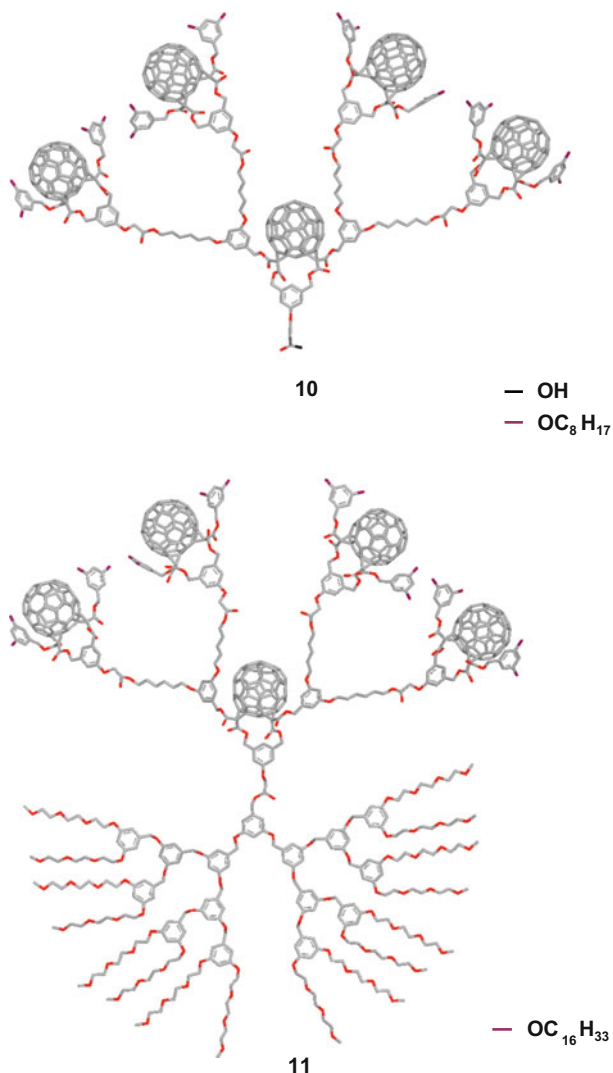
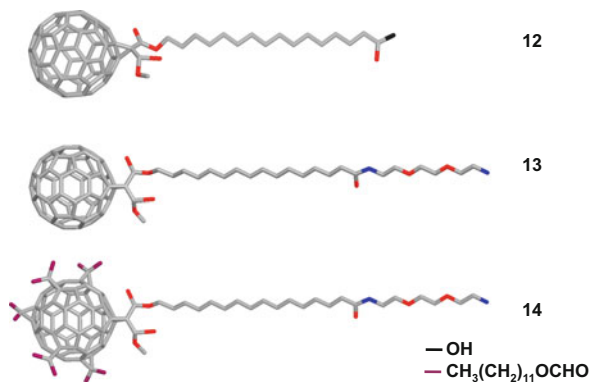


Fig. 11 Scheme of fullerene containing compounds **10** and **11**

alkyl chains and five C₆₀ in the branching shell, which has been attached to a Fréchet-type dendron functionalized with ethylene glycol chains (Fig. 11). Upon closer inspection, the peripheral substitution of the globular dendrimer with hydrophobic chains, on one hemisphere, and hydrophilic groups, on the other hemisphere, provides the perfect hydrophobic/hydrophilic balance allowing the formation of stable Langmuir films.

On the one side, placing the five C₆₀ in the center of the dendritic structure provides a compact insulating layer around the carbon spheres and, thus, preventing

Fig. 12 Scheme of amphiphilic fullerene derivatives **12**, **13**, **14**



reversible 3D aggregation. On the other side, the polar head group leads to attractive interactions with the subphase. This forces the molecules into a 2D arrangement on the water surface. **10** and **11** were successfully transferred onto quartz slides and silicon wafers with higher transfer ratios for **11** providing a perfectly balanced hydrophilic/hydrophobic functionalization.

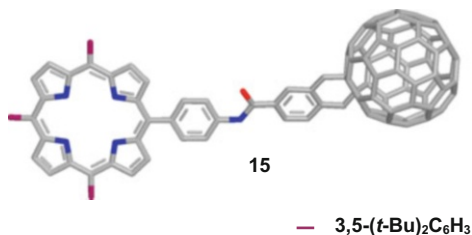
Another example reports on assembling three different amphiphilic C₆₀ derivatives (**12**, **13**, **14**) in mono- and multilayers by means of LB method. Two of the C₆₀ amphiphiles are mono-adducts possessing long alkyl chains terminated with either carboxylate (**12**) or amine groups (**13**) as hydrophilic headgroups. **14** exhibits the same amine group as **13**, but with 10 additional hydrophobic alkyl chains attached to C₆₀ (Fig. 12).

In the case of the amine-terminated C₆₀ (**13**) as well as the carboxylate-terminated C₆₀ (**12**) successful monolayer depositions were accomplished exclusively in the upward direction transfer (Z-type), whereas **14** gave rise to high transfer ratios in the down- and upward direction (Y-type). This observation is explained by the implemented alkyl chains, which enhance the hydrophobic interactions during the upward direction transfer in contrast to hydrophobic interactions between pristine C₆₀.

When turning to the role of C₆₀ in photoactive electron donor–acceptor conjugates the photochemistry is mainly studied in solution. Specifically, porphyrins and phthalocyanines have been widely studied as electron donors in combination with C₆₀. To this end, charge and energy transfer events for electron donor–acceptor systems in the solid state have rarely been explored. For the investigation of photoinduced intra- and interlayer processes, molecular films should be immobilized onto solid substrates by means of, for example, the LB technique.

Notable success was made in preparing solid porphyrin/C₆₀ films with electron donor–acceptor conjugates [153]. In the case of such a covalently linked porphyrin/C₆₀ system (**15**) (Fig. 13), the close proximity of the porphyrin and C₆₀ results in the formation of emitting charge transfer (CT) states not being observable in the liquid phase.

Fig. 13 Scheme of covalently linked porphyrin–fullerene dyad (**15**)



The non-amphiphilic nature of **15** failed to yield stable structures on the water surface. However, the film formation was accomplished by mixing **15** with suitable matrix molecules, such as octadecylamin (ODA). It was possible to transfer the layers from the water surface onto quartz substrates using the standard LB method with transfer ratios close to unity. Importantly, multilayer deposition showed a linear increase of absorption with the number of deposited layers.

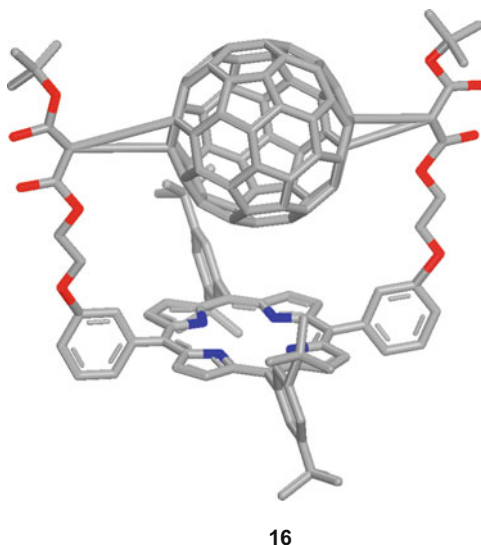
By the same token, monomolecular LB films of a doubly linked porphyrin/C₆₀ conjugate (**16**) (Fig. 14) with uniform electron donor–acceptor orientation have been prepared [154]. Under light illumination the films perform vectorial charge separation and can be used as, e.g., primary charge separating layers in solar cell applications. In LB films, **16** are packed close to each other with distances approaching van der Waals contacts. This enforces intermolecular interactions of the photoexcited species.

4.1.2 Carbon Nanotubes

In recent years, CNT have attracted great attention due to their exceptional electrical, mechanical, and thermal properties [155, 156]. Thin films of CNT are exploited extensively in the fields of electron field emitters [157], quantum wires [158], molecular filters [159], hydrogen storage [160], flat panel displays [161], and field effect transistors [162].

The transfer of CNT films onto solid substrates is a challenging procedure, since CNT exhibit rather moderate solubilities in organic and aqueous media without the assistance of surfactants. Strong van der Waals interactions between individual CNT, hydrophobicity, and low solubility at moderate concentrations hamper the use of wet chemistry techniques in preparing uniform films. Therefore, diverse modification processes – to improve the solubility of CNT in different solvents – were probed to overcome the solubility problem [163–165]. This facilitates to further manipulate or modify CNT for both, fundamental research and practical applications. CNT are normally produced by the techniques of arc discharge [156], chemical vapor deposition [166], high-pressure CO gas decomposition [167], or laser ablation [168]. However, all of the aforementioned methods result in randomly oriented nanotubes. This fact triggers the incentive in organizing CNT building blocks into functional assemblies and, ultimately, into devices. To succeed in aligning CNT together with an effective arrangement into patterns would

Fig. 14 Scheme of double linked porphyrin–fullerene dyad (**16**)

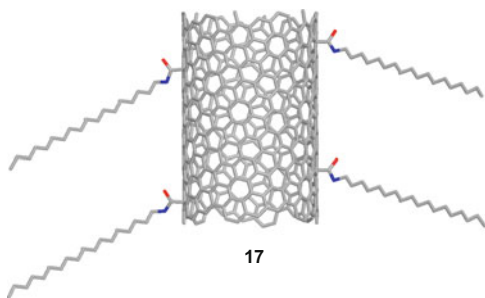


generate a tremendous impact to many fields of research. Reports on the growth of aligned CNT via thermal chemical vapor deposition [169] are certainly a milestone in this respect. However, this method is limited to certain substrates due to the requirement of high temperatures during the growth process. Therefore, various low-temperature techniques have been investigated. Hong et al. [170] demonstrated, for example, the alignment of pre-grown single wall carbon nanotubes (SWNT) onto chemically functionalized patterns on a surface (i.e., polar or non-polar groups). After immersing the substrate into SWNT suspensions, SWNT are attracted towards the polar regions and form pre-designed structures in a self-assembly process. Filter deposition from a suspension in strong magnetic fields is another approach to prepare films of preferentially oriented CNT [171]. Furthermore, the evaporation of CNT Triton X suspensions also secures the preparation of aligned thin films, although this technique is limited to colloidal dispersions and short CNT [172]. Finally, mentionable approaches of CNT alignment have been realized by electrophoresis [173, 174], electrospinning technique [175], and LB deposition.

Among all these methods, the LB technique is a promising candidate for organized and precisely aligned CNT assemblies. First of all, LB enables large area coatings of highly ordered monolayers on the air/water interface, which are easily transferred onto silicon and other substrates under mild temperature conditions. Second, the compression process supports the fine control over intermolecular distances and final superstructures. Third, consecutive layer deposition is feasible. Finally, in situ alignment is achieved by, for example, patterning and chemical modification of the substrates.

In a first example, a quasi-LB method was applied for depositing thin uniform CNT films onto alumina membranes [176]. The volume below the membrane is

Fig. 15 Scheme of ODA functionalized SWNT (**17**)



filled with a solvent (i.e., deionized water), which is immiscible with the solvent utilized to disperse the bare CNT (i.e., 1,2 dichlorobenzene). As a matter of fact, the CNT films float on top of an aqueous phase and are transferred uniformly onto any kind of substrate by drawing it through the free liquid surface. This procedure facilitates the deposition of uniform bare CNT films onto substrates, without, however, providing the means of control over the alignment.

Due to the rather moderate solubility of CNT in most common solvents, it is almost impossible to form LB films of pristine CNT. Even if CNT are suspended at low concentrations, flocculation takes place once the local concentration approaches the solubility limit. To overcome this problem, pre-modification of the CNT is indispensable with, for example, surfactants [177]. LB monolayers, consisting of SWNT homogeneously distributed in a matrix of amphiphilic molecules, were deposited on a substrate with electron lithographically defined electrode arrays by the Langmuir–Schaefer method.

In another approach, stable and robust vertically on mica substrates transferred CNT films were obtained utilizing LB method. The SWNT rendered hydrophilic by complexation with a quenched polyelectrolyte [178]. Atomic force microscopy (AFM) images revealed a surface pressure-dependent morphology of these films and aligned structures with a nematic-like order resulting in closely packed mono- or multilayer films.

Following the strategy of functionalization, large arrays of well-aligned CNT on glass, silicon, quartz, etc. have been successfully prepared by LB deposition of chemically modified SWNT [179]. In particular, oxidized CNT were reacted with thionyl chloride to introduce acyl chloride groups and then reacted with amphiphilic ODA [163]. The ODA functionalized CNT (see **17** in Fig. 15) disclosed substantial solubility in chloroform, CS_2 , and various aromatic solvents. With this procedure in hands, mono- and multilayers of highly oriented CNT were obtained utilizing the LB technique [180].

Successful alignment of CNT has been a considerable challenge, due to the high aspect ratio and ready formation of aggregates. A straightforward method to address this problem has emerged by nanoparticle modification. As-grown SWNT were modified by sonication in a toluene-based solution of dodecanethiol stabilized gold nanoparticles [181, 182]. Thereby, SWNT were covered with thiol-passivated gold nanoparticles, supporting the separation of nanotube bundles. Following this

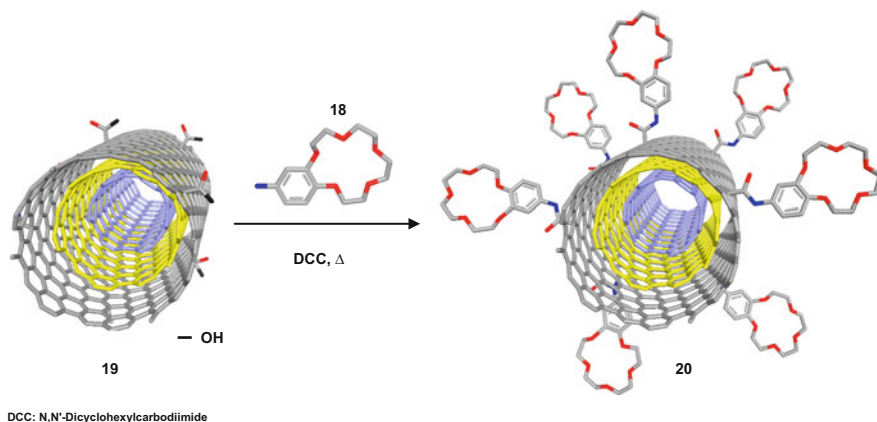


Fig. 16 Synthetic scheme for the introduction of crown ether groups (**18**) onto the surface of oxidized MWNT (**19**) to yield functionalized MWNT (**20**)

procedure, highly anisotropic LB monolayers of SWNT were deposited with a preferential orientation perpendicular to the compression direction. On the contrary, aligned multiwalled carbon nanotubes (MWNT) were realized by covalent functionalization with 4'-aminobenzocrown-5-ether (**18**) [183] (Fig. 16). To introduce crown ether groups, MWNT were initially oxidized to introduce carboxylic functionalities (**19**), which are subsequently condensed with **18** by a direct heating method. The amphiphilic crown ether functionalized MWNT (**20**) showed good properties as LB film material. To be precise, **20** was successfully transferred as monolayers onto several hydrophilic substrates, namely silicon, glass, and ITO.

Likewise, oxidized MWNT (**19**) were reacted with S-(2-aminoethylthio)-2-thiopyridine hydrochloride to form pyridine-dithiol-derivative-MWNT (**21**) [184]. These pyridine-dithiol-derivative-MWNT LB films were then used as a support to immobilize hydrogenase to form bionanocomposites of pyridine-dithiol-derivative-MWNT-hydrogenase (**22**) (Fig. 17).

Despite recent progress in the oriented assembly of CNT via the LB technique, it still turns out to be rather difficult to produce CNT films without altering their electronic and chemical properties by extensive covalent modifications. Taken the aforementioned into concert, an LB method utilizing a completely non-covalent approach was developed [185]. This procedure involves both, a high density and a high degree of alignment of SWNT. Herein, suspensions of SWNT in 1,2-dichloroethane solutions of poly(*m*-phenylenevinylene co-2,5-dioctoxy-*p*-phenylenevinylene) (PmPV) (see **23** in Fig. 18) were prepared by sonication, ultracentrifugation, and filtration. Strong π - π interactions between SWNT and PmPV entail an enhanced solubility in organic solvents. Especially DCE emerged as a suitable solvent in obtaining stable CNT suspensions after removing unbound PmPV. PmPV-SWNT hybrids were spread onto the water surface to afford LB monolayers of aligned SWNT with dense packing.

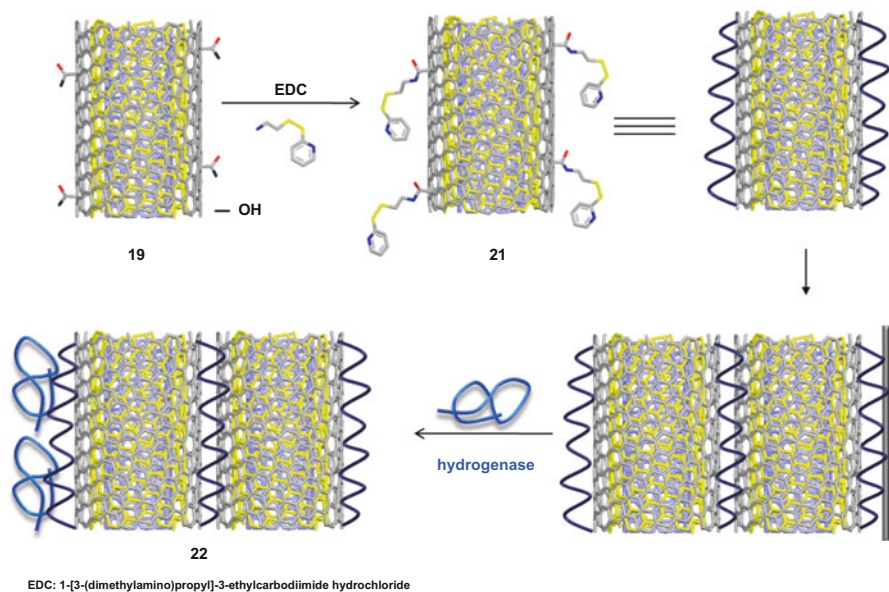


Fig. 17 Schematic representation for preparation of pyridine-dithiol-derivative-MWNT-hydrogenase bionanocomposites (**22**)

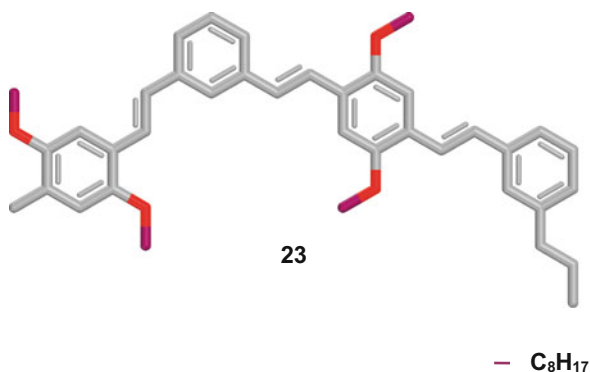


Fig. 18 Schematic representation of dimeric unit of a PmPV chain (**23**)

4.2 Layer-by-Layer Films

The mechanical failure of hybrid materials made from polymers and SWNT is primarily attributed to poor matrix–SWNT connectivity and severe phase segregation. Both problems have been successfully mitigated when the SWNT composite is made following the protocol of LbL assembly. This deposition technique prevents phase segregation of the polymer/SWNT system, and after subsequent

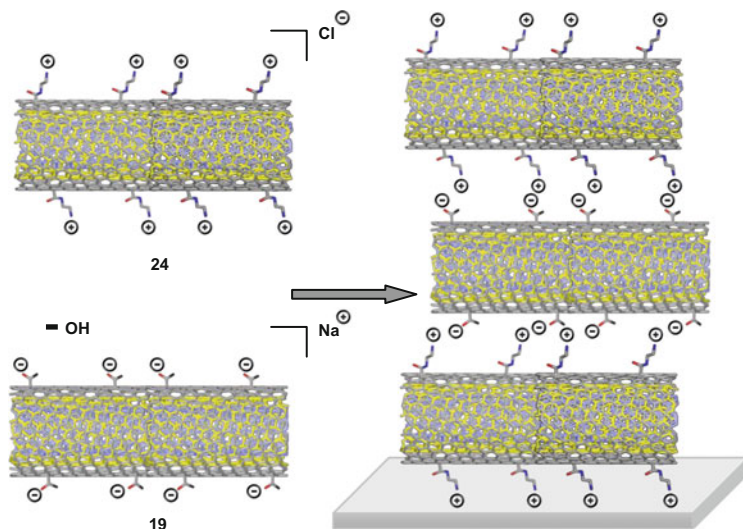


Fig. 19 Schematic representation of subsequent LbL assembly of **19** and **24** onto a solid substrate

cross-linking, the nanometer-scale uniform composite with SWNT loading as high as 50 wt% can be obtained.

SWNT/polyelectrolyte composites have been successfully assembled onto glass slides and silicon wafers by alternate dipping of a solid substrate into dispersions of SWNT and polyelectrolyte solutions [186]. For this approach, carboxylic acid group modified SWNT were prepared by acid treatment in order to introduce negative charges. These negatively charged SWNT were deposited by LbL technique with positively charged polyelectrolytes, such as branched poly(ethyleneimine) (PEI). Owing to the rather moderate overall negative charge on the SWNT, a layer of SWNT was replaced with a layer of poly(acrylic acid) (PAA) after every fifth deposition cycle. After completing the LbL procedure, the multilayer stacks with a cumulative structure of ((PEI/PAA) (PEI/SWNT)₅)₆ and ((PEI/PAA) (PEI/SWNT)₅)₈ containing 30 and 40 (PEI/SWNT) bilayers, respectively, were lifted off the substrate to obtain uniform free-standing membranes that can be handled as regular composites. Such films enable straightforward testing of their mechanical properties.

A strategy for LbL assembling pristine MWNT multilayers onto ITO coated glass substrates through non-covalent functionalization of MWNT implemented the use of surfactants [187]. Here, sodium dodecyl sulfate (SDS) was utilized as a surfactant, on the one hand, to increase the dispersability of MWNT in water and, on the other hand, to implement negative charges. In this approach alternating layers of PDDA and MWNT/SDS layers were transferred onto ITO.

In stark contrast, negatively and positively charged MWNT have been functionalized with carboxylic acid groups (MWNT-COOH) (**19**), and with amine groups (MWNT-NH₂) (**24**), respectively [188]. Out of the stable suspensions films with well-dispersed MWNT could be created (Fig. 19).

In summary, the LbL approach enables the successful modification of solid-condensed interfaces, including photoactive electrodes. Especially the strategy of employing electron donor–acceptor assemblies with multiply charged functionalities provides numerous advantages. Most importantly, the control over both the layer sequence and composition of the sandwich-like structures can be utilized for fine-tuning the electronic properties of the nanostructures. This method constitutes a potent alternative to traditional thin film techniques in fabricating photoactive molecular devices. Taken the aforementioned into account, the LbL assembly of CNT and fullerene films is therefore mainly focused on their application in photovoltaic devices, which will be discussed in the following section.

5 Applications of Multilayer Assemblies in Photovoltaic Devices

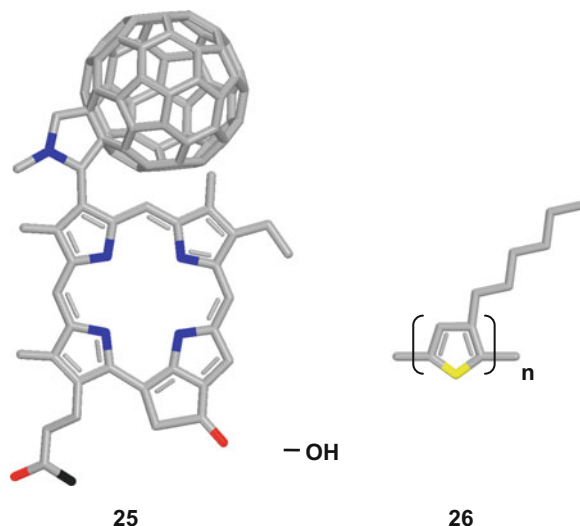
Carbon nanostructures represent a remarkable class of materials for applications in photovoltaic. In principle, solar cells using carbon nanostructures are expected to be cost-effective and simpler to manufacture when compared with those made out of inorganic semiconductors [189–191]. To further develop carbon nanostructures for solar cells it is imperative to optimize the individual steps as they relate to the overall photovoltaic conversion. First, improving the solar light harvesting from the electron donor and/or electron acceptor materials via exciton formation. Second, facilitating the charge separation via exciton dissociation and charge transport processes. Finally, reducing possible recombination events.

Since excitons have diffusion lengths of 7–20 nm, bulk-heterojunctions with large electron donor–acceptor surfaces/unit volumes are expected to improve solar cell efficiencies. Moreover, the construction of nanochannels for efficient electron and hole transport in electron donor–acceptor multilayers is highly crucial to attain efficient photocurrent generation. In fact, the importance of an interpenetrating, bicontinuous electron- and hole-transporting network in the films of bulk-heterojunction solar cells is well established [192–194].

LB and LbL assembly protocols offer means to order electron donor–acceptor systems in different layers with specifically designed interlayer separations. Importantly, the latter are tunable at the angstrom level to enhance photoinduced charge separation and minimize recombination losses. To this end, it may afford a way to mimic the natural photosynthetic process with its high level of control over intermolecular spacing, orientation, and local environments, resulting in a series of sequential energy and electron transfer reactions. [195–197]

Currently, sizeable efforts are directed towards increasing power conversion efficiencies while reducing the costs and increasing the device lifetimes to render them economically viable. Please note that sometimes different photocurrent characterization conditions (i.e., light power, intensities, and size of the cells) are used, which hamper a meaningful comparison only to solar cell performances that stem from the same laboratories.

Fig. 20 Phytochlorin/ C_{60} conjugate (**25**) and poly(3-hexylthiophene) (**26**)



5.1 Langmuir–Blodgett and Langmuir–Schaefer Film-Based Solar Cells

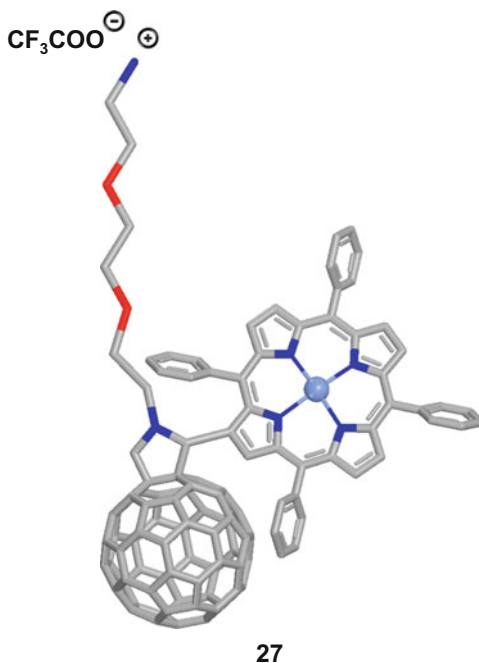
5.1.1 Fullerenes

The most studied organic material-based solar cells involve films of fullerenes together with conjugated polymers [5, 198–200], small molecules like phthalocyanines [201] or porphyrins [202–204]. In fact, the excellent properties of fullerenes as electron acceptors have prompted to the constructing of fullerene-based photoelectrochemical and photovoltaic devices. It is mainly the small reorganization energy of fullerenes in electron transfer, which leads to remarkable accelerations of charge separation as well as decelerations of charge recombination [189, 190, 205, 206].

The LB [108, 207] and LS [100] deposition methods have been used to construct highly ordered electron donor/fullerene heteromolecular multilayer films, needed to guarantee a fast vectorial photoinduced electron transfer. As a first example, alternating layers comprising a phytochlorin- C_{60} conjugate (**25**) and poly(3-hexylthiophene) (**26**) together with octadecylamine (ODA) as the matrix compound, anchored to ITO support and covered by an evaporated Al electrode were reported (see Fig. 20). Layers of **25** in the resulting ITO/ODA/**25**(**26/25**)₁₀/ODA/Al solar cell were found to act as a secondary electron donor following the primary photoinduced electron transfer by donating electrons to the phytochlorin cation [208].

An appealing variation involves an amphiphilic porphyrin/ C_{60} conjugate (**27**) designed for Langmuir film formation and transferred onto ITO substrates by LS monolayer deposition technique. An illustration is depicted in Fig. 21. Multilayers

Fig. 21 Nickel porphyrin/
C₆₀ conjugate (**27**)



of **27** were transferred from the air/water interface to modified ITO electrodes and probed in photocurrent experiments [209].

Utilizing a completely non-covalent strategy, LS thin films consisting of a C₆₀ derivative as electron acceptor (**28**) and a novel water-soluble porphyrin (**29**) as photoexcited electron donor were prepared by utilizing electrostatic interactions (see Fig. 22). The resulting ITO/**27/28**/ascorbate/Pt photoelectrochemical cell exhibited an increase in efficiency with increasing transfer pressure [210].

Following the same basic method (Fig. 23) – mixed composite thin films made of C₆₀ derivatives (**28** and **30**) and a water-soluble porphyrin *meso*-tetra (4-sulfonatophenyl) porphyrin (**33**) were constructed as integrative parts for photoelectrochemical cells. Internal photon to current efficiency (IPCE) maxima up to 0.29% were obtained for monostacks of **30/31** [211].

An intriguing concept involves a C₆₀ derivative that bears an imidazole ligand (i.e., 2-(phenylimidazolyl)fulleropyrrolidine (**32**)) axially coordinated to a water-soluble cationic zinc porphyrin (i.e., zinc tetrakis(*N*-methylpyridinium) porphyrin tetrachloride (**33**)) assembled as sketched in Fig. 24. This method was successfully applied to construct photoelectrochemical cells in combination with ascorbic acid (AA) or dimethylviologen (MV²⁺) as sacrificial electron donors in the form of ITO/**32/33**/AA/Pt or ITO/**32/33**/MV²⁺/Pt, respectively. The two cells reveal different *I*-*V* characteristics, namely photoanodic versus photocathodic behavior. Overall, highly ordered film stacking favored a vectorial electron transfer that, in turn, gives rise to a maximum IPCE value of 2.5% for a photoanode composed of 20 monolayered films [212].

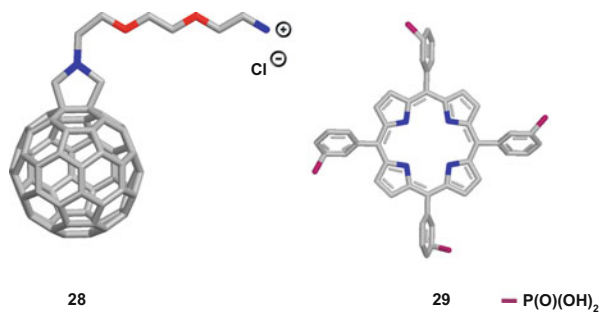


Fig. 22 Fulleropyrrolidine derivative (28) and a water-soluble porphyrin (29)

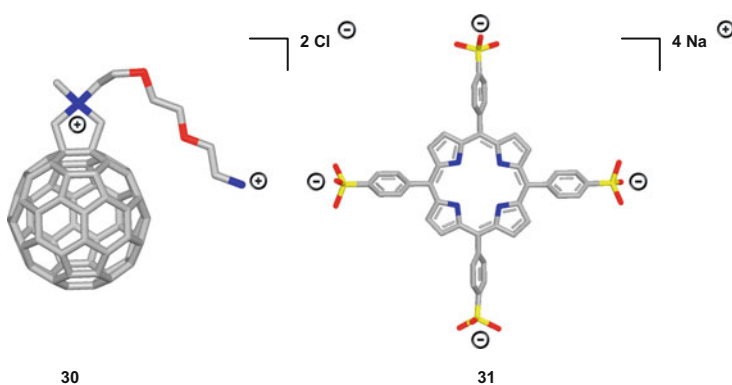


Fig. 23 C₆₀ derivative (30) and meso-tetra(4-sulfonatophenyl)porphyrin (31)

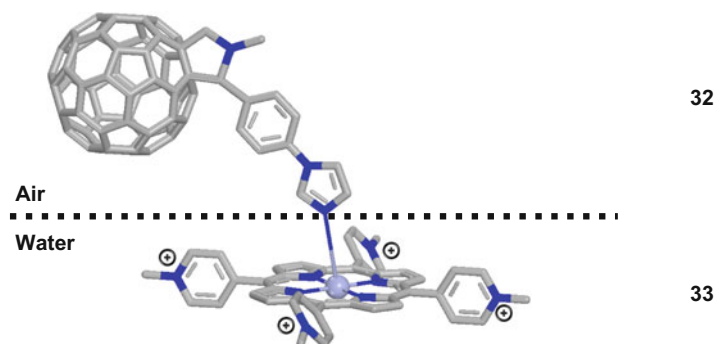
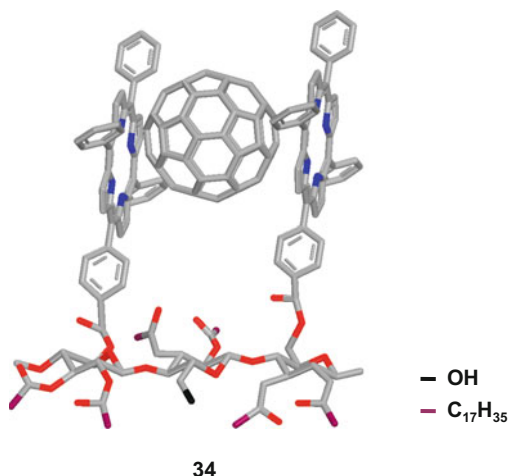


Fig. 24 Zinc tetrakis(*N*-methylpyridinium) porphyrin tetrachloride (33), and 2-(phenylimidazolyl)fulleropyrrolidine (34) that form an electron donor acceptor hybrid assembly

LB films consisting of C₆₀ (1) and 6-*O*-porphyrin-2,3-di-*O*-stearoylcellulose (34) (Fig. 25) were fabricated using cellulose as a scaffold in the LB films for anodic photocurrent generation systems. The photocurrent density generated from

Fig. 25 Fullerene (**1**) and 6-*O*-porphyrin-2,3-di-*O*-stearoylcellulose (**34**)



the **1/34** monolayer films exhibited an increase with increasing the **34** proportion and reached a maximum at a mixing ratio of 1:2 [213].

Recently, more complex multifunctional LB film structures were constructed by combining *N,N'*-bis(2,5-di-*tert*-butylphenyl)-3,4:9,10-perylenebis(dicarboximide) (**35**) or 16,17-bis(octyloxy)anthra[9,1,2-*cde*]-benzo[*rst*]pentaphene-5,10-dione (**36**) with poly(3-hexylthiophene) (**26**), porphyrin/ C_{60} conjugate (**37**), (**38**) and a phthalocyanine (**39**). Here (Fig. 26), the best solar cell performances were obtained for multifunctional films, where the efficient (**26**)/(**36**) heterojunction was combined with the (**39**)/(**37**) system [214].

5.1.2 Carbon Nanotubes

A unique contribution reported on LB photoactive films based on CNT [200]. In fact, Fig. 27 illustrates that SWNT were suspended with poly(2,5-dioctyloxy-1,4-phenylene-alt-2,5-thienylene) (POPT) (**40**) and transferred onto ITO substrates by means of the LB method. Highly organized bundles of SWNT originated. Several photoelectrochemical cells were prepared using the LB film as photocathodes. 55 POPT/SWNT stacks provided the optimal thickness and $V_{OC} = 0.18$ V, $I_{SC} = 85.8 \mu\text{A cm}^{-2}$, FF = 40.0%, and $\eta = 6.23 \cdot 10^{-3}$ % (AM 1.5) were recorded.

5.2 Layer-by-Layer Film-Based Solar Cells

LbL is a simple and versatile method for preparing supported thin films [51, 52, 186, 215–217]. In this context, its potential for obtaining heterojunctions at the monolayer level is very appealing. LbL features several important advantages over

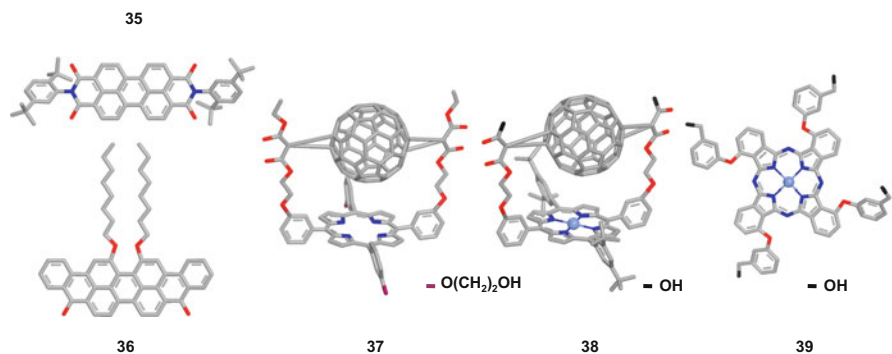


Fig. 26 *N,N*-bis(2,5-di-*tert*-butylphenyl)-3,4:9,10-perylenebis(dicarboximide) (**35**), (16,17-bis(octyloxy)anthracen[9,1,2-*cde*]benzo[*rst*]pentaphene-5,10-dione (**36**), porphyrin/C₆₀ conjugate (**37**), (**38**) and phthalocyanine (**39**)

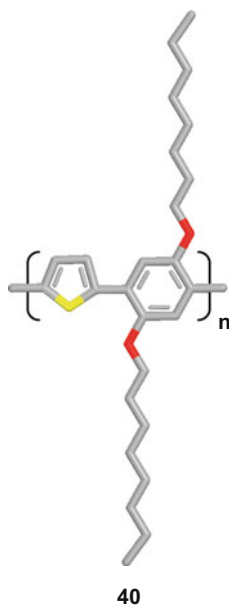


Fig. 27 Poly(2,5-dioctyloxy-1,4-phenylene-alt-2,5-thienylene) (**40**)

other techniques for preparing ordered multilayer thin films. In particular, the assembly is based on spontaneous adsorptions, the substrate may have, in principle, any size, shape, topography, or topology, surface functionality defects do not propagate and no stoichiometric control is necessary. A further technological advantage is the drastically reduced consumption of materials with respect to the conventional spin coating deposition method [218].

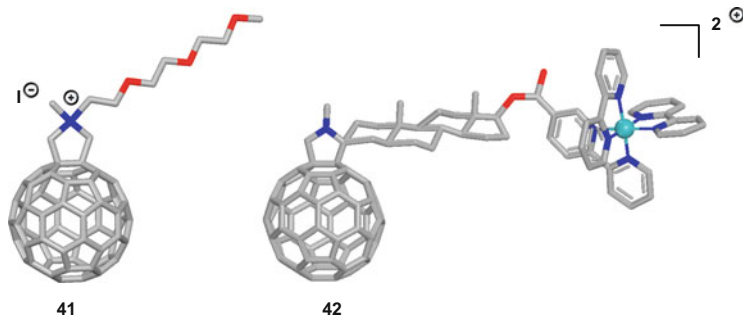


Fig. 28 Positively charged fulleropyrrolidinium ion (**41**) and ruthenium (II) polypyridyl/C₆₀ conjugate (**42**)

5.2.1 Fullerenes

In pioneering experiments, LbL photoelectrodes of a positively charged fulleropyrrolidinium ion (**41**) and a positively charged ruthenium (II) polypyridyl/C₆₀ conjugate (**42**) on ITO/poly(diallyl dimethylammonium)/polystyrene sulfonate (ITO/PDDA/PSS) – in combination with AA or MV²⁺ as sacrificial electron donors and acceptors – were studied (Fig. 28). Photocurrents increased with increasing the number of bilayer stacks from 1 to 10, but the maximum reported IPCE at 10 bilayers did not exceed 1.1% with monochromatic light [34].

Solid state LbL solar cells were also constructed evaporating aluminum onto an electrostatic assembly of polycationic (**43**) and polyanionic (**44**) C₆₀ derivatives together with a positively charged water-soluble precursor of poly(*p*-phenylene vinylene) (**45**), which, when heated, is converted into its conjugated form (**46**) (see Fig. 29) [219–222].

A supramolecular system, which builds on both electrostatic and van der Waals interactions, was also reported. C₆₀ (**1**)/free-base porphyrin (**47**) or zinc porphyrin (**48**) bilayer were prepared by electrostatic alternate adsorptions (see Fig. 30). In particular, the porphyrin is electrostatically assembled with a cationic homooxalix [3]arene (**49**) that encapsulates C₆₀ (**1**). This encapsulation prevents C₆₀ self-aggregation resulting in enhanced layer interpenetration. This approach was demonstrated to be beneficial in terms of optimizing photocurrent efficiencies [91].

Figure 31 summarizes follow-up work, in which a C₆₀/ferrocene conjugate bearing an androstane linker (**50**) was assembled in LbL films with PSS and evolved into linear nanowire structures due to the rigidity of the all- σ -bonded androstane linear skeleton. These nanowires were tested as photoactive films onto ITO/PDDA/PSS and result in photocurrent enhancement when compared to films lacking such nanowire organization. The authors attributed the photocurrent enhancement to the linear organization that facilitates the charge diffusion from the photoactive centers to the electrodes [223].

Following a similar approach, monolayers of a tetraphenylporphyrin/C₆₀ conjugate (**51**) (Fig. 32) on PSS gave rise to IPCEs of 0.36% and 0.6% under anaerobic

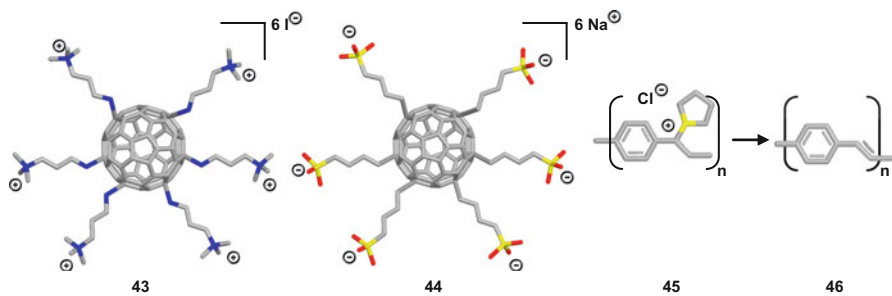


Fig. 29 Polyanionic (**43**), polycationic (**44**) C₆₀ derivatives, poly(*p*-phenylene vinylene) precursor (**45**), poly(*p*-phenylene vinylene) (**46**)

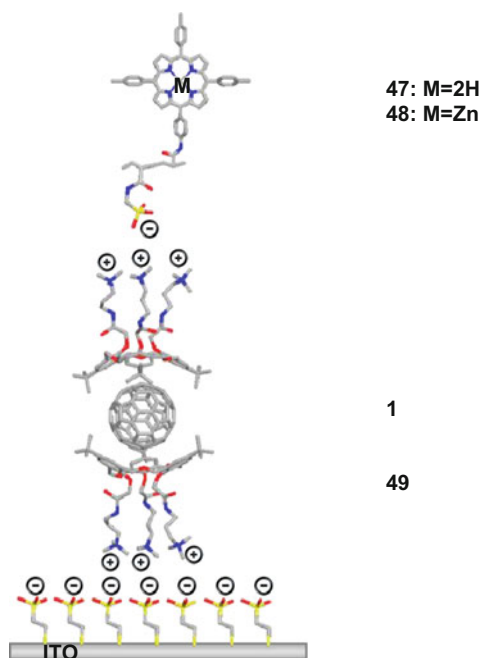


Fig. 30 C₆₀ (**1**)/free-base porphyrin (**47**) or zinc porphyrin (**48**) bilayer assembled with a cationic homooxalix[3]arenes (**49**)

and aerobic conditions, respectively. The increase in photocurrent under aerobic conditions was attributed to oxygen that assists in mediating the electron transfer [224].

An appealing variation is illustrated in Fig. 33. It involves a molecular-level switch that is built in a photoelectrochemical cell based on the polycationic redox

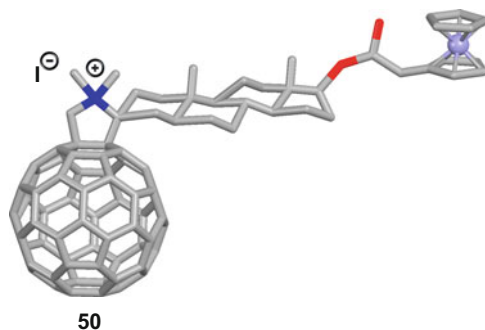


Fig. 31 Fulleropyrrolidinium–androstane–ferrocene conjugate (**50**)

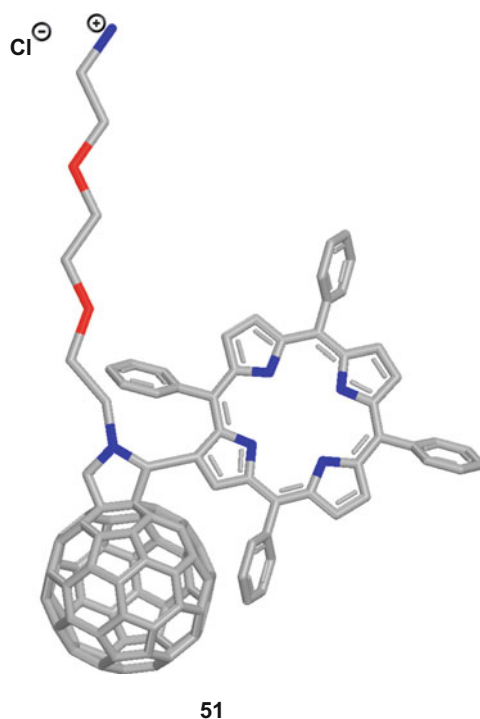


Fig. 32 Tetraphenylporphyrin/ C_{60} conjugate (**51**)

protein cytochrome *c* electrostatically linked to a negatively charged dendritic C_{60} (**52**) modified ITO/PDDA electrode [225].

A very effective strategy – *en route* towards enhancing solar light harvesting, unidirectional funneling of solar light, charge separation, and electron and hole transport in opposite directions – is shown in Fig. 34 and includes several energy/redox gradients with increasing oxidation strength within a series of chromophores

Fig. 33 Negatively charged dendritic C_{60} (**52**)

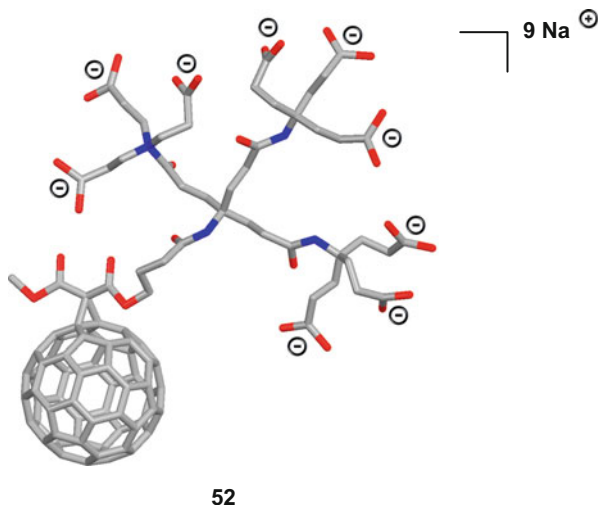
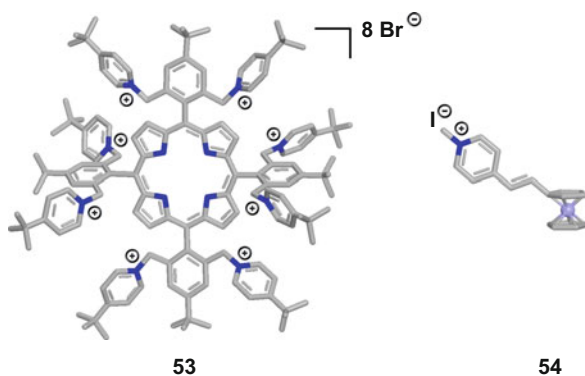


Fig. 34 Free-base porphyrin⁸⁺ (**53**)/ferrocene⁺ (**54**) derivatives

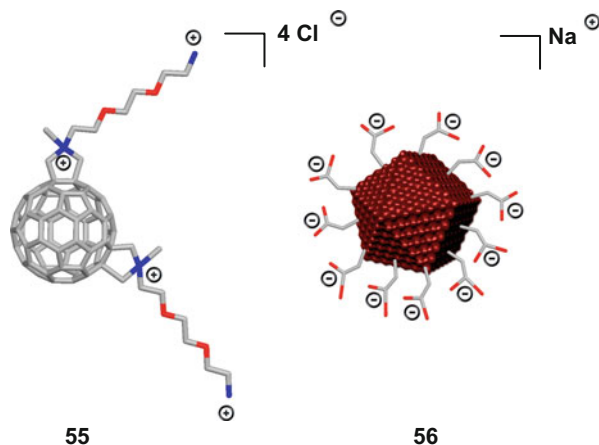


(fullerene dendron⁹⁻ **52**/free-base porphyrin⁸⁺ **53**/Znporphyrin⁸⁻ **4**/ferrocene⁺ **54**). An IPCE of 1.6% for the ITO/PDDA/**52**/**53**/**4**/**54** photoelectrode was obtained [226].

Finally, the most efficient LbL C_{60} devices are described. As a leading example, a water-soluble C_{60} derivative (**55**) as electron acceptor in combination with thioglycolic acid stabilized CdTe nanoparticles (**56**) as photoexcited electron donors (Fig. 35) led to promising LbL assembled photovoltaic thin films with IPCE values of 5.4% for a five-stack device [227].

Another exciting combination includes multilayer films of poly(phenylene ethynylene)-based anionic conjugated polyelectrolytes as electron donors and water-soluble cationic C_{60} derivatives as acceptors in a solid state device (see Fig. 36). The maximum IPCE of the ITO/((**58**/**59**)₅₀/LiF:Al photovoltaic cell was 5.5% [199].

Fig. 35 Water-soluble C₆₀ derivative (55)/thioglycolic acid stabilized CdTe nanoparticle (56)



5.2.2 Carbon Nanotubes

In most photoelectrochemical devices CNT are used as electron donors or acceptors in a photoactive layer – depending on the redox properties of the counterpart – even if the majority of these studies treat CNT as electron acceptors [228, 229]. Ever since their pioneering work [230], many groups have exploited CNT together with polythiophene derivatives in bulk heterojunction solar cells [231–238]. However, the power conversion efficiencies of polymer/CNT solar cells are with values of 0.2% [232] much lower than that of high-performance bulk heterojunction solar cells (3–6%) containing a combination of π -conjugated polymers and C₆₀ derivatives [194, 198, 239–242]. Despite the aforementioned, owing to their unique structure, CNT are presaged as ideal materials for the fabrication of lightweight, inexpensive, and flexible electronics. They possess in fact remarkable physical and chemical features like wide absorption from the UV to the NIR region matching the solar spectrum [243], high electrical [244] and thermal conductivity [245], extremely high specific surface area (1500 m² g^{−1}) [246], good thermal [247] and chemical [248] stability, ultrahigh strength and stiffness [186], and light weight [249].

From the perspective of manipulating and processing CNT, their insolubility in organic solvent and water imposes serious drawbacks. Up to today, the most commonly used approaches involve extensive sonication and/or the use of strongly oxidizing conditions, that is, nitric acid, sulfuric acid, and hydrogen peroxide. The synergy of these drastic conditions assists not only in suspending/dispersing CNT in a variety of solvents but also in destroying their electronic structure [24, 248, 250, 251]. A supramolecular approach, based on adding soluble conjugated polymers, shows remarkable progress towards debundling, wrapping, and solubilizing CNT without, however, impacting their chemical and electronic integrity [252, 253].

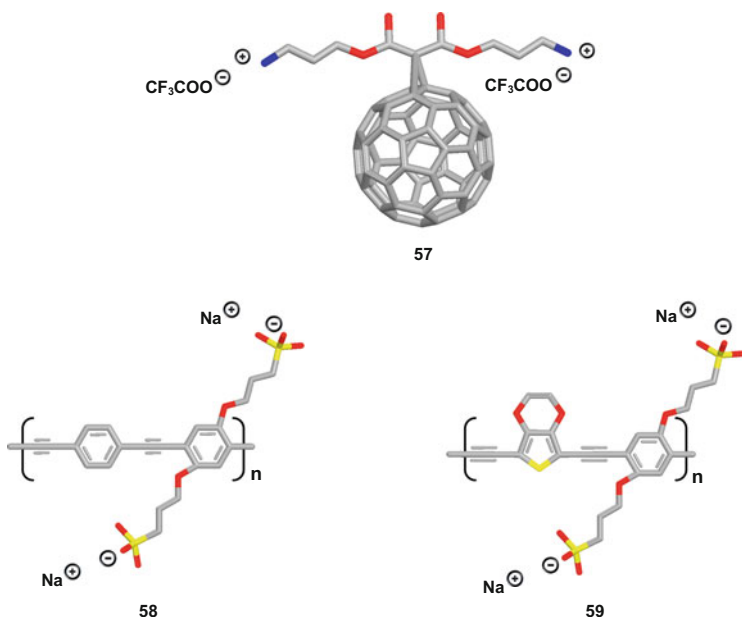


Fig. 36 Water-soluble cationic C₆₀ derivative (**57**) and poly(phenylene ethynylene)-based anionic conjugated polyelectrolytes (**58**) and (**59**)

Systematic and molecularly controlled organization of SWNT together with, for example, electron donors onto electrodes necessitates the use of van der Waals and electrostatic interactions [216, 254]. To realize SWNT-based photoelectrochemical devices, PDDA and PSS were initially adsorbed onto ITO as base layers. Next, the substrate was immersed into solutions of SWNT dispersed by pyrene derivatives bearing ammonium groups (**3**). Finally, a negatively charged Zn porphyrin⁸⁻ (**4**) was deposited to yield an LbL assembled film of ITO/PDDA/PSS/**3/4**. The photoelectrochemical measurements revealed a promising maximum IPCE value of 4.2%, which was much higher than the value (0.08%) of the ITO/PDDA/PSS/**4** device without SWNT. These results suggested that the charge separation between SWNT and photoexcited porphyrins promotes the photocurrent generation. The ITO electrodes collect the electrons from the reduced SWNT via the base layer of PDDA/PSS, and the sacrificial electron donor (i.e., AA) reduces the oxidized porphyrins. Furthermore, repetitive deposition steps allow modification of the base layer with multiply stacked (**3/4**)_n. The resulting absorption increased linearly up to 10 stacks with maximum IPCE values reaching ca. 8.5% at an applied potential of 0.2 V vs. SCE, which was two times higher than that of the device with a single layer of **3/4** [216, 254].

Poly[(vinylbenzyl)trimethylammonium chloride] (see Fig. 37) was covalently grafted and non-covalently wrapped around SWNT to form stable and positively charged nanohybrids, (**60**) and (**61**), respectively. When combined electrostatically with Zn porphyrin⁸⁻ (**4**) remarkable IPCE values of 3.81 and 9.9% for the **60/4** and

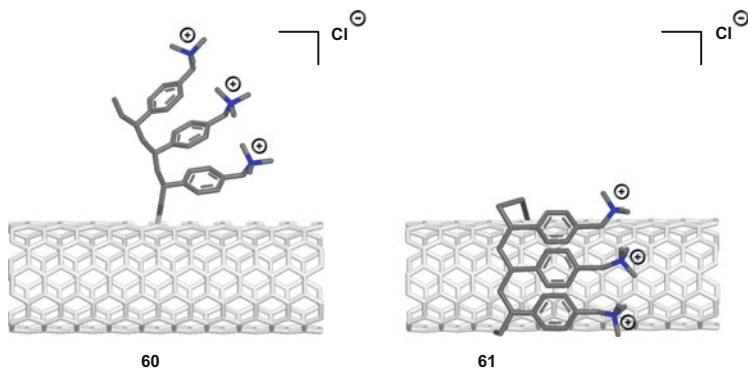


Fig. 37 SWNT covalently (**60**) and non-covalently (**61**) functionalized with poly[(vinylbenzyl)trimethylammonium chloride]

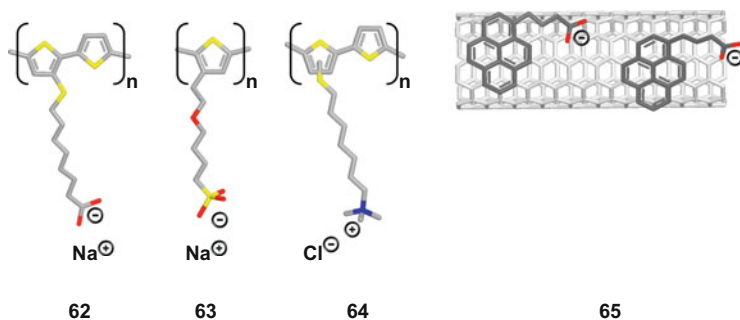


Fig. 38 Negatively (**62**) and (**63**) and positively charged (**64**) polythiophene derivatives and functionalized SWNT/pyrene-nanohybrids (**65**)

61/4 monostacks, respectively, were measured onto ITO/PDDA and an applied potential of 0.5 V [255].

In addition, nanohybrid films of **3** and CdTe nanoparticles **56** were fabricated through electrostatic interactions. IPCE values up to 2.3% have been noted [256].

Polythiophene carboxyl (**62**) and sulfonate (**63**) derivatives (see Fig. 38) were also integrated together with functionalized SWNT/pyrene⁺ nanohybrids (**3**) and polythiophene ammonium derivatives (**64**) with functionalized SWNT/pyrene-nanohybrids (**65**) into photoactive ITO electrodes by van der Waals and electrostatic interactions. In the device, polythiophene functions as the light-harvesting chromophore that donates an electron to the electron-accepting SWNT by photoinduced electron transfer [257, 258].

The higher maximum IPCE value of 9.3% was achieved in the device with eight stacks of **3/62**.

6 Summary and Outlook

In summary, we have demonstrated a variety of nanostructured multilayer assemblies of organic compounds – in particular carbon-based materials – prepared by means of LB and LbL techniques. Although these studies have demonstrated the feasibility of charge separation, hopping, and power generation at the nanocomposite polyelectrolyte assemblies, still low light conversion efficiencies resulted. Controlling with further precision the film morphology is needed in order to achieve favorable specific environments and gradients within the architectures that result in efficient charge separation and enhanced transport through the functional layers, thus minimizing carrier recombination losses and increasing the efficiency of light conversion at such ensembles.

The LbL approach is universal and can be extended to combinations of SWNT with various photoactive molecules.

Further improvement of the cell performances is expected from:

- elimination of metallic SWNT that causes short circuits in the device and facile deactivation in the excited state,
- complete SWNT debundling, since aggregation promotes self-quenching and energy transfer quenching of the excited states by metallic SWNT,
- complete removal of contamination of impurities including metal catalyst particles and amorphous carbon as well as purification (sorting of SWNT with different chiralities), in order to use SWNT having the best frontier orbital energy offset with the co-deposited material.

References

1. Lewis NS (1983) *Nature* 305:671
2. O'Regan B, Graetzel M (1991) *Nature* 353:737
3. Graetzel M (2001) *Nature* 414:338
4. Sariciftci NS, Smilowitz L, Heeger AJ, Wudl F (1992) *Science* 258:1474
5. Yu G, Gao J, Hummelen JC, Wudl F, Heeger AJ (1995) *Science* 270:1789
6. Brabec CJ, Sariciftci NS, Hummelen JC (2001) *Adv Funct Mater* 11:15
7. Shah A, Torres P, Tscharnner R, Wyrsh N, Keppner H (1999) *Science* 285:692
8. Peumans P, Uchida S, Forrest SR (2003) *Nature* 425:158
9. Halls JJM, Walsh CA, Greenham NC, Marseglia EA, Friend RH, Moratti SC, Holmes AB (1995) *Nature* 376:498
10. Katz HE, Lovinger AJ, Johnson J, Kloc C, Siegrist T, Li W, Lin YY, Dodabalapur A (2000) *Nature* 404:478
11. Nelson J (2001) *Science* 293:1059
12. Kern R, Van Der Burg N, Chmiel G, Ferber J, Hasenhindl G, Hinsch A, Kinderman R, Kroon J, Meyer A, Meyer T, Niepmann R, Van Roosmalen J, Schill C, Sommeling P, Spath M, Uhlendorf I (2000) *Opto-Electron Rev* 8:284
13. Padinger F, Ritterberger RS, Sariciftci NS (2003) *Adv Funct Mater* 13:85
14. Fendler JH, Dekany I (1996) *Nanoparticles in solids and solutions*. Kluwer, Dordrecht
15. Kamat PV, Meisel D (1997) *Semiconductor nanoclusters*. Elsevier, Amsterdam

16. Fendler JH (1998) Nanoparticle and nanostructured films. Wiley-VCH, Weinheim
17. Hagfeldt A, Grätzel M (1995) *Chem Rev* 95:49
18. Vögtle F (1991) *Supramolecular chemistry*. Wiley, Chichester
19. Lehn JM (1995) *Supramolecular chemistry: concepts and perspectives*. Wiley-VCH, Weinheim
20. Steed JW, Atwood JL (2000) *Supramolecular chemistry*. Wiley, Chichester
21. Poole CP, Owens J (2003) *Introduction to nanotechnology*. Wiley, Weinheim
22. Harris P (2001) *Carbon nanotubes and related structures: new materials for the twenty-first century*. Cambridge University Press, Cambridge
23. Dresselhaus MS, Dresselhaus G, Avouris P (2001) *Carbon nanotubes: synthesis, structure, properties and applications*. Springer, Berlin
24. Reich S, Thomsen C, Maultzsch J (2004) *Carbon nanotubes: basic concepts and physical properties*. Wiley-VCH, Weinheim
25. Taylor R (1999) *Lecture notes on fullerenes chemistry*. Imperial College, London
26. Hirsch A (1999) *Fullerenes and related structures, topics in current chemistry* 199. Springer, Berlin
27. Guldi DM, Martin N (2002) *Fullerenes: from synthesis to optoelectronic properties*. Kluwer Academic, Dordrecht
28. Roberts G (1990) *Langmuir–Blodgett films*. Plenum, New York
29. Ulman A (1991) *An introduction to ultrathin organic films*. Academic, Boston
30. Tredgold RH (1994) *Order in thin organic films*. Cambridge University Press, Cambridge
31. Moebius D, Miller R (2001) *Novel methods to study interfacial layers*. Elsevier, Amsterdam
32. Blodgett KB (1934) *J Am Chem Soc* 56:495
33. Blodgett KB, Langmuir I (1937) *Phys Rev* 51:964
34. Luo C, Guldi DM, Maggini M, Manna E, Mondini S, Kotov NA, Prato M (2000) *Angew Chem Int Ed* 39:3905
35. Franklin B (1774) *Phil Trans R Soc* 64:445
36. Rayleigh Lord (1899) *Phil Mag* 48:321
37. Pockels A (1891) *Nature* 43:437
38. Deveaux H (1932) *Kolloid Z* 58:260
39. Hardy WB (1913) *Pros R Soc London* 88:303
40. Roberts GG (1985) *Adv Phys* 34:475
41. Langmuir I (1917) *J Am Chem Soc* 39:1848
42. Langmuir I (1920) *Trans Faraday Soc* 15:62
43. Blodgett KB (1935) *J Am Chem Soc* 57:1007
44. Gaines GL (1966) *Insoluble monolayers at liquid–gas interface*. Wiley, New York
45. Roberts GG (1984) *Sens Actuat* 4:131
46. Cotton FA, Rice CE, Rice GW (1977) *J Am Chem Soc* 99:4704
47. Sagiv J (1980) *J Am Chem Soc* 102:92
48. Netzer L, Sagiv J (1983) *J Am Chem Soc* 105:674
49. Iler R (1966) *J Colloid Interface Sci* 21:569
50. Decher G, Hong J D, Schmitt J (1992) *Thin Solid Films* 210/211:831
51. Decher G (1997) *Science* 277:1232
52. Decher G, Hong JD (1991) *Makromol Chem Macromol Symp* 46:321
53. Schmitt J (1992) *Thin Solid Films* 210/211:831
54. Decher G (1996) *Comprehensive supramolecular chemistry, vol 9 templating, self-assembly, and self-organization*. Pergamon, Oxford, 507
55. Knoll W (1996) *Curr Opin Colloid Interface Sci* 1:137
56. Ferreira M, Cheung JH, Rubner MF (1994) *Thin Solid Films* 244:806
57. Tripathy SK, Katagi H, Kasai H, Balasubramanian S, Oshikiri H, Kumar J, Oikawa H, Okada S, Nakanishi H (1998) *Jpn J Appl Phys* 37:343
58. Zucolotto V, Gattás-Asfura KM, Tumolo T, Perinotto AC, Antunes PA, Constantino CJL, Baptista MS, Leblanc RM, Oliveira Jr ON (2005) *Appl Surface Sci* 246:397

59. Fendler JH (1996) *Chem Mater* 8:1616
60. Cassagneau T, Fendler JH (1999) *J Phys Chem B* 103:1789
61. He J-A, Valluzzo R, Yang K, Dolukhanyan T, Sung CM, Kumar J, Tripathy SK, Samuelson L, Balogh L, Tomalia DA (1999) *Chem Mater* 11:3268
62. Ferreira M, Rubner MF, Hsieh BR (1994) *Mater Res Soc Proc Symp* 328:119
63. Fou AC, Onitsuka O, Ferreira M, Rubner MF, Hsieh BR (1995) *Mater Res Soc Proc Symp* 369:575
64. Onoda M, Yoshino K (1995) *Jpn J Appl Phys* 34:260
65. Fou AC, Onitsuka O, Ferreira M, Rubner MF, Hsieh BR (1996) *J Appl Phys* 79:7501
66. Lehr B, Seufert M, Wenz G, Decher G (1996) *Supramol Sci* 2:199
67. Stroeve P, Vasquez V, Coelho MAN, Rabolt JF (1996) *Thin Solid Films* 284:708
68. Levasalmi J, McCarthy TJ (1997) *Macromolecules* 30:1752
69. Laschewsky A, Mayer B, Wischerhoff E, Arys X, Bertrand P, Delcorte A, Jonas A (1996) *Thin Solid Films* 284:334
70. Lvov Y, Yamada S (1997) *Kunitake T Thin Solid Films* 300:107
71. Hammond P T, Whitesides G M (1995) *Macromolecules* 28:7569
72. Stepp J, Schlenoff JB (1997) *J Electrochem Soc* 144:155
73. Laurent D (1997) *Schlenoff J B. Langmuir* 13:1552
74. Sun Y, Zhang X, Sun C, Wang B, Shen J (1996) *Macromol Chem Phys* 197:147
75. Stockton WB, Rubner MF (1997) *Macromolecules* 30:2717
76. Wang LY, Wang ZQ, Zhang X, Shen JC (1997) *Macromol Rapid Commun* 18:509
77. Wang LY, Cui SX, Wang ZQ, Zhang X (2000) *Langmuir* 16:10490
78. Fu Y, Chen H, Qiu DL, Wang ZQ, Zhang X (2002) *Langmuir* 18:4989
79. Lee H, Kepley LJ, Hong HG, Mallouk TE (1988) *J Am Chem Soc* 110:618
80. Ichinose I, Senzu H, Kunitake T (1996) *Chem Lett* 10:831
81. Ichinose I, Senzu H, Kunitake T (1997) *Chem Mater* 9:1296
82. Lee S, Ichinose I, Kunitake T (1998) *Langmuir* 14:2857
83. Shimazaki Y, Mitsuishi M, Ito S, Yamamoto M (1997) *Langmuir* 13:1385
84. Serizawa T, Hamada K, Kitayama T, Fujimoto N, Hatadaand K, Akashi M (2000) *J Am Chem Soc* 122:1891
85. Serizawa T, Hamada K, Kitayama T, Katsukawa K, Hatadaand K, Akashi M (2000) *Langmuir* 16:7112
86. Hamada K, Serizawa T, Kitayama T, Fujimoto N, Hatadaand K, Akashi M (2001) *Langmuir* 17:5513
87. Cheng L, Dong SJ (1999) *Electrochem Commun* 1:159
88. Cheng L, Dong SJ (2000) *J Electroanal Chem* 481:168
89. Zhang D, Zhang K, Yao YL, Xia XH, Chen HY (2004) *Langmuir* 20:7303
90. Sun JQ, Gao MY, Zhu M, Feldmann J (2001) *J Nanosci Nanotechnol* 1:133
91. Ikeda A, Hatano T, Shinkai S, Akiyama T, Yamada S (2001) *J Am Chem Soc* 123:4855
92. Nakashima N, Tomonari Y, Murakami H (2002) *Chem Lett* 6:638
93. Guldi DM, Rahman GMA, Jux N, Tagmatarchis N, Prato M (2004) *Angew Chem Int Ed* 43:5526
94. Schütte M, Kurth DG, Linford MR, Cölfen H, Möhwald H (1998) *Angew Chem Int Ed* 37:2891
95. Kurth DG, Osterhout R (1999) *Langmuir* 15:4842
96. Emoto K, Iijima M, Nagasaki Y, Kataoka K (2000) *J Am Chem Soc* 122:2653
97. Ma N, Zhang HY, Song B, Wang ZQ, Zhang X (2005) *Chem Mater* 17:5065
98. Anzai J, Kobayashi Y, Nakamura N, Nishimura M, Hoshi T (1999) *Langmuir* 15:221
99. Ichinose I, Tagawa H, Mizuki S, Lvov Y, Kunitake T (1998) *Langmuir* 14:187
100. Langmuir I, Schaefer VJ (1938) *J Am Chem Soc* 60:1351
101. Schulman JH, Waterhouse RB, Spink JA (1956) *Kolloid Z* 146:77
102. Day D, Lando JB (1980) *Macromolecules* 13:1478
103. Gaines GL Jr (1980) *Thin Solid Films* 68:1

104. Barraud A, Rosilio C, Ruauadel-Teixier A (1980) *Thin Solid Films* 68:7
105. Bonnerot A, Chollet PA, Frisby H, Hoclet M (1985) *Chem Phys* 97:365
106. Kimura F, Umemura J, Takenaka T (1985) *Langmuir* 2:96
107. Clint JH, Walker T (1974) *J Colloid Interface Sci* 47:172
108. Petty MC (1996) *Langmuir–Blodgett films – an introduction*. Cambridge University Press, Cambridge p, 43
109. Laschewsky A (1997) *European Chemistry Chronicle* 2:13
110. Shiratori SS, Rubner MF (2000) *Macromolecules* 33:4213
111. Crespilho FN, Zucolotto V, Oliveira Jr ON, Nart FC (2006) *Int J Electrochem Sci* 1194
112. Yoo D, Shiratori S, Rubner MF (1998) *Macromolecules* 31:4309
113. Dubas ST, Schlenoff JB (2001) *Macromolecules* 34:3736
114. Dubas ST, Schlenoff JB (1999) *Macromolecules* 32:8153
115. Schoeler B, Kumaraswamy G, Caruso F (2002) *Macromolecules* 35:889
116. Steitz R, Jaeger W, Klitzing R (2001) *Langmuir* 17:4471
117. Decher G, Schlenoff JB (2002) *Multilayer thin films*. Wiley-VCH, Weinheim, 394
118. Hoogeveen NG, Stuart MAC, Fleer G, Böhmer MR (1996) *Langmuir* 12:3675
119. Diederich F, Kessinger R (1999) *Acc Chem Res* 32:537
120. Hirsch A (1999) *Fullerenes and related structures*. *Top Curr Chem* 199:1
121. Prato M, Maggini M (1998) *Acc Chem Res* 31:519
122. Haddon RC, Rao CNR, Govindaraj A, Andrews R, Jacques D, Qian D, Rantell T, Ouyang M, Huang JL, Lieber CM, Avouris P, Dai H, Zhou O, Shimoda H, Gao B, Oh S, Fleming L, Yue G, Sloan J, Kirkland AI, Hutchison JL, Green MLH, Charlier JC, Dresselhaus MS, Dresselhaus G, Jorio A, Souza Filho AG, Pimenta MA, Saito R, Fischer JE, Khabashesku VN, Billups WE, Margrave JL, Sun YP, Fu K, Lin Y, Huang W, Niyogi S, Hamon MA, Hu H, Zhao B, Bhowmik P, Sen R, Itkis ME (2002) *Special issue on carbon nanotubes*. *Acc Chem Res* 35:997
123. Prato M (1997) *J Mater Chem* 7:1097
124. Prato M (1999) *Top Curr Chem* 199:173
125. Hebard AF, Rosseinsky MJ, Haddon RC, Murphy DW, Glarum SH, Palstra TTM, Ramirez AP, Kortan AR (1991) *Nature* 350:600
126. Wang P, Metzger RM, Bandow S, Maruyama Y (1993) *J Phys Chem* 97:2926
127. Wang P, Maruyama Y, Metzger RM (1996) *Langmuir* 12:3932
128. Jehoulet C, Obeng YS, Kim YT, Zhou F, Bard AJ (1992) *J Am Chem Soc* 114:4237
129. Bulhoes LOS, Obeng YS, Bard AJ (1993) *Chem Mater* 5:110
130. Hirsch A (1994) *The chemistry of the fullerenes*. Georg Thieme Verlag, Stuttgart
131. Martin N, Sanchez L, Illescas B, Perez I (1998) *Chem Rev* 98:2527
132. Back R, Lennox RB (1992) *J Phys Chem* 96:8149
133. Brousseau JL, Tian K, Gauvin S, Leblanc RM, Delhaes P (1994) *Chem Phys Lett* 202:521
134. Cardullo F, Diederich F, Echegoyen L, Habicher T, Jayaraman N, Leblanc RM, Stoddart JF, Wang S (1998) *Langmuir* 14:1955
135. Guldi DM, Tian Y, Fendler JH, Hungerbühler H, Asmus KD (1995) *J Phys Chem* 99:17673
136. Guldi DM, Tian Y, Fendler JH, Hungerbühler H, Asmus KD (1996) *J Phys Chem* 100:2753
137. Guldi D M, Asmus K D, Tian Y, Fendler J H (1996) *Proc Electrochem Soc* 3(96):501
138. Maggini M, Karlsson A, Pasimeni L, Scorrano G, Prato M, Valli L (1994) *Tetrahedron Lett* 35:2985
139. Maggini M, Pasimeni L, Prato M, Scorrano G, Valli L (1994) *Langmuir* 10:4164
140. Obeng YS, Bard AJ (1991) *J Am Chem Soc* 113:6279
141. Ravaine S, Agricole B, Mingotaud C, Cousseau J, Delhaes P (1995) *Chem Phys Lett* 242:478
142. Ravaine S, Mingotaud C, Delhaes P (1996) *Synth Met* 81:271
143. Ravaine S, Mingotaud C, Delhaes P (1996) *Thin Solid Films* 285:76
144. Tomioka Y, Ishibashi M, Kajiyama H, Taniguchi Y (1993) *Langmuir* 9:32
145. Vaknin D, Wang JY, Uphaus RA (1995) *Langmuir* 11:1435
146. Wang P, Chen B, Metzger RM, Da Ros T, Prato M (1997) *J Mater Chem* 7:2397

147. Wang S, Leblanc RM, Arias F, Echegoyen L (1997) *Langmuir* 13:1672
148. Wang S, Leblanc RM, Arias F, Echegoyen L (1998) *Thin Solid Films* 327:144
149. Shi X, Caldwell WB, Che K, Mirkin CA (1994) *J Am Chem Soc* 116:11598
150. Ruoff RS, Tse DS, Malhotra R, Lorents DC (1993) *J Phys Chem* 97:3379
151. Felder D, Gallani JL, Guillon D, Heinrich B, Nicoud J-F, Nierengarten J-F (2000) *Angew Chem Int Ed* 39:201
152. Nierengarten J-F, Eckert J-F, Rio Y, del Pilar CM, Gallani J-L, Guillon D (2001) *J Am Chem Soc* 123:9743
153. Tkachenko NV, Guenther C, Imahori H, Tamaki K, Sakata Y, Fukuzumi S, Lemmetyinen H (2000) *Chem Phys Lett* 326:344
154. Lehtivuori H, Lemmetyinen H, Tkachenko NV (2006) *J Am Chem Soc* 128:16036
155. Saito R, Dresselhaus G, Dresselhaus MS (1998) *Physical properties of carbon nanotubes*. Imperial College, London
156. Iijima S (1991) *Nature London* 354:56
157. de Heer WA, Bacsá WS, Châtelain A, Gerfin T, Humphrey-Baker R, Forro L, Ugarte D (1995) *Science* 268:845
158. Frank S, Poncharal P, Wang ZL, de Heer WA (1998) *Science* 280:1741
159. Che G, Lakshmi BB, Fisher ER, Martin CR (1998) *Nature* 393:346
160. Liu C, Fan YY, Liu M, Cong HT, Cheng HM, Dresselhaus MS (1999) *Science* 286:1127
161. Wang QH, Setlur AA, Lauerhaas JM, Dai JY, Seelig EW, Chang RPH (1998) *Appl Phys Lett* 72:2912
162. Snow ES, Novak JP, Campbell PM, Park D (2003) *Appl Phys Lett* 82:2145
163. Chen J, Hamon MA, Hu H, Chen Y, Rao AM, Eklund PC, Haddon RC (1998) *Science* 282:95
164. O'Connell MJ (2001) *Chem Phys Lett* 342:265
165. Hirsch A (2002) *Angew Chem Int Ed* 41:1853
166. Sohn JI, Lee S, Song Y-H, Choi S-Y, Cho K-I, Nam K-S (2001) *Appl Phys Lett* 78:901
167. Bachilo SM, Balzano L, Herrera JE, Pompeo F, Resasco DE, Weisman RB (2003) *J Am Chem Soc* 125:11186
168. Thess A, Lee R, Nikolaev P, Dai H, Petit P, Robert J, Xu C, Lee YH, Kim SG, Rinzler AG, Colbert DT, Scuseria GE, Tománek D, Fischer JE, Smalley RE (1996) *Science* 273:483
169. Li YL, Kinloch IA, Windle AH (2004) *Science* 304:276
170. Rao SG, Huang L, Setyawan W, Hong S (2003) *Nature* 425:36
171. Fischer JE, Zhou W, Vavro J, Llaguno MC, Guthy C, Haggemueller R (2003) *J Appl Phys* 93:2157
172. Shimoda H, Fleming L, Horton K, Zhou O (2002) *Physica B* 323:135
173. Yamamoto K, Akita S, Nakayama Y (1998) *J Phys* 31:34
174. Kumar MS, Lee SH, Kim TY, Kim TH, Song SM, Yang JW, Nahm KS, Suh E-K (2003) *Solid State Electron* 47:2075
175. Gao J, Yu A, Itkis ME, Bekyarova E, Zhao B, Niyogi S, Haddon RC (2004) *J Am Chem Soc* 126:16698
176. Armitage NP, Gabriel J-CP, Grüner G (2004) *J Appl Phys* 95:3228
177. Krstic V, Munster J, Duesberg GS, Philipp G, Burghard M, Rost S (2000) *Synth Met* 110:245
178. Hernández-López JL, Alvizo-Páez ER, Moya SE, Ruiz-García J (2006) *J Phys Chem B* 110:23179
179. J Li, Zhang Y (2007) *Carbon* 45:493
180. Jia L, Zhang Y, Li J, You C, Xie E (2008) *J Appl Phys* 104:074318
181. Cui J, Daghlán CP, Gibson UJ (2005) *J Phys Chem B* 109:11456
182. Cui JB, Daghlán CP, Gibson UJ (2005) *J Appl Phys* 98:044320
183. Feng L, Li H, Li F, Shi Z, Gu Z (2003) *Carbon* 41:2385
184. Sun Q, Zorin NA, Chen D, Chen M, Liu T-X, Miyake J, Qian D-J (2010) *Langmuir* 26:10259
185. Li X, Zhang L, Wang X, Shimoyama I, Sun X, Seo W-S, Dai H (2007) *J Am Chem Soc* 129:4890
186. Mamedov AA, Kotov NA, Prato M, Guldi DM, Wicksted JP, Hirsch A (2002) *Nat Mater* 1:190

187. Zhang M, Su L, Mao L (2006) *Carbon* 44:276
188. Lee SW, Kim B-S, Chen S, Shao-Horn Y, Hammond PT (2009) *J Am Chem Soc* 131:671
189. Brabec C, Dyakonov V, Parisi J, Sariciftci S (eds) (2003) In: *Organic photovoltaics: concept and realization*, Springer series in material science. Springer, Berlin
190. Brabec C, Scherf U, Dyakonov V (eds) (2008) In: *Organic photovoltaics: materials, device physics, and manufacturing technologies*, Wiley-VCH, New York
191. Archer MD, Nozik AJ (eds) (2009) In: *Nanostructured and photoelectrochemical systems for solar photon conversion*. Imperial College, London
192. Thimpson BC, Fréchet JM (2008) *Angew Chem Int Ed* 47:58
193. Ma W, Yang C, Gong X, Lee K, Heeger AJ (2005) *Adv Funct Mater* 15:1617
194. Kim Y, Cook S, Tuladhar SM, Choulis SA, Nelson J, Durrant JR, Bradley DDC, Giles M, McCulloch I, Ha CS, Ree M (2006) *Nat Mater* 5:197
195. Balzani V (ed) (2001) In: *Electron transfer in chemistry*, Wiley-VCH, Weinheim
196. Blankenship R E (ed) (2002) In: *Molecular mechanisms of photosynthesis*. Blackwell Science, Oxford
197. Collings A F, Critchley C (eds) (2006) In: *Artificial photosynthesis: from basic biology to industrial application*. Wiley-VCH, Weinheim
198. Chen HY, Hou J, Zhang S, Liang Y, Yang G, Yang Y, Yu L, Wu Y, Li G (2009) *Nature Photon* 3:649
199. Mwaura JK, Pinto MR, Witker D, Ananthkrishnan N, Schanze KS, Reynolds JR (2005) *Langmuir* 21:10119
200. Sgobba V, Giancane G, Ruland A, Valli L, Manno D, Serra A, Farinola GM, Omar OH, Guldi DM (2010) *Adv Funct Mat* 20:2481
201. Bottari G, de la Torre G, Guldi DM, Torres T (2010) *Chem Rev* 110:6768
202. Guldi DM, Rahman GMA, Ehli C, Sgobba V (2006) *Chem Soc Rev* 35:471
203. Imahori H, Fukuzumi S (2004) *Adv Funct Mat* 14:525
204. Hasobe T (2010) *Phys Chem Chem Phys* 12:44
205. Guldi DM (2003) *Pure Appl Chem* 75:1069
206. Kamat PV (2007) *J Phys Chem C* 111:2834
207. Zasadzinski JA, Viswanathan R, Madsen L, Garnæs J, Schwartz DK (1994) *Science* 263:1726
208. Alekseev AS, Tkachenko NV, Tauber AY, Hynninen PH, Osterbacka R, Stubb H, Lemmetyinen H (2002) *Chem Phys* 275:243
209. Guldi DM, Zilbermann I, Anderson GA, Kordatos K, Prato M, Tafuro R, Valli L (2004) *J Mat Chem* 14:303
210. Conoci S, Guldi DM, Nardis S, Paolesse R, Kordatos K, Prato M, Ricciardi G, Graça M, Vicente H, Zilbermann I, Valli L (2004) *Chem Eur J* 10:6523
211. Sgobba V, Guldi DM, Casilli S, Conoci S, Giancane G, Prato M, Ricciardi G, Valli L (2007) *J Am Chem Soc* 129:3148
212. Marczak R, Sgobba V, Kutner W, Gadde S, D'Souza F, Guldi DM (2007) *Langmuir* 23:1917
213. Sakakibara K, Nakatsubo F (2008) *Macromol Chem Phys* 209:1274
214. Vivo P, Vuorinen T, Chukharev V, Tolkki A, Kaunisto K, Ihalainen P, Peltonen J, Lemmetyinen H (2010) *J Phys Chem C* 114:8559
215. Caruso F, Niikura K, Furlong N, Okahata Y (1997) *Langmuir* 13:3427
216. Sgobba V, Rahman GMA, Guldi DM, Jux N, Campidelli S, Prato M (2006) *Adv Mater* 18:2264
217. Srivastava S, Kotov NA (2008) *Acc Chem Res* 41:1831
218. Hoven CV, Garcia A, Bazan GC, Nguyen TQ (2008) *Adv Mater* 20:1
219. Durstocka MF, Taylor B, Sprya RJ, Chiang L, Reulbacha S, Heitfelda K, Baur JW (2001) *Synth Met* 116:373
220. Mattoussi H, Rubner MF, Zhou F, Kumar J, Tripathy SK, Chiang LY (2000) *Appl Phys Lett* 77:1540

221. Baur JW, Durstock MF, Taylor BE, Spry RJ, Reulbach S, Chiang LJ (2001) *Synth Met* 121:1547
222. Durstock MF, Spry RJ, Baur JW, Taylor BE, Chiang Long Y (2003) *J Appl Phys* 94:3253
223. Guldi DM, Luo C, Koktysh D, Kotov NA, Ros TD, Bosi S, Prato M (2002) *Nano Lett* 2:775
224. Guldi DM, Pellarini F, Prato M, Granito C, Troisi L (2002) *Nano Lett* 2:965
225. Zilbermann I, Lin A, Hatzimarinaki M, Hirsch A, Guldi DM (2004) *Chem Commun* 96
226. Guldi D M, Zilbermann I, Anderson G, Li A, Balbinot D, Jux N, Hatzimarinaki M, Hirsch A, Prato M (2004) *Chem Commun* 726
227. Guldi DM, Zilbermann I, Anderson G, Kotov NA, Tagmatarchis N, Prato M (2005) *J Mater Chem* 15:114
228. Hatton RA, Miller AJ, Silva SRP (2008) *J Mater Chem* 18:1183
229. Sgobba V, Guldi DM (2008) *J Mater Chem* 18:153
230. Kymakis E, Amaratunga GAJ (2002) *Appl Phys Lett* 80:112
231. Kymakis E, Amaratunga GAJ (2003) *Sol En Mater Sol Cells* 80:465
232. Kymakis E, Alexandrou I, Amaratunga GAJ (2003) *J Appl Phys* 93:1764
233. Bhattachayya S, Kymakis E, Amaratunga GAJ (2004) *Chem Mater* 16:4819
234. Landi BJ, Raffaele RP, Castro SL, Bailey G (2005) *Prog Photovoltaics* 13:165
235. Kazaoui S, Minami N, Nalini B, Kim Y, Hara K (2005) *J Appl Phys* 98:084314
236. Kymakis E, Koudoumas E, Franghiadakis I, Amaratunga GAJ (2006) *J Phys D: Appl Phys* 39:1058
237. Geng J, Zeng T (2006) *J Am Chem Soc* 128:16827
238. Nogueira AF, Lomba BS, Soto-Ovideo MA, Correia CRD, Corio P, Furtado CA, Hümmelegen IA (2007) *J Phys Chem C* 111:18431
239. Li G, Shrotriya V, Huang J, Yao Y, Moriarty T, Emery K, Yang Y (2005) *Nat Mater* 4:864
240. Peet J, Kim JY, Coates NE, Ma WL, Moses D, Heeger AJ, Bazan GC (2007) *Nat Mater* 6:497
241. Ross RB, Cardona CM, Guldi DM, Gayathri Sankaranarayanan S, Reese MO, Kopidakis N, Peet J, Walker B, Bazan GC, Van Keuren E, Holloway BC, Drees M (2009) *Nature Mat* 8:208
242. Ross RB, Cardona CM, Swain FB, Guldi DM, Sankaranarayanan SG, Van Keuren E, Holloway BC, Drees M (2009) *Adv Funct Mat* 19:2332
243. Sgobba V, Guldi DM (2009) *Chem Soc Rev* 38:165
244. Ebbesen TW, Lezec HJ, Hiura H, Bennett JW, Ghaemi HF, Thio T (1996) *Nature* 382:54
245. Berber S, Kwon YK, Tománek D (2000) *Phys Rev Lett* 84:4613
246. Sgobba V, Guldi DM (2010) *Electrochem Soc Interf* 19:50
247. Cataldo F (2002) *Fullerenes, Nanotubes. Carbon Nanostruct* 10:293
248. Sgobba V, Rahman GMA, Guldi DM (2006) In: *Carbon nanotubes in electron donor–acceptor nanocomposites – chemistry of carbon nanotubes*. American Scientific Publishers, USA
249. Moniruzzaman M, Winey KI (2006) *Macromolecules* 39:5194
250. Guldi DM, Martin N (2010) (eds) In: *Carbon nanotubes and related structures*. Wiley-VCH, Weinheim
251. Langa de la Puente, F Nierengarten JF (eds) (2006) In: *Fullerene, principles and applications*. RSC Nanoscience and Nanotechnology Series, Cambridge
252. Guldi DM, Taieb H, Rahman GMA, Tagmatarchis N, Prato M (2005) *Adv Mat* 17:871
253. Didenko VV, Moore VC, Baskin DS, Smalley RE (2005) *Nano Lett* 5:1563
254. Guldi DM, Rahman GMA, Prato M, Jux N, Qin S, Ford W (2005) *Angew Chem Int Ed* 44:2015
255. Rahman GMA, Troeger A, Sgobba V, Guldi DM, Jux N, Tchoul MN, Ford WT, Mateo-Alonso A, Prato M (2008) *Chem Eur J* 14:8837
256. Guldi DM, Rahman GMA, Sgobba V, Kotov NA, Bonifazi D, Prato M (2006) *J Am Chem Soc* 128:2315
257. Rahman GMA, Guldi DM, Cagnoli R, Mucci A, Schenetti L, Vaccari L, Prato M (2005) *J Am Chem Soc* 127:10051
258. Sgobba V, Troeger A, Cagnoli R, Mateo-Alonso A, Prato M, Schenetti L, Guldi DM (2009) *J Mat Chem* 19:4319

Self- or Induced Organization of [60]Fullerene Hexakisadducts

Delphine Felder-Flesch

Abstract In the past few years, much attention has been devoted to the development of C_{60} multiadducts for high-added value materials. C_{60} fullerene can be considered as a versatile hard nanocore for globular systems due to its tuneable valency (1 to 6 based on cyclopropanation derivatization) and regioselective polyaddition. Therefore, hexakisadducts of C_{60} are becoming an important class of carbon-based macromolecules as they offer wider possibilities for structural variations than any other organic (or inorganic) scaffolds. For example, several types of molecular geometries can be designed and controlled, thanks to regioselective functionalization methodologies. This in turn leads to new building blocks for defined supramolecular organizations. In this review, an overview of the relationships between molecular architecture and self- or induced organization of C_{60} hexakisadducts is provided. This includes a description of thin films, liquid-crystalline mesophases, and nanospheres formed by such carbonaceous systems.

Keywords [60]Fullerene hexakisadducts · Buckysomes · Liquid crystals · Micelles · Thin films

Contents

1	Introduction	102
2	Thin Films as Induced Organization of [60]Fullerene Hexakisadducts	102
2.1	[5:1] Hexakisadducts	103
2.2	[3:3] Hexakisadducts	110
3	Thermotropic Liquid-Crystalline Hexakisadducts	118
3.1	Enantiotropic Smectic A Phase	119
3.2	Nematic Phase	123

4	Self-organization Through Micelles, Nanospheres	129
4.1	[6:0] Hexakisadduct	130
4.2	Dendritic [5:1] hexakisadduct	134
4.3	Dendritic [3:3] Hexakisadduct	136
5	Conclusions	137
	References	139

1 Introduction

Organic materials at the nanoscale have attracted broad attention in recent years. In the field of C_{60} materials science, studies deal with the self-organization of molecules having characteristic ordered structures [1] since the development of functional devices very often requires dedicated engineering of the molecules, i.e. functionalization of the molecules for controlling their self-organization. The preparation of 2D and 3D networks or discrete organizations is a major challenge. Still, controlling their structure is possible upon playing on the multifunctionalization of C_{60} [2–4; and references therein]. Indeed, the control of the regioselectivity [5–9] for the hexaaddition on the carbonaceous sphere allows a geometrical modulation around a unique nanometer-sized scaffold.

In this chapter, the self- or induced organization of [60]fullerene hexakisadducts obtained during recent years from various systems will be described and analyzed.

The next section describes the thin films elaboration at the air–water interface and highlights the most suitable structural motif for the formation of a good quality and stable film. Organized molecular thin film assemblies elicit an always renewed interest as they allow the study of physical or chemical phenomena in a two-dimensional space, which induces new phenomena or provides model materials. Moreover, thin films often constitute an important stage of devices downscaling processes, since many applications (in electronics, data storage and processing, magnetism, optics, chemistry, etc.) result from the use of modified surfaces or are elaborated on modified surfaces.

Then, examples of thermotropic liquid-crystalline supermolecules will be detailed and the emphasis will be put on the relationships between molecular architecture and supramolecular order.

Finally, arrangement through micelles, nanospheres, and other “buckysomes” will be presented as a function of dendritic or linear hexakisadducts of various symmetries.

2 Thin Films as Induced Organization of [60]Fullerene Hexakisadducts

The preparation, characterization, and functionalization of [60]fullerene thin films such as self-assembled monolayers (SAMs) [10–16], self-organized bilayers [17–21], or Langmuir–Blodgett (LB) films [22–27] are of great current interest

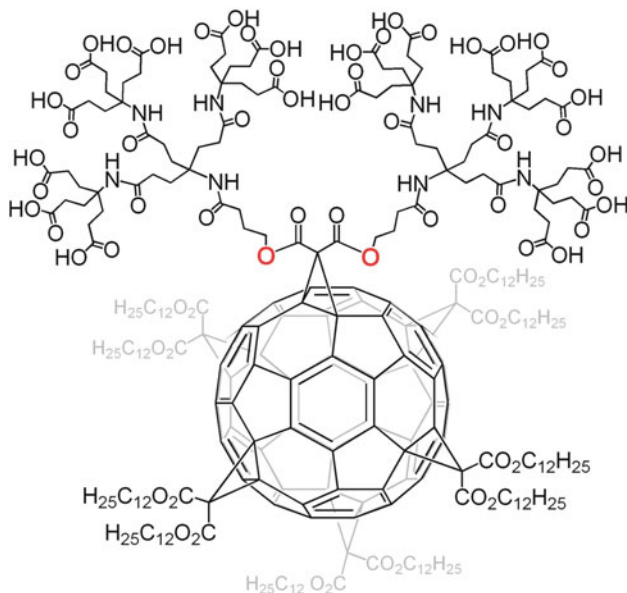
from both fundamental and practical viewpoints mainly owing to their unique electronic and/or structural characters. Not only the SAM approach achieved through junction moieties such as organosilane [28], organosulfur [29, 30], or carboxylic acid [31] but also the Langmuir technique allows the control over the formation and the structure of the resulting film at the molecular level. In the latter field, working at the air–water interface, various mono- [32–38] and bis- [39] [60]fullerene derivatives have been studied in the past years and showed encouraging results in terms of film quality and stability, roughness, reversibility, and transferability onto solid substrates. For example, F. Diederich and coworkers [40] or Imae and coworkers [41] showed that fullerene monoadducts bearing dendritic branches display good spreading characteristics and reversible compression/expansion behavior has been described. Working on [60]fullerene bisadducts, Nierengarten and coworkers have shown that encapsulation of the carbon sphere in a cyclic addend surrounded by either long alkyl chains [42, 43] or cholesterol subunits [44] is a method of choice for obtaining stable and reversible monomolecular thin films, easily transferred onto solid substrates in order to prepare high quality LB multilayers. Using an alternative approach to the previous studies, the same group demonstrated that the fullerene can be attached into the branching shell of a dendritic [45] or diblock dendritic [46, 47] structure. In this case, the C₆₀ units are buried in the middle of the dendrimer which provides an insulating layer around them, thus preventing the irreversible three-dimensional aggregation resulting from fullerene–fullerene interactions (for example, see: [48, 49]). Finally, various studies performed recently on [60]fullerene hexakisadducts showed that hexaaddition on the carbon sphere provides not only an ideal structure to prevent aggregation phenomenon but also an optimized hydrophilic–hydrophobic balance for preparing well-ordered supramolecular assemblies at the air–water interface. In the following sections, a review of the most recent and significant systems will now be presented.

2.1 [5:1] Hexakisadducts

2.1.1 Dendritic Structure

With Ester Link

In 2000, A. Hirsch and coworkers [50] studied the spreading behavior at the air–water interface of dendritic hexakisadduct **1** possessing a dendrimeric hydrophilic region connected via ester links to the fullerene cage, and ten long alkyl chains forming the hydrophobic part. Monolayers of **1** were studied at different lateral pressures by a combination of film balance techniques, neutron reflection (NR), and infrared reflection–absorption spectroscopy (IRRAS).



The dendrimer-like hydrophilic part of **1** comprises 18 carboxyl groups which release their protons under appropriate pH conditions. This allowed the variation of the surface charge density of the monolayer and the electrostatic repulsion between the molecules over a wide range. Pressure-area isotherms of **1** were recorded on subphases with pH values equal to 2.1, 3.9, 7.0, and 12.1 (Fig. 1). From these isotherms the increasing dominance of electrostatic repulsion with increasing pH values became obvious. Indeed, for low pH values (2.1 and 3.9), the low-pressure regime ($\pi < 5 \text{ mN m}^{-1}$) at a molecular area beyond 350 \AA^2 was characterized by a pressure-area behavior typical for a lipid monolayer in the gas phase. For areas equal to or below 350 \AA^2 the slope of the isotherm changed rather abruptly, indicating a diminished compressibility of the layer.

Monolayers of **1** could be compressed and expanded without significant hysteresis and the alkyl chains remained fluid at all pressures. By a titration series, the pK_a value of a monolayer was determined as 7.5 and pH-dependent measurements allowed a variation of the negative **1** headgroup charge by about 18 charges (Fig. 1). The steep increase of π from 6.0 mN m^{-1} at pH 6.0 to 37 mN m^{-1} at pH 9 was clearly a result of increasing electrostatic repulsion upon deprotonation of the carboxyl groups. The molecular area at 35 mN m^{-1} and pH < 6 was $247 \pm 3 \text{ \AA}^2$. Because there are ten C-12-chains attached to the fullerene cage, the area per C-12 chain at this pressure was still well above the lower packing limit of alkyl chains ($\geq 20 \text{ \AA}^2$). Hence, no squeeze-out of molecules can be expected at this pressure. This is consistent with the fact that the authors did not observe significant hysteresis upon multiple cycles of compression and expansion.

The properties of the monolayers of **1** may be useful in the design of dedicated biomimetic surfaces as negatively charged monolayers showed a strong coupling of the water-soluble protein cytochrome *c* from the subphase, leading to the formation of a 30 \AA thick protein layer underneath the layer.

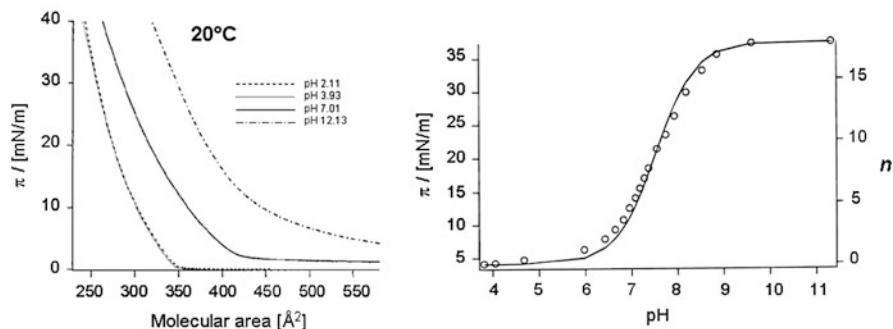
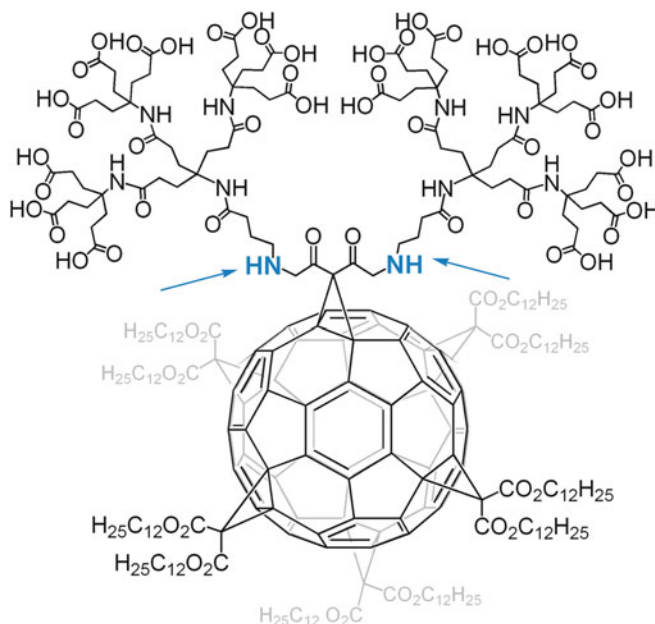


Fig. 1 *Left:* Pressure-area isotherms of monolayers of **1** at $T = 20^\circ\text{C}$ at different pH values. *Right:* Titration isotherm of a monolayer of **1**. The *solid lines* represent the number of negative charges n as calculated by equation $n = n_{\text{max}}/(1+10^{(\text{p}K_a-\text{pH})})$

With Amide Link

In 2005, the same group, in collaboration with J.-L. Gallani and coworkers [51] reported the formation of highly stable Langmuir–Blodgett (LB) organic steps made with a dendritic hexakisadduct **2**, differing from **1** by the amide links connected to the cyclopropane ring. This amphiphile formed stable and good quality films with a very low roughness. The stability of the films stemmed, among others, from the spheroid shape of the constituent dendritic molecules. This architecture makes it very difficult for the molecules to destroy the layers upon rearranging, as compared to more traditional amphiphiles with their cylindrical or conical shape (fatty acids).



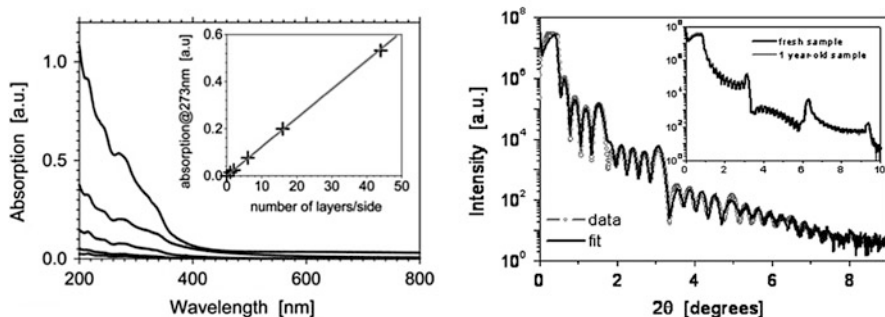


Fig. 2 *Left:* UV-vis absorption spectra of LB films of **2** having 1, 2, 6, 16, and 44 layers on each side of the fused silica plate. *Inset* is a plot of the absorption at 273 nm versus the number of layers on each side of the silica plate. *Right:* X-ray reflectivity of LB films. The main graph is the spectrum of a 10-layer-thick LB film (*linear curve*) together with the best fit (*dotted curve*). *Inset* is the spectrum of a 30-layer-thick LB film taken immediately after deposition and the spectrum of the same film after 12 months of storage

Compound **2** was transferred very nicely onto hydrophobic substrates as up to 250 layers have been easily deposited on silicon or silica plates coated with silane, at a pressure of 40 mN m^{-1} . As the transfer ratio was 1 at least for the 50 first layers, the amount of deposited material grew in a linear fashion with the UV-vis absorbance, as shown in Fig. 2. The grazing incidence X-ray reflectivity graph of a 10-layer-thick LB film proved not only the high quality of such multilayer but also the electronic density and roughness of the layers deposited during the up- and downstroke motions were different. Nevertheless, the thickness of each sublayer stayed constant and on average $28.2 \pm 0.6 \text{ \AA}$ thick. The inset in Fig. 2 compares two spectra recorded on the same LB film, immediately after deposition and after 12 months storage (on a shelf, at room temperature) and clearly shows an excellent stability in time. As assumed by the authors, such stability could essentially be the consequence of the spheroid shape of the molecules, the formation of a hydrogen-bonding network between the hydrophilic heads of adjacent layers (observation of a band at $3,340 \text{ cm}^{-1}$ in the IR spectrum of a multilayer LB film) and the possibility of dipole-dipole interactions between the carbonyl groups at the substitution site on C₆₀.

In the second part of the article, the authors investigated the potential use of **2** as a thickness gauge for atomic force microscopy (AFM) or light microscopy studies as the intrinsic stability of the films makes them suited for such an application. The layers are flat to within a few angstroms, and their thickness is constant and has the right order of magnitude. AFM studies have been conducted on multilayer samples and showed the presence of very flat steps (with an average edge thickness of 60 \AA), with each one actually corresponding to a bilayer (Fig. 3). This makes each monolayer 30 \AA thick, a value in excellent agreement with the experimental value of 28.2 \AA obtained by X-ray diffraction analysis.

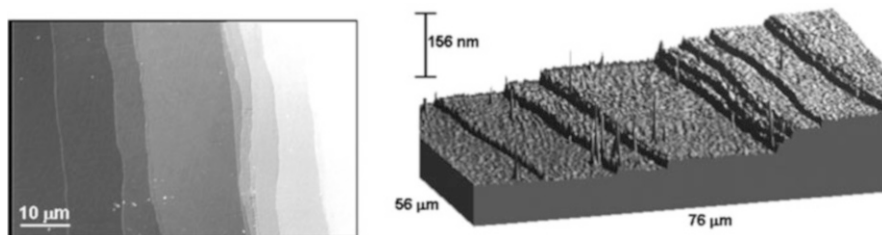
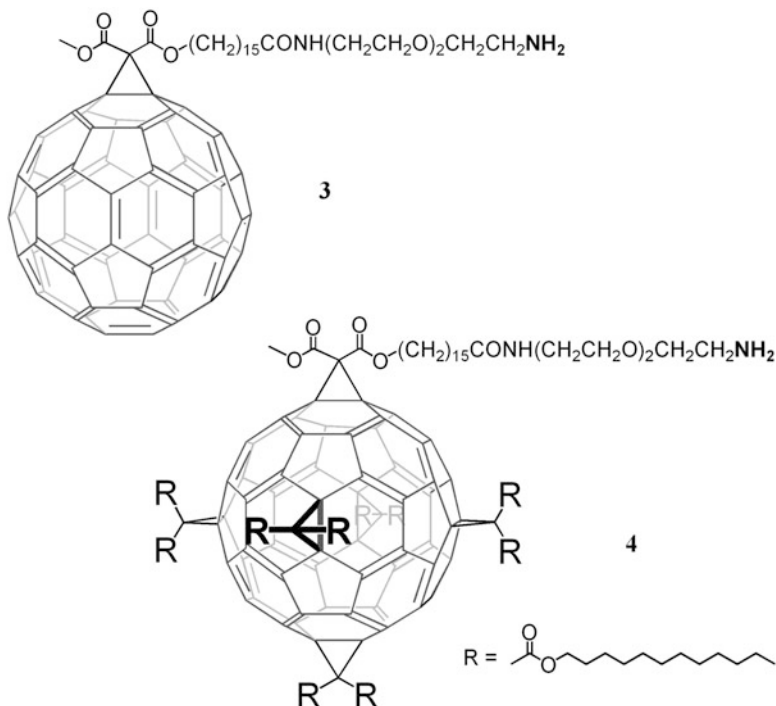


Fig. 3 *Left*: AFM image of a multilayered LB film of **2** with the Sarfus microscopy technique. The edge of the bilayers is clearly seen. *Right*: Three-dimensional rendering of the microscopic observation

2.1.2 Linear Structure

In 2005, the spreading behavior of linear monoadduct **3** and its hexakisadduct counterpart **4** was reported by H.-L. Wang and coworkers [52].



Both these amphiphiles formed stable, ordered monolayers at the air–water interface. The molecular packing and the mean area per molecule were similar to expected values assuming tight hexagonal packing. Hysteresis of pressure isotherms of **4** (Fig. 4) showed complete reversibility upon compression and

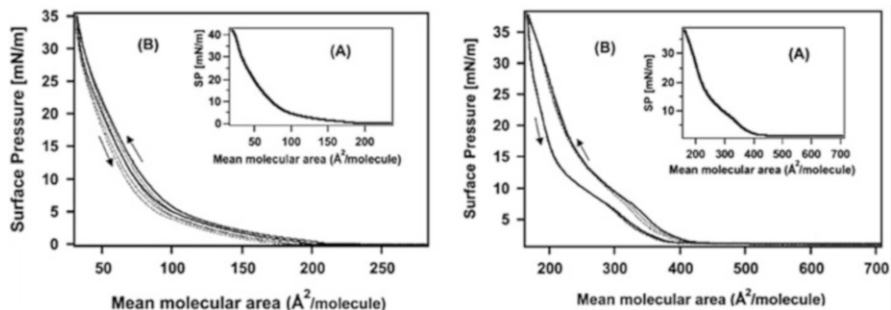


Fig. 4 (A) Pressure-area isotherm of *left* amine-terminated monoadduct **3**, *right* hexakisadduct **4**. (B) Three successive compression and recompression cycles with **3** (*left*) and **4** (*right*)

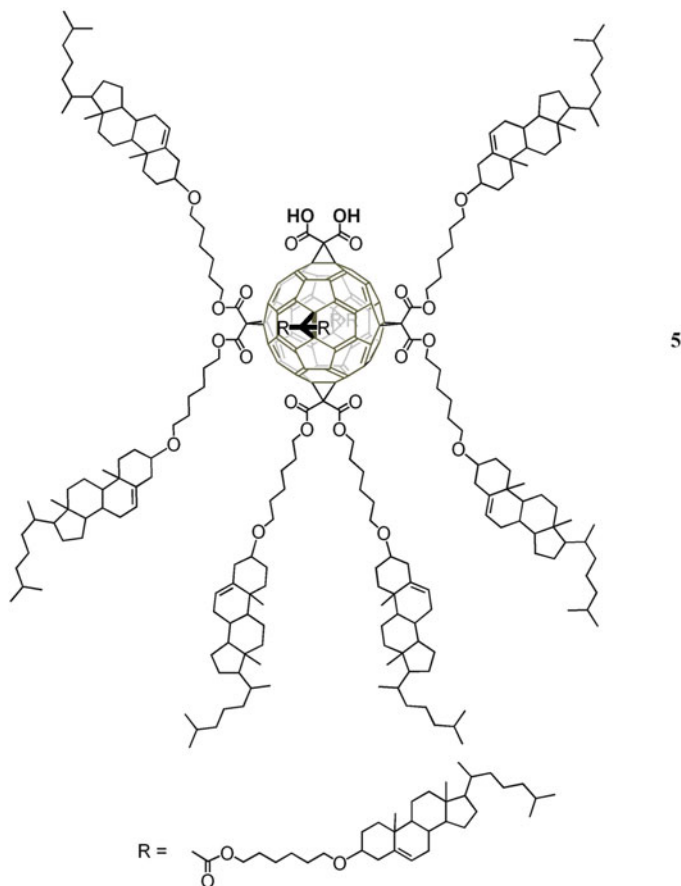
decompression, which suggested that the side chains on the C₆₀ sphere are sufficient to prevent intimate contacts between the C₆₀ spheres, thus inhibiting formation of aggregates at the interface.

If monolayers of monoadduct **3** were successfully transferred onto quartz substrates as Z-type multilayered Langmuir–Blodgett films, monolayers of hexakisadduct **4** were transferred as Y-type. In fact, detailed characterization of the multilayer films (Z-type deposition) prepared from amine-terminated **3** using X-ray and neutron reflectometry revealed staggering of C₆₀ spheres and a head-to-head (Y-type) structure presumably due to flipping and reattaching of C₆₀ amphiphiles to the previous underlying C₆₀ layer.

2.1.3 Steroid-Based

Steroids (e.g., cholesterol), on account of their wide natural occurrence, particularly in mammalian tissue, broad biological activity profile, ability to penetrate the cell membrane and bind to specific hormonal receptors, have found favor as building platforms for a variety of bioactive molecules. Therefore, coupling a fullerene with a steroid moiety can potentially produce a compound with good biocompatibility and enhanced therapeutic activity [53].

In 2005, D. Felder-Flesch and coworkers studied the LB film formation of amphiphilic hexakisadduct **5** bearing ten hydrophobic cholesterol units and a polar head group made of two carboxylic acid groups. It was expected that the derivatization with cholesterol units will enhance and favor the interaction of **5** with cells membrane. The liquid-expanded behavior observed between molecular areas of 600 and 350 Å² was indicative of long-range intermolecular interactions in the film. The final molecular area extrapolated to zero surface pressure was 370 ± 10 Å², a value corroborated by layer thickness measurements and molecular modeling, clearly proving that a monomolecular film was obtained.



Brewster angle microscopy (BAM) pictures taken at the end of the compression showed a high quality homogeneous film, without defects or aggregates. More evidence of the film cohesion was confirmed by the hysteresis curve which showed a good reversibility of the isotherm as long as the pressure was kept below the collapse pressure of $\approx 50 \text{ mN m}^{-1}$.

It has been possible to transfer the Langmuir film of **5** onto hydrophilic quartz slides and prepare multilayer LB films. As already observed for fatty acids, the films quality improved much when cadmium acetate was dissolved in the subphase (2.0 mmol). The average deposition ratio was 0.8 ± 0.1 , decreasing slowly from first layers to ca. 0.5 for the 60th layer. A transfer ratio < 1 implies either a reorganization of the molecules during transfer or the presence of defects. Since the X-ray analysis of the LB films revealed that the layers had a density lower than expected, the transfer ratio smaller than one therefore indicates that defects (voids) were present in the LB films. The roughness of the layers was also rather high. Still, given the size and structure of the molecule, the multilayers had a reasonably good quality.

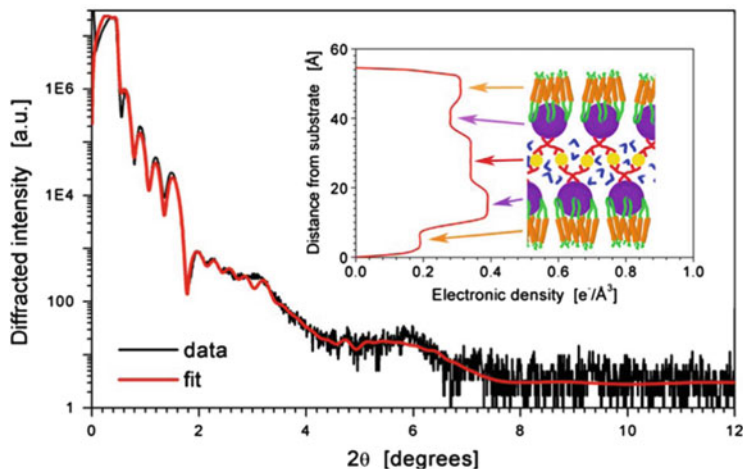


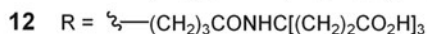
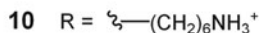
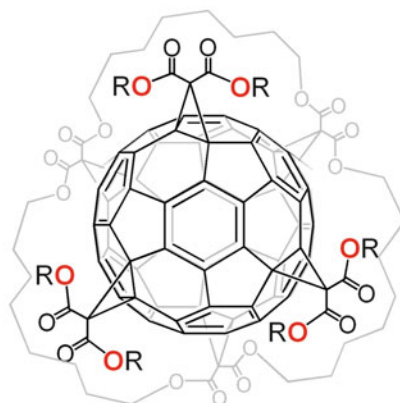
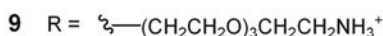
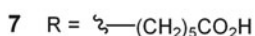
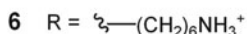
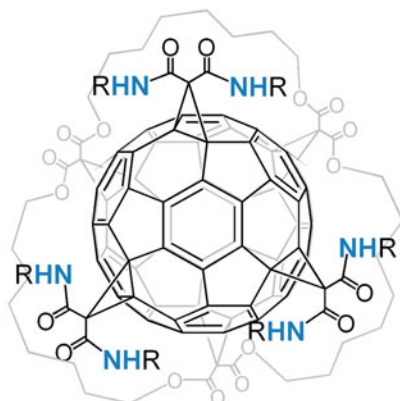
Fig. 5 X-ray scattering pattern of an 11-layer LB film of **5** and its best fit. *Inset* gives the electronic density of the repeat unit and a crude sketch of the molecular packing. The large circles are the C_{60} , the sticks are the cholesterol units, and the lines are the alkyl chains. In the middle layer, the *lines*, *circles*, and *boomerangs*, respectively, stand for the carboxylic groups, Cd^{2+} ions and water molecules

The grazing incidence X-ray scattering pattern of an 11-layer LB film of **5** is given in Fig. 5, together with the best fit. Inset in Fig. 5 also gives the electron density profile of the repeat unit of the LB film showing that it was not symmetric, thus meaning that the molecular packing was not the same in the up-stroke and down-stroke layers. The authors did not suggest any explanation for that, but pointed out that such a fact is consistent with the observation of a transfer ratio < 1 .

A bilayer thickness of 56 Å was obtained from X-ray scattering measurements. This was in agreement with the results of molecular modeling studies (Fig. 6) which gave a thickness of ca. 59 Å for the bilayer of **5**.

2.2 [3:3] Hexakisadducts

Hirsch and Felder-Flesch have recently conducted a systematic study on the spreading behavior at the air–water interface of a series of [3:3] [60]fullerene hexakisadducts (**6** to **12**) as a function of the chemical design and hydrophobic–hydrophilic balance [54]. For this purpose, various structural parameters have been taken into account (Fig. 7), such as the nature, anionic for **7** and **12** or cationic for **6**, **8**, **9**, **10**, and **11**, and the size of the polar headgroup ($-(CO_2H)_{18}$ for **12** compared to $-(CO_2H)_6$ for **7**); the nature of the chemical linker: amide for **6**, **7**, **8**, and **9** or ester for **10**, **11**, and **12**; the nature and/or the length of the spacer: hydrophobic chain (**6**, **7**, **10**, and **12**) or short (**8**) or long (**9**) hydrophilic chain or mixed alkyl-polyethyleneglycol chain (**11**).



It has been possible to record an isotherm for all of the compounds. Isotherms of **6** on pure water (pH 6.5) showed poor reproducibility, a rather small final molecular area, ca. 130 \AA^2 – still not unrealistic – and a rather low collapse pressure, ca. 5 mN m^{-1} . These observations were clearly consistent with the fact that the compound is essentially hydrophilic. Nevertheless, going to higher pH (10) for the subphase using potassium hydroxide yielded better results in terms of reproducibility, and collapse pressure reached 20 mN m^{-1} .

Comparison between the pressure-area isotherms of **8** and **6** revealed that going from an aliphatic to a hydrophilic spacer has a dramatic effect on the capacity of the compound to form a film on the water subphase. Indeed, **8** hardly formed a film and

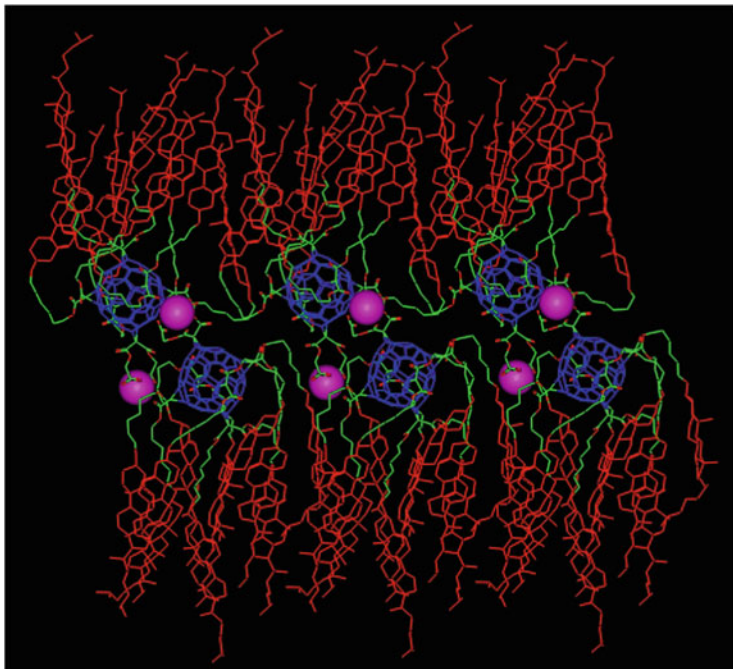


Fig. 6 Bilayer of steroid-based hexakisadduct **5** obtained by molecular modeling

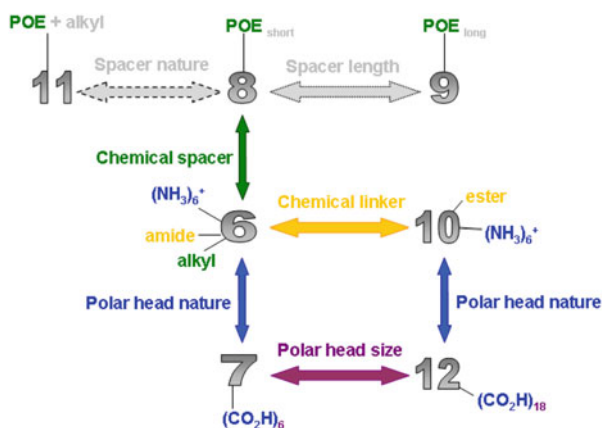


Fig. 7 Comparison points allowing the systematic study

no significant surface pressure (π_{\max} 2–3 mN m⁻¹) was observed at pH 10. Thus, it becomes obvious that **9**, having an even longer hydrophilic spacer, was unable to form a stable and high quality film on water (π_{\max} 2–3 mN m⁻¹). Pursuing the discussion on the derivatives for which the hydrophobic/hydrophilic balance leans

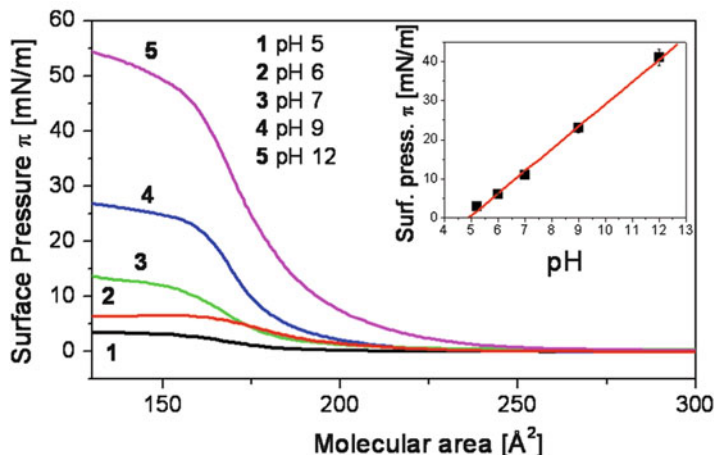


Fig. 8 Isotherms of **10** as a function of pH. *Inset* is a plot of the collapse pressure π_c with a fit to a *straight line*, showing the almost linear correlation of π_c with the pH variation, error bars of 5%

clearly towards hydrosolubility, it was pointed out that **12**, possessing a short aliphatic spacer and eighteen carboxylate polar heads, displayed a spreading behavior quite different than that of **6** (long aliphatic spacer, six amine polar heads) and **8** or **9** (hydrophilic spacer, six amine polar heads): indeed, the surface pressure reached negative values which is an indication that molecules dissolved into the water upon compression.

On pure water subphase **10** formed a film (Fig. 8) but with a rather low collapse pressure, ca. π_{\max} 6 mN m⁻¹. Going to higher pH yielded better results in terms of reproducibility and also gave a larger final molecular area of 190 \AA^2 and a quite satisfactory collapse pressure of 40–45 mN m⁻¹. In addition, collapse pressure varied almost linearly with the pH of the subphase (inset, Fig. 8).

Considering the film cohesion, BAM study showed that **10** did not form islands on the water subphase but arranged immediately after deposition into a homogeneous film. Moreover, the film seemed rigid and its formation was irreversible since nothing changed under the microscope immediately after decompression (Fig. 9): BAM images did not change while barriers were totally pushed away and after a few minutes (ca. 10 min), images evolved showing films with solid-type fractures and fragments floating on the water surface.

The authors focussed then their attention on the comparison between **6** and **10**. These two derivatives both possess six ammonium polar heads together with aliphatic spacers and differ from each other only by the nature of the chemical linker directly connected to the cyclopropane ring. However, this simple change strongly influenced the stability of the monomolecular film (Fig. 10). In fact, the maximum surface pressure (π_{\max}) went from 20 mN m⁻¹ for **6** bearing amide connections to 45 mN m⁻¹ for **10** with ester linkers. In order to clarify such a phenomenon, A. Hirsch and coworkers proposed a model based on intra- or intermolecular hydrogen bonds (Fig. 11).

Fig. 9 Scheme describing the rigidity of a monolayer of **10** together with BAM pictures showing solid-type fractures. Pictures collected at 20°C, pH 10, barrier speed: 10 mm min⁻¹

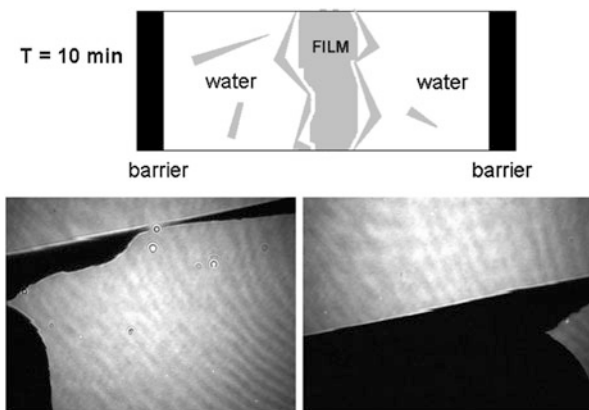
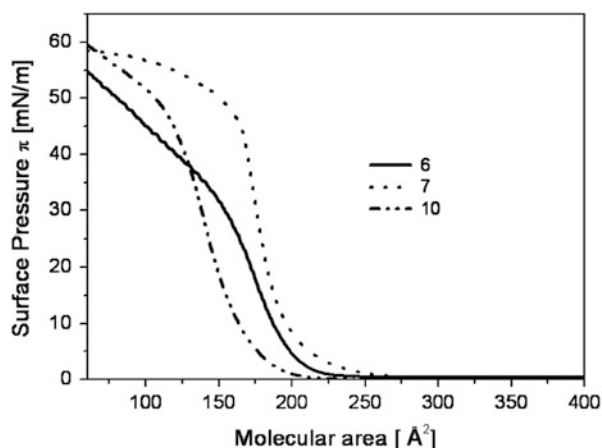


Fig. 10 Isotherms of **6**, **7**, and **10** recorded at pH 10 (**6** and **10**) or pH 2 (**7**)



As the slope of a compression isotherm is a measure of the film compressibility, a steeper slope meaning a larger rigidity, it becomes clear that films of **10** are more rigid than those of **6**. This implies a stronger cohesion between the molecules which could be ascribed to the formation of an H-bond network between through interactions between the amine polar heads of a molecule and the ester linker of its neighbor. Such interconnections are less likely for **6** as a consequence of the nature of its head and linker, the cohesion of the film is consequently lower and collapse pressure becomes weaker (Fig. 12).

Comparison between **10** and **7** showed that the nature of the polar head had a very pronounced influence on the properties of the film. For instance, in the case of amide as the linker, going from six ammonium to six carboxylic acid polar heads almost doubled the maximum surface pressure sustained by the monolayer which reached values of 40–45 mN m⁻¹. It appeared then that the couple acid polar

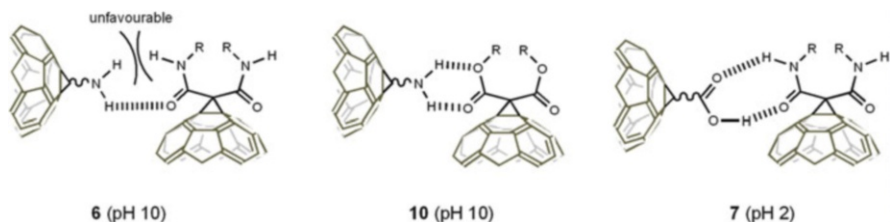


Fig. 11 Proposed intermolecular H-bonding possibilities for **6** (unfavorable), **7** and **10** explaining films cohesion and/or rigidity

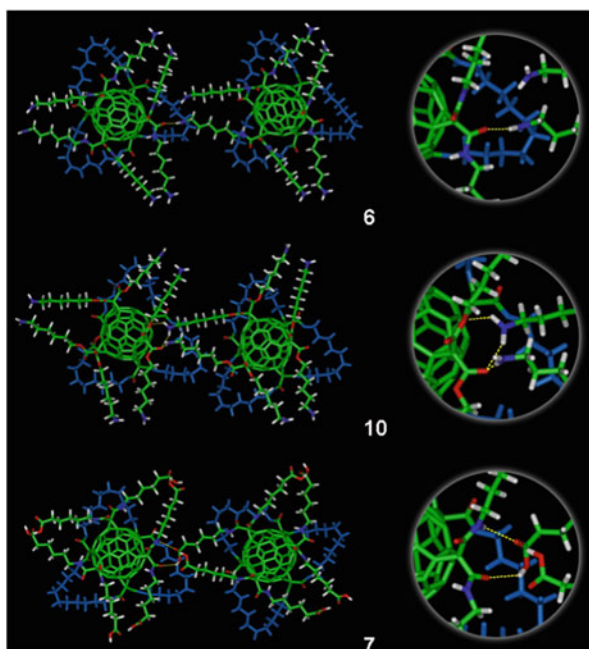


Fig. 12 Molecular modeling studies showing that those intermolecular interactions are possible

head/amide connection is a second means for optimal chemical design. Again, such an observation could be supported by the H-bonding model previously proposed: indeed, the chemical design of **7** allows intermolecular interactions between the carboxylic acid (pH 2) of a molecule and the amide linker of a close neighbor. A thorough study of the spreading behavior of **7** highlighted a good reproducibility at highly acidic pH as well as a linear correlation between the pH and the maximum collapse pressure, the latter increasing to reach 35 mN m^{-1} at pH 1.7 (Fig. 13). In that, **7** is the strict opposite of **10** which is only logical when going from amine to acid polar heads.

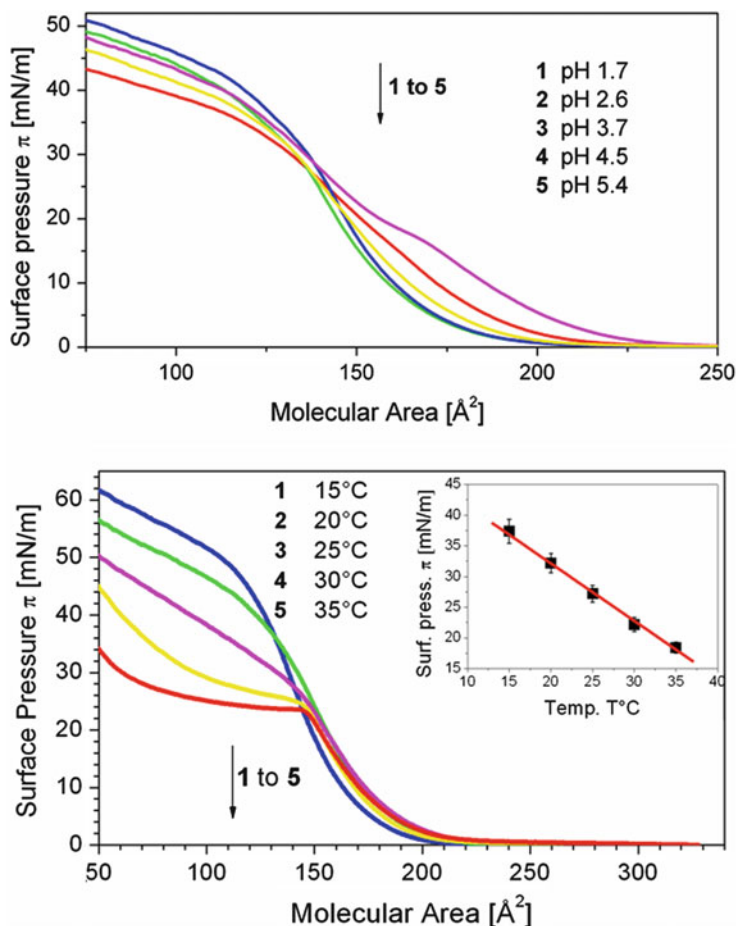


Fig. 13 Isotherms of **7** as a function of *top*: pH; *bottom*: variation of the temperature recorded at pH 2. *Inset* is a plot of the collapse pressure π_c with a fit to a *straight line*, showing the almost linear correlation of π_c with the T °C variation, error bars of 5%

On the opposite of **10**, isotherms of **7** showed temperature dependence, in the form of a fall of the maximum surface pressure withstood by the film when the temperature of the water subphase increased (Fig. 13).

Lastly, another difference between **7** and **10** came from the BAM observations (Fig. 14) showing many white spots corresponding to small islands of compound appearing once **7** was spread on the water. Their number decreased upon compression while their size increased. A transition seemed to occur around 230 \AA^2 and a homogeneous film appeared around 170 \AA^2 .

Finally, **11** also formed a thin film on water, the isotherm of which showed a plateau probably attributed to a first order transition. In terms of collapse pressure,

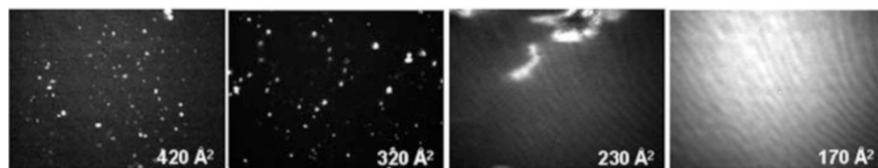


Fig. 14 BAM pictures of **7** for different molecular areas

Table 1 Parameters of the thin films isotherms as a function of the chemical structure of Hexakis **6** to **12**

Compound	Nature and number of polar head	Nature of the chemical linker ^a	Nature of the spacer ^b	pH	Collapse pressure π_c^c	Comments
6	$-(\text{NH}_3)^+_6$	Amide	Alkyl	10	20	Reproducible ^d
7	$-(\text{CO}_2\text{H})_6$	Amide	Alkyl	2	35	Reproducible ^d
8	$-(\text{NH}_3)^+_6$	Amide	POE short	–	–	Hardly forms a film on a water surface
9	$-(\text{NH}_3)^+_6$	Amide	POE long	–	–	Hardly forms a film on a water surface
10	$-(\text{NH}_3)^+_6$	Ester	Alkyl	10	40	Reproducible ^d
11	$-(\text{NH}_3)^+_6$	Ester	Alkyl +POE	10	20	Poorly reproducible ^d
12	$-(\text{CO}_2\text{H})_{18}$	Ester	Alkyl	–	–	Polar head too large

^aChemical group directly connected to the cyclopropane ring

^bBridge between the cyclopropane ring and the polar head

^cIn mN m^{-1}

^dRecorded at 20°C

best results were observed at 15°C but with poor reproducibility. Moreover, films were unstable, the surface pressure decreasing as soon as the compression was stopped, which is indicative of molecules dissolving into the water.

In conclusion, by changing both the nature and the size of the polar headgroups, by varying the nature of the chemical linker and/or spacer, by modifying the nature and/or the length of the spacer, the authors were able to highlight various behaviors and conclude that the optimal chemical design for this type of amphiphilic supermolecules is reached with the combination of ammonium polar head/ester linker (**10**) or carboxylic acid polar head/amide linker (**7**), as the possible formation of intermolecular H-bonds greatly enhances the film cohesion and/or rigidity. Thus, the authors have been able to establish a new relationship between the chemical design of these hexakisadducts (mainly control of the hydrophilic/hydrophobic balance) and their ability to form a monolayer of the Langmuir type (Table 1).

3 Thermotropic Liquid-Crystalline Hexakisadducts

Among all the possible molecular organizations, thermotropic liquid crystals play an important role in our everyday life. In fact, they are mainly used in watches, computers, or mobile phone screens [55]. Combining an aesthetic structure with interesting electronic properties [56; and references therein], C_{60} is a candidate of choice for the development of new materials [57–61] and ordered structures [2–4]. Indeed, the highly symmetric [60]fullerene represents a particularly versatile scaffold for the regioselective covalent assembly of a variety of regular three dimensionally structured molecules, some of which may widen the existing library of programmed molecular components for the construction of useful ordered materials. However, the development of functional devices very often requires dedicated molecular engineering, that is, functionalization of the molecules for controlling their organization. Combining C_{60} with a mesogenic entity leads to study the influence of a precise orientation of the mesogens obtained through regioselective grafting on the nanosphere on the physical properties of the chromophore and also to correlate the observed mesomorphic properties with the degree of addition on the carbon polyhedron. Nevertheless, the latter displaying no intrinsic mesomorphic behavior, the preparation of fullerene-based liquid-crystals proved to be difficult to achieve.

There are two main approaches to design fullerene-containing liquid crystals: covalent and non-covalent modifications. Two examples of the non-covalent approach are based on the formation of inclusion complexes in which C_{60} either resides within cavities of host molecules such as dendritic porphyrins [62], cyclotrimeratrylene [63], or is linked to hexaphenyltriphenylene forming a 1:1 mixture with hexakis(4-nonylphenyl)-dipyrazino[2,3-f:2',3'-h]quinoxaline [64]. Within the covalent approach a number of different mesogenic units have been introduced to obtain a variety of fullerene-containing thermotropic liquid-crystalline materials (methanofullerene LC derivatives: [65–67]; fulleropyrrolidines LC derivatives: [68–71]). For such systems the main criterion for LC phase induction is the adequacy of the fullerene and mesogenic side groups cross sections. In addition, small anisotropic units are often insufficient as interactions are too weak to generate mesomorphism [72]. Examples of C_{60} derivatives possessing a high LC character (bearing more than two anisotropic moieties per C_{60} via polyaddition [73] or dendritic approach [74–77]) showed either a transient nematic [78], a chiral nematic [79], or a smectic A phase [80, 81]. In these cases, the properties of the materials were mostly dominated by the anisotropic moieties, due to dilution of the C_{60} moiety. In another approach, C_{60} is placed at the apex of cone-shaped molecules, forming a new type of mesomorphic compound which self-assembles into thermo- and lyotropic columnar liquid-crystalline mesostructures [82–84].

The first mesomorphic methano[60]fullerene monoadduct was synthesized in 1996 by R. Deschenaux and coworkers [65]. Comprising two mesogenic cholesterol units, it developed a smectic A phase from 146°C to 190°C. In this seminal work, several structural conditions were applied in order to obtain a mesomorphic derivative of C_{60} . The carbon sphere being a priori incompatible with liquid-crystalline phase formation, it was necessary to incorporate a strong promoter of liquid-crystalline phases. Another condition was to decouple the two mesogenic units from the bulky C_{60} so that they could interact freely with those of a neighboring molecule.

Thereafter, the same group disclosed an important structure–mesomorphic activity relationship for new methanofullerene monoadducts substituted by or integrated in a dendritic structure [74, 75]. In this case, the studies showed the loss of the destructive influence of the carbon sphere on the thermal and liquid-crystalline properties. Indeed, due to the obstruction it generates, the dendritic structure thwarts the unfavorable interactions between C_{60} units, so does the polyfunctionalization which will be reviewed in the following sections.

3.1 Enantiotropic Smectic A Phase

With the aim to exploit the capacity of C_{60} to provide new macromolecules with novel properties, T. Chuard and coworkers [81] studied in 1999 the influence of the degree of substitution of the sphere on the liquid-crystalline properties of the compounds. Thus, methanofullerene monoadduct **14** and its hexakisadduct counterpart **15** were synthesized and studied. While the precursory malonate exhibited a monotropic nematic phase from 57°C to 87°C, the monoadduct did not display any mesomorphic behavior. Since the grafting of C_{60} led to the loss of the mesogenic properties brought by the promoter, it was concluded that the bulky spherical carbon moiety strongly disturbs the organization. But in the same example, the authors showed that polyaddition is a good alternative in the design of C_{60} -containing liquid crystals; indeed, the hexakisadduct counterpart formed a smectic A phase from 80°C to 133°C. Allowing the assembly of many mesomorphic units around C_{60} , polyaddition seemed thus adequate to achieve the preparation of thermotropic [60]fullerene-based liquid crystals even starting from weak mesogenic promoters.

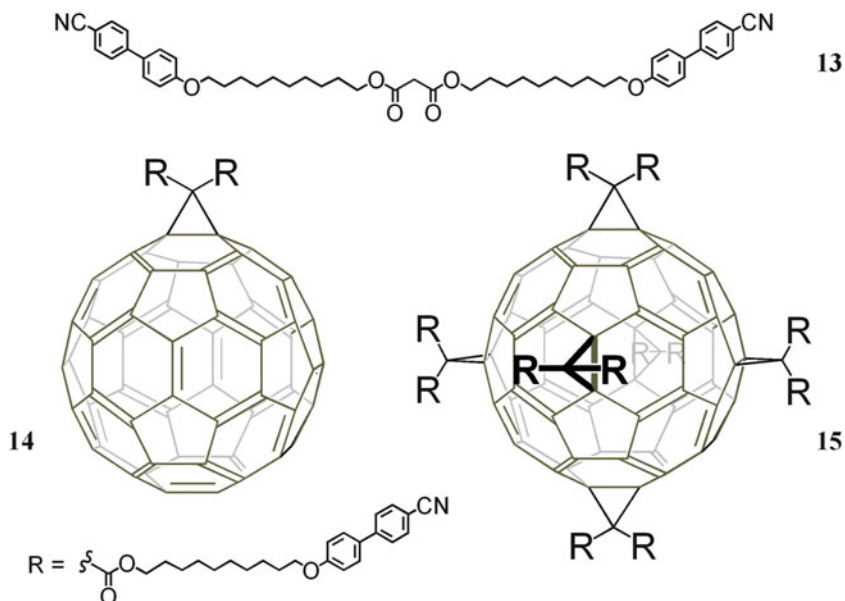
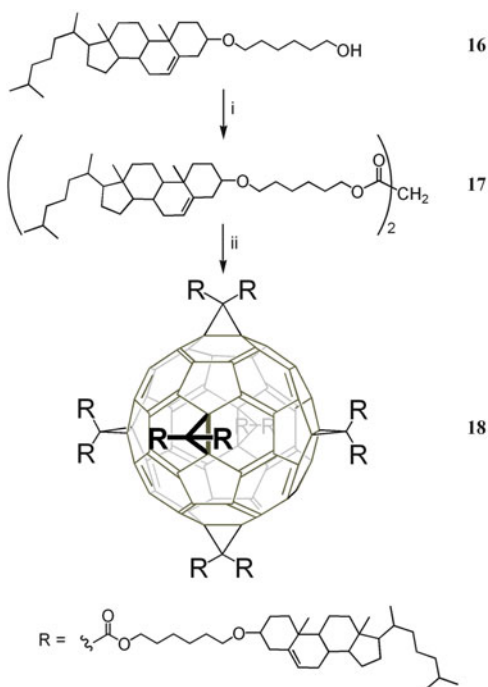


Fig. 15 Synthesis of [6:0] steroid-based hexakisadduct **18**. (i) Malonyl dichloride, DMAP, pyridine, CH_2Cl_2 , Ar, r. t., 39%; (ii) a: CBr_4 , DBU, toluene, Ar, r. t., 1 h, b: $\text{C}_{60}(\text{DMA})_6$, r. t., 16 h, 13%



A few years later, two novel cholesterol-based [60]fullerene hexakisadducts **18** (Fig. 15) and **21** (Fig. 16) bearing, respectively, 12 and 10 mesogenic cholesterol moieties were prepared with, respectively, 13% and 21% yield by D. Felder-Flesch and coworkers [80]. Unlike the first example described above, both hexakisadducts displayed a SmA phase over a very broad temperature interval, i.e. from slightly above room temperature up to 165°C for **18** and 180°C for **21**. This behavior is quite different from that of the precursory malonate **17** which displayed two monotropic unidentified phases at 41°C and 67°C and a chiral nematic phase between 67°C and 88°C (Table 2). An increase of the mesophase stability of about 100°C as well as a near room temperature mesomorphism was thus obtained through C_{60} grafting. The design consisting of the polyaddition of cholesterol moieties on the carbon truncated icosahedron used as a spherical template to create new 3D architectures appeared again to be a method of choice to obtain stable anisotropic materials and to prevent the C_{60} aggregation tendency.

As deduced by X-ray diffraction studies (Fig. 17), and supported by molecular modeling calculations (Fig. 18), the two macromolecules **18** and **21** self-organized into bilayer structures which consist of a median C_{60} -rich slab, sandwiched between cholesterol-containing outer layers.

Such results suggested the possible positive influence of the carbon sphere on the mesomorphic behavior of the material and revealed an interesting use of the carbon polyhedron as a template through hexaaddition in the preparation of new LC compounds.

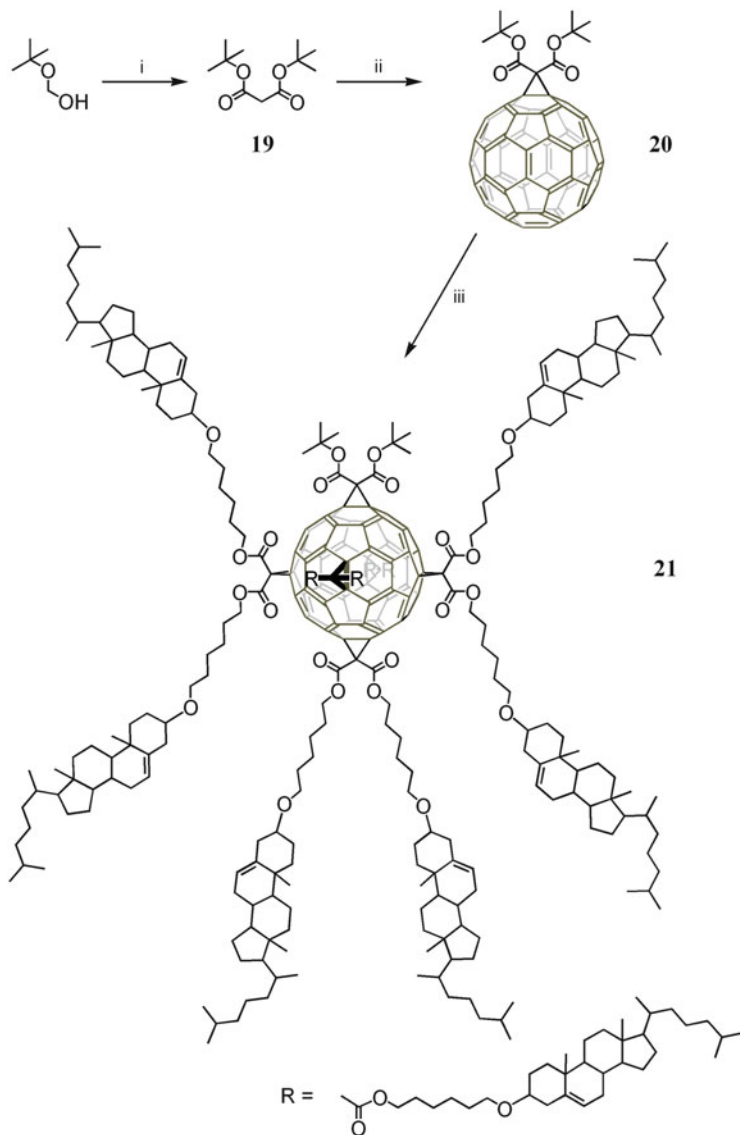
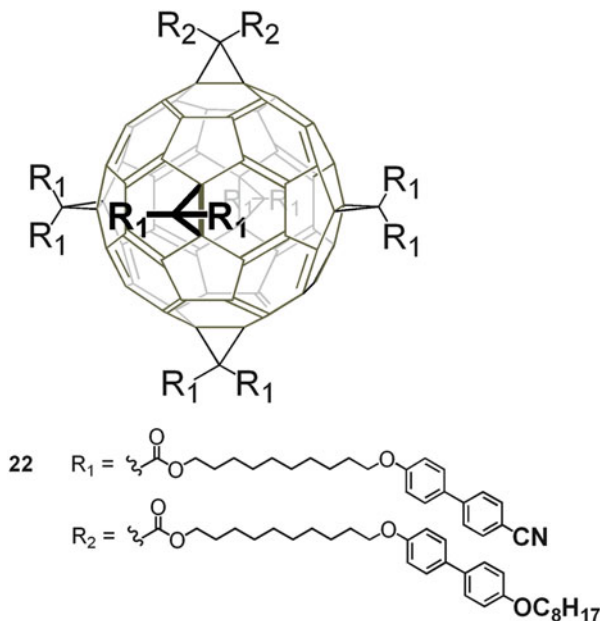


Fig. 16 Synthesis of steroid-based [5:1] [60]fullerene hexakisadduct **21** involving 10 cholesterol units. (i) Malonyl dichloride, DMAP, pyridine, CH_2Cl_2 , Ar, r. t., 38%; (ii) C_{60} , DBU, I_2 , toluene, Ar, r. t., 53% (iii) a: **17**, DMA, toluene, Ar, r. t., 2 h, b: CBr_4 , DBU, r. t., 21%

More recently, R. Deschenaux and collaborators [85] synthesized a mixed [5:1] hexakisadduct as the addition of two mesogens (or more in case of other addition patterns) onto C_{60} could be an elegant means for the design of fullerene-containing

liquid crystals with tailored properties. In that first example, they selected cyanobiphenyl and octyloxybiphenyl derivatives as mesomorphic promoters to prepare hexakisadduct **22**. In differential scanning calorimetry (DSC), a reversible endotherm was detected at 151°C and the formation of a liquid-crystalline phase between ca. 80°C and 151°C was observed by POM. Slow cooling of the sample from the isotropic fluid revealed the formation of a smectic A phase with typical focal-conic and homeotropic textures (Fig. 19). The fact that no melting point was detected by DSC was, most likely, a consequence of the amorphous character of **22** in the solid state.

Such result emphasized that assembling six malonate derivatives with two different mesogens in a 5:1 ratio around a focal point provides the required structural anisotropy and intermolecular interactions for mesomorphism to occur. In such a system, the mesogenic units formed a cylinder-like structure, the self-assembly of which gave rise to lamellar organization (Fig. 19). Interestingly, whereas the malonate derivatives gave rise to monotropic mesophases, **22** showed enantiotropic mesomorphism.



As shown by these seminal examples, polyaddition of mesomorphic units around the hard carbon nanocore is a method of choice for the elaboration of thermotropic derivatives displaying polypedic structures with controlled and tunable symmetries.

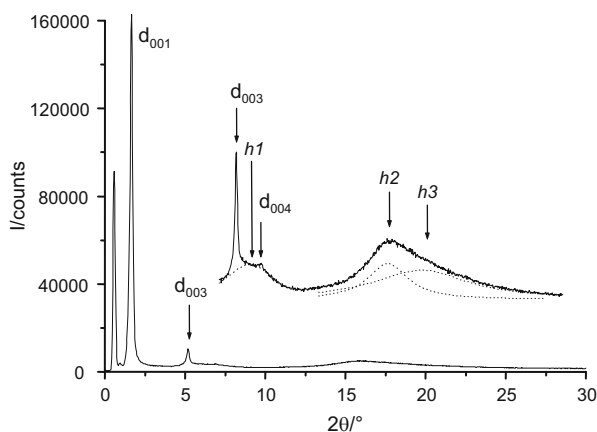
Table 2 Phase transition temperatures and enthalpy changes of malonate **17**, hexakisadducts **18** and **21**

Compound	T_g (°C)	Transition	T (°C) ^a	ΔH (kJ mol ⁻¹)
17	-12	M1 → M2	41	0.05
		M2 → N*	67	0.5
		N* → I	88	1.3
18	45	SmA → I	165	15.6
21	40	SmA → I	180	13.2

T_g glass transition temperature, *M1*, *M2* unidentified semicrystalline phases, *N** chiral nematic phase, *SmA* smectic A phase, *I* isotropic liquid

^aTemperatures are given as onset of the peaks obtained during the second heating

Fig. 17 Representative X-ray diffraction pattern obtained for **18** at 80°C



3.2 Nematic Phase

The design and selection of the molecular building blocks to reach nematic orderings close to or just above room temperature is challenging as shown in the literature reporting systems containing multivalent cores ranging from soft and flexible such as carbosilazane [86–88], siloxane [89–92], and silsesquioxane [93–98], to hard such as gold nanoparticles [99–109]. These systems are technologically relevant too, as the nematic phase allows often the control of the macroscopic alignment in thin films, important for potential technological applications.

3.2.1 Transient Phase

In 2000, F. Diederich and collaborators reported the first contribution to less ordered self-organizations of [60]fullerene hexakisadducts [78]. Their work, based on the study of mono-, di-, and hexakisadducts in the presence of a variable number of mesogenic 4-cyano-4'-oxybiphenyl units, highlighted the importance of

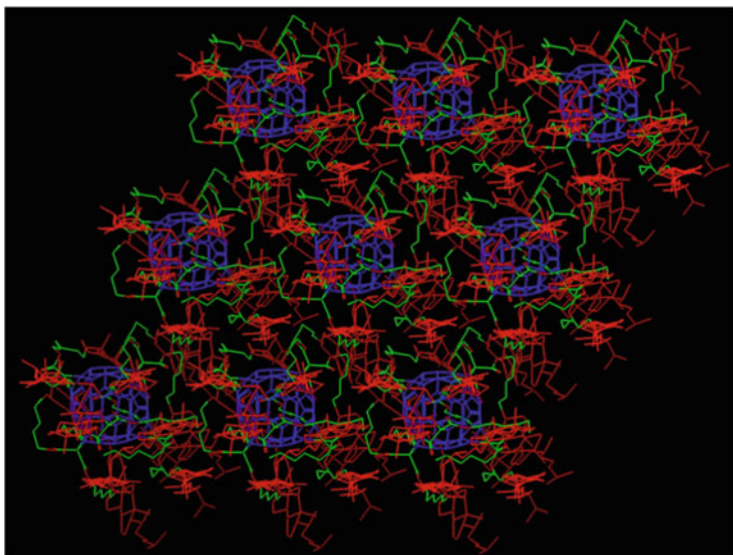


Fig. 18 Top view of the short-range hexagonal lattice obtained for **18** by molecular modeling

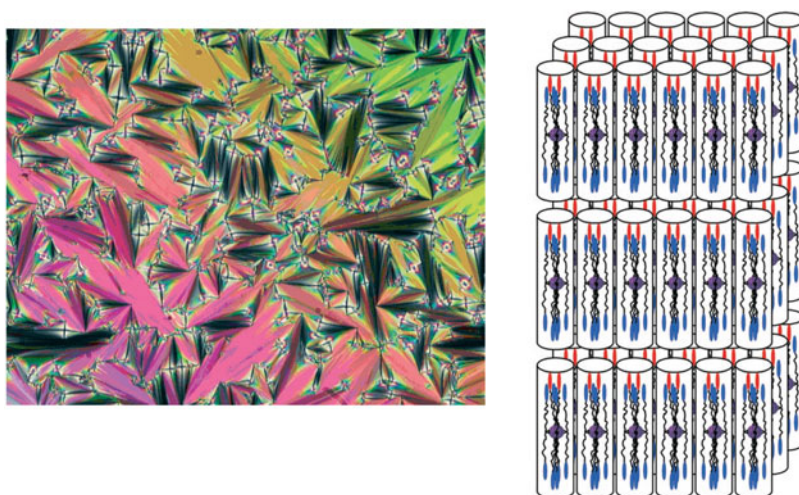
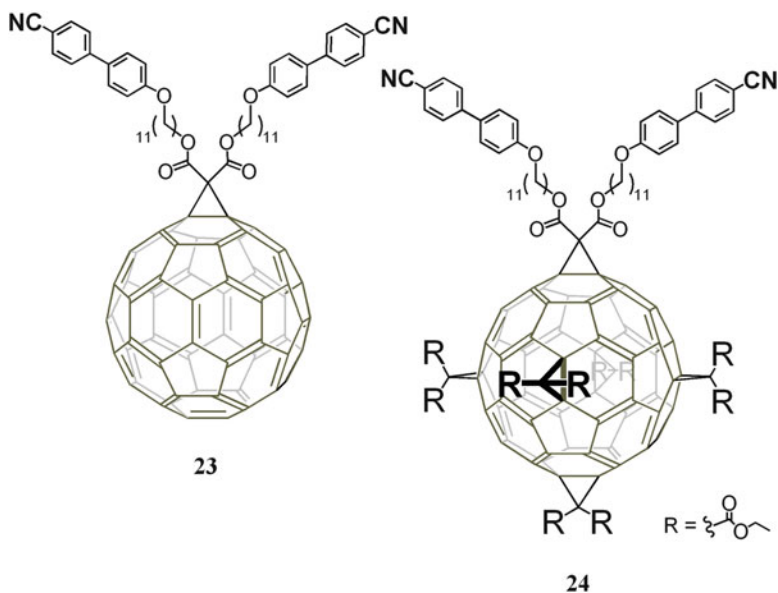


Fig. 19 *Left:* Thermal polarized optical micrograph of the focal-conic fan texture displayed by **22** in the smectic A phase upon cooling the sample from the isotropic liquid to a temperature of 151°C. *Right:* Proposed model for the supramolecular organization of X within the smectic A phase

the balance between the number of these units compared to the number of carbon spheres for the preservation of the mesomorphic properties of C₆₀-based materials. Indeed, while mesogenic malonate precursor showed a monotropic liquid-crystalline

behavior on cooling, exhibiting a nematic phase between 80°C and 58°C, the fullerene monoadduct **23** and hexakisadduct **24** exhibited markedly different phase behaviors. Monoadduct **23** showed only a glass transition temperature at $T_g = 50^\circ\text{C}$, samples of hexakisadduct **24** obtained by very slow crystallization from a CH_2Cl_2 /hexane mixture gave a nematic mesophase between 85°C and 157°C on first heating. This feature disappeared after isotropisation resulting in a completely amorphous material with a $T_g = 107^\circ\text{C}$; no mesogenic behavior could be recovered.



As a consequence of the poorer ordering within the mesophases, the tendency to increase the amorphous character on linking the sphere to liquid-crystalline precursors was here again highlighted.

3.2.2 Chiral

In 2006, R. Deschenaux, J. Goodby, and coworkers reported the synthesis (Fig. 20), in 1.4% yield, and the study of an optically active liquid-crystalline hexakisadduct displaying supramolecular helical organization [110].

Malonate **25** exhibited a chiral nematic phase identified by the formation of small focal-conic domains, while monoadduct **26** was found to be non-mesomorphic with only one glass transition observed upon cooling. On the opposite, on slow cooling from the isotropic liquid, hexakisadduct **27** displayed a highly birefringent texture but without characteristic defects. However, after 24 h annealing just below the clearing point, large areas evolved to show the Grandjean

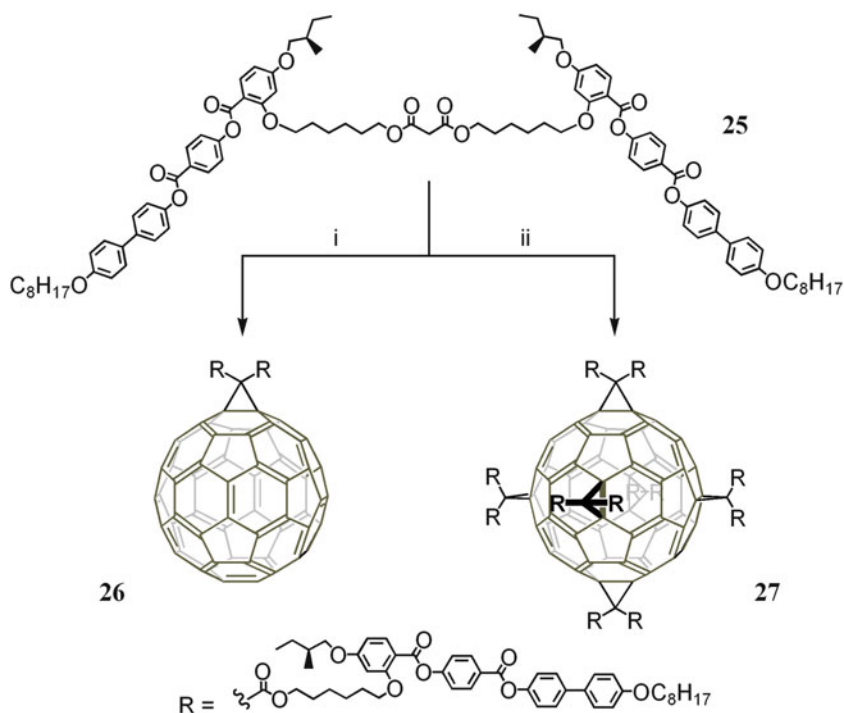


Fig. 20 Synthesis of chiral mono- and hexakisadducts. (i) C60, I2, DBU, toluene, rt, 64%; (ii) C60, 9,10-dimethylantracene, toluene, rt, and then **25**, CBr4, DBU, rt, 1.4%

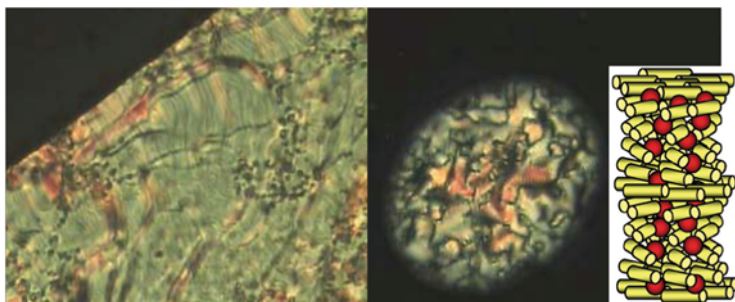


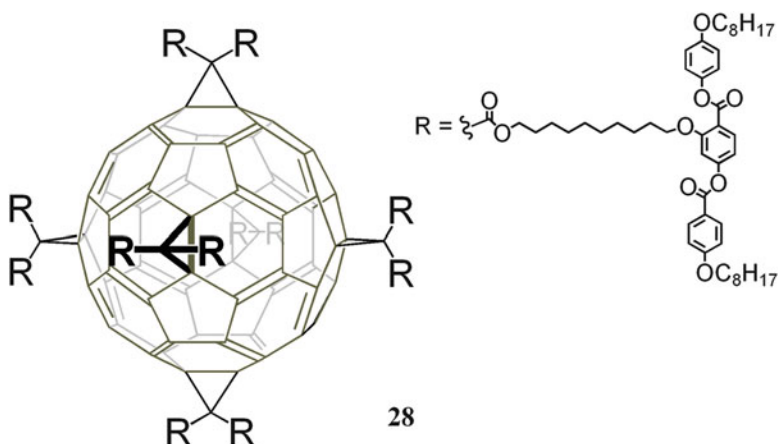
Fig. 21 Textures and supramolecular organization of **27** within the chiral nematic phase

plane texture and, where the sample was not in contact with the coverslip, pseudo-focal conics appeared (Fig. 21). In the Grandjean plane texture the sample was clearly helical, showing a left-handed helix from which the authors concluded that **27** exhibited a chiral nematic phase.

Thus, hexaaddition allowed C_{60} to be hidden in the mesogenic cloud, which did not alter the supramolecular organization encoded in the mesogens, but instead help in its amplification.

3.2.3 Constrained

A few months later, D. Felder-Flesch and coworkers [111] detailed the preparation, in 50% yield, of an enantiotropic, room temperature nematic material **28**, despite the absence of mesomorphism of the malonate side-group promoters: on subsequent heating-cooling cycles, a stable and reproducible behavior took place with the reversible sequence Glass (G) 13 Nematic (N) 60 Isotropic (I). Here, the authors showed that the specific architecture of the hexakisadduct induced a nematic phase with unusual features.



POM observations on a first heating showed that the compound was birefringent and very fluid above 38°C. On slow cooling from the isotropic liquid, point singularities with 2- and 4-Schlieren brushes slowly developed in the natural texture, indicating a nematic phase (Fig. 22).

Two phase transitions were detected by DSC during the first heating run. A broad exothermic transition at 38°C followed by a sharp transition at 60°C could be measured. On cooling, the same sharp peak at 60°C was detected, but the mesophase was strongly supercooled down to room temperature and frozen into a glassy solid ($T_g = 13^\circ\text{C}$).

In order to identify the mesophase and elucidate the supramolecular organization, the authors conducted a wide and small angles XRD analysis on aligned samples with a magnetic field (1.0 T). The diffractogram registered at 50°C revealed three reflections (Fig. 23):

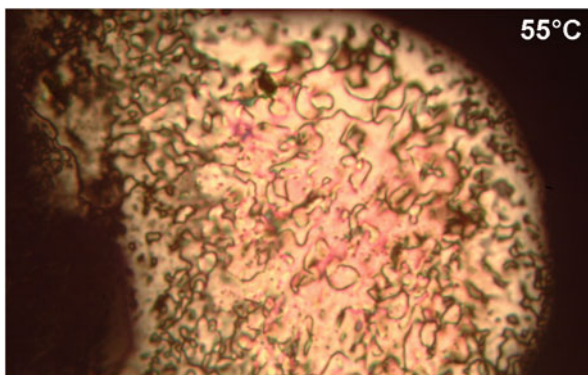


Fig. 22 POM image obtained for **28** on slow cooling from the isotropic liquid

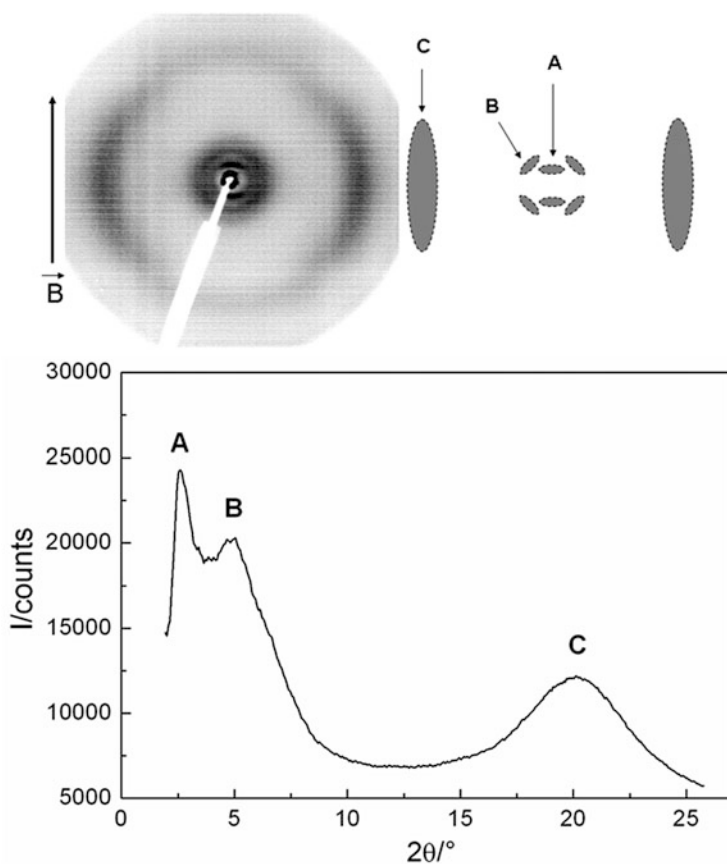


Fig. 23 X-ray pattern recorded at 50°C for the hexakisadduct **28**. *Top* oriented pattern in the magnetic field (*left*) and sketch representing the three reflections (*right*). *Bottom* 2θ profile of oriented pattern by integration over full azimuthal φ range

1. A rather diffuse reflection in the small angle part, centered on the field direction ($\varphi = 0^\circ$), with a spacing $d_A = 33.35 \text{ \AA}$ (A, Fig. 23). The correlation length of this reflection (radial extension) was estimated to be ca. $L \sim 190 \text{ \AA}$ (from $\Delta 2\theta$ using the Scherrer formula), with an azimuthal distribution $\Delta\varphi = 40^\circ$ (FWHM).
2. A diffuse reflection in the medium angle part, tilted with respect to the field direction with a maximum intensity at $\varphi = 45^\circ$, with a spacing of $d_B = 18.1 \text{ \AA}$ and a much shorter correlation length, $L' \text{ (B, Fig. 23, } L' \sim 22 \text{ \AA, } \Delta\varphi = 50^\circ)$.
3. A diffuse wide angle reflection, perpendicular to the field direction ($\varphi = 90^\circ$), with a spacing of $d_C = 4.4 \text{ \AA}$ (C, Fig. 23). The correlation length is of the same magnitude as that of the medium reflection B ($L'' \sim 21 \text{ \AA, } \Delta\varphi = 50^\circ$).

According to the authors, both the reflections A and C reflect the nematic ordering of the system: C was assigned to the molten chains, and to the mesogenic side-groups, which are aligned in the same direction of the magnetic field, whilst A corresponds to a short-range lamellar ordering with a mean molecular area of about 500 \AA^2 (cybotactic groups). The periodicity B and the abnormal width of A are specific to the molecular structure of hexakisadduct **28** with respect to classical nematogens, in that the supermolecular organization takes a hierarchical structure, made of 12 lateral side-mesogenic groups which are covalently connected to C_{60} . Thus, this periodicity B is necessarily associated with the position of the C_{60} moieties which should be slightly correlated between two adjacent neighboring layers. This additional ordering within the nematic phase is consistent with the abnormal large correlation length of the reflection A. The absence of any visible signal corresponding to some correlations between the C_{60} moieties within these layers embryos could be attributed to the continuity of the electronic density between the C_{60} embedded by the polarizable parts of the mesogens, as proposed by the model of Fig. 24 constructed by a molecular dynamics (MD) simulation.

4 Self-organization Through Micelles, Nanospheres

Over the past 25 years, conventional phospholipid-based liposomes have been developed for a variety of biomedical applications ranging from targeted drug delivery [112], diagnostic imaging [113], gene therapy [114] to biosensors [115]. Liposomal vesicles have been well studied and a number of commercially available liposomes are readily used today in healthcare applications and mainly as nanotherapeutics [116].

If liposomes that mimic biological membranes typically comprise glycerol-based phospholipids [117], many other functional artificial nanostructures such as polymeric micelles have been synthesized that offer an alternative choice to phospholipid-based liposomes [118]. For instance, carbon-based nanoparticles are of great interest and will be outlined in the following section.

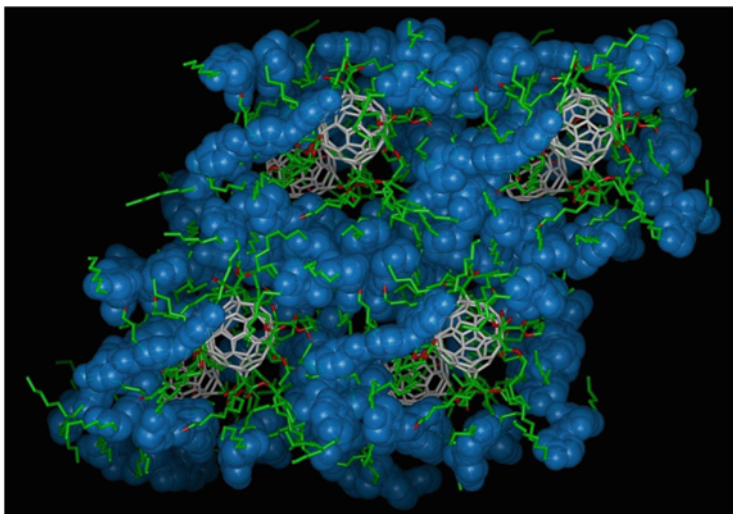
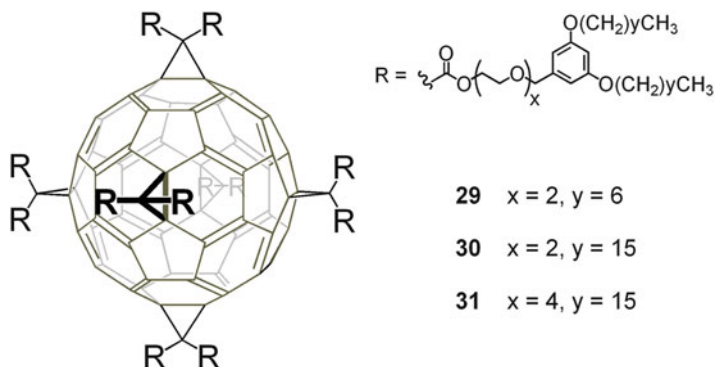


Fig. 24 Molecular modeling picture showing the local organization within the cybotactic groups. View along the direction of the magnetic field showing the hexagonal close packing of the supermolecules

4.1 [6:0] Hexakisadduct

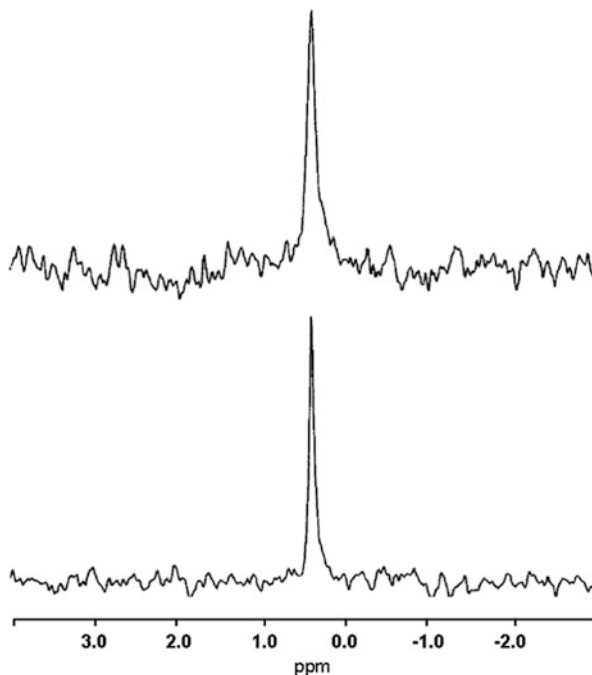
4.1.1 As Unimolecular Micelles

In 2000, A. Hirsch and coworkers [119] reported the synthesis and aggregation behavior of dendrimer-like fullerene-centered hexakisadducts **29**, **30** and **31**.



As the structure of these macromolecules consisted of a polar/hydrophilic cavity (polyethylene glycol layer) surrounded by an outer shell of lipophilic long chains, all compounds exhibited unimolecular micelle properties which were, in particular, probed in terms of ^7Li NMR spectroscopy. The ^7Li NMR signal intensity was dependent on the concentration of the initial solution in dodecane. A lower

Fig. 25 Comparison of the ^7Li NMR spectra of the core-shell macromolecules encapsulated with $\text{LiCl}/\text{H}_2\text{O}$ in dodecane solutions (Top **30**, 17,000 scans, Bottom **31**, 1,020 scans but still a significantly better signal-to-noise ratio)



concentration (0.6 mM instead of 3 mM) would result in a significantly lower signal-to-noise ratio. The LiCl/water intake (average intake was 15 D_2O molecules/ macromolecule **31**) was also shown to be dependent on the size of the ethylene glycol layer in the macromolecular structures. Indeed, when **31** instead of **29** was used under the same experimental conditions, the ^7Li NMR signal at 0.4 ppm became more intense, corresponding to a better signal-to-noise ratio with significantly fewer scans (Fig. 25).

The authors have experienced the use of these unimolecular micelles as nanoreactors tested for the preparation of nanocrystalline silver particles. Interestingly, these particles appear to be uniform in size, each exhibiting a small core of higher electron density, indicating that the particles have their own structures.

4.1.2 Lipofullerenes

In 1997, T. M. Bayerl and collaborators [17] have shown that dipalmitoylphosphatidylcholine (DPPC) self-assembles into multilamellar vesicles (MLVs) in an aqueous medium with a high content of lipophilic hexakisadduct **32** or **33**, while the incorporated lipofullerenes form rod-like fullerene nanoaggregates (several millimeter long, diameters up to 30 nm) within the lecithin bilayers. These intercalated lipofullerenes significantly change the micromechanical properties of the corresponding composite membranes. An increase of the bilayers' bending stiffness was observed, along with a decoupled lateral diffusion of lipids and lipofullerenes within the double layer.

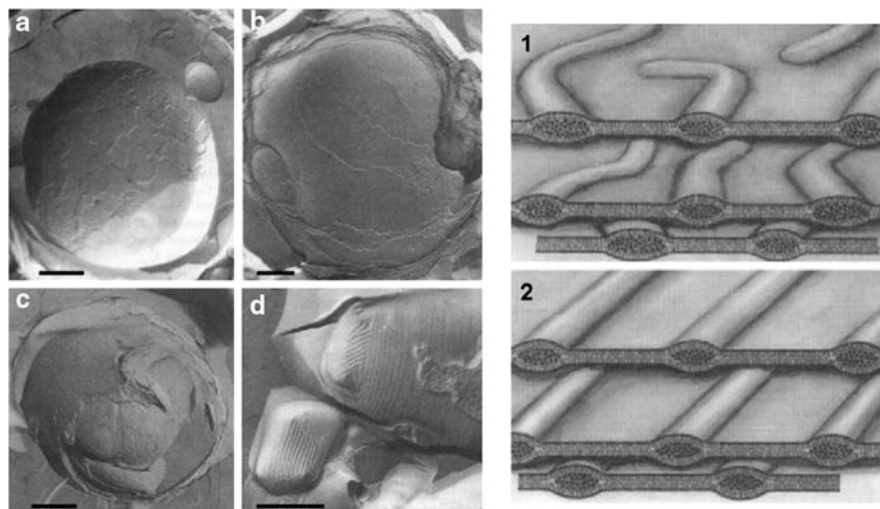
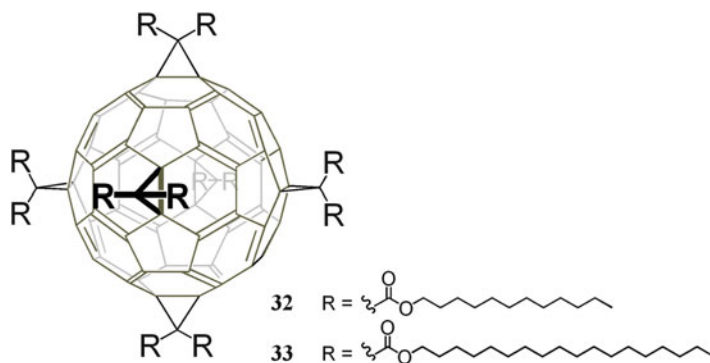


Fig. 26 *Left:* Freeze fracture micrographs of multilamellar vesicles of DPPC- d_{62} without (**a, b**) and with (**c, d**) 15 mol% of **32**. The samples were quenched from either 60°C (**a, c**), 40°C (**b**) or 25°C (**d**). Scale bar 0.5 μm . *Right:* Schematic representation of the proposed arrangement of lipo-fullerenes in a fluid (**1**) and in a gel phase (**2**) bilayer



Freeze fracture electron microscopy was employed to study the morphological changes in the MLVs caused by the lipo-fullerenes. Figure 26 shows freeze fracture replicas of DPPC- d_{62} (completely chain deuterated) MLVs with (Fig. 26c) and without (Fig. 26a) 15 mol% of **32** under fluid phase conditions of the bilayer. In both cases predominantly large MLVs, with diameters up to 5 μm and the typical onion-like structure, were observed. However, while the plain MLVs showed smooth fracture features in the bilayer plane, **32** or **33** caused both the formation of a rod-like surface structure (rods diameter increasing with increasing fullerene concentration) exhibiting long-range ordered superstructures in the gel phase. This spatial correlation was drastically reduced, or even lost, in the fluid phase of the bilayer.

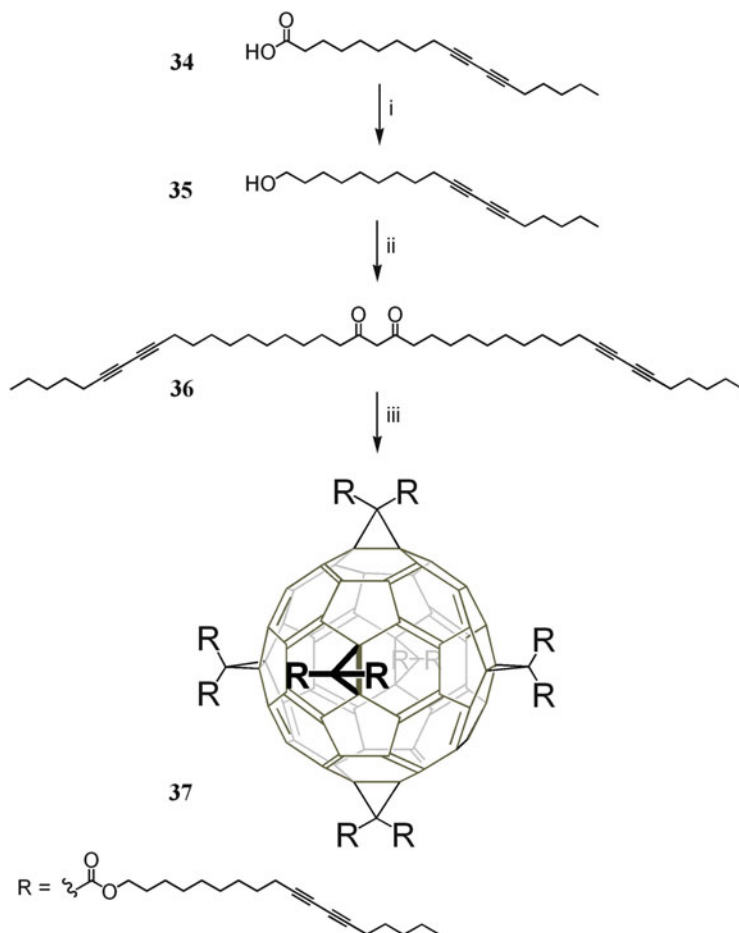


Fig. 27 Synthesis of the polymerizable lipofullerene **37**. (i) LiAlH₄, diethyl ether, (ii) Malonyl dichloride, pyridine, CH₂Cl₂, (iii) C₆₀, DMA, CBr₄, DBU, toluene

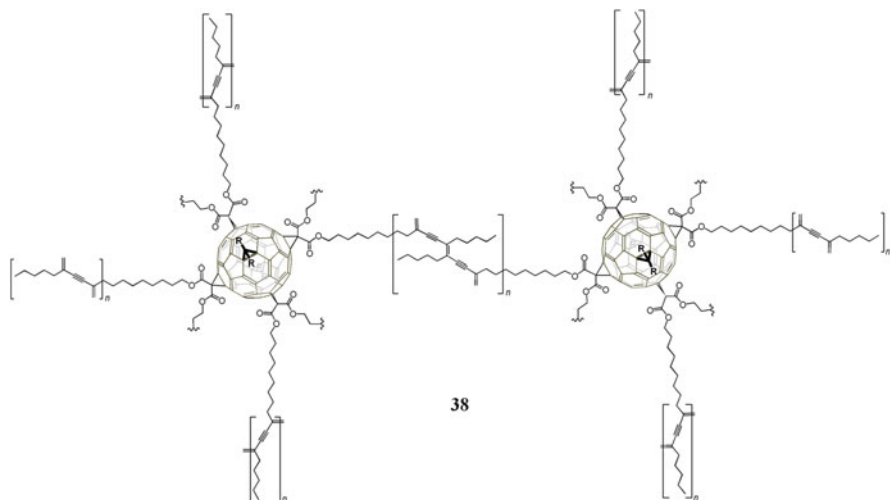
4.1.3 Polymerized Lipofullerenes

In order to achieve the formation of stable nanoarchitectures based on fullerenes, A. Hirsch, T. M. Bayerl, and collaborators reported in 1999 the synthesis of photochemically polymerizable lipofullerene **37** which was hyperfunctionalized by 12 octadecadiynyl side chains [120]. Such hyperfunctionality is of high interest as it ensures the formation of a perfect network in three dimensions Fig. 27.

Photochemical networkability was first studied through irradiation (300 W lamp, 2 days) of a film coating of neat **37** on a glass plate: while monomer **37** melted at 42.8°C, the shiny red-brownish and insoluble photopolymerized product **38** did not exhibit any phase transition up to 280.8°C.

The authors also studied matrix controlled polymerization as **37** was intercalated into multilamellar phospholipid vesicles: from subsequent freeze fracture electron

microscopy analyses they were able to conclude that **37** and its saturated and non-polymerizable analogous **32** and **33** exhibited the same tendency toward self-aggregation.



Photochemical networkability was also studied on an aqueous dispersion of multilamellar DPPC vesicles containing 15 mol% of **37**. After 12 h of UV irradiation (8 W, 256 nm) in the fluid lipid phase (50.8°C) [121] in a quartz glass cuvette, the system showed significant changes: an investigation by freeze fracture electron microscopy showed that the rod-like structures at the MLV surface observed prior to polymerization (Fig. 28a) had vanished. Instead, perfectly spherical objects made up from **38** with diameters ranging from 100 nm up to several millimeter were obtained (Fig. 28b). If the smaller spheres (diameters below 150 nm) were hollow and transparent, the larger beads were filled and their centers impenetrable to the electron beam. Dried nanospheres (Fig. 28c) were then accessible to TEM studies after extraction with organic solvent allowing for DPPC removal.

It is important to mention that isotropic polymerization of **37** could also be performed: indeed, **37** polymerized to spherical polymers in the absence of DPPC, through irradiation of a 5 mg mL⁻¹ decane solution (80 W, 256 nm, room temperature, 30 min). In this case, however, no hollow spheres were found. Such an isotropic polymerization is likely made possible by the spherical shape and the hyperfunctionality of the highly symmetrical T_h hexakisadduct **37**.

4.2 Dendritic [5:1] hexakisadduct

In order to better apprehend the influence of molecular structure on superstructure formation, A. Hirsch and coworkers studied aggregation tendency of dendritic hexakisadducts **1** [50] and **2** [51]. Interestingly, they were able to show that the nature of the chemical linkage to the hydrophobic backbone has a dramatic effect on the

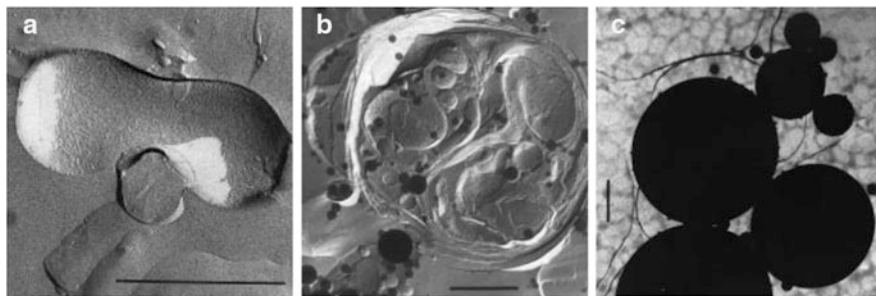


Fig. 28 TEM pictures of 15 mol% lipofullerene **37** in DPPC multilamellar vesicles prior (a) and after (b) UV-initiated polymerization. (c) **38** polymerspheres after extraction of DPPC and subsequent vacuum drying. Scale bar 1 μm

nanoobject formation capacity. Indeed, if the dendritic head groups are connected by ester bonds to the fullerene cage, a variety of aggregation motifs resulted, most notably extensive bilayered liposomal structures [58]. If, however, the hydrophilic dendrons are linked by amide bonds, as in amphiphile **2**, the formation of diverse molecular architectures was definitely more restricted and solely small micelles were formed [122]. This behavior was attributed to the more pronounced rigidity of the amide links, which disfavors such a planar alignment of the amphiphiles as seen in bilayer sheets or liposomes. Additionally, this effect could be controlled by the pH value: indeed, the degree of protonation apparently determines the extent of dendron repulsion and therefore the size of the hydration shell, which results in different degrees of curvature in the aggregates. For example, whereas at neutral pH a mixture of cylindrical and spherical aggregates could be obtained, switching to pH 9.2 led to the exclusive formation of structurally defined spherical micelles with a diameter of about 8.5 nm.

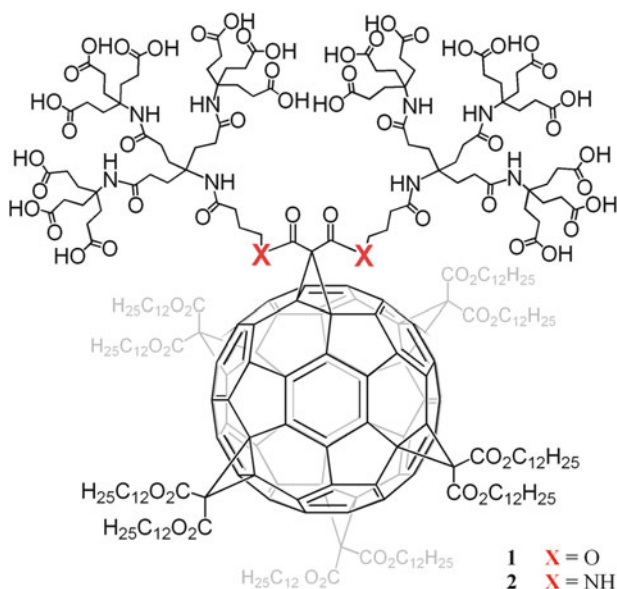
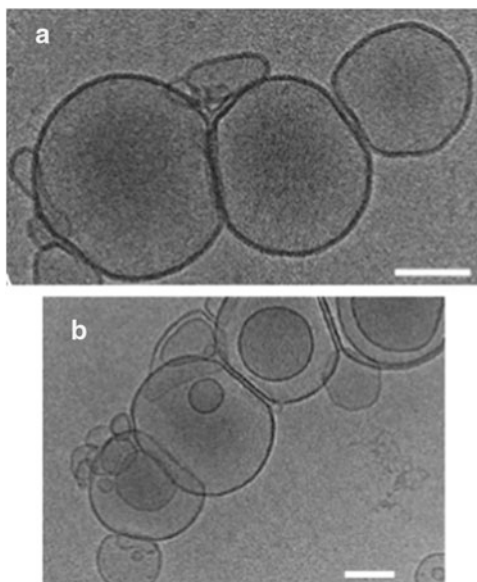


Fig. 29 Representative cryo-electron micrographs of unilamellar (a) and multilamellar (b) buckysomes of **1**. Scale bar 100 nm



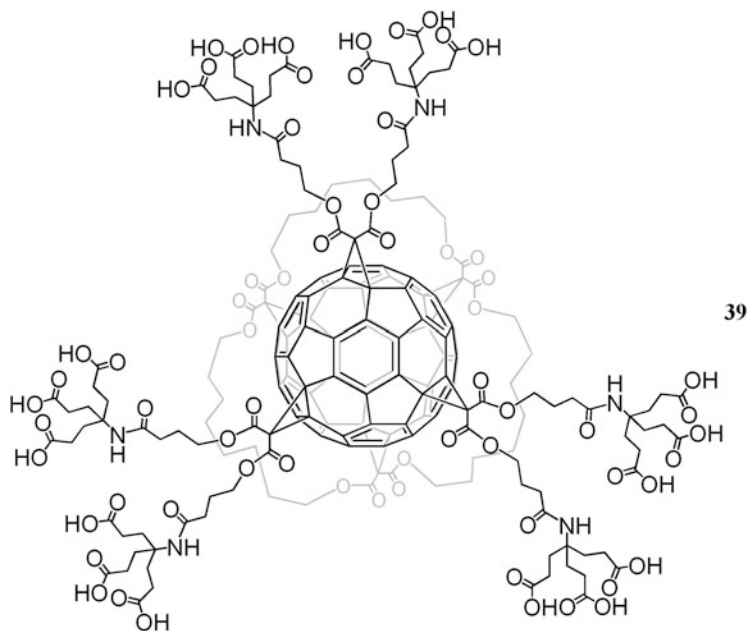
Ester-connected dendritic hexakisadduct **1** was able to self-assemble into both vesicular structures of 50–400 nm and long cylindrical micelles of about 5–200 nm length. The cryo-electron microscopy (cryo-EM) studies clearly confirmed the presence of unilamellar and multilamellar vesicles which bilayer depth was around 6.5 nm (Fig. 29).

The aggregation behavior of **1** was also studied in different physiological buffers using negative-stained TEM (Fig. 30) [123]. In addition to vesicles, other interesting supramolecular structures formed (rod-like elongated or worm-like micelles). For example, in both phosphate citrate (Fig. 30d–f) and phosphate buffer saline (PBS) (Fig. 30g–i) buffers, a mixture of vesicles and cylindrical micelles were observed. In this case, a complex interplay between three major factors, namely (1) the charges on the carboxylic acid groups present in the dendrimer which is controlled by the pH, (2) the solvation process (affected by the solvent), and (3) the methods of preparation (sonication or vortexing).

4.3 Dendritic [3:3] Hexakisadduct

In order to study and understand in more detail the fundamental principles and interdependence between molecular design and supramolecular architecture, A. Hirsch, C. Böttcher and collaborators reported on the aggregation of amphiphilic [3:3]-hexakisadduct **39** (dimensions 2.5–3 nm) [124] which, in contrast to **1** and **2**, contains three instead of one pair of dendritic carboxylate branches, displays G1 instead of G2 dendrons resulting in only three instead of nine carboxylates per

dendritic branch. However, it should be noted that the total number of charges in **39** is still equal to that in compounds **1** and **2**. The hydrophobic part of **39** was also significantly reduced in size by the use of the trifunctional cyclo-[3]-octylmalonate as the addend, which occupies three equatorial sites in the hemisphere opposite to the head groups. The hydrophobic macrocycle covers one hemisphere of the fullerene, whereas the three pairs of Newkome dendrons are located on the opposite side.



The authors were then able to show that by compressing of the hydrophobic part (**39** compared to **1** or **2**) a more densely packed aggregate formed. TEM studies (Fig. 31) showed the formation of uniform spherical objects with a diameter of about 5 nm which is significantly smaller than the diameter of aggregates of **2** (8.5 nm). In summary, the aggregation process of such type of original and complex dendritic amphiphiles appears to be driven by classical parameters such as the effective volume ratio of the hydrophilic and hydrophobic building blocks.

5 Conclusions

The research on organic materials at the nanoscale has shown broad attention over the past few years. The different topics reviewed in this chapter show that [60]fullerene is a versatile 3D rigid nanoscaffold for the development of fascinating materials mainly thanks to its tuneable valency (1 to 6) and regioselective

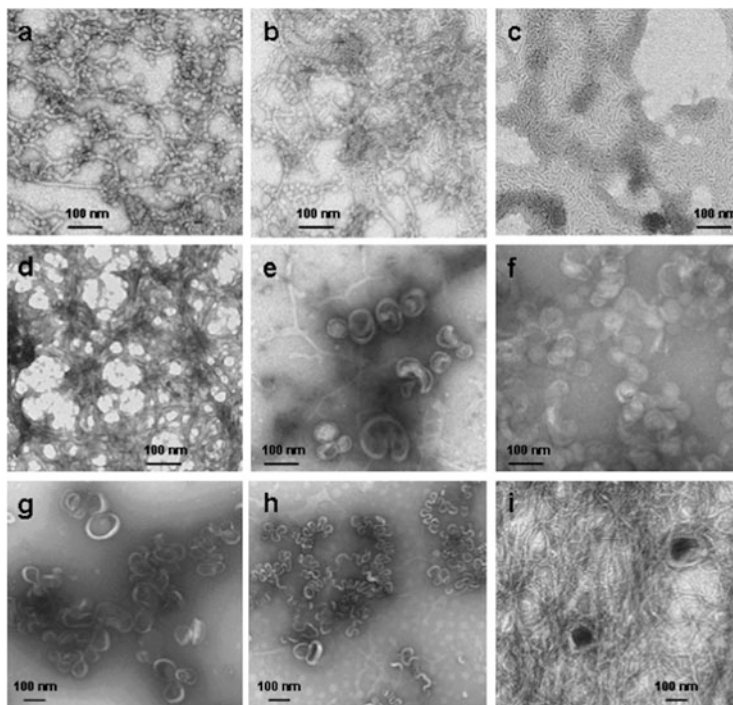


Fig. 30 Uranyl acetate negative-stained transmission electron micrographs of various supramolecular structures of **1**. Combined morphologies of rod-like, branched, and elongated micelles are seen in addition to buckysomes. In (a–c), **1** was prepared in 10 mM HEPES at pH 8.0; in (d–f), **1** was prepared in 0.2 M phosphate–citrate and in (g–i), in PBS buffer at pH 7.4. The concentration of **1** was 2 mg mL^{-1} and preparations were made at room temperature

polyaddition. Indeed, through hexaaddition it is possible to prepare new structural motif not attainable starting from other symmetrical cores such as silsesquioxanes [93–98], metal nanoparticles [99–109] or even from inorganic metallaclusters [125]. It becomes then possible to investigate the physical properties of the materials of a precise orientation of the substituent obtained through regioselective grafting on the sphere and also to correlate the obtained properties with the degree of addition on the carbon sphere. Moreover, it is of interest to rationalize the influence of the functionalization pattern (the number and the position of substituents grafted on the sphere) on the thin film formation capacity or on the liquid-crystalline behavior.

Finally, the last section devoted to nanostructures formation has demonstrated that fundamental investigations on the stability of micelles, vesicles, and other Buckysomes, in particular tolerance to chemical modification and functionalization of the head group, are of high importance as tuneable supramolecular containers will have a considerable impact in the field of nanotechnology (tailor-made transport systems).

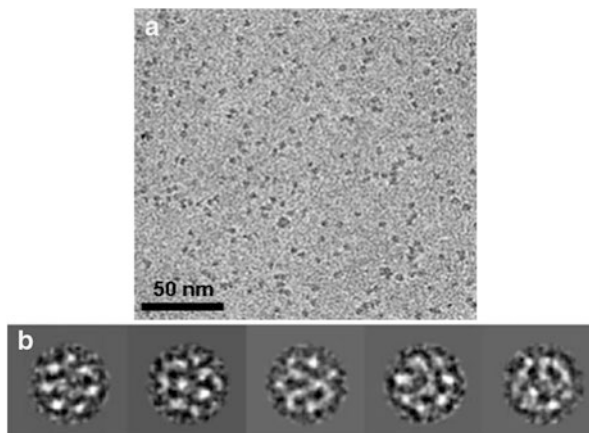


Fig. 31 3D structure determination of aggregates of **39**. (a) Negative staining preparation of **39** showing several tens of individual aggregates. (b) Typical spatial views of micelles (diameter 5 nm) after filtering, multireference alignment, data compression by multivariate statistical analysis, and automatic classification

A further extremely important step and still very open field in the organization of fullerene-based materials concerns endohedrals. Although their chemical properties may considerably differ from those of the empty fullerenes, addressed and regioselective multifunctionalization of magnetic, luminescent, or hydrosoluble carbon nanocages would allow important achievements concerning materials exhibiting original optical, magnetic, and catalytic properties, finding uses in energy, electronic, medicine, and biology. Such compounds shall be nanostructured, be able to self-assemble in multiscale architectures, and intrinsically possess several physicochemical properties making them new materials in essence.

Acknowledgments I would like to thank, in particular, Drs. J.-L. Gallani and B. Donnio for many discussions. I would also like to thank my research colleagues, Drs. B. Heinrich, C. Bourgogne, D. Guillon for their collaboration, and N. Beyer, E. Couzigné and E. Voirin for their technical assistance.

References

1. Guldi DM, Zerbetto F, Georgakilas V, Prato M (2005) *Acc Chem Res* 38:38
2. Kraütler B, Maynollo J (1995) *Angew Chem Int Ed Engl* 34:87
3. Schwenninger R, Müller T, Kraütler B (1997) *J Am Chem Soc* 119:9317
4. Kraütler B, Müller T, Duarte-Ruiz A (2001) *Chem Eur J* 7:3223
5. Isaac L, Haldimann RF, Diederich F (1994) *Angew Chem Int Ed Engl* 33:2339
6. Isaac L, Seiler P, Diederich F (1995) *Angew Chem Int Ed Engl* 34:1466
7. Diederich F, Thilgen C (1996) *Science* 271:317

8. Cardullo F, Isaac L, Diederich F, Gisselbrecht JP, Boudon C, Gross M (1996) *Chem Comm* 797
9. Isaac L, Diederich F, Haldimann RF (1997) *Helv Chim Acta* 80:317
10. Tsukruk VV, Everson MP, Lander LM, Brittain WJ (1996) *Langmuir* 12:3905
11. Akiyama T, Imahori H, Ajawakom A, Sakata Y (1996) *Chem Lett* 907
12. Dominguez O, Echegoyen L, Cunha F, Tao N (1998) *Langmuir* 14:821
13. Kelly KF, Shon YS, Lee TR, Halas N (1999) *J Phys Chem B* 103:8639
14. Enger O, Nuesch F, Fibbioli M, Echegoyen L, Preysch E, Diederich F (2000) *J Mater Chem* 10:2231
15. Imahori H, Norieda H, Yamada H, Nishimura Y, Yamazaki I, Sakata Y, Fukuzumi S (2001) *J Am Chem Soc* 123:100
16. Hirayama D, Takimiya K, Aso Y, Otsubo T, Hasobe T, Yamada H, Imahori H, Fukuzumi S, Sakata Y (2002) *J Am Chem Soc* 124:532
17. Hetzer M, Bayerl S, Camps X, Vostrowsky O, Hirsch A, Bayerl TM (1997) *Adv Mater* 9:913
18. Nakashima N, Nonaka Y, Nakanishi T, Sagara T, Murakami HJ (1998) *Phys Chem B* 102:7328
19. Nakashima N, Tokunaga T, Nakanishi T, Murakami H, Sagara T (1998) *Angew Chem Int Ed* 37:2671
20. Hetzer M, Karakatsanis P, Casalta H, Hirsch A, Camps X, Vostrowski O, Bayerl TM (2000) *J Phys Chem A* 7:1766
21. Nakashima N, Sakai M, Murakami H, Sagara T, Wakahara T, Akasaka TJ (2002) *Phys Chem B* 106:3523
22. Obeng YS, Bard AJ (1991) *J Am Chem Soc* 113:6279
23. Bulhoes LOS, Obeng YS, Bard AJ (1993) *Chem Mater* 5:110
24. Matsumoto M, Tachibana H, Azumi R, Tanaka M, Nakamura T, Yunome G, Abe M, Yamago S, Nakamura E (1995) *Langmuir* 11:660
25. Jonas U, Cardullo F, Belik P, Diederich F, Gügel A, Harth E, Herrmann A, Isaacs L, Müllen K, Ringsdorf H, Thilgen C, Uhlmann P, Vasella A, Waldruff CAA, Walter M (1995) *Chem Eur J* 1:243
26. Wang S, Leblanc RM, Arias F, Echegoyen L (1997) *Langmuir* 13:1672
27. Guldi DM, Maggini M, Mondini S, Guérin F, Fendler JH (2000) *Langmuir* 16:1311
28. Chen K, Caldwell WB, Mirkin CA (1993) *J Am Chem Soc* 115:1193
29. Kitajima N, Komatsuzaki H, Hikichi S, Osawa M, Morooka Y (1994) *J Am Chem Soc* 116:11596
30. Yamada H, Imahori H, Fukuzumi S (2002) *J Mater Chem* 12:2034
31. Wei TX, Zhai J, Ge JH, Gan LB, Huang CH, Luo GB, Ying LM, Liu TT, Zhao XS (1999) *Appl Surf Sci* 151:153
32. Hernandez MP, Monroy F, Ortega F, Rubio RG (2001) *Langmuir* 17:3317
33. Noworyta K, Kuran P, Nantsis EA, Bilewicz R, Dunsch L, Kutner W (2001) *Synth Metals* 123:157
34. Gallani JL, Felder D, Guillon D, Heinrich B, Nierengarten JF (2002) *Langmuir* 18:2908
35. Mouri E, Nakanishi T, Nakashima N, Matsuoka H (2002) *Langmuir* 18:10042
36. Metzger RM, Baldwin JW, Shumate WJ, Peterson IR, Mani P, Mankey GJ, Morris T, Szulczewski G, Bosi S, Prato M, Comito A, Rubin Y (2003) *J Phys Chem B* 107:1021
37. Conoci S, Guldi DM, Nardis S, Paolesse R, Kordatos K, Prato M, Ricciardi G, Vicente MGH, Zilbermann I, Valli L (2004) *Chem Eur J* 10:6523
38. Tang Z, Padmawar PA, Canteenwala T, Gao Y, Watkins E, Majewski J, Chiang LY, Wang HL (2006) *Langmuir* 22:5366
39. Cardinali F, Gallani JL, Schergna S, Maggini M, Nierengarten JF (2005) *Tetrahedron Lett* 46:2969
40. Cardullo F, Diederich F, Echegoyen L, Habicher T, Jayaraman N, Leblanc RM, Fraser Stoddart J, Wang S (1998) *Langmuir* 14:1955
41. Hirano C, Imae T, Fujima S, Yanagimoto Y, Takaguchi Y (2005) *Langmuir* 21:272

42. Nierengarten JF, Schall C, Nicoud JF, Heinrich B, Guillon D (1998) *Tetrahedron Lett* 39:5747
43. Felder D, Gutiérrez Nava M, del Pilar CM, Eckert JF, Luccisano M, Schall C, Masson P, Gallani JL, Heinrich B, Guillon D, Nierengarten JF (2002) *Helv Chim Acta* 85:288
44. Felder D, del Pilar CM, Gallani JL, Guillon D, Nierengarten JF, Chuard T, Deschenaux R (2001) *Helv Chim Acta* 84:1119
45. Felder D, Gallani JL, Guillon D, Heinrich B, Nicoud JF, Nierengarten JF (2000) *Angew Chem Int Ed* 39:201
46. Nierengarten JF, Eckert JF, Rio Y, del Pilar CM, Gallani JL, Guillon D (2001) *J Am Chem Soc* 123:9743
47. Zhang S, Rio Y, Cardinali F, Bourgogne C, Gallani JL, Nierengarten JF (2003) *J Org Chem* 68:9787
48. Nakamura T, Tachibana H, Yamura M, Matsumoto M, Azumi R, Tanaka M, Kawabata Y (1992) *Langmuir* 8:4
49. Wang P, Shamsuzzoha M, Wu SL, Lee WJ, Metzger RM (1992) *J Phys Chem* 96:9025
50. Maierhofer AP, Brettreich M, Burghardt S, Vostrowsky O, Hirsch A, Langridge S, Bayerl TM (2000) *Langmuir* 16:8884
51. Burghardt S, Hirsch A, Medard N, Kachfhe RA, Aussere D, Valignat MP, Gallani JL (2005) *Langmuir* 21:7540
52. Gao Y, Tang Z, Watkins E, Majewski J, Wang HL (2005) *Langmuir* 21:1416
53. Felder-Flesch D, Bourgogne C, Gallani JL, Guillon D (2005) *Tetrahedron Lett* 46:6507
54. Hartnagel U, Hirsch A, Felder-Flesch D, Gallani JL, Bourgogne C (2008) *J Exp Nanosci* 3:229
55. Pauluth D, Geelhaar T (1997) *Nachr Chem Tech Lab* 45:9
56. Imahori H, Fukuzumi S (2004) *Adv Funct Mater* 14:525
57. Prato M (1999) In: Hirsch A (ed) *Fullerenes and related structures*. Springer, Heidelberg
58. Brettreich M, Burghardt S, Böttcher C, Bayerl TM, Bayerl S, Hirsch A (2000) *Angew Chem Int Ed* 39:1845
59. Wudl F (2002) *J Mater Chem* 12:1959
60. Chuard T, Deschenaux R (2002) *J Mater Chem* 12:1944
61. Braun M, Hartnagel U, Ravanelli E, Schade B, Böttcher C, Vostrowsky O, Hirsch A (2004) *Eur J Org Chem* 1983
62. Kimura M, Saito K, Ohta K, Hanabusa K, Shirai H, Kobayashi N (2002) *J Am Chem Soc* 124:5274
63. Felder D, Heinrich B, Guillon D, Nicoud JF, Nierengarten JF (2000) *Chem Eur J* 6:3501
64. Bushby RJ, Hamley IW, Liu Q, Lozman OR, Lydon JE (2005) *J Mater Chem* 15:4429
65. Chuard T, Deschenaux R (1996) *Helv Chim Acta* 79:736
66. Even M, Heinrich B, Guillon D, Guldi DM, Prato M, Deschenaux R (2001) *Chem Eur J* 7:2595
67. Allard E, Oswald F, Donnio B, Guillon D, Delgado JL, Langa F, Deschenaux R (2005) *Org Lett* 7:383
68. Campidelli S, Deschenaux R, Eckert J-F, Guillon D, Nierengarten J-F (2002) *Chem Commun* 656
69. Campidelli S, Vasquez E, Milic D, Prato M, Barbera J, Guldi DM, Marcaccio M, Paolucci D, Paolucci F, Deschenaux R (2004) *J Mater Chem* 14:1266
70. Campidelli S, Lenoble J, Barbera J, Paolucci F, Marcaccio M, Paolucci D, Deschenaux R (2005) *Macromolecules* 38:7915
71. Lenoble J, Maringa N, Campidelli S, Donnio B, Guillon D, Deschenaux R (2006) *Org Lett* 8:1851
72. Deschenaux R, Even M, Guillon D (1998) *Chem Commun* 5:537
73. Hetzer M, Gutberlet T, Brown MF, Camps X, Vostrowsky O, Schönberger H, Hirsch A, Bayerl TM (1999) *J Phys Chem A* 103:637
74. Dardel B, Deschenaux R, Even M, Serrano E (1999) *Macromolecules* 32:5193

75. Dardel B, Guillon D, Heinrich B, Deschenaux R (2001) *J Mater Chem* 11:2814
76. Campidelli S, Deschenaux R (2001) *Helv Chim Acta* 84:589
77. Guillon D, Nierengarten JF, Gallani JL, Eckert JF, Rio Y, del Pilar CM, Dardel R, Deschenaux R (2003) *Macromol Symp* 192:63
78. Tirelli N, Cardullo F, Habicher T, Suter UW, Diederich F (2000) *J Chem Soc Perkin Trans* 2:193
79. Campidelli S, Eng C, Saez IM, Goodby JW, Deschenaux R (2003) *Chem Commun* 1520
80. Felder-Flesch D, Rupnicki L, Bourgogne C, Donnio B, Guillon D (2006) *J Mater Chem* 16:304
81. Chuard T, Deschenaux R, Hirsch A, Schönberger H (1999) *Chem Commun* 2103
82. Sawamura M, Kawai K, Matsuo Y, Kanie K, Kato T, Nakamura E (2002) *Nature* 419:702
83. Nakamura E, Isobe H (2003) *Acc Chem Res* 36:807
84. Matsuo Y, Muramatsu A, Hamasaki R, Mizoshita N, Kato T, Nakamura E (2004) *J Am Chem Soc* 126:432
85. Gottis S, Kopp C, Allard E, Deschenaux R (2007) *Helv Chim Acta* 90:957
86. Merkel K, Kocot A, Mehl GH, Meyer T (2004) *J Chem Phys* 121:5012
87. Frigoli M, Mehl GH (2004) *Eur J Org Chem* 3:636
88. Tajber L, Kocot A, Vij JK, Merkel K, Kalewska-Rejda J, Mehl GH, Elsasser R, Goodby JW, Veith M (2002) *Macromolecules* 35:8601
89. Alvarez R, Mehl GH (2005) *Mol Cryst Liq Cryst* 439:2125
90. Merkel K, Kocot A, Vij JK, Korlacki R, Mehl GH, Meyer T (2004) *Phys Rev Lett* 93:237801
91. Frigoli M, Mehl GH (2004) *Chem Commun* 2040
92. Shepperson KJ, Meyer T, Mehl GH (2004) *Mol Cryst Liq Cryst* 41:1227
93. Mehl GH, Goodby JW (1996) *Angew Chem Int Ed Engl* 35:2641
94. Goodby JW, Mehl GH, Saez IM, Tuffin RP, Mackenzie G, Auzély-Velty R, Benvegna T, Plusquellec D (1998) *Chem Commun* 2057
95. Mehl GH, Saez IM (1999) *Appl Organomet Chem* 13:261
96. Saez IM, Goodby JW (2001) *J Mater Chem* 11:2845
97. Saez IM, Goodby JW, Richardson RM (2001) *Chem Eur J* 7:2758
98. Saez IM, Goodby JW (2005) *J Mater Chem* 15:26
99. Cseh L, Mehl GH (2006) *J Am Chem Soc* 128:13376
100. Qi H, Hegmann TJ (2006) *Mater Chem* 16:4197
101. Hegmann T, Qi H, Marx VM (2007) *J Inorg Organomet Polym Mater* 17:483
102. Marx VM, Girgis H, Heiney PA, Hegmann TJ (2008) *Mater Chem* 18:2983
103. Qi H, Hegmann T (2008) *Adv Funct Mater* 18:212
104. Qi H, Kinkead B, Marx VN, Zhang HR, Hegmann T (2009) *Chem Phys Chem* 10:1211
105. Frein S, Boudon J, Vonlanthen M, Scharf T, Barbera J, Süß-Fink G, Bürgi T, Deschenaux R (2008) *Helv Chim Acta* 91:2321
106. Donnio B, García-Vázquez P, Gallani JL, Guillon D, Terazzi E (2007) *Adv Mater* 19:3534
107. Zeng X, Liu F, Fowler AG, Ungar G, Cseh L, Mehl GH, Macdonald JE (2009) *Adv Mater* 21:1746
108. Demortière A, Buathong S, Pichon B, Panissod P, Guillon D, Bégin-Colin S, Donnio B (2010) *Small* 6:1341
109. Donnio B, Derory A, Terazzi E, Drillon M, Guillon D, Gallani JL (2010) *Soft Matter* 6:965
110. Campidelli S, Brandmüller T, Hirsch A, Saez IM, Goodby JW, Deschenaux R (2006) *Chem Commun* 4282
111. Mamlouk H, Heinrich B, Bourgogne C, Donnio B, Guillon D, Felder-Flesch D (2007) *J Mater Chem* 17:2199
112. Freeman AI, Mayhew E (1986) *Cancer* 58:573
113. Seltzer SE (1989) *Radiology* 171:19
114. Lasic DD, Papahadjopoulos D (1995) *Science* 267:1275
115. Tien HT, Salamon Z, Ottova A (1991) *Crit Rev Biomed Eng* 18:323
116. Ferrari M (2005) *Nat Rev Cancer* 5:161

117. Litman BJ (1973) *Biochemistry* 12:2545
118. Nishiyama N, Kataoka K (2006) *Pharmacol Ther* 112:630
119. Fu K, Kitaygorodskiy A, Sun YP (2000) *Chem Mater* 12:2073
120. Hetzer M, Clausen-Schaumann H, Bayerl S, Bayerl TM, Camps X, Vostrowsky O, Hirsch A (1999) *Angew Chem Int Ed* 38:1962
121. Hetzer M, Bayerl S, Bayerl TM, Camps X, Vostrowsky O, Hirsch A (1997) In: Kuzmany H, Fink J, Mehring M, Roth S (eds) *Molecular nanostructures*. World Scientific, New York, USA
122. Burghardt S, Hirsch A, Schade B, Ludwig K, Böttcher C (2005) *Angew Chem Int Ed Engl* 44:2976
123. Partha R, Lacjey M, Hirsch A, Ward Casscells S, Conyers JL (2007) *J Nanobiotech* 5:6
124. Schade B, Ludwig K, Böttcher C, Hartnagel U, Hirsch A (2007) *Angew Chem Int Ed* 46:4393
125. Terazzi E, Bourgogne C, Welter R, Gallani JL, Guillon D, Rogez G, Donnio B (2008) *Angew Chem Int Ed* 47:490

Dual Role of Phthalocyanines in Carbon Nanostructure-Based Organic Photovoltaics

Andrés de la Escosura, Olga Trukhina, and Tomás Torres

Abstract Organic solar cells are based on the photoinduced separation of charges at donor–acceptor interfaces and on the transport of these charges to the electrodes through *n*-type and *p*-type materials. Carbon nanostructures, such as fullerenes and carbon nanotubes, are considered to be the most effective electron-acceptors, and their use is widely spread. Besides, proper electron-donor and light-harvesting molecules are also fundamental for organic photovoltaics. Phthalocyanines are excellent candidates to play the dual role of *p*-type materials and antennas. Moreover, their structural and synthetic versatility allows them to act as donors or acceptors depending on their counterpart materials in the device. Herein, such functional dualities will be reviewed with regard to the use of phthalocyanines in donor/acceptor systems for photovoltaic devices.

Keywords Carbon nanotubes · Fullerenes · Organic solar cells · Photoinduced electron transfer · Phthalocyanines · Supramolecular organization

Contents

1	Introduction	146
2	Basic Principles of Organic Solar Cells	148
3	Phthalocyanines as Electron-Donor Photoactive Materials	149
4	Carbon Nanostructures as Electron-Acceptor Materials	150

A. de la Escosura
Departamento de Química Orgánica, Facultad de Ciencias, Universidad Autónoma de Madrid,
Cantoblanco, 28049 Madrid, Spain

O. Trukhina and T. Torres (✉)
Departamento de Química Orgánica, Facultad de Ciencias, Universidad Autónoma de Madrid,
Cantoblanco, 28049 Madrid, Spain

IMDEA-Nanociencia, Cantoblanco, 28049 Madrid, Spain
e-mail: tomas.torres@uam.es

5	(Sub)Phthalocyanine/Fullerene Donor/Acceptor Systems	151
5.1	Covalent (Sub)Phthalocyanine–Fullerene Ensembles	152
5.2	Self-Assembly and Supramolecular Organization of (Sub) Phthalocyanine–Fullerene Ensembles	160
5.3	(Sub)Phthalocyanine/Fullerene-Based Organic Solar Cells	166
6	Phthalocyanine/Carbon Nanotube Donor/Acceptor Systems	171
6.1	Covalent Attachment of Pcs to Carbon Nanotubes	172
6.2	Non-Covalent Interactions Between Pcs and Carbon Nanotubes	174
7	(Sub)Phthalocyanines as Electron-Acceptor Photoactive Materials	176
8	Conclusions	183
	References	183

1 Introduction

One of the main objectives in the twenty-first century is to develop environmentally friendly renewable energies such as solar power. Organic solar cells (OSCs) have shown to be promising candidates in the search for efficient and cheap alternatives to the well-established but expensive silicon-based solar cells [1, 2]. Organic photovoltaics, which convert sunlight into electricity within thin films of organic semiconductors, have been the subject of active research for more than 20 years. In 1986, Tang reported the fabrication of an OSC with power conversion efficiency (PCE) of ~1% [3]. The key innovation that allowed exceeding the efficiency of most devices at that time consisted in the introduction of a donor–acceptor (DA) interface between two layers of organic semiconductors. Many improvements of this concept have been achieved since then by employing different organic molecules and polymers and by developing more sophisticated device architectures. As a consequence, OSCs with PCEs as high as 5–7% can be produced nowadays, and conversion efficiencies of 10% are estimated to be necessary for the commercial exploitation of OSCs in the near future [4–6].

A number of material classes are employed as either electron-donors or acceptors. Organic chromophores such as perylene bisimide (PBI) derivatives and carbon nanostructures such as *fullerenes* and *carbon nanotubes* (CNTs) are the most widely used acceptors, while π -conjugated polymers, porphyrins (Pors), and phthalocyanines (Pcs) are usually the donors (Fig. 1) [7]. The major advantage of polymeric (or plastic) solar cells is their easy processing by spin-casting from solution [8]. They present, however, some drawbacks related to the phase behavior of π -conjugated polymers in blends. Their limited miscibility often produces segregation into large domains of the donor and acceptor components, which in turn affects the overall device efficiency. Moreover, the mechanisms by which charges are generated and transported in these cells are not yet well understood. In this respect, replacing π -conjugated polymers by small organic molecules represents several advantages [9]: (1) a precisely defined chemical structure enables to establish relationships between material structure and the device performance; (2) charge-carriers' mobility is normally higher in molecular materials than in polymers; and (3) the high absorption coefficients of many organic dyes in the

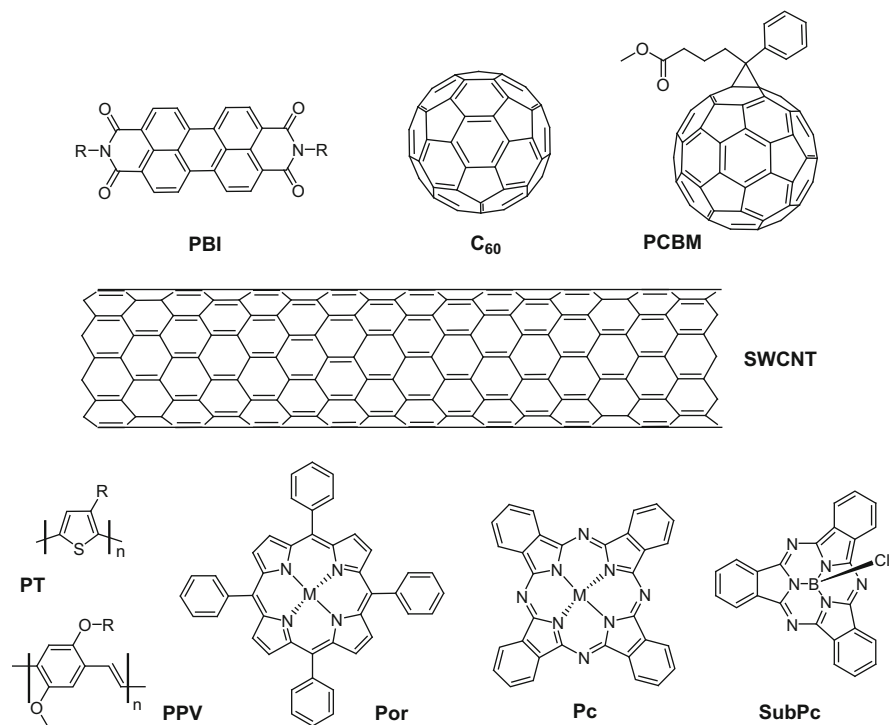


Fig. 1 Molecular structures of some of the most common materials used in OSCs

visible/near-infrared region permits reducing the thickness of the active layer, thus facilitating the transport of charges to the contact electrodes.

Among the donor chromophores that can be used for the construction of OSCs, Pcs [10–12] have been the preferred choice due to their intense optical absorption and rich redox chemistry [13–16]. Pcs are thermally and chemically stable compounds, with extinction coefficient values over $1 \times 10^5 \text{ M}^{-1} \text{ cm}^{-1}$ in the red/near-infrared region. In addition, these macrocycles are synthetically very versatile: more than 70 different atoms can be introduced in their central cavity, and a variety of axial and/or peripheral substituents have been incorporated in their structure. These modifications allow tuning the physical properties of Pc derivatives. Subphthalocyanines (SubPcs), which are lower Pc analogues with a cone-shaped aromatic surface and a boron atom in the macrocycle cavity, have also been utilized in DA systems for the harvest of light and its conversion into a useful form of energy.

Herein, we intend to review the most significant examples of DA (photovoltaic) systems where (Sub)Pcs play the function of antennas and electron-donors, while carbon nanostructures are the electron-acceptors. These DA systems lead, in solution, to long-lived charge-separated (CS) states, while when incorporated in heterojunction devices they are able to generate photocurrent from sunlight. The 3D arrangement of the photoactive units determines important processes such as

light absorption, exciton diffusion, charge separation, and charge-carrier mobility. The efficiency of these processes will be discussed in relation to the PCEs obtained in (Sub)Pc-based OSCs. The role of (Sub)Pcs as electron-acceptor materials will also be examined.

2 Basic Principles of Organic Solar Cells

In contrast to silicon solar cells, where charge-carriers are created directly from photons absorbed by the inorganic semiconductor, the absorption of light in OSCs leads to the formation of excitons (i.e., Coulombically bounded electron-hole pairs) due to the low dielectric constant of organic materials [17–20]. In order to produce charges, excitons must be dissociated by an electric field of sufficient intensity. That is the reason why a critical issue in OSCs is the occurrence of a heterojunction between electron-donor and electron-acceptor materials. It is the energy offset between the HOMO of the donor and the LUMO of the acceptor that actually provides the driving force for exciton dissociation.

There are two categories of device architectures: the planar heterojunction (PHJ) [3], with two successively deposited films of donor and acceptor materials, typically small molecules; and the bulk heterojunction (BHJ) [21, 22], where the two materials, either small molecules or polymers, form an interpenetrating DA interface with a much larger area than that of the PHJ. The main limitation to the performance of PHJs is the short exciton diffusion length in organic materials (10–20 nm). This inherent aspect of organic matter limits the maximum thickness of the active layers and thus the amount of light that the cell can absorb. Intensive research is being carried out on the design and synthesis of new chromophores and polymers with higher extinction coefficients, especially in the near-infrared/infrared region, where the maximum photon flux of the sun is located [23–27].

An efficient way to bypass this obstacle consists in the use of BHJs, where a DA interface is achieved by the intimate intermixing of the components all along the device [8, 9]. Unfortunately, BHJs usually suffer from morphological problems such as phase separation and clustering phenomena. For an efficient transport of holes and electrons through the donor and acceptor phases, respectively, a truly bicontinuous network is required. The adequate morphology of BHJs is achieved, in the case of polymeric solar cells, by simple processing techniques from solution. This is clearly an advantage, since the production of flexible, low-cost, and large-area devices is potentially possible. In contrast, co-evaporation is commonly used to prepare blends of small molecules, pursuing the enhancement of their inherently low charge transport ability by the consecution of a proper 3D arrangement in the crystalline state. Multilayer configurations, in which the active blend is sandwiched between the layers of pure donor and acceptor, are used for the same reason.

For any of the two possible device configurations, photocurrent is generated through a cascade of four steps: (1) exciton formation by the absorption of light, (2) exciton diffusion, (3) exciton dissociation at the DA interface, and (4) charge-carrier transport towards the electrodes. The efficiency of any of these steps has an

influence on the current-voltage ($I-V$) curve of the device. The PCE, defined as the percentage of input power that is converted from light into electric power at the operating point where the device produces the maximum power, is the most important parameter to characterize the cell performance. Two other key parameters are the open-circuit voltage (V_{OC}) (i.e., the voltage when the current density in the device is zero) and the short-circuit current (J_{SC}) (i.e., the current density when the voltage across the device is zero). Obviously, the cell does not produce power at any of these two points, but V_{OC} and J_{SC} are useful indicators of the maximum current and voltage that the system can produce under illumination. The short-circuit current is directly related, among other factors, to the amount of light that can be absorbed by the photoactive material, while the open-circuit voltage is correlated with the difference between the HOMO of the donor and the LUMO of the acceptor. Any aspect of the device that exerts a positive effect on the amount of photons absorbed by the active layer, and/or on the HOMO-LUMO energy gap of the DA system, will ultimately lead to an improved PCE of the photovoltaic cell. This implies a contradiction, though. Reducing the energy band-gap of the DA heterojunction allows absorbing more light from the solar spectrum but at the same time reduces the open-circuit voltage [28]. More research must then be done in order to properly design new DA systems with fine-tuned optical and redox characteristics.

3 Phthalocyanines as Electron-Donor Photoactive Materials

Pcs and related compounds are benchmark materials for organic photovoltaics [13–16]. The important place that (Sub)Pcs occupy in this field owns much to their dual ability to function as absorbers of photons and electron-donors. Pcs absorb light very efficiently in the spectral region of the maximum solar flux (at ca. 700 nm, Fig. 2). Once photoexcited, they transfer electrons to any electron-acceptor, provided that it has adequately featured energetic levels and is in close proximity to the Pc molecules. Additionally, Pcs are thermally stable compounds and present, when organized in cofacial stacks, longer exciton diffusion lengths (ca. 30 nm) and higher charge-carrier mobility than their Por homologues. All these properties have made Pcs cornerstone building blocks in both dye-sensitized solar cells and all-organic photovoltaic devices.

Most of the success of Pcs in organic photovoltaics has been based on the use non-substituted Pcs. The solubility of these compounds in organic solvents is very low, and they have a strong tendency to aggregate. Because a solution processing cannot be applied to the preparation of non-substituted Pc thin films, vapor deposition techniques are generally used, increasing the cost of the devices and thus reducing their commercial interest.

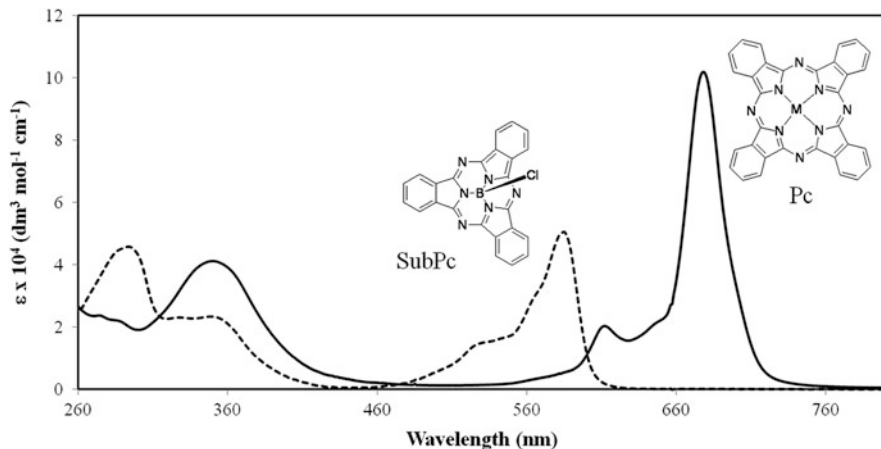


Fig. 2 Typical UV-Vis spectra of Pcs (*solid line*) and SubPcs (*dashed line*)

(Sub)Pcs functionalized with solubilizing axial and/or peripheral substituents are not stable enough for the application of high-vacuum vapor deposition. Efficient solar cells based on solution-processed (Sub)Pcs are still scarce, yet the available synthetic toolbox of organic chemistry allows integrating (Sub)Pcs in a wide number of DA covalent dyads, multicomponent arrays, polymers, dendrimers, and so on. This type of DA ensembles have not met for the moment the required features to be successfully applied in OSCs, but they are excellent artificial photosynthetic models, the study of which is providing a fundamental insight into the factors involved in electron transfer.

The possible functionalization of (Sub)Pcs with different kinds of organic substituents also confers them the ability to self-organize into supramolecular architectures, especially because of their extended aromatic surface. Controlling the nanoscopic, non-covalent arrangement of these macrocycles within the active layer of solar cells certainly enables more efficient charge separation, improved charge transport properties and better overall device performances. After all, supramolecular organization is one of the bases for which photosynthesis approaches optimal efficiencies in the conversion of sunlight into useful chemical energy. (Sub)Pcs are in place to substitute photosynthetic chromophores in artificial mimics of this extraordinary natural process.

4 Carbon Nanostructures as Electron-Acceptor Materials

Among the electron-acceptor units employed in organic photovoltaics, carbon nanostructures such as fullerenes and CNTs have a particular relevance. In 1992, Sariciftci and coworkers reported that photoexciting a mixture of C_{60} and

MEH-PPV (i.e., a poly-*p*-phenylenevinylene derivative) results in an ultrafast highly efficient photoinduced electron transfer (PET) [29]. Furthermore, the CS state in this system presented a very long lifetime, as a consequence of the delocalization of positive and negative charges across the polymeric and fullerene phases, respectively. The efficient transport and collection of charge-carriers at the electrodes could explain the high PCE obtained for this photovoltaic device [30].

Since then, fullerenes have gained a great popularity in the field of OSCs. Fullerenes are extraordinary electron-acceptors, owing to their low LUMO level, small reorganization energy, and very slow charge recombination in electron transfer processes [31–42]. As a matter of fact, soluble C₆₀ derivatives such as [6,6]-phenyl-C₆₁butyric acid methyl ester (PCBM) have been crucial for the development of solution-processed solar cells [43]. The spherical geometry of C₆₀ is also appropriate for charge transport in disordered media, by means of isotropic electron transport through 3D percolation.

The synthetic methodologies developed nowadays for the modification of fullerenes are very broad, involving a number of reaction types such as hydrogenation, nucleophilic and electrophilic additions, pericyclic reactions, and oxidations [41]. In recent years, fullerenes different than C₆₀ (e.g., endohedral fullerenes and fullerene cages with various sizes and symmetries) are being extensively investigated. This synthetic toolbox offers a wide number of building blocks for which the optical and electronic properties, and the supramolecular behavior, can be tuned. The incorporation of (Sub)Pcs in DA systems with fullerene derivatives can be beneficial for both planar and bulk heterojunctions. (Sub)Pcs can also be used as dopants to improve the light-harvesting capacity of polymer/fullerene blends.

CNTs [44–46] consist of graphene sheets rolled up into a cylinder and provide continuous electronic states in their conduction band for collecting electrons. These electrons can be transported under nearly ideal conditions along the nanotube 1D axis. Thus, the combination of CNTs with a light-harvesting/electron-donor material emerges as a promising possibility for electron transfer studies [47]. Different electro- and photoactive units can be attached to the nanotube surface, through either covalent or non-covalent bonds [48]. The occurrence of PET in these assemblies can be used to generate current in photovoltaic cells. Together with the excellent mechanical properties of CNTs, these hybrid nanostructures open broad perspectives for solar energy conversion [49].

5 (Sub)Phthalocyanine/Fullerene Donor/Acceptor Systems

A fundamental process involved in the generation of electricity from sunlight in OSCs is exciton dissociation at a DA interface. Understanding how the nature, arrangement, and electronic coupling of the donor and acceptor photoactive units affect the efficiency of this process is very important for device performance

optimization [50]. In this respect, natural photosynthetic systems are excellent models to orientate research towards artificial photovoltaic cells [51, 52].

The complexity of natural photosynthesis is clearly beyond synthetic chemistry. It is entirely plausible, however, that simple photosynthetic functions such as PET [53, 54] can be mimicked by relatively simple artificial systems [55–60]. In their most simple version, these systems can be represented as D–(L)–A ensembles, where L means the spacer that connects the donor and acceptor moieties through covalent bonds or non-covalent interactions. Upon light absorption by the chromophores, energy is stored in an excited state of the system. Several exergonic intercomponent events may subsequently take place, the most important ones being energy and electron transfer. In the latter, excitation energy induces the generation of a CS state which may ultimately be employed to perform useful work.

Among the most common photoactive building blocks, the light-harvesting and electron-donor properties of (Sub)Pcs make them perfectly suited to be integrated in light energy converters [61]. Besides, fullerenes have occupied in the last two decades a central position as acceptor components for electron transfer studies [37]. The interactions between these two types of photoactive units (i.e., (Sub)Pcs and fullerenes) can be studied in both covalent and non-covalent ensembles in solution, as well as in thin film photovoltaic devices.

5.1 Covalent (Sub)Phthalocyanine–Fullerene Ensembles

Most classical molecular designs for the synthesis and optimization of artificial photosynthetic systems are based on the covalent linkage of chromophoric electron-donor and acceptor units. The nature of the spacer in these systems is very important for controlling the distance, orientation, and electronic coupling between the photoactive building blocks. The first report on a covalent Pc–C₆₀ dyad appeared in 1997, when Hanack, Hirsch, and coworkers reported the synthesis of what they called a “green fullerene” [62, 63]. This dyad was prepared through a Diels–Alder reaction and owed its intense green color to the Pc moiety. Since then, a large number of covalent Pc–C₆₀ systems have been described.

The synthetic strategies commonly employed for the preparation of Pc–C₆₀ dyads are based on the consecutive utilization of three types of methodologies [13, 15]. First, low-symmetry Pcs are synthesized by condensation of different phthalonitrile derivatives (Fig. 3), generating a statistical mixture of all the possible macrocycles. A proper choice of the reactant ratios and the chromatographic workup are crucial to attain optimal yields of the desired compound. Asymmetrically substituted Pcs can be subsequently functionalized by a variety of simple organic and metal-catalyzed coupling reactions (Fig. 3) [64]. In the final step, the electrophilicity of fullerenes, due to their electronegativity and high strain energy, is usually exploited. Among the rich chemistry of fullerenes, the most characteristic reactions for their incorporation into covalent DA ensembles are nucleophilic additions (such as the Bingel reaction) and the 1,3-dipolar cycloaddition of

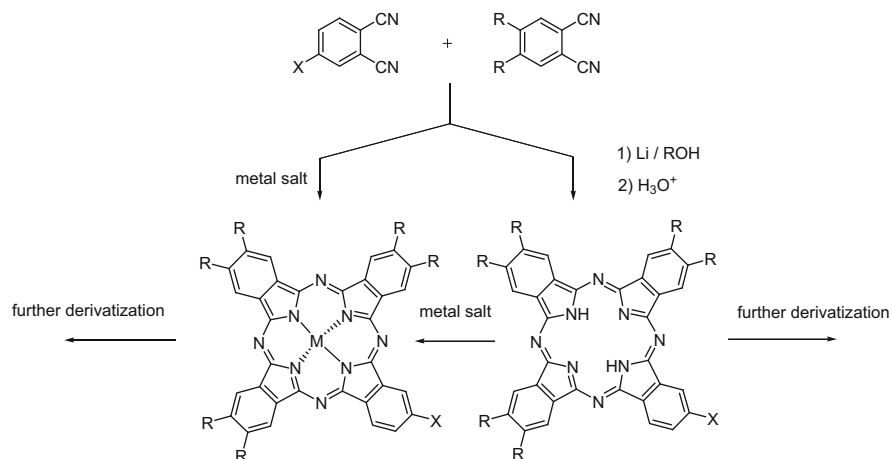


Fig. 3 Preparation of asymmetrically substituted Pcs by statistical condensation, and further derivatization by simple organic and metal-catalyzed transformations

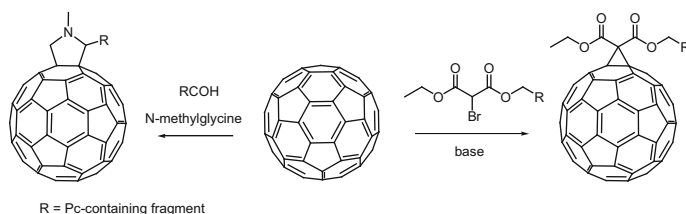


Fig. 4 Schematic representation of the Prato (*left*) and Bingel (*right*) reactions, commonly used for the linkage of Pcs and C₆₀

azomethine ylides (also known as the Prato reaction) to the fullerenes double bonds (Fig. 4).

The first Pc–C₆₀ system whose photophysical behavior was studied in detail is dyad **1** (Fig. 5a) [65, 66]. The UV–Vis spectrum of **1** showed a charge transfer (CT) absorption band at 740 nm, revealing a redistribution of charge density from the electron-donor ZnPc to the electron-acceptor C₆₀. This is a consequence of the direct linkage of both photoactive components. Only another ZnPc–C₆₀ dyad (**2**) (Table 1) has presented similar CT characteristics in its UV–Vis spectrum, as a result of the close proximity between the Pc and fullerene moieties [55–60]. The influence of the proximity and orientation between the photoactive units on their electronic communication has also been studied on dyads similar to **2**, in which the Pc and the fullerene are connected by malonic bridges [70, 71]. For the rest of Pc–C₆₀ conjugates reported up to now, no electronic communication has been observed between the donor and acceptor moieties in the ground state.

The photophysical behavior of Pc–C₆₀ ensembles can be probed by transient absorption measurements (Fig. 5b) [66, 72]. In **1**, for example, upon

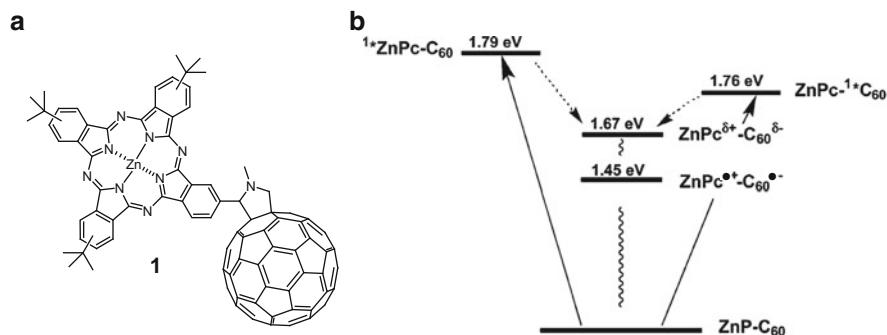


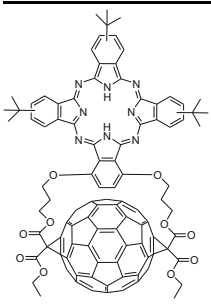
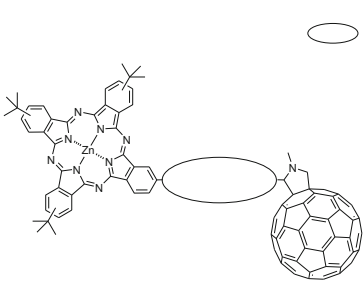
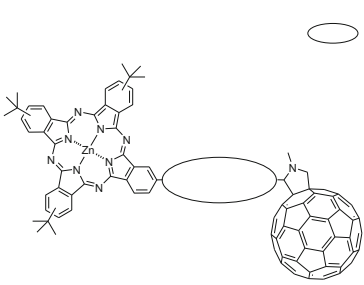
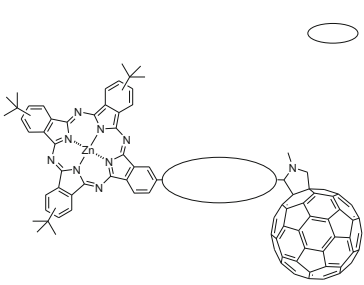
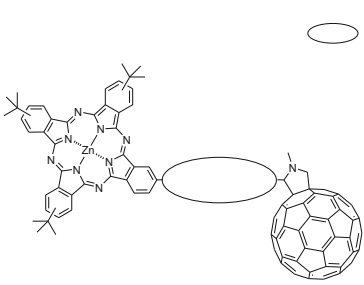
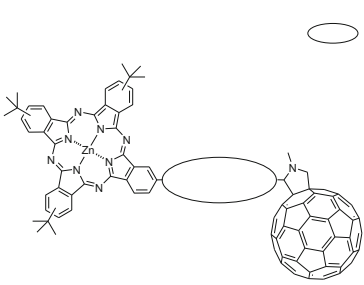
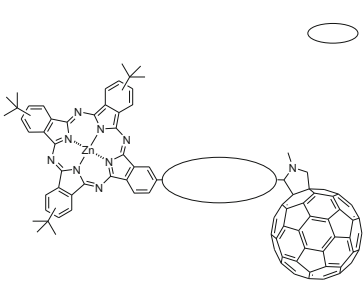
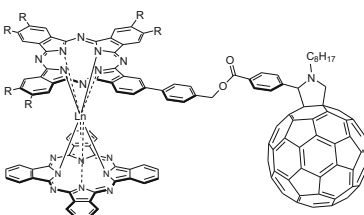
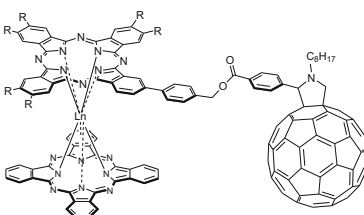
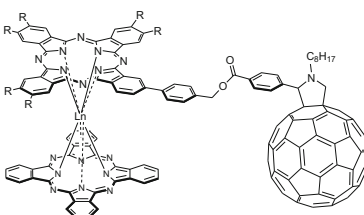
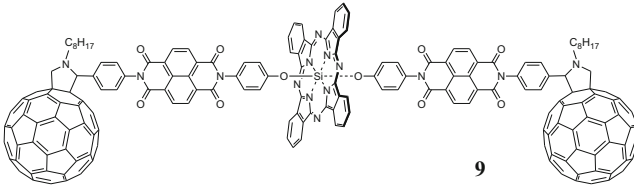
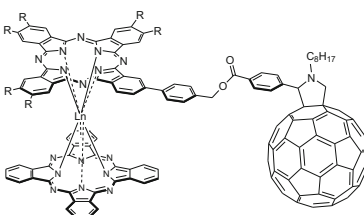
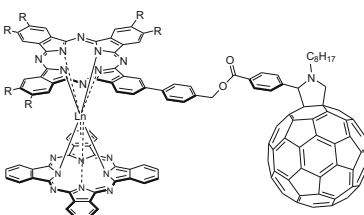
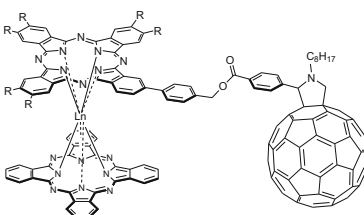
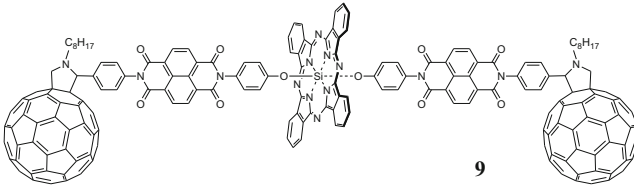
Fig. 5 (a) Molecular structure of the ZnPc–C₆₀ dyad **1**. (b) Energetic levels the ZnPc–C₆₀ dyad **1** when photoexcited in toluene (reprinted with permission from [72], copyright 2004, American Chemical Society)

photoexcitation of the ZnPc unit, its singlet excited state features are observed (i.e., a broad transient maximum at 490 nm, followed by bleaching between 610 and 685 nm). When electron transfer occurs, the ZnPc singlet excited state decays rather quickly, leading to the formation of new transient species. The presence of ZnPc radical cations (ZnPc^{•+}) is hallmarked by transient absorption maxima at 520 and 840 nm, whereas a maximum at 1,000 nm indicates the formation of C₆₀ radical anions (C₆₀^{•-}). The lifetime of the radical ion pair for a certain dyad strongly depends on factors such as the polarity of the solvent, the presence or absence of oxygen, and the nature of the Pc metal center [72]. Moreover, the lifetime of the CS state is usually several orders of magnitude higher in bulk than in solution. This fact has stimulated the utilization of Pc–C₆₀ covalent systems as active materials in photovoltaic devices (see Sect. 5.3) [73, 74].

The influence that the arrangement of Pc and C₆₀ units has on electron transfer dynamics has been studied, at first glance, by comparing the photophysical parameters of ZnPc–C₆₀ dyads with different spacers (Table 1, entries for dyads 1–7) [75, 76]. The lack of a spacer results in the shortest lifetimes observed [72]. Conjugated and rigid saturated hydrocarbon linkers elongate the CS state lifetime by spatial separation of the fullerene and the Pc. Interestingly, the triple bond spacer leads to a longer-lived CS state than the double bond [75, 77, 78]. The longest CS state lifetime from this set of molecules was obtained, however, for the dyad containing [2, 2]paracyclophane [76]. In contrast to classical conjugated connectors, [2,2]paracyclophane can be viewed, in **7**, as a biased double potential well, separated by a tunneling barrier. Linking Pc and C₆₀ moieties to this cyclophane provides the bias, promoting through space electron transfer.

Similar Pc–C₆₀ dyads have been prepared in which the fullerene cage is bigger than C₆₀ (e.g., C₈₀) and contains a trimetallic nitride [79]. Endohedral metallofullerenes present several advantages over empty C₆₀, such as larger extinction coefficients and lower HOMO–LUMO energy gaps [80]. Unfortunately, the corresponding dyads are rather unstable and their synthesis is more complicated

Table 1 CS state lifetimes for some Pc-C₆₀ dyads and multicomponent systems

Compound	Reference	CS lifetime (ps)
	[67]	83 ^a
	[66]	32 ^a
	[75]	1.1 × 10 ⁴ ^b
	[75]	50 ^a
	[75]	1 × 10 ⁴ ^b
	[75]	30 ^a
	[75]	1.4 × 10 ⁴ ^b
	[76]	36 ^a
	[76]	1.4 × 10 ⁴ ^b
	[76]	3.5 × 10 ⁴ ^b
	[76]	330 ^a
	[81]	4.58 × 10 ⁵ ^b
	[81]	>3 × 10 ³ ^b
	[85]	1.0 × 10 ³ ^a
	[90]	2.0 × 10 ⁵ ^a
SiPc-(C ₆₀) ₈ dendrimer (molecular structure not shown)	[90]	1.6 × 10 ⁵ ^b
ZnPc/C ₆₀ polynorbornenes (structures shown in Fig. 10)	[91]	12.6 × 10 ⁶ ^c

^aBenzonitrile^bToluene^c*o*-DCB

than for their C₆₀-based counterparts. Analogously, Pc macrocycles with different architectures have been used instead of planar Pcs. In dyads **8a–c**, where a double-decker lanthanide bisphthalocyaninato complex is connected to C₆₀, CS states with lifetimes of ca. 3 ns in toluene were observed by transient absorption experiments (Table 1), but only when the fullerene moiety was photoexcited [81]. The excitation of the Pc unit in these systems leads to very short lifetimes of the singlet excited state, enabling deactivation mechanisms different than electron transfer.

With the aim of improving the light-harvesting process, molecules containing multiple Pc and C₆₀ units have been designed and synthesized [82–84]. Photophysical studies on these systems showed that the presence of more than one donor and/or acceptor moieties does not necessarily elongate the lifetime of the radical ion pair. The order of chromophores in multicomponent DA molecules is crucial to stabilize the CS state, as revealed by the long-lived radical ion pair in pentad **9** (Table 1) [85–88].

The strategy of using multicomponent systems has reached its maximum level of complexity with the preparation of dendrimers and polymers containing Pcs and C₆₀ as building blocks. The formation of silicon–oxygen bonds has been used to obtain SiPc-based dendrimeric systems (Table 1) [89, 90]. Increasing the dendron generation (i.e., the number of fullerene fragments from 2 to 8), a stabilization of the CS state was observed, probably due to electron migration among the C₆₀ subunits. This phenomenon illustrates what needs to occur when electrons and holes are dissociated at the DA interface of BHJs.

On the other hand, the Grubbs methodology for ring-opening metathesis polymerization was used to prepare copolymers from different ratios of the adequately substituted Pc- and C₆₀-norbornene monomers [91]. Fluorescence studies on these systems indicated that the quenching of the Pc fluorescence within the polymer depends on the relative content of Pcs and C₆₀. It is noteworthy that the lifetime of the photoinduced radical ion pair in the copolymers is in the scale of microseconds (Table 1). A rational explanation for these results implies delocalizing effects when going from Pc/fullerene molecular ensembles to polymeric frameworks.

Besides Pcs, SubPcs have also received much attention with regard to the construction of DA conjugates [92–95]. SubPcs present several advantages: (1) they are excellent antennas (500–700 nm) with excitation energies above 2.0 eV and possess relatively low reorganization energies [96]. Moreover, SubPcs do not aggregate due to their conical shape and are strong fluorophores with high quantum yields. In summary, these lower homologues of Pcs are versatile and stable chromophores suitable for nonlinear optics [97–100], light-emitting diodes [101], anion sensing [102–104], and photovoltaic applications [15].

The preparation of SubPc-based DA systems has been possible thanks to the development of novel synthetic methodologies in the last decade [105, 106]. The SubPc core can be functionalized both at the periphery and axial positions. The strategy employed for the asymmetric modification of periphery is based on the statistical condensation of different phthalonitrile derivatives [107], as for the case of Pcs, and subsequent organic or metal-catalyzed coupling reactions [64]. The substitution of axially connected ligands is nevertheless more advantageous

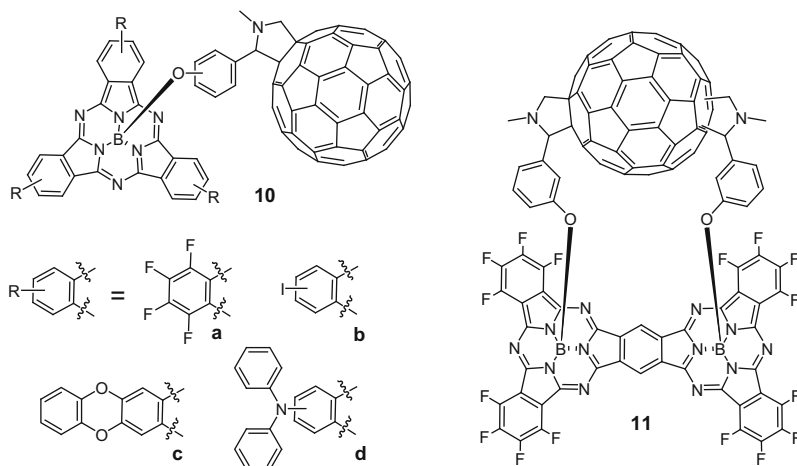


Fig. 6 Examples of SubPc–C₆₀ (**10**) and fused SubPc–C₆₀ (**11**) molecular systems

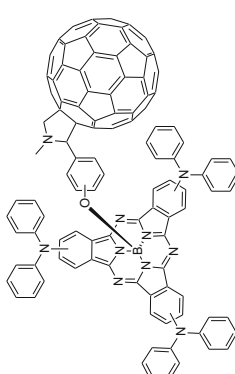
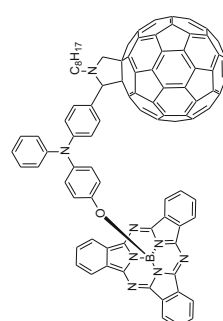
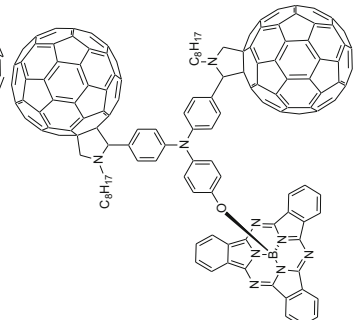
because the SubPc benzene rings remain unchanged and the macrocycle preserves its electronic characteristics [108].

By using these methodologies, a series of SubPc–C₆₀ (**10**) and fused SubPc–C₆₀ (**11**) molecular systems have been prepared (Fig. 6). The latter required a complex synthetic strategy that involved both axial and asymmetric peripheral derivatization of the SubPc ring. Unfortunately, only a complex cascade of photoinduced energy transfer events has been revealed for **11**, with no evidence of electron transfer. The absence of PET in this case may be explained by the extended conjugation of fused SubPcs, which lowers the HOMO–LUMO energy gap and, consequently, the energy of the singlet excited state [109].

The interplay between energy and electron transfer in SubPc–C₆₀ dyads depends on the nature of the groups at the periphery of the macrocycle [110, 111] and on the spatial orientation of the photoactive moieties, as revealed by photophysical experiments with **10**-type dyads. The SubPc and C₆₀ units are connected in these derivatives through the axial position by phenoxy group. The specificity of electronic communication between the two components was examined by varying the substitution mode (*ortho*, *meta*, or *para*) in the benzene ring of the spacer. Electrochemical and photophysical measurements revealed that *m*-dyads are the easiest to get reduced and oxidized, indicating their smaller HOMO–LUMO gap [112, 113]. *m*-Dyads **10a–d**, with electron-withdrawing (*m*-**10a**, *m*-**10b**) or electron-donating (*m*-**10c**, *m*-**10d**) substituents, were studied. The photoactive components in these dyads are electronically communicated through bonds instead of through space. Furthermore, increasing the electron-donating character of the SubPc unit lowers the energy of the radical pair state and determines that electron transfer dominates over energy transfer.

The longest CS lifetimes were obtained for dyads with diphenylamine groups in peripheral positions (**10d**) [112] or an axial triphenylamine (TPA) spacer connecting the SubPc with one (**12**) or two (**13**) fullerene buckyballs (Table 2)

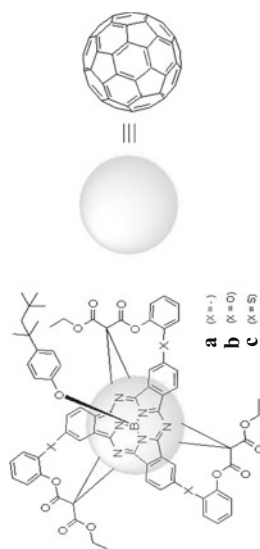
Table 2 CS state lifetimes for some SubPc-C₆₀ dyads and multicomponent systems

Compound	Reference	CS lifetime (ps)
	[112]	73 ^a 133 ^b 4.05 × 10 ³ ^c 111 ^a 192 ^b 4.35 × 10 ³ ^c 235 ^a 319 ^b >5 × 10 ³ ^c 6.7 × 10 ⁵ ^a <7 × 10 ³ ^c 4 × 10 ⁵ ^d
<i>m</i> -10d		
<i>p</i> -10d		
12	[114]	
		
13	[114]	1.05 × 10 ⁶ ^a 4.7 × 10 ⁴ ^c
		

97×10^3 ^b

[115]

14

^aBenzonitrile^bTHF^cToluene^dDMF

[114]. In **12**, efficient photoinduced charge separation was observed from the TPA to the SubPc excited state, and subsequently to the C₆₀ moiety, yielding the [SubPc-TPA^{•+}-(C₆₀)^{•-}] radical ion pair with a lifetime of 670 ns in benzonitrile. The CS state was even further stabilized in tetrad **13**, revealing the effect of having two C₆₀ buckyballs instead of one. These results show, as for the case of Pcs, the importance of multicomponent systems for modulating charge separation events. It has also been observed that a rigid connection between the SubPc and C₆₀ building blocks, like in compounds **14a–c**, does not substantially enhance the CS state lifetime (Table 2), despite the exceptional surface complementarities achieved in these adducts [115].

5.2 Self-Assembly and Supramolecular Organization of (Sub)Phthalocyanine–Fullerene Ensembles

It is well known that a major drawback associated with intramolecular electron transfer concerns the rapid back electron transfer (BET) that occurs if the donor and acceptor moieties are in close proximity. Natural photosynthesis teaches us that the achievement of long-lived CS states requires highly organized supramolecular assemblies. The supramolecular strategy to build artificial photosynthetic systems relies on the reversible association between donor and acceptor components, which enables the radical ion pair to split by diffusion of the photoinduced radical ions (Fig. 7). In other words, charge recombination can be retarded by keeping the radical ions distantly isolated. In OSCs, charge separation needs to be optimized. Important lessons about the 3D organizational requirements for OSCs can be learned from the study of supramolecular effects on PET processes at the molecular level.

A variety of biomimetic recognition motifs such as hydrogen bonding, π - π stacking, metal-ligand coordination and electrostatic interactions have been successfully used to engineer the formation of supramolecular Pc/fullerene ensembles. Several examples of supramolecular Pc/C₆₀ systems and their photoinduced CS lifetimes are summarized in Table 3. In general, a comparison with covalently linked Pc-C₆₀ dyads, in which lifetimes several orders of magnitude lower are normally found, shows that these supramolecular architectures are extremely efficient in collecting light and using its energy for charge separation. Threading a dibenzylammonium-fullerene derivative through a Pc-containing dibenzo-24-crown-8 macrocycle, for example, affords reasonably stable pseudorotaxane-like complexes (e.g., **15**) [116] with microsecond-long photoinduced radical ion pairs [117]. Another recognition motif that can be used with the same purpose is a metal-ligand coordination of fullerene-pyridine derivatives and metal Pcs. The most common metal centers utilized are Zn [118–121], Ti [122], and Ru [123]. RuPcs are useful chromophores for OSCs because of the high-lying triplet excited state of ruthenium, which suppresses charge recombination by

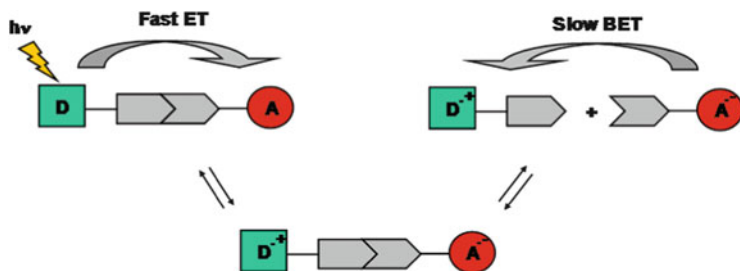


Fig. 7 Schematic representation of the supramolecular strategy to extend the lifetime of CS states by isolation of the photoinduced radical ions

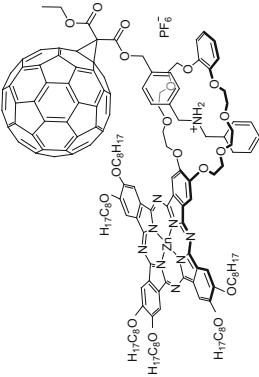
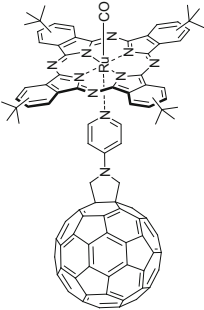
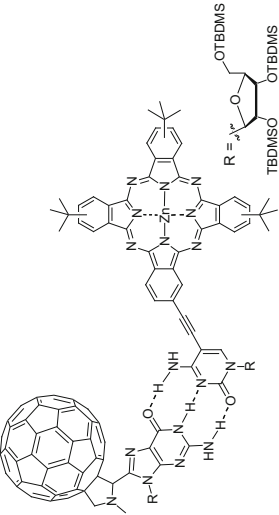
pushing the CS state into the Marcus inverted region (e.g., in dyad **16**). Watson–Crick hydrogen bonding has shown to be less effective for the consecution of long-lived CS states in Pc/ C_{60} systems [124, 125]. Significantly short lifetimes were measured for the radical ion pair formed upon photoexcitation of the Pc unit in dyad **17** (Table 3). The association constant of the complex was very large ($(1.7 \pm 0.7) \times 10^7 \text{ M}^{-1}$), which could explain that BET was not efficiently retarded by the radical ion pair dissociation.

The self-assembly of Pc and fullerene compounds has also been achieved through the use of DA π -stacking interactions between Pc fragments bearing adequate peripheral substituents [126]. The covalent ZnPc- C_{60} dyad **18**, which comprises a Pc unit bearing six butoxy groups and zinc as central metal (Table 3), was designed and synthesized to form stable DA complexes with the electron-acceptor octakis(propylsulfonyl)PdPc **19**. The heteroassociation of both Pc derivatives allowed a substantial stabilization of the CS state. The longer lifetime for the ZnPc $^{\bullet+}$ - $C_{60}^{\bullet-}$ radical ion pair in the complex (i.e., 475 ns) compared to that in the dyad (i.e., 130 ns) can be rationalized by the delocalization of the photoinduced positive charge within the Pc stacks.

In contrast to single mode supramolecular binding, which usually gives flexible supramolecular structures, the use of multiple binding modes results in ensembles of defined distances and orientation between the donor and acceptor entities [127]. Following this concept, a supramolecular tetrad (**20**), constituted by two crown ether-containing ZnPc units, four potassium ions that favor the stacking and two fulleropyrrolidine derivatives, has been reported (Table 3). This tetrad showed a substantially longer lifetime of the photoinduced CS state (i.e., $6.7 \times 10^3 \text{ ns}$) than the related crown ether-based supramolecular ZnPc- C_{60} dyad (i.e., $4.8 \times 10^3 \text{ ns}$) [128]. Self-assembled monoPc/multifullerene DA conjugates have been recently prepared using the same strategy [129] and showed similar charge separation rates as tetrad **20**. In general, photoinduced charge separation is five times faster for these systems than for analogous porphyrin/fullerene ensembles. The advantages of crown ether-based Pc self-assembled systems seem to result from a combination of electronic and topological factors.

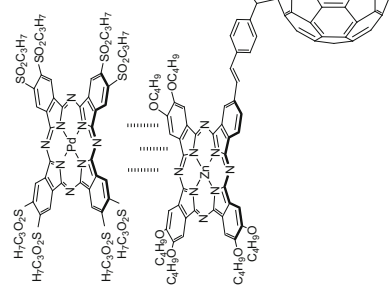
The employment of π -stacking interactions for Pc self-organization could be brought to a major extent by preparing liquid crystals composed of Pc- C_{60} dyads. Long exciton diffusion lengths (ca. 100 nm) and high charge-carrier mobility

Table 3 CS state lifetimes for some (Sub)Pc/C₆₀ supramolecular systems

Compound	Reference	CS lifetime (ps)
	[117]	1.5×10^6 ^a
	[123]	1.5×10^5 ^b 1.7×10^5 ^c
	[125]	3×10^3 ^c

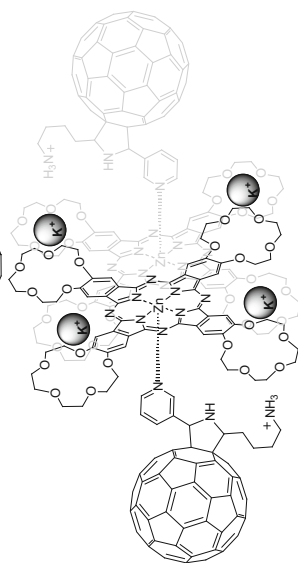
18/19

[126]

 4.8×10^5 d

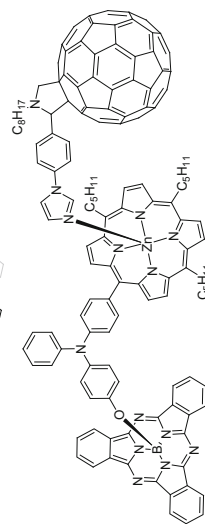
20

[128]

 6.7×10^6 e

21

[133]

 6.6×10^6 c

(continued)

Table 3 (continued)

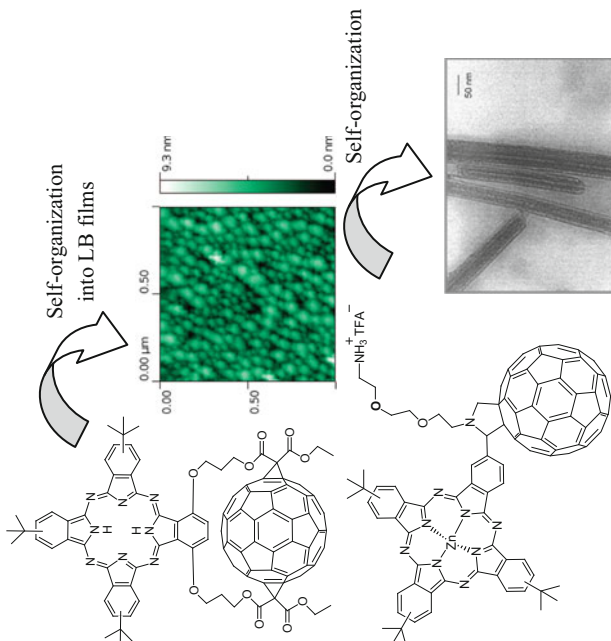
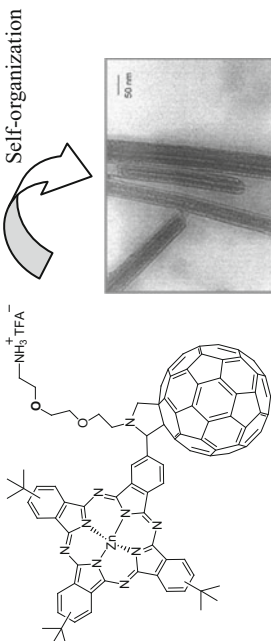
Compound	Reference	CS lifetime (ps)
 <p>Chemical structure of compound 2, a porphyrin derivative with a C₆₀ fullerene cage and a long alkoxy chain. An arrow labeled "Self-organization into LB films" points to an AFM image of the film. The AFM image shows a textured surface with a color scale from 0.00 nm to 9.3 nm. A second arrow labeled "Self-organization" points to a TEM image showing nanorods with a 50 nm scale bar.</p>	[140]	3.3×10^6
 <p>Chemical structure of compound 23, a porphyrin derivative with a C₆₀ fullerene cage and a long alkoxy chain with a trimethylammonium group. An arrow labeled "Self-organization" points to a TEM image showing nanorods with a 50 nm scale bar.</p>	[141]	1.4×10^9 f

Image in row 7 reprinted with permission from [140], copyright 2008, American Chemical Society and the image in row 8 reprinted with permission from [141], copyright 2005, American Chemical Society

^aDichloromethane

^bAnisole

^cToluene

^dTHF

^eBenzonitrile

^fWater



Fig. 8 Representation of side (*left*) and top (*right*) views of the ZINDO/1 optimized geometry of complex **22**, formed by a SubPc cage complexing C₆₀ (adapted with permission from [15], copyright 2010, American Chemical Society)

(ca. 0.5 cm²/V) have been measured in the ordered liquid-crystalline phase of discotic molecules such as triphenylenes, hexabenzocoronenes, hexaazatrinaphthylenes, and Pcs. Hence, these self-organized condensed phases are promising materials for organic photovoltaics. Liquid-crystalline Pcs have been tested as photoactive materials in solar cells [130]. The first example of a mesogenic Pc–C₆₀ dyad contained a Pc unit with three swallowtail alkoxy groups, which was covalently connected to a PCBM moiety [131]. Unfortunately, the synthesis of mesogenic Pc–C₆₀ dyads turns out to be difficult, taking into account the tedious purification of the asymmetrically substituted Pcs necessary as starting compounds. The use of blends in which a mesogenic compound induces mesomorphism to a non-mesogenic one represents an elegant strategy to resolve this problem. In particular, the organization of non-mesogenic Pc–C₆₀ dyads by simply blending with the well-known liquid-crystalline zinc octakis(hexadecylthio)Pc, allowed to overcome the synthetic problems related to the preparation and isolation of mesogenic, asymmetrically substituted Pc derivatives [132].

Very recently, SubPcs also were incorporated into self-assembled supramolecular systems for PET. Fukuzumi et al. reported long-lived CS states for the multicomponent system **21** (Table 3) [133]. To increase the donor ability of the zinc Por (i.e., the primary electron-donor), the electron-rich triphenylamine was attached at its *meso* position, thus lowering the Por oxidation potential. In this system, the SubPc and TPA molecular fragments were used as antennas, transferring their excitation energies to the Por, and subsequently to the fullerene, in a cascade of electron transfer events.

SubPcs substituted with pyridines, on the other hand, have been used for the construction of supramolecular cages [134–136]. The rigid and concave geometry of SubPcs [137] offers a suitable cavity for the complexation of spherical guest molecules such as fullerenes [138]. Evidences for the encapsulation of C₆₀ by a SubPc cage (Fig. 8) was obtained from electrospray mass spectrometry and ¹H NMR spectroscopy. The photophysical properties of complex **22** have unfortunately not been measured so far.

The effect of supramolecular organization on the photophysical properties of Pc–C₆₀ molecular systems has been studied in Langmuir–Blodgett (LB) films of dyad **2** (Table 3) [139, 140]. In solution, the geometrical restrictions imposed by

the double Bingel addition on the fullerene scaffold led to a strong electronic communication in the ground state and to an activationless exciplex and CS state when photoexcited [67, 68]. In the LB film, a notable stabilization of the CS state (i.e., from the picosecond to the microsecond time scale) was observed, probably due to migration of the $\text{ZnPc}^{+\cdot}$ radical cations and $\text{C}_{60}^{\cdot-}$ radical anions to spatially close, homologue units. The same can be concluded from studies carried out with the amphiphilic ZnPc-C_{60} salt **23**, which forms uniformly structured 1D nanotubes in water [141]. Such self-organizational process results in an ultrafast charge separation ($\sim 10^{12} \text{ s}^{-1}$) and an ultraslow charge recombination ($\sim 10^3 \text{ s}^{-1}$), as compared with the photophysical parameters for the same compound in solution. As a consequence, the CS state within the nanotubes presents a lifetime of 1.4 μs . Interestingly, this value is within the time domain typically found in the DA films of BHJ solar cells. These findings teach us an important lesson for the application of Pc/fullerene ensembles in photovoltaic devices: charge separation can be much more efficient if the donor and acceptor units are adequately organized in the solid state.

5.3 (Sub)Phthalocyanine/Fullerene-Based Organic Solar Cells

The fabrication in 1986 of a bilayer solar cell with 1% of efficiency, by using the configuration ITO/CuPc/perylene-3,4,9,10-tetracarboxylic-dibenzimidazole (PTCBI)/Ag [3], marked the starting point of a race towards the PCE target value of 10%, which would in principle permit a commercial use of OSCs [4, 5]. In this respect, there are two possibilities for the increase of PCEs in OSCs: the discovery of new donor and acceptor photoactive materials, and the development of more effective device architectures. Two main types of device configuration have been developed: the PHJ (Fig. 9a) and the BHJ (Fig. 9b); yet along the years other structural designs that combine both concepts have been described (Fig. 9c,d). In this section, we review the most important photovoltaic systems having (Sub)Pcs as antenna and electron-donor materials, and fullerene compounds as electron-acceptors. The discussion will be carried out on the basis of the device architecture type.

5.3.1 PHJ Devices

Some improvements of the initial Tang's device design have been achieved by: (1) the introduction of a blocking layer of bathocuproine (BCP) between the active layer and the cathode [142, 143]; (2) the concept of tandem cell [144, 145], which consists of connecting cells in series; (3) the use of triple heterojunction devices [146]; (4) the introduction of a buffer layer next to the ITO electrode [147, 148]; (5) the chemical modification of the electrodes [149]; and (6) the invention of the so-called inverted solar cells [150–152], where the donor layer is

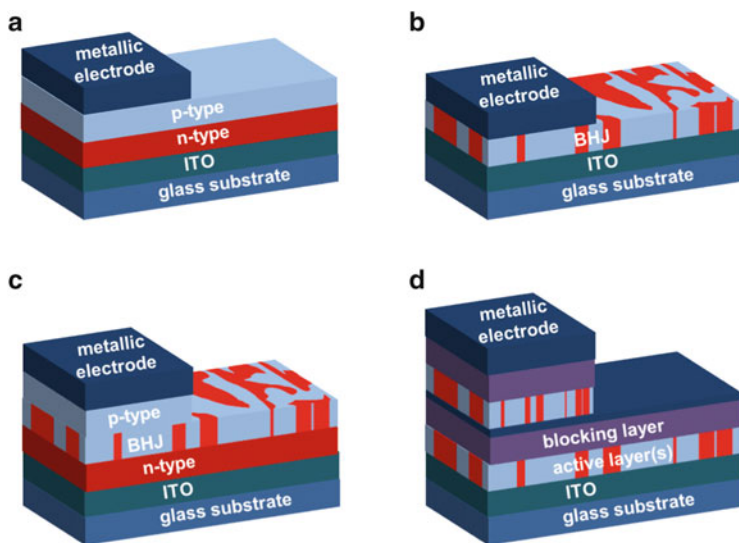


Fig. 9 Schematic representation of different architectures for OSCs: (a) PHJ, (b) BHJ, (c) p-i-n configuration, and (d) tandem cell

placed adjacent to the transparent cathode. Unfortunately, none of these strategies have led to PCEs higher than 2.5% when PCTBI was used as the acceptor material.

Other electron-acceptor materials have been combined with Pcs in PHJ devices. The best results have been obtained when utilizing fullerenes, mainly because of their substantially longer exciton diffusion paths (~40 nm). Non-substituted Pc and C₆₀ derivatives are deposited on the substrate by evaporation under high vacuum. This enables a high crystallinity of the two layers, also ensuring high charge-carrier mobilities. The efficiency of these PHJ devices made of evaporated Pc and C₆₀ can be tuned by varying the metal center of the macrocycle [153]. Several Pcs have been studied, including Fe, Co, Ni, Cu, Zn, Pd, Ru, Sn, Ti, and H₂ as the central metal. Good performances are obtained with ZnPc, CuPc [154], H₂P [155], and PdPc [156–158], while the use of RuPc results in a high series resistance and strong recombination of charges at the DA interface [159]. Pcs with near-infrared absorption (e.g., the non-planar SiPc [160] or TiOPc) [161] have shown more promising results. One of the best PCE values (i.e., 4.2%) was obtained for a solvent-annealed ITO/TiOPc (20 nm)/C₆₀(40 nm)/BCP(10 nm)/Al device [162].

As for the case of solar cells containing PCTBI, the device architecture can also be tailored when C₆₀ is the electron-acceptor material in the cell. Covering the ITO electrode with a thin film of 3,4-polyethylenedioxythiophene:polystyrenesulfonate (PEDOT:PSS) planarizes the rough surface of ITO [154], thus avoiding shorts and leading to a PCE of 4.2% in a small-area device containing CuPc [163]. Another key issue to be tackled in these PHJ devices is the improvement of charge-carrier mobility in the Pc phase [153]. As learned from systems in solution, the packing and arrangement of Pcs in the thin film is very important. This goal has been pursued

either by doping the Pc layer, for instance with pentacene [164], or by introducing additional layers between the photoactive material and the electrodes in single [165, 166] or tandem cells [167]. A device with the configuration ITO/MoOx (5 nm)/PTCDA(1 nm)/ClAlPc(20 nm)/C₆₀(40 nm)/BCP(8 nm)/Al showed a PCE of 3% under simulated AM 1.5G illumination [168]. The role of PTCDA (3,4,9,10-perylenetetracarboxylic acid) in this system was to template the stacking of Pc molecules in perpendicular direction to the electrodes. Other interlayers that have been used with the same purpose are 2,5-bis(4-biphenyl)-bithiophene [169] and PTCDI liquid-crystalline derivatives [130]. Short-circuit currents can also be increased by the incorporation of microcavity structures within the device [170].

SubPcs have also been used as donor materials in combination with fullerenes for the construction of bilayer device architectures [171]. Since SubPcs absorb at shorter wavelengths than Pcs, the cell structure demands thinner layers, in comparison with Pc-based cells, to ensure that light of shorter wavelengths is able to reach the SubPc/C₆₀ interface. The parameter that determines the critical distance to the SubPc/C₆₀ heterojunction over which photoinduced excitons can be harvested has been studied in detail [172]. Exciton diffusion lengths of 28 nm, and a lifetime of 0.3 ns, have been determined by fluorescence quenching experiments with SubPc thin films of 40 nm. Nevertheless, PHJ photovoltaic devices made of SubPcs have not achieved the PCE values typical for Pc-based cells. A device with the structure ITO(100 nm)/SubPc(13 nm)/C₆₀(32.5 nm)/BCP(10 nm)/Al(100 nm) showed, for example, a PCE of 3.0% under 1 sun illumination [173]. In inverted PHJ devices, on the other hand, a maximum PCE of $2.4 \pm 0.2\%$ has been demonstrated [174]. This configuration is promising for its use in opaque and/or flexible substrates.

5.3.2 Co-evaporated Devices

As it has been discussed in Sect. 2, the use of blends of donor and acceptor materials is a widely spread strategy to enlarge the DA interface at which exciton dissociation occurs. These blends can be prepared by co-evaporation, typically for non-derivatized Pcs and fullerenes, or by solution processing, which is frequently used for derivatives of the photoactive components that are soluble in organic solvents. The study of co-evaporated blends in photovoltaic devices started in the 1990s [175, 176], and important efforts have been devoted to the fabrication of devices containing co-evaporated layers of Pcs and *n*-type materials such as PTCDI and fullerene cages. Because the charge transport ability of the blends is still low, the insertion of a mixed layer between thin films of the pure components is a common approach that gives rise to the so-called hybrid planar-mixed heterojunctions.

For instance, efficiencies of 5% have been obtained in a device with the structure ITO/CuPc(10 nm)/Cu(II)Pc:C₆₀(1:1)(33 nm)/C₆₀(10 nm)/BCP(7.5 nm)/Ag [177]. A further increase of PCE up to 5.7% was possible by using of the tandem geometry [178]. Other strategies to enhance the PCEs are (1) the variation of ratios [179] and deposition rates [180] to generate gradients of the donor and acceptor

materials in the blend; (2) the introduction of layers of wide band-gap materials between the blend and the electrodes (i.e., the so-called p–i–n solar cells (Fig. 9c) [181–184], which can also adopt a tandem configuration (Fig. 9d) [185] in order to augment the absorption of light; (3) the use of semitransparent electrodes, for the same reason [186], and (4) the substitution of C₆₀ by C₇₀, which results in ca. 20% increased efficiencies with regard to related devices containing the buckminsterfullerene [187]. More recently, it has been discovered that better charge percolation pathways within the blend can be induced by heating the substrate while the Pc and C₆₀ are being co-evaporated [188]. In this direction, new deposition techniques are being developed as a way to control the nanostructure of the Pc/C₆₀ mixed crystalline layer [189–193].

5.3.3 Small-Molecule Bulk Heterojunction Devices

High-vacuum deposition techniques are very expensive, for which evaporated devices are hardly applicable from a commercial point of view. Utilizing Pc and C₆₀ derivatives that are soluble in organic solvents and therefore can be processed from solution seems in principle a cheaper and more straightforward option. PCBM, the best known C₆₀ derivative, has been used in blends with conjugated organic polymers for almost two decades. Concerning the donor, many Pcs with organic-solubilizing substituents are known and their synthesis is relatively simple. It has been recently suggested that blending fullerenes and phthalocyanine derivatives with different optical band gaps may improve solution-processed BHJ solar cells [194]. Nevertheless, there is only one example where a soluble Pc derivative was blended with PCBM and successively applied in photovoltaic devices. In this work, the authors connected pyridine-functionalized dendritic oligothiophenes to an RuPc bearing bulky organic peripheral groups [195]. The result was a series of supramolecular, non-aggregated Pc/dendron molecules. In BHJs of these systems with PCBM or PC₇₁BM, the best performances were obtained for the first generation complex, showing PCEs of 1% and 1.6%, respectively. These values represent the highest efficiencies reported for Pc-containing BHJ solar cells.

The incorporation of covalently linked Pc–C₆₀ dyads in solar cells could be envisioned as a valuable possibility to avoid macroscopic phase segregation and to ensure efficient charge separation along the entire active layer. The Pc–C₆₀ dyad **1** [73] and triad **24** (Fig. 10, left) [82] have been deposited on a modified ITO electrode (with PEDOT:PSS) by spin-casting from toluene solutions. Their photovoltaic performance was tested, showing very low short-circuit currents and open-circuit voltages. Polynorbornenes **25** (Fig. 10, right), having Pc and C₆₀ units pending from the polymeric backbone, also gave very poor conversions (i.e., 0.07%) when studied in similar devices, even though these polymers had shown microsecond-lived CS states in solution [91]. It seems from these studies that connecting Pc and fullerene moieties in close proximity through a covalent backbone allows efficient charge separation, but the transport of charges to the electrodes is very poor, the overall PCE of the devices being not satisfactory.

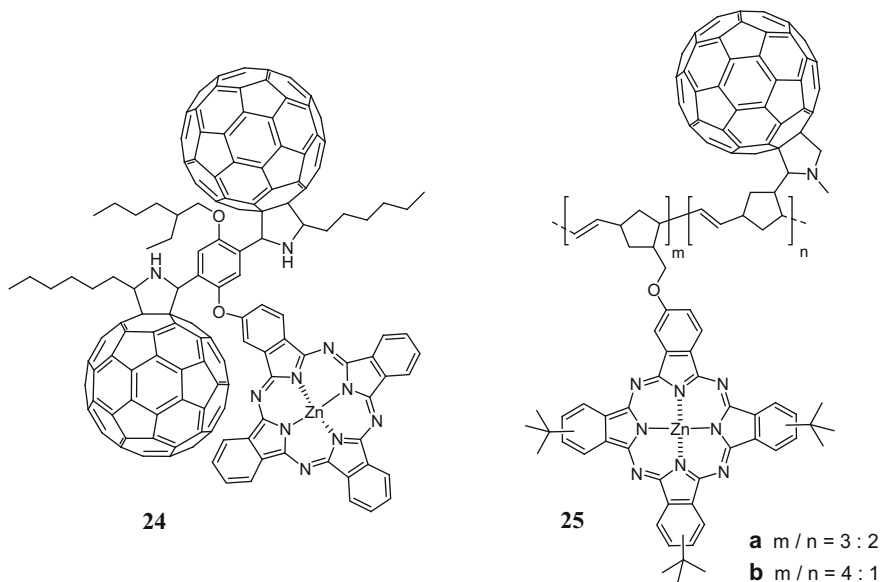


Fig. 10 Molecular structures of the Pc-(C₆₀)₂ triad **24** and polynorbornenes **25**

5.3.4 Polymer-Based BHJ Devices

Finally, the excellent optical properties of Pcs can be used to enhance the absorption of polymer/PCBM BHJs in the near-infrared region. This approach was explored for the first time by adding non-substituted H₂Pc to a C₆₀/MEH-PPV (poly[2-methoxy-5-(2'-ethylhexyloxy)-1,4-phenylenevinylene]) blend, inducing higher V_{OC} and J_{SC} values [196]. Yet the most widely used conjugated polymer in this type of devices is poly-3-hexylthiophene (P3HT) [197–199]. P3HT unfortunately presents some drawbacks [200, 201]: its absorption spectrum is very narrow (300–650 nm), which means that this material can absorb only a limited fraction of the solar photon flux. In addition, the high energy of its HOMO level determines a maximum cell voltage of 0.60–0.65 volts and a significant instability in atmospheric conditions. Low band-gap small molecules such as Pcs can offer solutions to these problems.

For example, in a solar cell composed of P3HT, PCBM, and the peripherally substituted octabutoxy-H₂Pc, blended in a 10:10:1 ratio, maximum internal quantum efficiencies of 40% were observed in the main absorption region of the Pc (i.e., around 700 nm) [202]. Transient laser spectroscopy showed that exciting the Pc molecules results in the formation of a long-lived P3HT⁺/dye/PCBM⁻CS state. Furthermore, a novel concept has been recently proposed to enhance the performance of these devices by charge generation based on long-range energy transfer [203].

The efficiency by which Pcs funnel energy in polymer/fullerene devices increases when aggregation of the Pc is disrupted, as revealed for the case of an SiPc spin-coated in a 10:10:1 ratio with P3HT and PCBM [204]. The silicon atom is

able to axially coordinate two branched hydrocarbon chains (i.e., trihexylsilyl oxide). This avoids aggregation and permits the allocation of SiPc molecules at the P3HT/PCBM interface, giving rise to a PCE of 2.7%. Further PCE enhancement to 4.3% was achieved by multicolored dye sensitization with the same SiPc and the related silicon naphthalocyanine (SiNc) bis(trihexylsilyl oxide) [205]. Inserting the Pc-C₆₀ dyad **1** in a P3HT/C₆₀ bilayer produced a similar effect [74].

Sariciftci has followed another strategy, taking advantage of the supramolecular interaction between a pyridine-containing C₆₀ derivative, which is part of a blend with MDMO-PPV, and the ZnPc molecules of an adjacent layer. A PCE of 2% resulted from this approach [206]. The best performance has been achieved, however, in a tandem cell with its active layers being a solution-processed P3HT/PCBM blend and a CuPc:C₆₀ blend processed by gradient co-evaporation [207]. The two subcells were connected by a transparent, high-work function WO₃ layer. The efficiency of the device was 4.6%, which is close to the sum of efficiencies of the individual subcells. From these studies, the double character of Pcs is revealed: they behave as antennas and also as an intermediate station in the relay of electron transfer events, first from the Pc unit to the fullerene, and later on from the polymer to the Pc.

6 Phthalocyanine/Carbon Nanotube Donor/Acceptor Systems

Besides fullerenes, CNTs [208, 209] can also act as electron-acceptors and possess continuous electronic states for collecting charges when confronted with electron-donor dyes. CNT/Pc conjugates could potentially be used in organic photovoltaics. The formation of CNT/Pc composites is known to improve the inherent photoconductive properties of Pcs. For example, the photoconductivity of metal Pcs (TiOPc [210], CuPc [211] or the sandwich-type europium phthalocyaninate (HErPc₂) [212]) doped with modified multiwalled carbon nanotubes (MWCNTs) as a charge generating material is higher than that of the pristine Pcs. It was expected then that the direct chemical modification of CNTs with electron-donors may afford better electronic communication between the photoactive units.

There are two general approaches for the functionalization of CNTs: (1) by covalent attachment of organic molecules to the CNT open edges or side walls and (2) through non-covalent π - π interactions with the nanotube wall. While the covalent approach leads to more stable structures, the non-covalent one presents the advantage that the electronic structure of the nanotube remains almost unaffected. Both strategies have been used to attach ferrocene [213, 214], tetrathiafulvalene [215, 216] and Pors [217–226] to CNTs, and to subsequently generate photocurrent in photoelectrochemical cells [227–229].

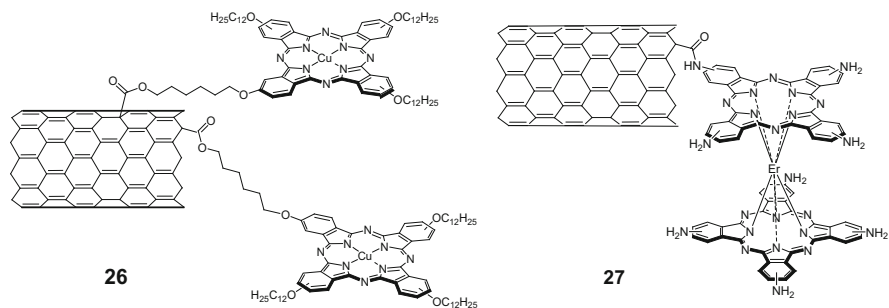


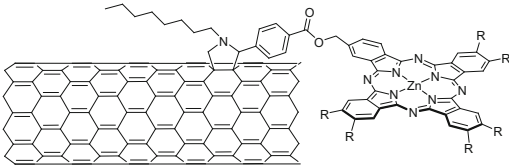
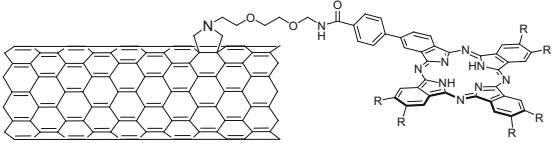
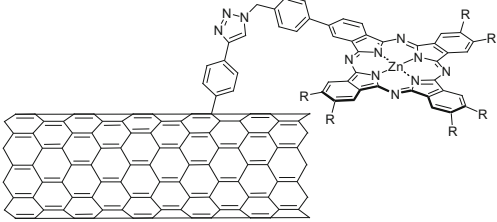
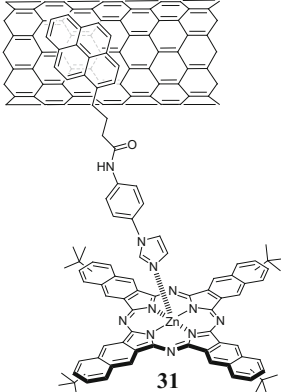
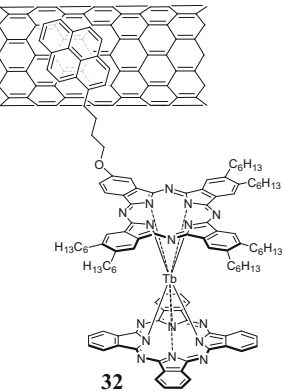
Fig. 11 Covalent Pc/CNT hybrids **26** and **27**

6.1 Covalent Attachment of Pcs to Carbon Nanotubes

There are two main synthetic methodologies for covalently attaching Pcs to CNTs: (1) through oxidation of the nanotube and modification of the resulting carboxylic acid functionalities and (2) by cycloaddition reactions on the wall double bonds. The oxidation of CNTs with mixtures of concentrated sulfuric and nitric acids [230] results in uncapped CNTs (of 100–300 nm). The nanotube derivatization by this methodology is hardly selective, being possible to occur at walls and ends. On the contrary, CNTs with Pcs attached only to the side walls can be prepared by cycloaddition of reactive species such as aryl radicals, aryl cations, nitrenes, carbenes, and 1,3-dipoles.

Nanotubes presenting carboxylic acids can be reacted with alcohols and amines to form esters or amide bonds, by a methodology that was employed to attach, among others, a zinc aminoPc to single-walled carbon nanotubes (SWCNTs) [231]. Although the Pc units bore bulky *tert*-butyl substituents at the periphery of the macrocycle, the resulting material was scarcely soluble in most organic solvents, thus ruling out its photophysical characterization. A similar methodology was employed to prepare the CuPc–MWCNT hybrid **26** (Fig. 11a) [232]. The weight content of CuPc in hybrid **26** was estimated to be ~10% by thermogravimetric analysis. Nanotube's carboxylic groups can also be transformed into acid chlorides by treatment with SOCl_2 , and subsequently coupled to amines and alcohols. It was in this way that manganese tetraaminoPc [233] and a sandwich-type octaamino-substituted erbium bisphthalocyaninato complex [234] have been incorporated into MWCNTs and SWCNTs (hybrid **27**, Fig. 11b), respectively. In general, all these Pc–CNT hybrid materials showed better photoconductivity than the pristine Pc and Pc/MWCNT blended composites. Photophysical studies showed a substantial decrease of the Pc fluorescence [233], suggesting a quenching of the Pc singlet excited state by the directly linked CNTs. In the case of **27**, charge transfer from the ErPc_2 unit to the nanotube excited states was evidenced from the Raman shift. More recently, a hybrid free-base Pc/MWCNTs system was prepared, with enhanced optical limiting properties [235].

Table 4 CS state lifetimes for some Pc/CNT covalent and non-covalent systems

Compound	Reference	CS lifetime (ps)
	28 [236]	3.05×10^5 ^a
	29 [237]	6.67×10^5 ^b
	30 [238]	– ^c
	31 [241]	6.0×10^4 ^a
	32 [242]	7.0×10^4 ^b
		– ^c

^aDMF^bTHF^cThe CS lifetimes for **30** and **32** were not reported, R = C₆H₄O-*p-tert*-butyl

Concerning the functionalization of CNTs by cycloaddition reactions, Torres et al. have reported the preparation of Pc–SWCNT ensembles (**28** and **29**, Table 4) using the 1,3-dipolar cycloaddition of azomethine ylides to the nanotube double bonds, known as the Prato reaction [236, 237]. The UV–Vis spectra of the ensembles showed the absorption features of both components: the Q-band of the Pc core and the typical van Hove singularities of SWCNTs ranging from the visible to the near-infrared. The presence of these bands confirms that the electronic structure of the SWCNTs is preserved to some extent. In addition, Raman

spectroscopy provides evidence for the covalent attachment of Pc molecules to the nanotube sidewalls.

Fluorescence spectroscopy, on the other hand, showed a strong quenching of the ZnPc emission for hybrids **28** and **29**. Transient absorption studies in the femtosecond time scale indicated that, upon photoexciting the ZnPc, its singlet excited state fingerprints decayed, and led to the formation of the ZnPc radical cation (with transient maximum at 840 nm). Photobleaching of the van Hove singularities was also observed. Interestingly, this behavior and the lifetime of the CS state were very similar in both systems (Table 4), and significantly higher than for Pc-C₆₀ dyads with similar covalent spacers. This fact suggests that the nature of the spacer, which can be flexible or rigid, does not have a notable influence on the PET process in this type of hybrid systems.

Another synthetic method to prepare Pc-SWCNT hybrids (e.g., hybrid **30**, Table 4) is the so-called click chemistry [238], specifically the addition of aromatic radicals to the CNT sidewalls [239]. Hybrid **30** possesses a higher content of ZnPc than **28** and showed photoinduced electron injection from the ZnPc units to the nanotube. Moreover, the photovoltaic potential of this material was tested by measuring the photocurrent generated in a photoelectrochemical cell. The cell was built by deposition of a thick film of **30** over an ITO electrode, which was afterwards immersed in the electrolyte solution (0.1 M Na₃PO₄). The experiments revealed stable and reproducible photocurrents with monochromatic incident photon-to-current efficiency (IPCE) values as large as 17.3%.

6.2 *Non-Covalent Interactions Between Pcs and Carbon Nanotubes*

The electronic network of CNTs can be fully preserved if they are non-covalently functionalized. The supramolecular immobilization of Pcs on their sidewalls is possible by π - π interactions between the aromatic surfaces of both systems. This approach may give rise to nanodevices where the photophysical and conducting properties of the nanotubes are not spoiled.

A remarkable way to connect organic molecules to CNTs by non-covalent interactions consists in the use of a pyrenyl supramolecular linkage. It is known that pyrene strongly binds to the SWCNT's sidewalls through π - π stacking [240]. Two different groups have described the non-covalent functionalization of SWCNTs with zinc tetra-*tert*-butylnaphthalocyanine (ZnNc) (hybrid **31**, Table 4) [241] and a heteroleptic bis(phthalocyaninato) terbium complex (hybrid **32**, Table 4) [242] using this pyrene-based strategy. Nanosecond transient absorption experiments showed that photoexciting the ZnNc units in **31** leads to a CS state with around 70 ns lifetime. The rationale behind the preparation of system **32** lays, on the other hand, on the magnetic properties of the TbPc₂ complex, which exhibits temperature and frequency dependency of the magnetic susceptibility, a typical behavior of

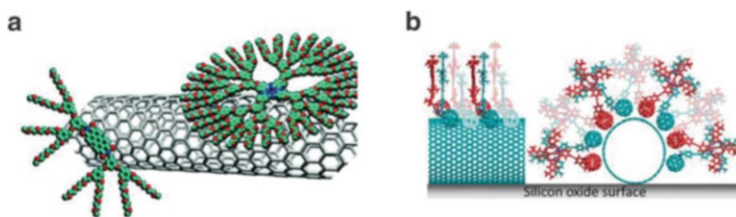


Fig. 12 Schematic representation of (a) the CuPc/SWCNT hybrid **33** (reprinted with permission from [245], copyright 2010, American Chemical Society), and (b) the Pc–C₆₀/SWCNT supramolecular assembly **34** [246]

single-molecule magnets (SMMs). Magnetization studies revealed that the SMM character of the TbPc₂ complex is retained and even improved in the hybrid system, compared to the original Pc and its composites with SWCNTs.

It has been found that effective Pc/SWCNT π – π interactions can also take place even if the Pc lacks any pyrenyl anchoring group. Wang et al. reported that CNTs can fade the color of chloroform solutions of zinc tetra-*tert*-butylPc as a result of the immobilization of Pc molecules on the nanotube sidewalls [243]. The adsorption of the Pc molecules on the CNT's surface was characterized by TEM and AFM, showing nanoparticles of several to tens of nanometers. Water-soluble Pcs have also been deposited onto CNTs. Hydrogen bonding interactions between the sodium salt of CuPc tetrasulfonic acid and oxidized MWCNTs take place in concentrated dispersions of both components (see Sect. 7) [244]. Upon spin casting of such dispersions, uniform thin films were obtained. Spectroscopic and morphological studies evidenced that the Pc cores were stacked in columns along the MWCNT scaffold, in such a way that the plane of the macrocycle was parallel to the nanotube surface. Interestingly, the Pc moieties act here as electron-acceptors. Other water-soluble Pc with dendritic oligoethylene glycol chains at the periphery have shown to adsorb onto CNTs as well (hybrid **33**, Fig. 12a) [245]. This type of water-soluble SWCNT/Pc supramolecular system might be used in the future for processing these materials under environmentally friendly conditions.

A bright example of self-assembly from Pc–C₆₀ dyads and SWCNTs was described by Bottari et al. (hybrid **34**, Fig. 12b) [246, 247] and discloses the competitive nature of supramolecular organization. In contrast to previous examples, Pcs in this case do not undergo π – π stacking with the SWCNT side walls. This Pc–C₆₀ dyad, with its rigid linker, self-organizes around the SWCNTs in a radial arrangement, and the fullerene moieties are pointing downwards, due to the tendency of fullerenes to interact with CNTs. Moreover, such an arrangement allows the existence of C₆₀/C₆₀ and Pc/Pc π – π interactions between neighbors, thus further stabilizing the Pc–C₆₀/SWCNT hybrid. The possibility of using these assemblies as a photoswitchable gate in nanoelectronics is under investigation.

7 (Sub)Phthalocyanines as Electron-Acceptor Photoactive Materials

(Sub)Pcs are generally regarded as electron-donor chromophores with excellent light-harvesting properties. Their dual nature in organic photovoltaics, as donors and antennas, can, however, be understood in a different way. Owing to the structural and synthetic versatility of (Sub)Pcs, and consequently of their redox and photophysical behavior, they act as electron-acceptors in certain cases [11]. Whether (Sub)Pcs are donors or acceptors in a dyad or multicomponent system mainly depends on the electronic character of their peripheral substituents and metal center, and on the photoactive units they are confronted with. Pcs decorated with electron-rich substituents, such as alkoxy groups, never play as acceptors, independently of which photoactive unit is their counterpart. For the case of Pcs with electronically neutral substituents (e.g., H, alkyl, *tert*-butyl), Pors are usually the donor in Pc-Por molecular systems, which usually give rise to photoinduced energy [248–250] and electron transfer [251, 252]. SubPcs possess redox properties similar to those of Pors, associated with their strong absorption at ca. 570 nm, and their electronic character can also be modulated by the nature of the peripheral and axial substitution. Playing around with the electron affinity of substituents, several Pc–Pc [253, 254] and Pc–SubPc [255–257] systems have been prepared in which one of the macrocycles is the donor and the other one the acceptor.

The electronic affinity of Pcs increases with the incorporation of electron-withdrawing peripheral substituents. Alkylsulfonyl-substituted Pcs were covalently grafted onto a conjugated polymer (P3HT), affording efficient photoinduced charge separation from the polythiophene backbone to the Pc units (polymer **35**, Fig. 13a) [258]. Furthermore, the sodium salt of CuPc tetrasulfonic acid (TsCuPc) has been organized on the oxidized surface of MWCNTs, playing the role of acceptor (hybrid **36**, Fig. 13b) [244]. Efficient charge transfer in the ground state was observed between the two components, according to ultraviolet photoelectron spectroscopy (UPS) and X-ray photoelectron spectroscopy (XPS) studies. The hybrid material was then incorporated between a BHJ layer, composed of P3HT and PCBM, and the ITO electrode. The resulting device showed an increased light-harvesting ability. This is so far the only example where a Pc molecule is the electron-acceptor within a hybrid material with a carbon nanostructure.

SubPcs can also be conferred with electron-accepting features, when derivatized with fluoro, nitro, or sulfonyl peripheral functionalities. Chromophores that, inserted in their axial position, have played the role of donor versus these SubPcs include ferrocene [259], pyrene and truxene axial ligands [260], triphenylamine [261], BODIPY [262], metal bipyridyl complexes [263], Pors [264], and naphthalocyanines (Ncs) [265]. It could actually be argued that some (Sub)Pcs enjoy electron-accepting properties comparable to those of fullerenes: their first reduction potential can reach lower values than that of fulleropyrrolidines, and their rigid, three-dimensional structure provides them with low reorganization energies [96].

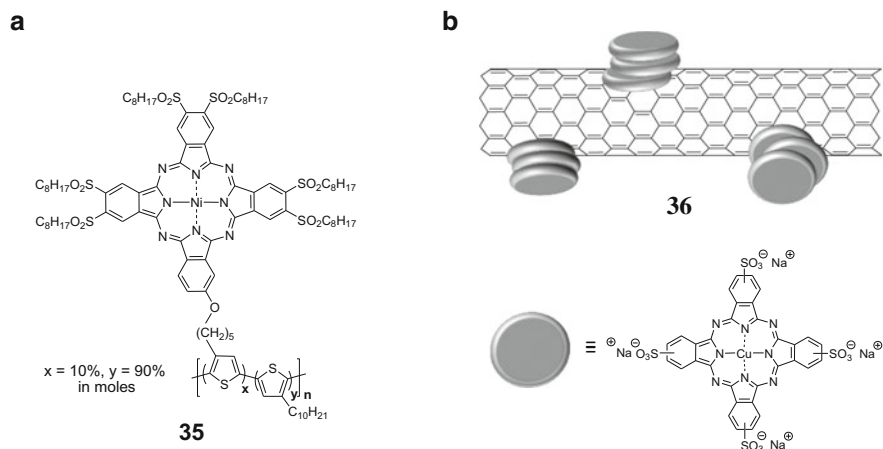


Fig. 13 (a) Structure of a polythiophene (P3HT) **35**, grafted with electron-acceptor alkylsulfonyl-Pc molecules. (b) Schematic view of the water-soluble Pc/SWCNT hybrid **36** (adapted with permission from [15], copyright 2010, American Chemical Society)

Fluorinated Pcs and SubPcs, in particular, have been used to substitute C_{60} as the acceptor component in small molecule OSCs. Devices with a PHJ of F_{13} SubPc and SubPc were fabricated according to the structure ITO(100 nm)/SubPc(13 nm)/ F_{13} SubPc(33 nm)/BCP(10 nm)/Al(80 nm) [266]. Both electron and hole transfer processes were demonstrated under AM 1.5D simulated solar illumination, but their efficiencies were lower than that of similar C_{60} -containing devices. Evaporated BHJs, on the other hand, have been prepared from SubPc and F_{16} CuPc [267]. This system possessed several advantages such as a good coverage of the solar spectrum, and appropriate energy levels to induce an efficient exciton separation. Conductivity studies suggested, in fact, the presence of conductive pathways in the F_{16} CuPc phase. For small contents of SubPc, electron transfer to the F_{16} CuPc, and parallel photoconduction in both phases, were found. For larger contents of SubPc, undesired trapping reactions occurred, triggered by interaction of the SubPc excited state with the charge-carriers in the F_{16} PcCu phase. A decreased conductivity under illumination was also detected, thus revealing the presence of isolated clusters of both macrocycles.

Finally, Song et al. have recently proven that exciton dissociation is not the only possible mechanism for charge-carrier generation. The authors showed that intermolecular exciton recombination in solar cells composed of F_{16} ZnPc and C_{60} (i.e., a $n-n$ type device) allows generating free charges from such semiconductors [268]. The mechanism of the process lays on the recombination of electrons from the fluorinated ZnPc with holes from the fullerene, leaving free their counterpart carriers. Although the efficiencies of the devices reported are low, these results represent a new way to harvest electricity from sunlight.

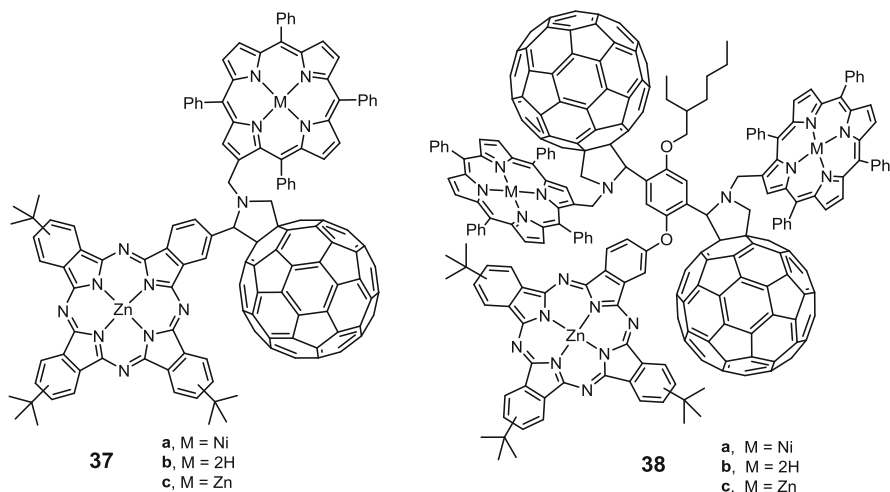


Fig. 14 Molecular structures of covalent triads **37a–c** and pentads **40a–c**

Note Added in Proof. During the editing process of this review article, the intense research activity on donor–acceptor systems for OSC applications has brought light to various new systems with unprecedented properties. For instance, the incorporation of Por units into Pc–C₆₀ dyads tunes their optoelectronic features. Bright examples of the covalent connection of three different photoactive moieties, such as C₆₀, Por, and Pc, in triads (**37a–c**) and pentads (**38a–c**) have been reported (Fig. 14) [269]. These compounds were prepared in one-step through 1,3-dipolar cycloaddition to C₆₀ of the corresponding azomethine ylides, generated in situ by condensation of *N*-porphyrinylmethylglycine with an appropriately substituted formyl- or diformyl-Pc derivative. For all systems, photoexcitation of their Por components gives rise to a sequence of energy and charge transfer reactions, with CS lifetimes in the range from picoseconds to nanoseconds for pentads and triads, respectively. In all triads and in pentad **38b**, the C₆₀ unit performs as an electron-acceptor, whereas the ZnPc moiety acts as an electron-donor. In pentad **38c**, on the contrary, the photoinduced radical cation localizes in the Por unit.

The same research groups have reported supramolecular systems based on identical photoactive units (i.e., C₆₀, Pc and Por). These systems were assembled *via* coordination interactions between *N*-(4-pyridyl)fulleropyrrolidine and covalent conjugates of Pc and Por. Triads **39a–b** [270] and **40a–c** [271] provide complementary absorption in a wide range of the solar spectrum, and yield longer CS lifetimes than their covalent counterparts (Fig. 15). Moreover, fusing the Pc and Por moieties guarantees a strong electronic coupling and red shift of their absorption. Photophysical measurements revealed that, upon photoexcitation, intramolecular energy transfer from the Por tetrapyrrole (either free-base or metallated) to the energetically lower-lying ZnPc macrocycle takes place. This phenomenon is followed by an intramolecular charge transfer from the excited ZnPc to C₆₀, leading

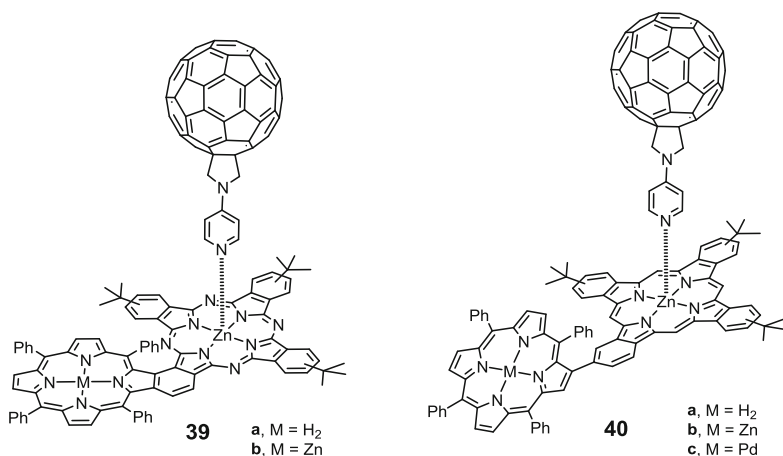


Fig. 15 Supramolecular triads **39** and **40**, assembled via coordination interactions

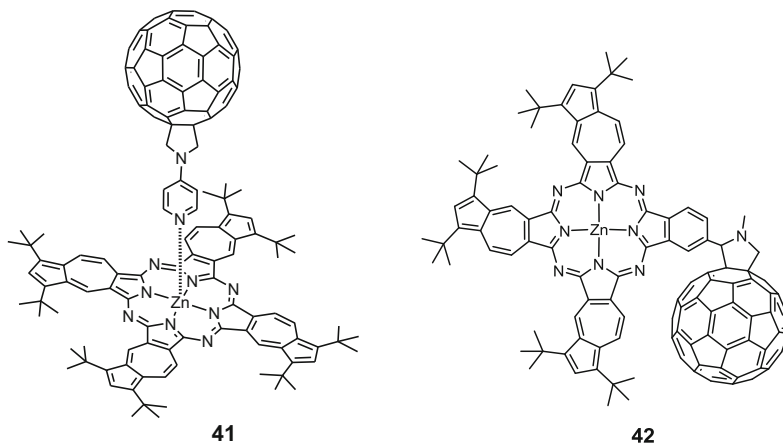


Fig. 16 Supramolecular and covalent azulenocyanine-C₆₀ dyads **41** and **42**, respectively

to the Por-ZnPc^{+/•}/C₆₀^{-•} radical ion pair formation. The deactivation of the transient radical ion pair occurs with no charge shift reaction to the Por.

Modifying the electronic structure of Pcs is, on the other hand, promising for the fine-tuning of charge transfer properties of the corresponding donor-acceptor systems. With this in mind, new azulenocyanines and their covalent (**41**) and non-covalent (**42**) ensembles with C₆₀ have been prepared for the first time (Fig. 16). These systems show a remarkable panchromatic absorption of the cyanine unit from the UV-Vis to the near-infrared regions of the solar spectrum [272]. Axial coordination in system **41** leads to a 0.78 ns lived radical ion pair state, despite the extremely short-lived excited state of the azulenocyanine moiety (i.e., 10 ps). On

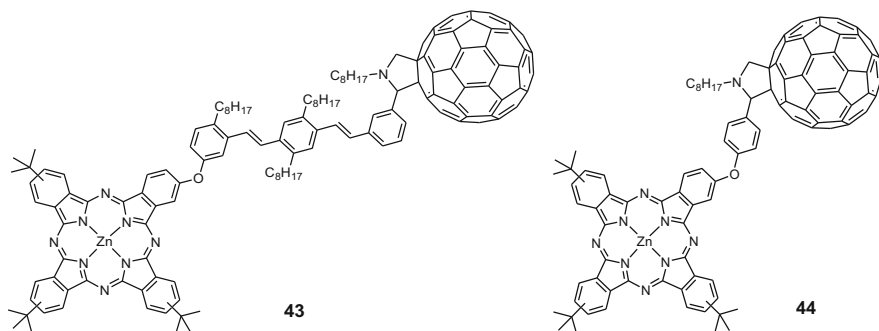


Fig. 17 Molecular structures of the donor–acceptor systems ZnPc-*o*PPV-C₆₀ **43** and ZnPc-C₆₀ **44**

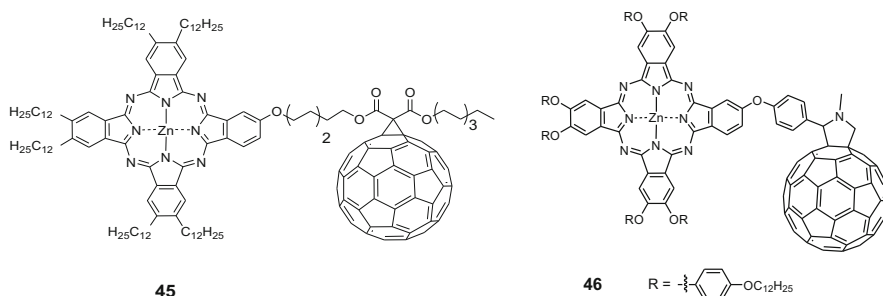


Fig. 18 Molecular structures of mesogenic Pc-C₆₀ dyads **45** and **46**

the contrary, the azulenocyanine moiety excited state in **42** fails to power electron transfer upon photoexcitation.

Another attempt to achieve additional CS lifetime stabilization has been undertaken by connecting the electron-donor (i.e., ZnPc) and the electron-acceptor (i.e., C₆₀) through an oligo(*p*-phenylenevinylene) (*o*PPV). In particular, compound **43** (Fig. 17) was prepared in a multi-step synthesis, through two consecutive Wadsworth–Horner–Emmons reactions and a dipolar 1,3-cycloaddition as key steps [273]. The simpler ZnPc–C₆₀ dyad **44** was also prepared as a reference compound for photophysical studies. A clear dependence between charge transfer kinetics and spatial arrangement manifested by means of fluorescence, flash photolysis, and transient-absorption spectroscopies. In both systems (i.e., **43** and **44**), intramolecular charge separation evolves from the photoexcited ZnPc and yields ZnPc^{•+}/C₆₀^{•-} radical ion pairs with maximum lifetimes of 2.9 and 5.53 ns, respectively.

The possibility to self-assemble covalent, donor–acceptor conjugates into large length-scale aggregates is highly desirable for molecular photovoltaics [274–276] and field effect transistor applications, where the order of both the acceptor and donor components in the solid state is a key issue for achieving high carrier mobilities. In this respect, the mesogenic ZnPc–C₆₀ dyad **45** has been recently described, consisting of a hexadecyl-substituted ZnPc covalently connected through a flexible spacer to C₆₀ (Fig. 18) [277]. Polarized optical microscopy (POM) and differential scanning

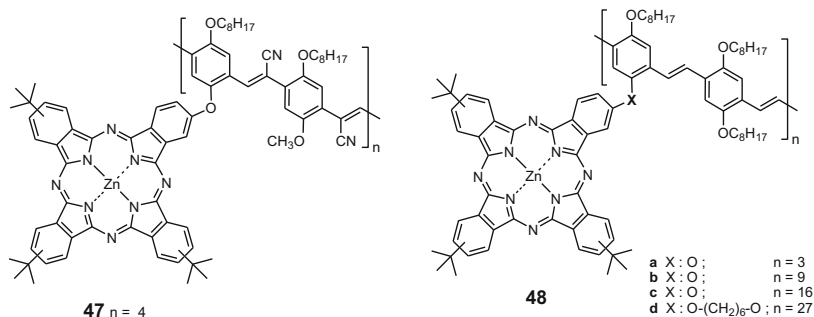


Fig. 19 Molecular structures of ZnPc-based PPV oligomers **47** and **48**

calorimetry (DSC) studies revealed liquid-crystalline behavior between 80 and 180°C. Complementary X-ray diffraction (XRD) studies showed that compound **45** adopts a rectangular symmetry within the columnar mesophase (i.e., Col_r). The liquid-crystalline donor–acceptor heterojunction formed by another mesogenic ZnPc–C₆₀ conjugate (i.e., **46**), on the other hand, exhibits highly efficient short-range and long-range charge transport properties [278]. Interestingly, when heating up the mesophase, a 5-times increase of the total charge mobility occurs, with respect to the unheated sample. The improvement of ZnPc–C₆₀ column alignment upon heating possibly explains this phenomenon, because it may facilitate the charge transport between columns.

Besides fullerenes, Pcs are ideal partners of CNTs for photovoltaic applications. In this case, both photoactive units can interact through strong intermolecular interactions. For this purpose, the ZnPc derivatives **47** and **48**, covalently linked to a PPV oligomer, were designed and synthesized for SWCNT exfoliation (Fig. 19) [279]. A complete spectroscopic and microscopy study demonstrated that oligomer **47** affords stable and finely dispersed SWCNT suspensions, whereas oligomers **48a–c** failed to disperse the nanotubes [280]. Analysis on the different electronic character of these two PPV oligomers sheds light on the obtained experimental data. In the case of **47**, the presence of electron-withdrawing cyano substituents confers n-type character to the PPV oligomer, thus favoring strong interactions with SWCNTs, since they are p-type materials. On the contrary, PPV oligomers **48a–c** possess a p-type character that suppresses the interactions with SWCNTs. Transient absorption measurements carried out on the **47**/SWCNT supramolecular system revealed the formation of a metastable CS photoproduct.

The supramolecular interactions of azuleno-cyanine **49** and its derivative bearing a pyrene unit (**50**) with SWCNTs have been studied as well (Fig. 20) [281]. Stable suspensions of SWCNTs in a mixture of 25% THF and 75% DMF were titrated with variable amounts of **49** or **50**. These assays demonstrated the successful immobilization of azuleno-cyanine derivatives onto the SWCNT surface to yield the supramolecular hybrids SWNT/**49** and SWNT/**50**. Moreover, they showed strong interactions in the ground state and a rapid charge separation in the excited state.

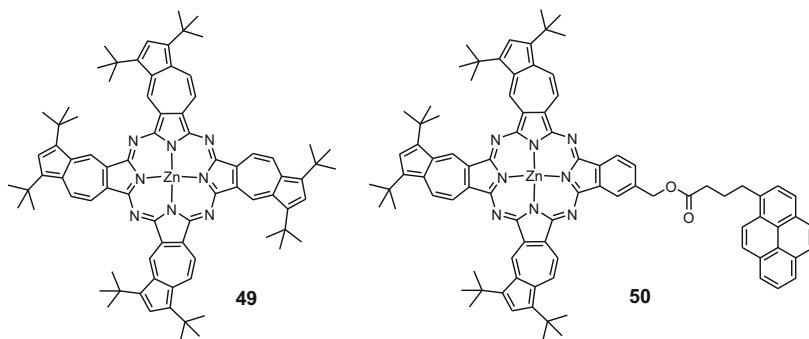


Fig. 20 Molecular structures of Zn azulenocyanines **49** and **50**

The accordingly formed radical ion pair states decay with lifetimes of 124 and 137 ps for SWNT/**49** and SWNT/**50**, respectively. Finally, both systems revealed, in photoelectrochemical cells, a response throughout the visible and near-infrared region of the solar spectrum, with moderate IPCE maxima of 2.5%.

SubPc also interacts with carbon nanostructures, such as fullerenes, and forms supramolecular complexes in solution. More precisely, thioalkyl-substituted SubPc derivatives with an electronically different concave shape allowed testing the influence of structural factors, such as the length of alkyl substituents, on the encapsulation of C_{60} [282]. By using the Job plot methodology, it was found that the obtained supramolecular inclusion complexes possess a 2:1 stoichiometry, with binding constants as large as $10^5 M^{-1}$. Moreover, unidirectional energy transfer from the periphery (i.e., the donor SubPcs) to the core (i.e., the acceptor fullerene) occurs upon photoexcitation. The ability of SubPcs to disrupt fullerene aggregation might be useful for achieving better architectures in bulk-heterojunction solar cells.

The properties of SubPc as electron-donor have triggered its incorporation into small-molecule OSCs, together with a perfluorinated SubPc-dimer as electron-acceptor [283]. Due to the complementary absorption of both materials, an enhanced photocurrent is achieved within this system, while preserving the high open-circuit voltage characteristic of SubPc-based devices. Additionally, introducing a C_{60} interlayer between the perfluorinated SubPc-dimer and BCP layers led to a cell efficiency of 4%. Deep inspection of the device spectral response and reflection data showed that the SubPc/SubPc-dimer interface is the photoactive one, whereas C_{60} mainly functions as a transport layer that enhances electron extraction.

In light of the increasing interest in environmentally friendly technologies, the development of OSCs processed in aqueous solutions represents one of the most appealing goals of today's materials chemistry. Recently, OSCs based on a series of water-soluble ZnPc, with varying numbers of sulfonate peripheral substituents, and C_{60} have been fabricated and characterized [284]. The number of sulfonate substituents affects both the V_{oc} and J_{sc} device values, with the disulfonated ZnPc being the one best performing (0.46% efficiency under standard conditions).

Additionally, the number of negatively charged substituents determines the morphology of the ZnPc thin film, which in turn affects device performance. Developing water-soluble acceptor molecules, in order to provide both an environmentally friendly and an inexpensive route towards fully water-processed OSCs, is the next cornerstone in this research area.

8 Conclusions

OSCs promise to occupy a central position in the future renewable energy policy. They offer a cheaper and more flexible alternative to silicon-based solar cells. In all-organic photovoltaic devices, it is widely accepted that carbon nanostructures, such as fullerenes and CNTs, are the best electron-acceptor materials for being integrated in DA planar or bulk heterojunctions. In addition, molecules or polymers able to efficiently absorb sunlight and transfer its energy by electron transfer to the acceptor are necessary. (Sub)Pcs have been benchmark materials in the field of OSCs for more than 20 years, due to their dual nature as electron-donor and light-harvesting molecules.

When these chromophores are integrated in molecular systems with fullerenes, through either covalent or non-covalent interactions, they lead to efficient electron transfer processes. Hence, such molecular systems (in solution) are excellent mimics of photosynthetic systems and give valuable information on the organizational requirements to achieve charge separation in thin film devices. The incorporation of (Sub)Pc and fullerene derivatives in solar cells have led, through years of development of the material design and device architecture, to PCEs of ca. 5%. When the dual function of (Sub)Pcs is combined with organic conjugated polymers and fullerenes, the efficiency of the cells can even be increased.

More recently, systems in which Pcs are attached to CNTs are attracting much interest. Furthermore, it is noteworthy that Pcs are regarded not only as donors but also as acceptors, depending on their structure and on the photoactive counterpart they are confronted with. The possibilities of utilizing Pc/CNT hybrid materials or substituting fullerenes by electron-acceptor (Sub)Pcs in OSCs is currently being explored in several laboratories around the world and may give in the near future a new impulse to this technologically important research field.

Acknowledgment This work has been supported by the Spanish MICINN and MEC (CTQ2011-24187/BQU and CONSOLIDER INGENIO 2010, CSD2007-00010 Nanociencia Molecular), and the Comunidad de Madrid (MADRISOLAR-2, S2009/PPQ/1533).

References

1. Bredas JL, Norton JE, Cornil J, Coropceanu V (2009) *Acc Chem Res* 42:1691
2. Armstrong NR, Wang WN, Alloway DM, Placencia D, Ratcliff E, Brumbach M (2009) *Macromol Rapid Commun* 30:717

3. Tang CW (1986) *Appl Phys Lett* 48:183
4. Koster LJA, Mihaiilechi VD, Blom PWM (2006) *Appl Phys Lett* 88:3511
5. Riede M, Mueller T, Tress W, Schueppel R, Leo K (2008) *Nanotechnology* 19:4001
6. Scharber MC, Wuhlbacher D, Koppe M, Denk P, Waldauf C, Heeger AJ, Brabec CL (2006) *Adv Mater* 18:789
7. Heremans P, Cheyens D, Rand BP (2009) *Acc Chem Res* 42:1740
8. Peet J, Heeger AJ, Bazan GC (2009) *Acc Chem Res* 42:1700
9. Roncali J (2009) *Acc Chem Res* 42:1719
10. de la Torre G, Claessens CG, Torres T (2007) *Chem Commun* 2000
11. Claessens CG, Hahn U, Torres T (2008) *Chem Rec* 8:75
12. Martínez-Díaz MV, Torres T (2010) In: Kadish KM, Smith KM, Guillard R (eds) *Handbook of porphyrin science*. Academic, San Diego, p 2000
13. González-Rodríguez D, Bottari G (2009) *J Porphyrins Phthalocyanines* 13:624
14. de la Torre G, Bottari G, Hahn U, Torres T (2010) *Struc Bond* 135:1
15. Bottari G, de la Torre G, Guldi DM, Torres T (2010) *Chem Rev* 110:6768
16. Martínez-Díaz MV, de la Torre G, Torres T (2010) *Chem Commun* 7090
17. Gunes S, Neugebauer H, Sariciftci NS (2007) *Chem Rev* 107:1324
18. Mayer AC, Scully SR, Hardin BE, Rowell MW, McGehee MD (2007) *Mater Today* 10:28
19. Kroon R, Lenes M, Hummelen JC, Blom PWM, De Boer B (2008) *Polym Rev* 48:531
20. Kippelen B, Bredas JL (2009) *Energy Environ Sci* 2:251
21. Halls JJM, Walsh CA, Greenham NC, Marseglia EA, Friend RH, Moratti SC, Holmes AB (1995) *Nature* 376:498
22. Yu G, Gao J, Hummelen JC, Wudl F, Heeger AJ (1995) *Science* 270:1789
23. Muhlbacher D, Scharber M, Morana M, Zhu ZG, Waller D, Gaudiana R, Brabec C (2006) *Adv Mater* 18:2931
24. Shi CJ, Yao Y, Yang Y, Pei QB (2006) *J Am Chem Soc* 128:8980
25. Slooff LH, Veenstra SC, Kroon JM, Moet DJD, Sweelssen J, Koetse MM (2007) *Appl Phys Lett* 90:3506
26. Chen CP, Chan SH, Chao TC, Ting C, Ko BT (2008) *J Am Chem Soc* 130:12828
27. Lee JY, Shin WS, Haw JR, Moon DK (2009) *J Mater Chem* 19:4938
28. Potscavage WJ, Sharma A, Kippelen B (2009) *Acc Chem Res* 42:1758
29. Sariciftci NS, Smilowitz L, Heeger AJ, Wudl F (1992) *Science* 258:1474
30. Brabec CJ, Sariciftci NS, Hummelen JC (2001) *Adv Funct Mater* 11:15
31. Imahori H, Sakata Y (1997) *Adv Mater* 9:537
32. Echegoyen L, Echegoyen LE (1998) *Acc Chem Res* 31:593
33. Martin N, Sanchez L, Illescas B, Perez I (1998) *Chem Rev* 98:2527
34. Diederich F, Gomez-Lopez M (1999) *Chem Soc Rev* 28:263
35. Guldi DM, Prato M (2000) *Acc Chem Res* 33:695
36. Guldi DM (2000) *Chem Commun* 321
37. Fukuzumi S, Guldi DM (2001) In: Balzani V (ed) *Electron transfer in chemistry*, vol 2. Wiley-VCH, New York, p 270
38. Guldi DM, Martin N (2002) *Fullerenes: from synthesis to optoelectronic properties*. Kluwer Academic Publishers, Dodrecht
39. Guldi DM (2002) *Chem Soc Rev* 31:22
40. Giacalone F, Martin N (2006) *Chem Rev* 106:5136
41. Langa F, Nierengarten J-F (2007) *Fullerenes: principles and applications*. The Royal Society of Chemistry, Cambridge
42. Guldi DM, Illescas BM, Atienza CM, Wielopolskia M, Martin N (2009) *Chem Soc Rev* 38:1587
43. Hummelen JC, Knight BW, Lepeq F, Wudl F, Yao J, Wilkins CL (1995) *J Org Chem* 60:532
44. Dresselhaus MS, Dresselhaus G, Avouris P (2001) *Carbon nanotubes: synthesis, structure, properties and applications*. Springer-Verlag, Berlin

45. Harris P (2001) Carbon nanotubes and related structures: new materials for the twenty-first century. Cambridge University Press, Cambridge
46. Reich S, Thomsen C, Maultzsh J (2004) Carbon nanotubes: basic concepts and physical properties. Wiley-VCH, Weinheim
47. Sgobba V, Guldi DM (2009) *Chem Soc Rev* 38:165
48. Tasis D, Tagmatarchis N, Bianco A, Prato M (2006) *Chem Rev* 106:1105
49. Sgobba V, Guldi DM (2008) *J Mater Chem* 18:153
50. Special issue (2009) *Acc Chem Res* 42:1859
51. Deisenhofer J, Norris JR (1993) The photosynthetic reaction center. Academic, New York
52. Blankenship RE (2002) Molecular mechanisms of photosynthesis. Blackwell, Malden
53. Fox MA, Chanon M (1988) Photoinduced electron transfer. Elsevier, Amsterdam
54. Balzani V (2001) Electron transfer in chemistry. Wiley-VCH, Weinheim
55. Wasielewski MR (1992) *Chem Rev* 92:435
56. Gust D, Moore TA, Moore AL (1993) *Acc Chem Res* 26:198
57. Gust D (1997) *Nature* 386:21
58. Gust D, Moore TA, Moore AL (2001) *Acc Chem Res* 34:40
59. Balzani V, Credi A, Venturi M (2008) *ChemSusChem* 1:26
60. Benniston AC, Harriman A (2008) *Mater Today* 11:26
61. Gust D, Moore TA (2000) In: Kadish KM, Smith KM, Guillard G (eds) The porphyrin handbook, vol 8. Academic, New York p 153
62. Linssen TG, Durr K, Hanack M, Hirsch A (1995) *J Chem Soc Chem Commun* 103
63. Durr K, Fiedler S, Linssen T, Hirsch A, Hanack M (1997) *Chem Ber* 130:1375
64. Martinez-Diaz MV, Quintiliani M, Torres T (2008) *Synlett* 1:20
65. Gouloumis A, Liu SG, Sastre A, Vazquez P, Echegoyen L, Torres T (2000) *Chem Eur J* 6:3600
66. Guldi DM, Gouloumis A, Vazquez P, Torres T (2002) *Chem Commun* 2056
67. Isosomppi M, Tkachenko NV, Efimov A, Vahasalo H, Jukola J, Vainiotalo P, Lemmetyinen H (2006) *Chem Phys Lett* 430:36
68. Niemi M, Tkachenko NV, Efimov A, Lehtivuori H, Ohkubo K, Fukuzumi S, Lemmetyinen H (2008) *J Phys Chem A* 112:6884
69. Lemmetyinen H, Tkachenko NV, Efimov A, Niemi M (2009) *J Phys Chem C* 113:11475
70. Ranta J, Kumpulainen T, Lemmetyinen H, Efimov A (2010) *J Org Chem* 75:5178
71. Lemmetyinen H, Kumpulainen T, Niemi M, Efimov A, Ranta J, Stranius K, Tkachenko NV (2010) *Photochem Photobiol Sci* 9:949
72. Guldi DM, Zilbermann I, Gouloumis A, Vazquez P, Torres T (2004) *J Phys Chem B* 108:18485
73. Loi MA, Denk P, Hoppe H, Neugebauer H, Winder C, Meissner D, Brabec C, Sariciftci NS, Gouloumis A, Vazquez P, Torres T (2003) *J Mater Chem* 13:700
74. Neugebauer H, Loi MA, Winder C, Sariciftci NS, Cerullo G, Gouloumis A, Vazquez P, Torres T (2004) *Sol Energy Mater Sol Cells* 83:201
75. Quintiliani M, Kahnt A, Wolffe T, Hieringer W, Vazquez P, Gorling A, Guldi DM, Torres T (2008) *Chem Eur J* 14:3765
76. Kahnt A, Guldi DM, de la Escosura A, Martin-Diaz MV, Torres T (2008) *J Mater Chem* 18:77
77. Giacalone F, Segura JL, Martin N, Guldi DM (2004) *J Am Chem Soc* 126:5340
78. Atienza C, Martin N, Wielopolski M, Haworth N, Clark T, Guldi DM (2006) *Chem Commun* 3202
79. Pinzon JR, Cardona CM, Herranz MA, Plonska-Brzezinska ME, Palkar A, Athans AJ, Martin N, Rodriguez-Forteza A, Poblet JM, Bottari G, Torres T, Gayathri SS, Guldi DM, Echegoyen L (2009) *Chem Eur J* 15:864
80. Stevenson S, Rice G, Glass T, Harich K, Cromer F, Jordan MR, Craft J, Hadju E, Bible R, Olmstead MM, Maitra K, Fisher AJ, Balch AL, Dorn HC (1999) *Nature* 401:55

81. Ballesteros B, de la Torre G, Shearer A, Hausmann A, Herranz MA, Guldi DM, Torres T (2010) *Chem Eur J* 16:114
82. Gouloumis A, de la Escosura A, Vazquez P, Torres T, Kahnt A, Guldi DM, Neugebauer H, Winder C, Drees M, Sariciftci NS (2006) *Org Lett* 8:5187
83. Quintiliani M, Kahnt A, Vazquez P, Guldi DM, Torres T (2008) *J Mater Chem* 18:1542
84. Kahnt A, Quintiliani M, Vazquez P, Guldi DM, Torres T (2008) *ChemSusChem* 1:97
85. El-Khouly ME, Kim JH, Kay KY, Choi CS, Ito O, Fukuzumi S (2009) *Chem Eur J* 15:5301
86. Martin-Gomis L, Ohkubo K, Fernandez-Lazaro F, Fukuzumi S, Sastre-Santos A (2007) *Org Lett* 9:3441
87. Martin-Gomis L, Ohkubo K, Fernandez-Lazaro F, Fukuzumi S, Sastre-Santos A (2008) *J Phys Chem C* 112:17694
88. Fukuzumi S, Honda T, Ohkubo K, Kohima T (2009) *Dalton Trans* 20:3880
89. Kim KN, Choi CS, Kay KY (2005) *Tetrahedron Lett* 46:6791
90. El-Khouly ME, Kang ES, Kay KY, Choi CS, Aaraki Y, Ito O (2007) *Chem Eur J* 13:2854
91. de la Escosura A, Martinez-Diaz MV, Torres T, Grubbs RH, Guldi DM, Neugebauer H, Winder C, Drees M, Sariciftci NS (2006) *Chem Asian J* 1:148
92. Kobayashi N (2003) In: Kadish KM, Smith KM, Guillard R (eds) *The porphyrin handbook*, vol 15. Academic, San Diego, p 161
93. Rodriguez-Morgade MS, de la Torre G, Torres T (2003) In: Kadish KM, Smith KM, Guillard R (eds) *The porphyrin handbook*, vol 15. Academic, San Diego, p 125
94. Claessens CG, Gonzalez-Rodriguez D, Torres T (2002) *Chem Rev* 102:835
95. Torres T (2006) *Angew Chem Int Ed* 45:2834
96. Kipp RA, Simon JA, Beggs M, Ensley HE, Schmehl RH (1998) *J Phys Chem A* 102:5659
97. Sastre A, Torres T, Diaz-Garcia MA, Agullo-Lopez F, Dhenaut C, Brasselet S, Ledoux I, Zyss J (1996) *J Am Chem Soc* 118:2746
98. del Rey B, Keller U, Torres T, Rojo G, Agullo-Lopez F, Nonell S, Marti C, Brasselet S, Ledoux I, Zyss J (1998) *J Am Chem Soc* 120:12808
99. Martin G, Rojo G, Agullo-Lopez F, Ferro VR, Garcia de la Vega JM, Martinez-Diaz VM, Torres T, Ledoux I, Zyss J (2002) *J Phys Chem B* 106:13139
100. Claessens CG, Gonzalez-Rodriguez D, Torres T, Martin G, Agullo-Lopez F, Ledoux I, Zyss J, Ferro VR, Garcia de la Vega JM (2005) *J Phys Chem B* 109:3800
101. Diaz DD, Bolink HJ, Cappelli L, Claessens CG, Coronado E, Torres T (2007) *Tetrahedron Lett* 48:4657
102. Xu S, Chen K, Tian K (2005) *J Mater Chem* 15:2676
103. Palomares E, Martinez-Diaz MV, Haque SA, Torres T, Durrant JR (2004) *Chem Commun* 2112
104. Palomares E, Martinez-Diaz MV, Torres T, Coronado E (2006) *Adv Funct Mater* 16:1166
105. Claessens CG, Gonzalez-Rodriguez D, McCallumb CM, Nohr RS, Schuchmann H-P, Torres T (2007) *J Porphyrins Phthalocyanines* 11:181
106. Gonzalez-Rodriguez D, Torres T (2009) *Eur J Org Chem* 1871
107. Gonzalez-Rodriguez D, Claessens CG, Torres T (2009) *J Porphyrins Phthalocyanines* 13:203
108. Claessens CG, Gonzalez-Rodriguez D, del Rey B, Torres T, Mark G, Schuchmann H-P, von Sonntag C, MacDonald JG, Nohr RS (2003) *Eur J Org Chem* 2547
109. Iglesias RS, Claessens CG, Torres T, Herranz MA, Ferro VR, Garcia de la Vega JM (2007) *J Org Chem* 72:2967
110. Gonzalez-Rodriguez D, Torres T, Guldi DM, Rivera J, Echegoyen L (2002) *Org Lett* 4:335
111. Kim J-H, El-Khouly ME, Araki Y, Ito O, Kay K-Y (2008) *Chem Lett* 37:544
112. Gonzalez-Rodriguez D, Torres T, Herranz MA, Echegoyen L, Carbonell E, Guldi DM (2008) *Chem Eur J* 14:7670
113. Gonzalez-Rodriguez D, Torres T, Guldi DM, Rivera J, Herranz MA, Echegoyen L (2004) *J Am Chem Soc* 126:6301
114. El-Khouly ME, Shim SH, Araki Y, Ito O, Kay K-Y (2008) *J Phys Chem B* 112:3910

115. Gonzalez-Rodriguez D, Carbonell E, Guldi DM, Torres T (2009) *Angew Chem Int Ed* 48:8032
116. Martinez-Diaz MV, Fender NS, Rodriguez-Morgade MS, Gomez-Lopez M, Diederich F, Echevoyen L, Stoddart JF, Torres T (2002) *J Mater Chem* 12:2095
117. Guldi DM, Ramey J, Martinez-Diaz MV, de la Escosura A, Torres T, Da Ros T, Prato M (2002) *Chem Commun* 2774
118. El-Khouly ME, Rogers LM, Zandler ME, Suresh G, Fujitsuka M, Ito O, D'Souza F (2003) *ChemPhysChem* 4:474
119. D'Souza F, Gadde S, El-Khouly ME, Zandler ME, Araki Y, Ito O (2005) *J Porphyrins Phthalocyanines* 9:698
120. El-Khouly ME, Araki Y, Ito O, Gadde S, Zandler ME, D'Souza F (2006) *J Porphyrins Phthalocyanines* 10:1156
121. Rio Y, Seitz W, Gouloumis A, Vazquez P, Sessler JL, Guldi DM, Torres T (2010) *Chem Eur J* 16:1929
122. Ballesteros B, de la Torre G, Torres T, Hug GL, Rahman GMA, Guldi DM (2006) *Tetrahedron* 62:2097
123. Rodriguez-Morgade MS, Plonska-Brzezinska ME, Athans AJ, Carbonell E, de Miguel G, Guldi DM, Echevoyen L, Torres T (2009) *J Am Chem Soc* 131:10484
124. Sessler JL, Jayawickramarajah J, Gouloumis A, Pantos GD, Torres T, Guldi DM (2006) *Tetrahedron* 62:2123
125. Torres T, Gouloumis A, Sanchez-Garcia D, Jayawickramarajah J, Seitz W, Guldi DM, Sessler JL (2007) *Chem Commun* 292
126. de la Escosura A, Martinez-Diaz MV, Guldi DM, Torres T (2006) *J Am Chem Soc* 128:4112
127. D'Souza F, Ito O (2009) *Chem Commun* 4913
128. D'Souza F, Maligaspe E, Ohkubo K, Zandler ME, Subbaiyan NK, Fukuzumi S (2009) *J Am Chem Soc* 131:8787
129. D'Souza F, Maligaspe E, Sandanayaka ASD, Subbaiyan NK, Karr PA, Hasobe T, Ito O (2010) *J Phys Chem A* 114:10951
130. Kim JY, Bard AJ (2004) *Chem Phys Lett* 383:11
131. Geerts YH, Debever O, Amato C, Sergeev S (2009) *Beilstein J Org Chem* 5:49
132. de la Escosura A, Martinez-Diaz MV, Barbera J, Torres T (2008) *J Org Chem* 73:1475
133. El-Khouly ME, Ju DK, Kay K-Y, D'Souza F, Fukuzumi S (2010) *Chem Eur J* 16:6193
134. Claessens CG, Torres T (2002) *J Am Chem Soc* 124:14522
135. Claessens CG, Sanchez-Molina I, Torres T (2009) *Supramol Chem* 21:44
136. Claessens CG, Vicente-Arana MJ, Torres T (2008) *Chem Comm* 6378
137. Claessens CG, Gonzalez-Rodriguez D, Iglesias RS, Torres T (2006) *Comptes Rendus Chimie* 9:1094
138. Claessens CG, Torres T (2004) *Chem Commun* 1298
139. Lehtivuori H, Kumpulainen T, Hietala M, Efimov A, Lemmetyinen H, Kira A, Imahori H, Tkachenko NV (2009) *J Phys Chem C* 113:1984
140. Lehtivuori H, Kumpulainen T, Efimov A, Lemmetyinen H, Kira A, Imahori H, Tkachenko NV (2008) *J Phys Chem C* 112:9896
141. Guldi DM, Gouloumis A, Vazquez P, Torres T, Georgakilas V, Prato M (2005) *J Am Chem Soc* 127:5811
142. Peumans P, Bulovic V, Forrest SR (2000) *Appl Phys Lett* 76:2650
143. Peumans P, Yakimov A, Forrest SR (2003) *J Appl Phys* 93:3693
144. Hiramoto M, Suezaki M, Yokoyama M (1990) *Chem Lett* 327
145. Yakimov A, Forrest SR (2002) *Appl Phys Lett* 80:1667
146. Triyana K, Yasuda T, Fujita K, Tsutsui T (2005) *Jpn J Appl Phys* 44:1974
147. Khodabakhsh S, Sanderson BM, Nelson J, Jones TS (2006) *Adv Funct Mater* 16:95
148. Lare Y, Godoy A, Cattin L, Jondo K, Abachi T, Diaz FR, Morsli M, Napo K, del Valle MA, Bernede JC (2009) *Appl Surf Sci* 255:6615

149. Singh VP, Singh RS, Parthasarathy B, Aguilera A, Anthony J, Payne M (2005) *Appl Phys Lett* 86:2106
150. Wohrle D, Kreienhoop L, Schnurpfeil G, Elbe J, Tennigkeit B, Hiller S, Schlettwein D (1995) *J Mater Chem* 5:1819
151. Song QL, Wang ML, Obbard EG, Sun XY, Ding XM, Hou XY, Li CM (2006) *Appl Phys Lett* 89:1118
152. Tong XR, Bailey-Salzman RF, Wei GD, Forrest SR (2008) *Appl Phys Lett* 93:3304
153. Terao Y, Sasabe H, Adachi C (2007) *Appl Phys Lett* 90:3515
154. Peumans P, Forrest SR (2001) *Appl Phys Lett* 79:126
155. Murata K, Ito S, Takahashi K, Hoffman BM (1996) *Appl Phys Lett* 68:427
156. Peumans P, Uchida S, Forrest SR (2003) *Nature* 425:158
157. Kim I, Haverinen HM, Wang ZX, Madakuni S, Li J, Jabbour GE (2009) *Appl Phys Lett* 95:3305
158. Kim I, Haverinen HM, Wang ZX, Madakuni S, Kim Y, Li J, Jabbour GE (2009) *Chem Mater* 21:4256
159. Capobianchi A, Tucci M (2004) *Thin Solid Films* 451:33
160. Li N, Lassiter BE, Lunt RR, Wei G, Forrest SR (2009) *Appl Phys Lett* 94:3307
161. Brumbach M, Placencia D, Armstrong NR (2008) *J Phys Chem C* 112:3142
162. Placencia D, Wang WN, Shallcross RC, Nebesny KW, Brumbach M, Armstrong NR (2009) *Adv Funct Mater* 19:1913
163. Xue JG, Uchida S, Rand BP, Forrest SR (2004) *Appl Phys Lett* 84:3013
164. Chen WB, Xiang HF, Xu ZX, Yan BP, Roy VAL, Che CM, Lai PT (2007) *Appl Phys Lett* 91:11091
165. Hong ZR, Lessmann R, Maennig B, Huang Q, Harada K, Riede M, Leo K (2009) *J Appl Phys* 106:4511
166. Cheng CH, Wang J, Du GT, Shi SH, Du ZJ, Fan ZQ, Bian JM, Wang MS (2010) *Appl Phys Lett* 97:3305
167. Schueppel R, Timmreck R, Allinger N, Mueller T, Furno M, Uhrich C, Leo K, Riede M (2010) *J Appl Phys* 107:4503
168. Chauhan KV, Sullivan P, Yang JL, Jones TS (2010) *J Phys Chem C* 114:3304
169. Yu B, Huang LZ, Wang HB, Yan DH (2009) *Adv Mater* 22:1017
170. Lee J, Kim SH, Kim C, Kim JJ (2010) *Appl Phys Lett* 97:3306
171. Mutolo KL, Mayo EI, Rand BP, Forrest SR, Thompson ME (2006) *J Am Chem Soc* 128:8108
172. Gommans H, Schols S, Kadashchuk A, Heremans P, Meskers SCJ (2009) *J Phys Chem C* 113:2974
173. Gommans H, Cheyns D, Aernouts T, Giroto C, Poortmans J, Heremans P (2007) *Adv Funct Mater* 17:2653
174. Tong X, Lassiter BE, Forrest SR (2010) *Org Electronics* 11:705
175. Hiramoto M, Fujiwara H, Yokoyama M (1991) *Appl Phys Lett* 58:1062
176. Hiramoto M, Fujiwara H, Yokoyama M (1992) *J Appl Phys* 72:3781
177. Xue JG, Rand BP, Uchida S, Forrest SR (2005) *Adv Mater* 17:66
178. Xue JG, Uchida S, Rand BP, Forrest SR (2004) *Appl Phys Lett* 85:5757
179. Heutz S, Sullivan P, Sanderson BM, Schultes SM, Jones TS (2004) *Sol Energy Mater Sol Cells* 83:229
180. Chen L, Tang Y, Fan X, Zhang C, Chu Z, Wang D, Zou D (2009) *Org Electron* 10:724
181. Gebeyehu D, Maennig B, Drechsel J, Leo K, Pfeiffer M (2003) *Sol Energy Mater Sol Cells* 79:81
182. Drechsel J, Mannig B, Kozlowski F, Gebeyehu D, Werner A, Koch M, Leo K, Pfeiffer M (2004) *Thin Solid Films* 451:515
183. Maennig B, Drechsel J, Gebeyehu D, Simon P, Kozlowski F, Werner A, Li F, Grundmann S, Sonntag S, Koch M, Leo K, Pfeiffer M, Hoppe H, Meissner D, Sariciftci NS, Riedel I, Dyakonov V, Parisi J (2004) *Appl Phys A* 79:1
184. Higashi Y, Kim KS, Jeon HG, Ichikawa M (2010) *J Appl Phys* 108:4502

185. Gebeyehu D, Pfeiffer M, Maennig B, Drechsel J, Werner A, Leo K (2004) *Thin Solid Films* 451:29
186. Meiss J, Leo K, Riede MK, Uhrich C, Gnehr WM, Sonntag S, Pfeiffer M (2009) *Appl Phys Lett* 95:3306
187. Pfuetzner S, Meiss J, Petrich A, Riede M, Leo K (2009) *Appl Phys Lett* 94:3307
188. Pfuetzner S, Meiss J, Petrich A, Riede M, Leo K (2009) *Appl Phys Lett* 94:3303
189. Yang F, Shtein M, Forrest SR (2005) *Nat Mater* 4:37
190. Zheng Y, Bekele R, Ouyang JM, Xue JG (2009) *Org Electron* 10:1621
191. Li N, Forrest SR (2009) *Appl Phys Lett* 95:3309
192. Hein C, Mankel E, Mayer T, Jaegermann W (2010) *Sol Energy Mater Sol Cells* 94:662
193. Wei HX, Li J, Xu ZQ, Cai Y, Tang JX, Li YQ (2010) *Appl Phys Lett* 97:3302
194. Varotto A, Nam CY, Radivojevic I, Tomé JPC, Cavaleiro JAS, Black CT, Drain CM (2010) *J Am Chem Soc* 132:2552
195. Fischer MKR, Lopez-Duarte I, Wienk MM, Martinez-Diaz MV, Janssen RAJ, Bauerle P, Torres T (2009) *J Am Chem Soc* 131:8669
196. Ltaief A, Ben Chadbane R, Bouazizi A, Davenas J (2006) *Mater Sci Eng C* 26:344
197. Li G, Shrotriya V, Huang JS, Yao Y, Moriarty T, Emery K, Yang Y (2005) *Nat Mater* 4:864
198. Ma WL, Yang CY, Gong X, Lee K, Heeger AJ (2005) *Adv Funct Mater* 15:1617
199. Reyes-Reyes M, Kim K, Carroll DL (2005) *Appl Phys Lett* 87:3506
200. Jeffries M, McCullough RD (2007) In: Skotheim TA, Reynolds JR (eds) *Handbook of conducting polymers*. CRC, Boca Raton
201. Thompson BC, Frechet MJM (2008) *Angew Chem Int Ed* 47:58
202. Johansson EMJ, Yartsev A, Rensmo H, Sundstrom V (2009) *J Phys Chem C* 113:3014
203. Coffey DC, Ferguson AJ, Kopidakis N, Rumbles G (2010) *ACS Nano* 4:5437
204. Honda S, Nogami T, Ohkita H, Benten H, Ito S (2009) *ACS Appl Mater Interfaces* 1:804
205. Honda S, Ohkita H, Benten H, Ito S (2010) *Chem Commun* 46:6596
206. Troshin PA, Koeppe R, Peregodov AS, Egginger M, Lyubovskaya RN, Sariciftci NS (2007) *Chem Mater* 19:5363
207. Janssen AGF, Riedl T, Hamwi S, Johannes HH, Kowalsky W (2007) *Appl Phys Lett* 91:3519
208. Karousis N, Tagmatarchis N, Tasis D (2010) *Chem Rev* 110:5366
209. Sgobba V, Rahman GMA, Ehli C, Guldi DM (2007) In: Langa F, Nierengarten JF (eds) *Fullerenes: principles and applications*. RSC, Cambridge, p 329
210. Cao L, Chen H, Wang M, Sun J, Zhang X, Kong F (2002) *J Phys Chem B* 106:8971
211. Wang Y, Chen H-Z, Li H-Y, Wang M (2005) *Mater Sci Eng B* 117:296
212. Cao L, Chen H-Z, Zhou H-B, Zhu L, Sun J-Z, Zhang X-B, Xu JM, Wang M (2003) *Adv Mater* 15:909
213. Guldi DM, Marcaccio M, Paolucci D, Paolucci F, Tagmatarchis N, Tasis D, Vázquez E, Prato M (2003) *Angew Chem Int Ed* 42:4206
214. Yang X, Lu Y, Ma Y, Li Y, Du F, Chen Y (2006) *Chem Phys Lett* 420:416
215. Herranz MA, Martin N, Campidelli S, Prato M, Brehm G, Guldi DM (2006) *Angew Chem Int Ed* 45:4478
216. Herranz MA, Ehli C, Campidelli S, Gutierrez M, Hug G. L, Ohkubo K, Fukuzumi S, Prato M, Martin N, Guldi DM (2008) *J Am Chem Soc* 130:66
217. Murakami H, Nomura T, Nakashima M (2003) *Chem Phys Lett* 378:481
218. Guldi DM, Rahman GMA, Jux N, Tagmatarchis N, Prato M (2004) *Angew Chem Int Ed* 43:5526
219. Baskaran D, Mays JW, Zhang XP, Bratcher MS (2005) *J Am Chem Soc* 127:6916
220. Guldi DM, Taieb H, Rahman GMA, Tagmatarchis N, Prato M (2005) *Adv Mater* 17:871
221. Tanaka H, Yajima T, Matsumoto T, Otsuka Y, Ogawa T (2006) *Adv Mater* 18:1411
222. Guldi DM, Rahman GMA, Quin S, Tchoul M, Ford WT, Marcaccio M, Paolucci D, Paolucci F, Campidelli S, Prato M (2006) *Chem Eur J* 12:2152
223. Ehli C, Rahman GMA, Jux N, Balbinot D, Guldi DM, Paolucci F, Marcaccio M, Paolucci D, Melle-Franco M, Zerbetto F, Campidelli S, Prato M (2006) *J Am Chem Soc* 128:11222

224. Alvaro M, Atienzar P, de la Cruz P, Delgado JL, Troiani V, García H, Langa F, Palkar A, Echegoyen L (2006) *J Am Chem Soc* 128:6626
225. Yu J, Mathew S, Flavel BS, Johnston MR, Shapter JG (2008) *J Am Chem Soc* 130:8788
226. Palacin T, Khanh HL, Jousseme B, Jegou P, Filoramo A, Ehli C, Guldi DM, Campidelli S (2009) *J Am Chem Soc* 131:15394
227. Guldi DM, Rahman GMA, Prato M, Jux N, Qin S, Ford W (2005) *Angew Chem Int Ed* 44:2015
228. Sgobba V, Rahman GMA, Guldi DM, Jux N, Campidelli S, Prato M (2006) *Adv Mater* 18:2264
229. Hasobe T, Fukuzumi S, Kamat PV (2006) *J Phys Chem B* 110:25477
230. Liu J, Rinzler AG, Dai H, Hafner JH, Bradley RK, Boul PJ, Lu A, Iverson T, Shelimov K, Huffman CB, Rodriguez-Macias F, Shon YS, Lee T, Colbert DT, Smalley RE (1998) *Science* 280:1253
231. de la Torre G, Blau W, Torres T (2003) *Nanotechnology* 14:765
232. Yang Z, Pu H, Yuan J, Wan D, Liu Y (2008) *Chem Phys Lett* 465:73
233. Yang Z-L, Chen H-Z, Cao L, Li H-Y, Wang M (2004) *Mat Sci Eng B* 106:73
234. Xu HB, Chen HZ, Shi MM, Bai R, Wang M (2005) *Mat Chem Phys* 94:342
235. He N, Chen Y, Bai J, Wang J, Blau WJ, Zhu J (2009) *J Phys Chem B* 113:13029
236. Ballesteros B, de la Torre G, Ehli C, Rahman GMA, Agulló-Rueda F, Guldi DM, Torres T (2007) *J Am Chem Soc* 129:5061
237. Ballesteros B, Campidelli S, de la Torre G, Ehli C, Guldi DM, Prato M, Torres T (2007) *Chem Commun* 2950
238. Campidelli S, Ballesteros B, Filoramo A, Diaz Díaz D, de la Torre G, Torres T, Rahman GMA, Ehli C, Kiessling D, Werner F, Sgobba V, Guldi DM, Cioffi C, Prato M, Bourgojn JP (2008) *J Am Chem Soc* 130:11503
239. Bahr J, Tour JM (2001) *Chem Mater* 13:3823
240. Chen RJ, Zhang Y, Wang D, Dai H (2001) *J Am Chem Soc* 123:3838
241. Chitta R, Sandanayaka ASD, Schumacher AL, D'Souza L, Araki Y, Ito O, D'Souza F (2007) *J Phys Chem C* 111:6947
242. Kyatskaya S, Mascaros JRG, Bogani L, Henrich F, Kappes M, Wernsdorfer W, Ruben M (2009) *J Am Chem Soc* 131:15143
243. Wang BX, Liu YQ, Qiu WF, Zhu DB (2002) *J Mater Chem* 12:1636
244. Hatton RA, Blanchard NP, Stolojan V, Miller AJ, Silva SRP (2007) *Langmuir* 23:6424
245. Hahn U, Engmann S, Oelsne CR, Ehli C, Guldi DM, Torres T (2010) *J Am Chem Soc* 132:6392
246. Bottari G, Olea D, Gomez-Navarro C, Zamora F, Gomez-Herrero J, Torres T (2008) *Angew Chem Int Ed* 47:2026
247. Bottari G, Olea D, Lopez V, Gomez-Navarro C, Zamora F, Gomez-Herrero J, Torres T (2010) *Chem Commun* 46:4692
248. Kameyama K, Satake A, Kobuke Y (2004) *Tetrahedron Lett* 45(41):7617
249. Soares ARM, Martinez-Diaz MMV, Bruckner A, Pereira AMVM, Tome JPC, Alonso CMA, Faustino MAF, Neves MGPMS, Tome AC, Silva AMS, Cavaleiro JAS, Torres T, Guldi DM (2007) *Org Lett* 9(8):1557
250. Durmus M, Chen JY, Zhao ZX, Nyokong T (2008) *Spectrochim Acta A Mol Biomol Spectrosc* 70:42
251. Bian Y, Chen X, Wang D, Choi C-F, Zhou Y, Zhu P, Ng DKP, Jiang J, Weng Y, Li X (2007) *Chem Eur J* 13:4169
252. Maligaspe E, Kumpulainen T, Lemmetyinen H, Tkachenko NV, Subbaiyan NK, Zandler ME, D'Souza F (2010) *J Phys Chem A* 114:268
253. De la Escosura A, Martinez-Diaz MV, Thordarson P, Rowan AE, Nolte RJM, Torres T (2003) *J Am Chem Soc* 125:12300
254. Maya EM, Vazquez P, Torres T (1999) *Chem Eur J* 5:2004

255. Gonzalez-Rodriguez D, Claessens CG, Torres T, Liu S, Echegoyen L, Vila N, Nonell S (2005) *Chem Eur J* 11:3881
256. Zhao Z, Cammidge AN, Cook MJ (2009) *Chem Commun* 7530
257. Xu H, Ng DKP (2008) *Inorg Chem* 47:7921
258. Martinez-Diaz MV, Esperanza S, de la Escosura A, Cattellani M, Yunus S, Luzzatib S, Torres T (2003) *Tetrahedron Lett* 44:8475
259. Gonzalez-Rodriguez D, Torres T, Olmstead MM, Rivera J, Herranz MA, Echegoyen L, Atienza Castellanos C, Guldi DM (2006) *J Am Chem Soc* 128:10680
260. Camerel F, Ulrich G, Retailleau P, Ziessel R (2008) *Angew Chem Int Ed* 47:8876
261. Medina A, Claessens CG, Rahman GMA, Lamsabhi AM, Mo O, Yañez M, Guldi DM, Torres T (2008) *Chem Commun* 1759
262. Liu J-Y, Yeung H-S, Xu W, Li X, Ng DKP (2008) *Organic Lett* 10:5421
263. Ziessel R, Ulrich G, Elliott KJ, Harriman A (2009) *Chem Eur J* 15:4980
264. El-Khouly ME, Ryu JB, Kay K-Y, Ito O, Fukuzumi S (2009) *J Phys Chem C* 113:15444
265. El-Khouly ME (2010) *Phys Chem Chem Phys* 12:12746
266. Gommans H, Aernouts T, Verreet B, Heremans P, Medina A, Claessens CG (2009) *Torres T Adv Funct Mater* 19:3435
267. Klaus D, Knecht R, Dragasser A, Keil C, Schlettwein D (2009) *Phys Status Solidi A* 206:2723
268. Song QL, Yang HB, Gan Y, Gong C, Ming CL (2010) *J Am Chem Soc* 132:4554
269. Enes RF, Cid J-J, Hausmann A, Trukhina O, Gouloumis A, Vazquez P, Cavaleiro JAS, Tome AC, Guldi DM, Torres T (2012) *Chem Eur J* 18:1727
270. Pereira AMVM, Soares ARM, Hausmann A, Neves MGPMS, Tome AC, Silva AMC, Cavaleiro JAS, Guldi DM, Torres T (2011) *Phys Chem Chem Phys* 13:11858
271. Pereira AMVM, Hausmann A, Tome JPC, Trukhina O, Urbani M, Neves MGPMS, Cavaleiro JAS, Guldi DM, Torres T (2012) *Chem Eur J* 18:3210
272. Ince M, Hausmann A, Martinez-Diaz MV, Guldi DM, Torres T (2012) *Chem Commun* 48:4058
273. Cid J-J, Kahnt A, Vazquez P, Guldi DM, Torres T (2012) *J Inorg Biochem* 108:216
274. Bottari G, Suanzes JA, Trukhina O, Torres T (2011) *J Phys Chem Lett* 2:905
275. Bottari G, Trukhina O, Ince M, Torres T (2012) *Coord Chem Rev* 256:2453
276. Claessens CG, Martinez-Diaz MV, Torres T (2012) In: Gale PA, Steed JW (eds) *Supramolecular chemistry: from molecules to nanomaterials*. Wiley, p 1075
277. Ince M, Martinez-Diaz MV, Barbera J, Torres T (2011) *J Mater Chem* 21:1531
278. Hayashi H, Nishashi W, Umeyama T, Matano Y, Seki S, Shimizu Y, Imahori H (2011) *J Am Chem Soc* 133:10736
279. Bartelmess J, Ehli C, Cid J-J, García-Iglesias M, Vazquez P, Torres T, Guldi DM (2011) *Chem Sci* 2:652
280. Bartelmess J, Ehli C, Cid J-J, Garcia-Iglesias M, Vazquez P, Torres T, Guldi DM (2011) *J Mater Chem* 21:8014
281. Ince M, Bartelmess J, Kiessling D, Dirian K, Martinez-Diaz MV, Torres T, Guldi DM (2012) *Chem Sci* 3:1472
282. Sanchez-Molina I, Claessens CG, Grimm B, Guldi DM, Torres T (2013) *Chem Sci* 4:1338
283. Verreet B, Rand, Barry P, Cheyins D, Hadipour A, Aernouts T, Heremans P, Medina A, Claessens CG, Torres T (2011) *Adv Energy Mat* 1:565
284. Ryan JW, Anaya-Plaza E, de la Escosura A, Torres T, Palomares E (2012) *Chem Commun* 48:6094

Supramolecular Chemistry of Carbon Nanotubes at Interfaces: Toward Applications

Riccardo Marega, Davide Giust, and Davide Bonifazi

Abstract The properties at interfaces play important roles in biology and electronics. In the last 20 years, new carbon allotropes, like carbon nanotubes, have emerged as novel suitable substrates for the production of derivatives with wide range of technological applications. Since then, a great attention has been drawn in the study of the biological and technological properties of these novel allotropes at interfaces. Among the plethora of chemical reactions adopted to improve the properties of these nanostructured carbon species, the one employing supramolecular approaches have rapidly increased during the last years. In this chapter we will review the supramolecular approaches aimed at the functionalization of these carbon-based nanostructures focusing on their properties and applicative uses as self-organized materials at interfaces.

Keywords Carbon nanotubes · Interfaces · Supramolecular chemistry

R. Marega

Department of Chemistry, University of Namur (UNamur), Rue de Bruxelles 61, Namur, Belgium

D. Giust

Department of Organic, Inorganic and Biochemistry, University of Castilla la Mancha, Av.da José Cela 10, Ciudad Real, Spain

D. Bonifazi (✉)

Department of Chemistry, University of Namur (UNamur), Rue de Bruxelles 61, Namur, Belgium

Department of Chemical and Pharmaceutical Sciences, University of Trieste, Piazzale Europa 1, Trieste, Italy

e-mail: davide.bonifazi@unamur.be

Contents

1	Introduction	194
2	Supramolecular Chemistry of Carbon Nanotubes at the Interfaces	195
2.1	Carbon Nanotubes at the Solid/Liquid Interface	195
2.2	Carbon Nanotubes at the Liquid/Liquid Interface	199
2.3	Carbon Nanotubes at the Gas/Solid Interface	202
2.4	Carbon Nanotubes at the Biological Interface	205
3	Conclusions	212
	References	212

1 Introduction

Interfaces can be considered as the shared boundary between two phases, bodies or spaces. The interfacial properties between different phases are of fundamental importance in both chemical and life sciences, since they are involved in many bio-technological fields. As an example, the production of novel materials heavily involves interfacial processes: thin film deposition and growth onto substrates are often dictated by surface effects, and some examples are related to coatings and paint production and latex films. In tribology, the science and engineering of interacting surfaces in relative motion, the phenomena of friction can be reduced by lubrication, which is a pivotal surface phenomenon. Lubrication, catalysis and electrochemistry, crystal growth, all occurs at solid/liquid interface. In the biological domain, dynamics and structure of bio-membranes, which surrounds both cell and its internal organelles, play critical roles in fundamental physio-pathological processes. As an example, cell–cell interactions not only lead to the formation of differentiated tissues, but are also the basis for third-body recognition by our immune system. Also energy production biological pathways, like photosynthesis in chloroplasts and oxidative phosphorylation in mitochondrion, occur at the interface between membranes and the surrounding environment. Those are only a few situations in which in a proper understanding of both physical and chemical phenomena requires a detailed interfacial-structure knowledge at molecular or even atomic scale. It is widely accepted that interfacial physicochemical properties (for instance, composition, wettability, or tribology) can be modified and tuned by both inorganic- [1] and organic-based chemical modifications [2]. In the recent years, supramolecular chemistry [3] played important roles on the control of both structure and the properties of organic molecules confined at interfaces. The use of reversible, weak interactions has been inspired by the need to develop smaller and smaller components in order to maximize, for example, the information storage capabilities of silicon-based devices [4]. In this review we will focus on the most significant advances in the use of supramolecular chemistry for the implementation of specific carbon nanotube (CNT) derivatives displaying exploitable properties at interfaces. The examples that we propose in this chapter, which accounts two

different approaches, are described: at first the supramolecular chemistry tools used to combine CNTs' properties with that of organic moieties (displaying useful technological or biological functions) will be highlighted. Secondly, pristine or covalently modified CNT derivatives (subsequently post-functionalized through noncovalent interactions) useful for specific applications will be illustrated. A particular focus will be given on the fundamental discoveries that might bring these carbon-rich nanostructures closer to real applications.

2 Supramolecular Chemistry of Carbon Nanotubes at the Interfaces

CNTs were discovered in 1991 by Ijima [5], and since then they have given a significant contribution to the advancement of nanotechnology [6] and nanomedicine [7]. CNTs possess excellent optical, electrical, thermal and mechanical properties [8] and therefore they have been proposed for the production of field-emission transistors [9], molecular electronics [10, 11], energy [12] and gas storage [13], composites [14–16] and biosensors [17, 18].

2.1 Carbon Nanotubes at the Solid/Liquid Interface

Several aromatic molecules, such as porphyrin [19–24], pyrene [25–27], and their derivatives, interact with the outer SWNTs sidewalls through both hydrophobic and π - π stacking interactions, thus allowing for their supramolecular functionalization [28–30]. Dai and coworkers have first reported a versatile protocol for SWNT noncovalent derivatization that allows the subsequent conjugation of (bio) molecules onto SWNTs [31, 32]. Starting from either *N,N*-dimethylformamide (DMF) or MeOH the bifunctional molecule *N*-succinimidyl-1-pyrenebutanoate used in their studies can be permanently adsorbed onto the hydrophobic sidewalls of SWNTs (Fig. 1). The *N*-succinimidyl-1-pyrenebutanoate molecules anchored onto SWNTs surfaces are highly resistant to desorption in aqueous solution, allowing additional SWNTs functionalization through succinimidyl ester groups, which are reactive to nucleophilic substitution by amino groups of proteins (such as streptavidin) or the useful linker biotiny-3,6-dioxaoctanediamine [31].

This procedure has opened up the way for the immobilization of an ample range of molecules on the SWNT sidewalls with high specificity, for the development of SWNT/FET and biosensors. In general, SWNT/FET devices have been found to be responsive to many analytes at the solid/liquid interface [33, 34]. After noncovalent functionalization of SWNT, these analytes can modulate SWNTs conductivity in two different manners. First, there may be a charge/electron transfer between SWNTs and the analytes, upon changing carrier concentration (n); secondly, the adsorbed analytes can operate as randomly distributed scattering potentials,

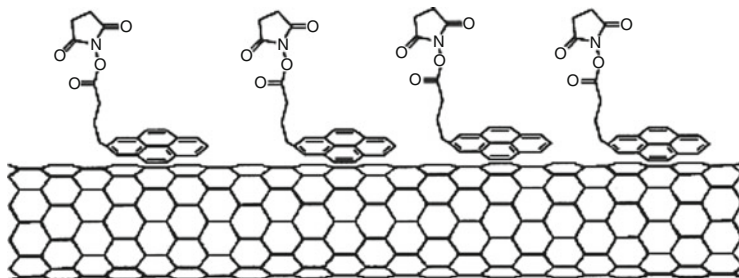


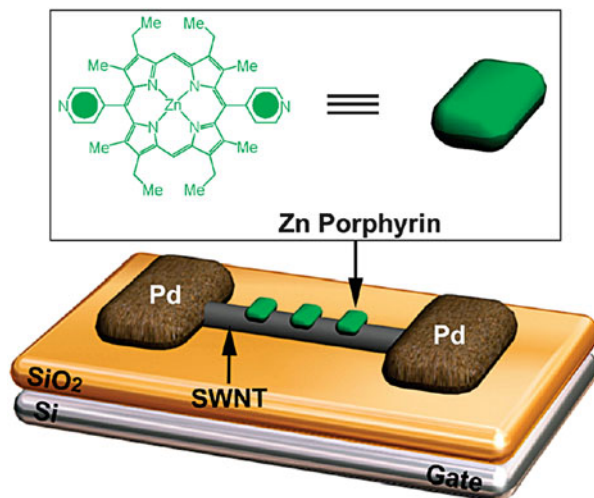
Fig. 1 Representation of the irreversible adsorption of *N*-succinimidyl-1-pyrenebutanoate onto SWNT outer walls. Adapted with permission from [31], Copyright 2001, American Chemical Society

therefore changing charge carrier mobility (μ). The conductivity is generally defined by $G = ne\mu$, where e is the electron charge, therefore the transistor measurements of the transfer characteristics in the SWNT/FET devices can be distinguished between (1) a change in carrier concentration and (2) a change in electrons mobility. Extensive characterizations has established that [33], in SWNT/FET devices, changes in n determine shifts of the threshold voltage (the voltage at which the device turns on for the first time). The binding of electron-accepting molecules (such as NO_2), to the SWNTs usually leads to a threshold voltage shift toward positive gate voltages, while the binding of electron-donating molecules (such as NH_3) leads to a shift toward negative gate voltages. On the other hand, a change in the mobility μ results in a change in the tilt (device transconductance), which is defined by the ratio of the slope of the $I_{\text{SD}}-V_{\text{g}}$ curve to its initial slope, where both slopes are measured at zero gate voltage. The decrease in device mobility can be determined by geometric deformations introduced on the nanotube structure by the properties of the analyte, through change occurring at the intertube interface or by randomly charged scattering centres.

Stoddart and coworkers designed SWNT/FET devices with the aim to clarify the electron/charge transfer at the donor-acceptor SWNT interface. As an example, a SWNT/FET device, noncovalently functionalized with a zinc porphyrin moiety [35], was employed to directly determine a photoinduced electron transfer within the device (Fig. 2).

The SWNTs act as the electron donors, while the porphyrin molecules act as the electron acceptors. The photoresponse of the zinc porphyrin-coated SWNT/FET was investigated by its illumination at 420 nm, a value closer to the maximum absorption wavelength (416 nm) of the Soret band (characteristic of the zinc porphyrin). The photoresponse of the device causes a shift of the threshold voltage toward positive values, suggesting hole doping of the SWNTs. The direction of the threshold voltage shift suggest that the photoresponse occurs through the electron transfer from the SWNTs to the zinc porphyrin, a fact which is unexpected since porphyrins are usually considered to be electron donors [36]. A possible explanation for this electron-transfer process is that, after photoexcitation of the zinc porphyrin, some of the electrons, which had been transferred to the SWNT (ground

Fig. 2 Schematic representation of the SWNT/FET device based on Zn-porphyrin/SWNT hybrid. Reprinted with permission of [35] Copyright 2006, American Chemical Society



state), are transferred back to the zinc porphyrin molecule in the excited state. The magnitude of the photoinduced electron transfer was found to be a function of both the intensity and wavelength of the applied light, with a maximum of 0.37 electrons per zinc porphyrin for light of 100 W m^{-2} at 420 nm [35]. With the aim of performing quantitative investigations on the chemical sensors based on noncovalently functionalized SWNT/FET devices, Gruner and coworkers synthesized a pyrene-modified cyclodextrin (pyrenecyclodextrin) derivative [37]. They employed such hybrid to fabricate pyrenecyclodextrin-decorated SWNT/FET devices, which can serve as chemical sensors for the selective detection of specific organic molecules, on the basis of their molecular recognition by the cyclodextrin inner cavity, thus acting as the sensing host (Fig. 3).

In the presence of certain organic molecules, the transistor characteristics of the SWNT/FET device shifted toward negative gate voltage, with the following guest sensitivity: 1-adamantanol > 2-adamantanol > 1-adamantanecarboxylic acid > sodium deoxycholate > sodium cholate. These observations suggest that the electrical conductance of the device is highly sensitive to determined organic molecules and moreover it changes appreciably with variations in the surface adsorption of the aforementioned molecules. Interestingly, in the presence of the organic molecules, the level of the transistor characteristic movements in the SWNT/FET devices depends linearly on the strength of the complex formation constants (K_S) exhibited by the pyrenecyclodextrin device with these analytes. As a consequence, the pyrenecyclodextrin-decorated SWNT/FET devices can be used as chemical sensors to detect organic molecules in aqueous solution, in a selective and quantitative manner.

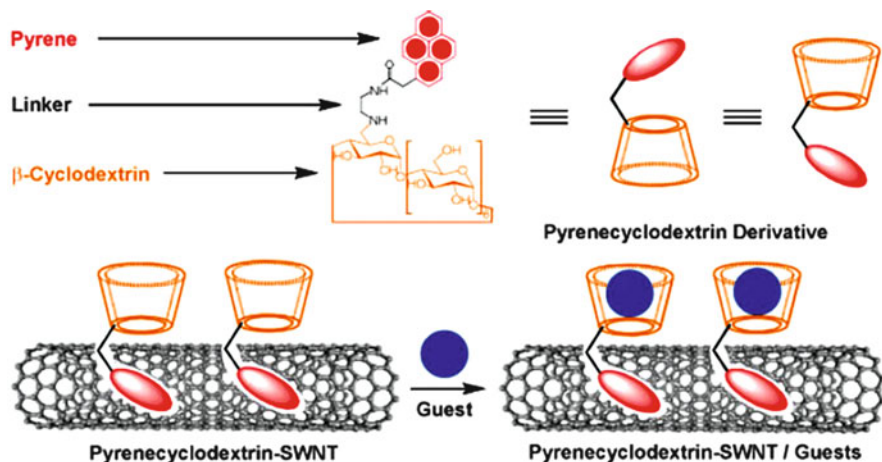


Fig. 3 Schematic drawing of the pyrenecyclodextrin-decorated SWNT hybrids and the interaction mode with the guest analytes as the working principle of the FET device. Reprinted with permission from [37], Copyright 2008, Wiley-VCH

It is widely accepted that the surfaces of SWNT networks, typically used as thin-film transistors or sensors, irreversibly adsorb a wide range of analytes [38–47], despite the mechanism has not been fully elucidated. Using thionyl chloride as a model electron-poor adsorbate, Young Lee and Strano demonstrated that reversible adsorption sites can be created on the nanotube array via supramolecular functionalization with amine terminated molecules of $pK_a < 8.8$ [48]. A nanotube network composed by single, mostly unbundled nanotubes, near the electronic percolation threshold, was necessary for the effective conversion to a reversibly binding array. By testing different amine-containing molecules, such as pyridine, aniline, hydrazine, and ethylenediamine the authors reported that analyte adsorption is largely affected by the basicity (pK_b) of the surface groups. The analyte-binding energy was apparently reduced by the adsorption on the surface chemical groups instead of directly on the SWNT array itself. X-ray photoelectron spectroscopy (XPS) and molecular potential calculations supports this model of adsorption mechanism. By creating a higher adsorption site density with an amino-polymer-like polyethyleneimine (PEI), reversible detection at the parts-per-trillion level for the first time was then demonstrated. It should be pointed out that some other amines, such as benzylamine, diethylenetriamine, dimethylamine, and triethylamine determined an irreversible binding to the sensor, as a consequence of strong device–analyte interactions. Another example of the employment of CNT derivatives at the solid–liquid interface is related to their general property to act as sorbents. CNTs present large and biocompatible surface areas, which afford not only huge potential for biotechnological applications but also promising scenario in separation science. A survey of the published literature provides a range of applications of CNTs serving as solid-phase extraction media [49] for the separation/isolation of organic species [50–75] and trace metal [76–78]. In fact, Wang and coworkers used

MWCNTs for the isolation of basic proteins from other protein species in biological sample matrices by solid-phase extraction (SPE) [79]. After appropriate pretreatment into a sequential injection system a microcolumn packed with MWCNTs was incorporated. This device facilitated online selective sorption of basic protein species like hemoglobin and cytochrome c. In fact, oxidized MWCNTs are negatively charged at pH 6 whereas hemoglobin (isoelectric point, $pI = 7$) and cytochrome c ($pI = 10$) are both positively charged. As a consequence, electrostatic interactions occurred between the MWCNT surfaces and the basic proteins, therefore determining their adsorption onto MWCNT surfaces. The retained protein species were subsequently isolated from each other by sequential elution from the microcolumn, by the use of appropriate eluents. Phosphate buffer solution (0.025 mol L^{-1} at pH 8.0) allowed the efficient isolation of hemoglobin, while a NaCl solution (0.5 mol L^{-1}) afforded the quantitative recovery of the retained cytochrome c. By using a sample loading volume of 2.0 mL, enrichment factors of 11 and 15 were obtained for hemoglobin and cytochrome c, with retention efficiencies of 100% for both species and recovery rates of 98% and 90%, respectively. The practical applicability of this system was demonstrated by processing human blood for isolation of hemoglobin, and satisfactory results were obtained by assay with SDS-PAGE.

2.2 Carbon Nanotubes at the Liquid/Liquid Interface

Through an interfacial trapping approach, Ziegler and coworkers showed that SWNT bundles can be selectively removed from an aqueous dispersion containing individually suspended carbon nanotubes which resulted coated with a gum Arabic moiety [80]. After the dispersion of the nanotubes in water through the gum Arabic interaction, a two-phase system was created by the addition of toluene. The absorbance spectra of the bulk aqueous phase showed high absorbance, due to the presence of both individual and bundled SWNTs. After the interfacial trapping the absorbance of the suspension was clearly reduced, while the spectral features were better resolved and blue-shifted (Fig. 4).

These changes are in agreement with the removal of nanotubes from the aqueous phase, and the presence of a higher fraction of individualized SWNTs. By the comparison of the fluorescence intensities between these solutions and the ones obtained in similar conditions (by using ultracentrifugation), it was concluded that the amount of individual nanotubes significantly increased.

The same group also reported on the use of the common phase-transfer catalyst tetraoctylammonium bromide (TOAB) to afford length-dependent extraction of SWNTs [81]. The sidewalls of the purified nanotube were functionalized with chloroaniline sulfonate using a previously described method [82]; then, concentrated nanotube solutions in water were prepared without surfactants. The functionalized nanotubes showed a relatively high solubility in water and in other polar solvents (e.g., MeOH, EtOH). As a consequence, the nanotubes were dissolved in water

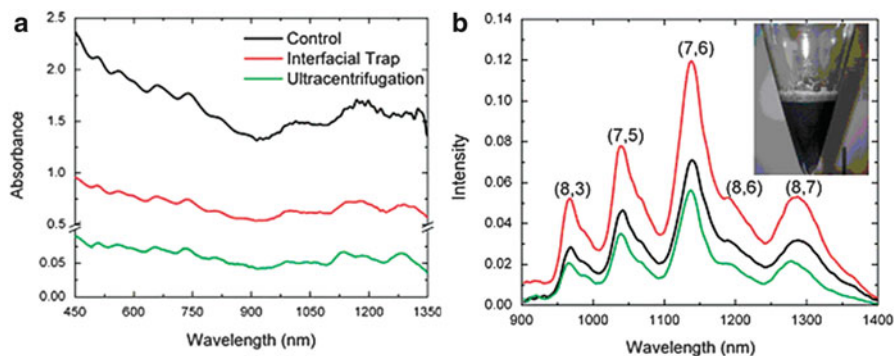


Fig. 4 (a) Absorbance and (b) fluorescence (exc. 662 nm) spectra for the interfacial trapping process of gum Arabic-suspended SWNTs (SWNT mass concentration = 0.03 mg mL^{-1}). The control spectra (black lines) are the SWNTs after homogenization and ultrasonication. The inset shows the interfacial trapping process in a separatory funnel. The control sample is then subjected to either ultracentrifugation (green lines) or interfacial traps (red lines). The fluorescence from specific (n, m) types is labeled. Reprinted with permission of [80] Copyright 2008, American Chemical Society

($0.04\text{--}0.2 \text{ mg mL}^{-1}$) and placed in a vial. Then, a solution of TOAB in an organic solvent (EtOAc, toluene) was added to the vial at a 1:1 volume ratio resulting in a liquid–liquid phase system. After the two-phase mixture is shaken, the system becomes a gray emulsion. By using an excess of TOAB, the emulsions settled and complete extraction of the nanotubes into the organic layer occurred. It should be pointed out that previous approaches that have involved sulfonate or other groups [83] interacting with TOAB have shown an electrostatic interaction. It is therefore most likely to occur that nanotubes extraction occurs via stoichiometric electrostatic interactions between the anionic SO_3^- moiety on the functional groups on the nanotube sidewall and the cationic TOA^+ . Length-dependent extractions were thus obtained by employing a substoichiometric ratio of TOAB. Under these TOAB-starved conditions, the nanotube solubility and their colloidal interactions can be efficiently controlled, allowing separations based on the length of the nanotubes. The starting material had a broad distribution of nanotube lengths with an average of 275 nm. The addition of a TOAB amount enough to complex 30% of all SO_3^- moieties resulted in only very short nanotubes being extracted into the organic layer as determined by AFM. Increased ion-pairing results in longer nanotubes being extracted and, after 75% of the SO_3^- moieties are ion paired, the length distribution matched that of the starting material.

Niu and coworkers reported an elegant example of SWNT assembly at the water/oil (W/O) interface, by preparing imidazolium-modified SWNTs (SWNTs-Im) [84]. At first, SWNTs-Im were dispersed in water by ultrasonication and after chloroform addition, they remained in the upper layer. Then, after ultrasonication for few seconds and standing overnight, SWNTs-Im spontaneously transferred onto the W/O interface. By fixing the area of the W/O interface and controlling the concentration of SWNTs-Im aqueous solution, films with different thicknesses were obtained. Interfacial

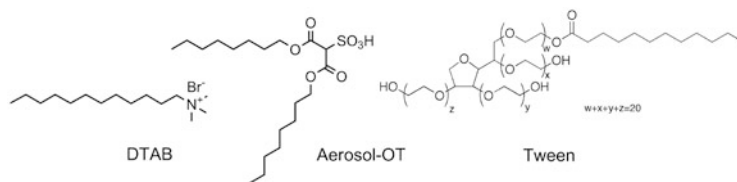


Fig. 5 Structural representation of some surfactants employed for the SWNT transfer at the aqueous/hexane interface

assembly of SWNTs was driven by minimizing the interfacial energy, ΔE . Due to SWNTs assembly from the aqueous solution to the W/O interface, ΔE can be given by $-\pi R^2 \gamma_{ow}(1 - \cos \theta)$, where R , γ_{ow} and θ represent the equivalent radius of SWNTs, the tension of the W/O interface and the contact angle of SWNTs with the interface, respectively. Therefore, the utilization of the W/O interface on one hand offered an alternative pathway for assembling SWNTs but also provided a functional SWNT-sandwiched W/O interface, which would have potential applications in electron-transfer (ET) process. Therefore, the contribution of the SWNTs-Im to ET at the W/O interface was investigated by scanning electrochemical microscopy, by preparing water phases containing electroactive species ($\text{Ru}(\text{NH}_3)_6^{3+}$). Without SWNTs-Im at the W/O interface, the tip current decreased when the tip approached the interface (negative feedback). This means that the initial redox species ($\text{Ru}(\text{NH}_3)_6^{3+}$) in water could not be regenerated and the diffusion of the original redox species ($\text{Ru}(\text{NH}_3)_6^{3+}$) to the tip was hampered. However at the SWNT-Im-sandwiched interface, the tip current increased when the tip approached the interface. This facet indicated that, in the presence of SWNTs-Im, the initial form of the redox species could be regenerated at the W/O interface.

Dordick and coworkers observed that an aqueous dispersion of purified SWNTs, when contacted with an equal volume of hexane (or isooctane, CHCl_3 , or CH_2Cl_2) containing a 2 mM concentration of the anionic surfactant Aerosol-OT (AOT, 1,4-dioctoxy-1,4-dioxobutane-2-sulfonic acid, Fig. 5), led to SWNTs transfer from the aqueous phase to the interface [85]. The interfacial assembly was also observed when a dispersion of SWNTs in hexane was poured in solutions of the neutral surfactant Tween (Polyoxyethylene (20) sorbitan monolaurate), the cationic surfactant dodecyltrimethylammonium bromide (DTAB), or the cationic lipid 1,2-dimyristoyl-3-trimethylammonium propane (DMTAP).

On the basis of these observations, the authors reasoned that the nanotubes could be exploited as carriers for the transportation of proteins to an aqueous–organic interface, enabling the possibility to enhance the rate of interfacial (bio) transformations. As an example, they adsorbed onto SWNTs the protein soybean peroxidase (SBP), which requires a hydrophobic phenol and the hydrophilic H_2O_2 , in order to test interfacial catalysis [86]. In the presence of AOT, the SWNT–SBP conjugates assembled at the hexane–water interface. By using UV-Vis spectroscopy no protein or SWNTs were detected in either of the bulk phases. The catalytic activity

of the interfacial SWNT–SBP was determined using *p*-cresol, a model peroxidase substrate. Consequently, the product was detectable only in the organic phase, with an initial reaction rate for interfacial SWNT–SBP of ca. 75 nM s^{-1} . This rate is three orders of magnitude higher than what is observed with identical enzyme concentrations either for native SBP or SWNT–SBP in the aqueous phase of a biphasic system in the absence of AOT or for native SBP in the aqueous phase in the presence of AOT.

Valcárcel and coworkers employed MWCNTs as extractant for the benzene, toluene, ethylbenzene, the three xylenes isomers (ortho, meta, and para) and styrene, all referred as BTEX-S [87]. The detection was carried out through headspace/gas chromatographic/mass spectrometric (HS/GC/MS) determination of different olive oil samples [88]. BTEX-S are substances that are emitted from a variety of sources into the environment, including aerosols, combustion products of fuels and wood, adhesives, industrial paints and degreasing agents. Their lipophilic nature and common presence in the environment (air, water, and soil) lead to their accumulation in foodstuffs, as fats and edible oils. In this work they employed surfactant-coated MWCNTs as additive in liquid–liquid extraction (LLE) for the determination of single-ring aromatic compounds in olive oil samples. After sample treatment, the aqueous extracts collected by this way were analyzed by HS/GC/MS, permitting the quantification of BTEX-S within ca. 15 min. Each step of the reported LLE/HS/GC/MS setup determines a selectivity enhancement, avoiding the interference of other compounds of the sample matrix. The detection limits resulted in the range of 0.25 ng mL^{-1} (obtained for ethylbenzene) and 0.43 ng mL^{-1} (for benzene).

2.3 Carbon Nanotubes at the Gas/Solid Interface

Ha and coworkers studied the effects of molecular adsorption on the electrical properties of carbon nanotube gas sensors over a wide range of gas concentrations [89]. Gas sensors were fabricated by depositing one to two drops of a solution of purified SWCNTs and dichloroethane on Au electrodes pre-patterned on a SiO₂ 500-nm/Si100 substrate. SWNT networks functionalization with polyethyleneimine (PEI) or nafion was carried out by following previously reported conditions [90]. The p-type characteristic was maintained after functionalization of the device with PEI, contrary to the case of individual SWCNTs in which the PEI coating changes the behavior from p-type to n-type due to electron donation of the amine groups in PEI. In the linear $I-V_g$ region, dI/dV_g is about $1.1 \times 10^{-7} \text{ A/V}$ for both raw ($V_{SD} = 50 \text{ mV}$) and PEI-coated ($V_{SD} = 200 \text{ mV}$) networks. From the relation $dI/dV_g = \mu_h(C/L^2)V_{SD}$ where C is the capacitance and L is the distance between source and drain, the hole mobility μ_h decreased by about four times after PEI coating, suggesting that the local deformations of the electronic structure at the PEI-adsorption sites acted as scattering center for conducting carriers. These observations highlight that the PEI coating decreases both hole concentration and hole mobility in CNTs because the conductance decreases by about ten times after PEI coating. The nafion coating, however, did not

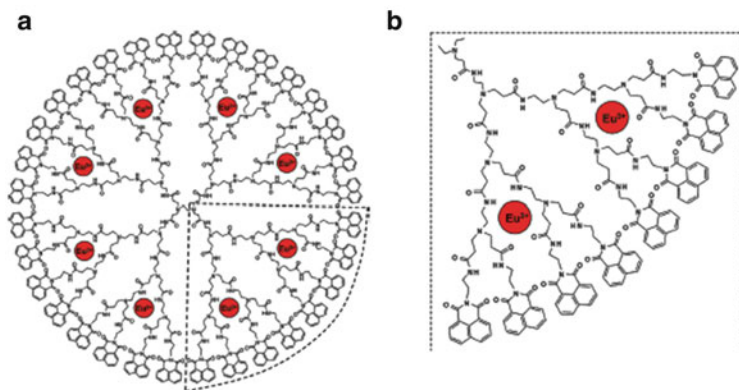


Fig. 6 (a) Structural representation of the Eu_8 complex, which contains eight Eu^{3+} cations (red circles) coordinated within a 1,8-naphthalimide-terminated, G3-PAMAM dendrimer core. (b) Detailed view of the Eu_8 complex illustrating Eu^{3+} ions coordination domains. Reprinted with permission of [91] Copyright 2009, Nature Publishing Group

cause any noticeable change in the $I-V_g$ characteristics. The conductance of PEI-coated devices increases rapidly when exposed to NO_2 , but the conductance of the nafion-coated devices decreases upon exposure to NH_3 molecules. Neither device exhibits any noticeable change upon exposure to pure N_2 , O_2 , Ar, or H_2 , the major components of the air.

The simple and tough architecture of microelectronic devices based on carbon nanotubes, along with their environmental sensitivity, places them among the most important candidates for incorporation into ultraportable or wearable chemical analysis devices. Star and coworkers described the spectroscopic and electrical behavior of simple chemiresistor devices composed of SWNT networks decorated with an oxygen-sensitive Eu^{3+} -containing dendrimer complex [91]. Complexes that contain lanthanides show solution-phase sensitivity toward oxygen, a characteristic that the authors exploited by immobilizing a Eu_8 -G3-PAMAM-(1,8-naphthalimide) dendrimer on highly conductive and optically transparent SWNT-based devices (Fig. 6).

In the Eu_8 structure, the 1,8-naphthalimide groups act as sensitizing moiety. Specifically, photoexcited electrons in the excited naphthalimide singlet state undergo intersystem crossing (ISC) into a triplet state (T3) and subsequent energy transfer into the accepting levels of the Eu^{3+} ions produces the sharp Eu^{3+} -centered emission bands in solution. The reversible and reproducible quenching effect of oxygen on the solution-phase Eu_8 -emission intensity is in accordance with its predicted behavior. However, it was then found that the Eu^{3+} -centered emission bands show a larger sensitivity to oxygen compared with the 1,8-naphthalimide band. The relative emission intensity of solid-state Eu_8 (drop casted onto a quartz substrate) was constant when cycled between atmospheres of pure oxygen and argon, which highlighted a fundamental difference between the behavior of solid-state and solution-phase samples. Indeed, after illuminating the sample with 365-nm light for 30 min (in flowing argon), the emission profile of the solid-state Eu_8

developed sensitivity toward oxygen such that the intensity decreased after illumination and partially restored under flowing oxygen.

By using simultaneous ultraviolet–visible–near-infrared (UV–Vis–NIR) absorbance spectroscopy and network conductance measurements on Eu_8 -SWNT devices, they found that the underlying SWNT network was able to transduce changes in the electronic properties of the Eu_8 layer during illumination with 365-nm light and exposure to pure oxygen gas. After an illumination period of 30 min the device experienced a decrease in the first semiconducting SWNT absorption band. Additionally, illumination triggered an increase in the network conductance. By combining the optical and electrical resistance measurements, the Eu_8 -decorated SWNT (Eu_8 -SWNT) devices demonstrate a linear sensitivity toward oxygen gas in the environmentally relevant concentration range of 5–27% when they operate at room temperature and ambient pressure, which represents an important step in the development of small-scale and low-power detection platforms for oxygen.

In another avenue, Strano and coworkers reported the ability to engineer molecular reversibility of the gas adsorption onto polymer-functionalized SWCNTs sensor array to enable the development of new types of nanoelectronic devices for analyte detection using microelectromechanical system (MEMS)-based micro gas chromatography (μGC) [92]. An interdigitated electrode design was chosen to maximize the nanotube surface area for analyte adsorption, as predicted from their model. A SWNT network was formed across the electrodes through ac dielectrophoresis; then, polypyrrole (PPy), an amine of $\text{p}K_{\text{b}} = 5.4$, was selected as a functionalization material for the binding of dimethyl methylphosphonate (DMMP), a nerve agent simulant, at the end of a μGC column.

Control experiments with only PPy on the electrode gap showed no response to DMMP, whereas a typical change in sensor conductance, upon device exposure to 1 mL pulses of DMMP vapor, was assessed. The responses have fallen within the ppb range and were completely reversible, with full width at half maximum (FWHM) of only about 4 s. The decrease in conductance was attributed to electron-donating DMMP molecules adsorbed on p-type semiconducting SWNTs.

Also the response from unfunctionalized sensors was reversible, but only after PPy functionalization, the sensitivity was increased by three orders of magnitude, with the reversibility retained. With H_2 carrier gas flowing at 40 psi, a DMMP headspace (2 mL) was manually injected (<0.3 s) at a 7:1 split and the conductance was monitored (Fig. 7). The injector and column temperature were 250°C and 30°C , respectively. The sensor response was reversible and negative, with full width at half maximum (FWHM) of 26 s. The 150-ppb pulse corresponds to approximately 10^9 DMMP molecules, a number that was confirmed by the downstream flame ionization detector (FID). This experimental approach and the reported detection limits (as low as 10^9 molecules) were not demonstrated before with any similar analytical platform.

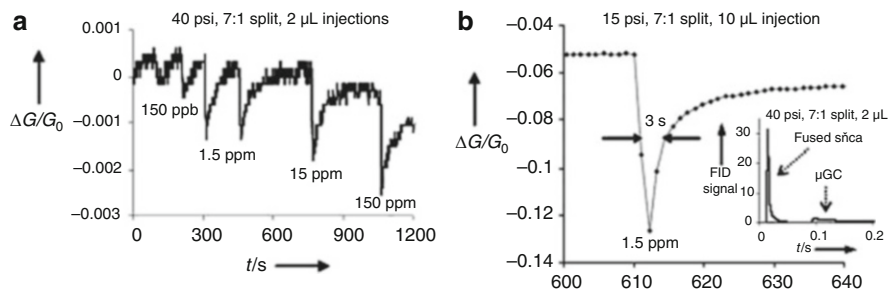


Fig. 7 Reversible SWNT sensor integration within a μ GC column. (a) DMMP pulses through the μ GC column detected by a PPy-functionalized sensor. A 150-ppb pulse corresponds to 10^9 DMMP molecules. (b) Response of a PPy-functionalized sensor to a DMMP pulse through a conventional fused-silica column. The peak is much sharper (FWHM ~ 3 s) than that from the μ GC column (FWHM ~ 26 s). This is because of peak broadening in the μ GC column, as confirmed by the FID signal (*inset*) (Reprinted with permission of [92] Copyright 2008, Wiley-VCH)

2.4 Carbon Nanotubes at the Biological Interface

Several CNT properties, like the optical adsorption in the visible near-infrared (Vis-NIR) region [93], the electrical conductivity [8, 94], and the wide chemical processability [28, 29, 95], make these carbon allotropes very attractive for biomedical applications [32, 96–98]. The most relevant studies of CNT employment at the biological interface are related to their use as substrate for cellular growth [99–107], as drug-delivery and anticancer platforms [7, 108–111] and as gene transfection or silencing mediators [112–117]. As substrates for cellular growth, CNTs and CNT derivatives were successfully employed for neuronal cells growth and differentiation [99–103, 105, 106]. The rationale consisted in the consideration of both CNTs electrical conductivity and high length-to-diameter ratio, which allows comparing them to the natural occurring dendrites and axons. Prato and coworkers demonstrated the possibility of using carbon nanotubes (CNTs) as potential devices able to improve neural signal transfer, while supporting both cell adhesion and dendrite elongation processes [102]. At first, they performed 1,3 dipolar cycloaddition on MWCNTs, in order to impart them organic solvent solubility, allowing for a product purification [118]. The MWCNTs were then deposited onto glass coverlips, which were subsequently heated at 350°C in order to defunctionalize the MWCNTs and leave a purified and nonfunctionalized materials on the glass surface. The problem of CNT integration within a functional neuronal network was addressed by using hippocampal neurons isolated and seeded directly on glass coverslips, taken as control, or on a film of purified CNTs, directly layered on glass as described above (Fig. 8).

To investigate neural network activity when neurons grew integrated to a CNT substrate, they used single-cell patchclamp measurements. They monitored the occurrence of spontaneous postsynaptic currents (PSCs), since the appearance of PSCs provides clear evidence of functional synapse formation. Under these conditions, neurons deposited on CNTs displayed on an average of sixfold increase

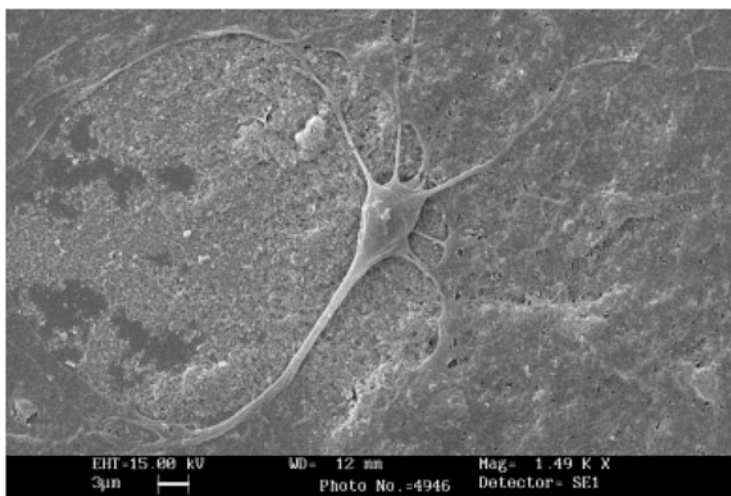


Fig. 8 SEM image of a neonatal hippocampal neuron growing on dispersed MWNT after 8 days in culture. Reprinted with permission of [102] Copyright 2005, American Chemical Society

in the frequency of spontaneous PSCs (6.67 ± 1.04 , $n = 15$ cultures, five culture series). Then, they further investigated the possibility that CNT substrates affected the balance between inhibition and excitation, by estimating the percentage of excitatory PSCs toward the total number of PSCs. This value was similar in control ($64 \pm 8\%$, $n = 4$ cells) and CNT ($64 \pm 3\%$, $n = 4$ cells) sister-cultured neurons. The increase in the efficacy of neural signal transmission could be related to the specific properties of CNTs materials, such as the high electrical conductivity. Because the transmembrane voltage is a quantity of interest that will affect voltage-dependent membrane processes [119], nanotubes could in principle provide a pathway allowing direct electrotonic current transfer, causing charge redistribution along the surface of the cell membrane. This could account for a reinforcement of a direct electrical coupling between neurons. In a more recent work, the authors showed, by using single-cell electrophysiology techniques, electron microscopy analysis and theoretical modeling, that nanotubes improve neuronal responsiveness by forming tight contacts with the cell membranes that might favor electrical shortcuts between the proximal and distal compartments of the neuron [120]. The authors thus proposed the “electrotonic hypothesis” to explain the physical interactions between the cell and nanotube, and the mechanisms of how carbon nanotubes might affect the collective electrical activity of cultured neuronal networks. On the basis of these findings, it is possible to predict a further research interest in developing novel carbon nanotubes-neurons integrated platforms.

Jan, Kotov and coworkers have recently reported an interesting example of differentiation of mouse neural stem cells (NSCs) on layer-by-layer assembled SWCNT composite [105]. SWNTs were dispersed in a poly(sodium 4-styrene-sulfonate) (PSS, 1 wt%) solution and then LBL assembled with the polyelectrolyte polyethyleneimine (PEI). The resulting thin film was referred as (PEI/SWNT)₆.

To explore the actions of NSCs on LBL-assembled SWNT composite films, mouse embryonic 14-day neurospheres (spherical clonal structures of NSCs) from the cortex were seeded and induced to differentiate on the top of round glass coverslips coated with (PEI/SWNT)₆. As a control, neurospheres were also seeded and differentiated on poly-L-ornithine (PLO) coated coverslips, a standard substratum commonly used for NSC cultures and biochemical studies. In this study, neurospheres efficiently adhered to both types of substrates and developed neural processes away from the edge of the neurospheres as early as after 1 day in culture. The lengths of processes from differentiated NSCs constantly increased over the 7-day culture time. During this time, neural processes developed on PLO-coated substrates remained longer than those developed on (PEI/SWNT)₆-coated substrates; however, the differences were not particularly marked. These cells extended long neurites that developed into many secondary processes, branching in many directions on the surface. The original shape of the NG105-15 cells is round and fairly small; therefore, such morphology was a clear evidence of the occurred successful cellular differentiation. The authors then attempted to stimulate the cells by passing current through the nanotube film. The shape of the recorded transients resembles that of the whole-cell stimulation curves obtained for intrinsic excitation with an inserted pipette electrode. These representative currents were evoked by 100 ms, 1–2 μ A pulses across the nanotube film at 1 Hz. After an initial capacitive charging artifact, the cells showed strong inward Na⁺ currents, which were similar in duration and magnitude to those produced by step changes in membrane potential. All the cells that reported inward currents with defined voltage changes could also be stimulated via extrinsic stimulation through the (PEI/SWNT)₆-coated substrates. These observations are evidence of the natural electrical response of the cells to excitation through the laterally applied voltage to the nanotube film, suggesting that such materials can be employed to electrically determine significant ion conductance in neuronal cells.

An interesting example that involved the interfacing of CNTs with cell membranes was reported by Bertozzi and coworkers. In such study, the authors coated CNTs with a biomimetic polymer designed to mimic cell surface mucin glycoproteins [121]. The polymers were based on a poly(methyl vinyl ketone) [poly(MVK)] backbone decorated with R-*N*-acetylgalactosamine (R-GalNAc) residues. These sugar residues are reminiscent of the O-linked glycans that decorate mucin glycoproteins. The C₁₈ lipid tail provided a hydrophobic anchor for CNT surface assembly (Fig. 9a).

The so-coated CNT derivatives were stable in aqueous solution for several months without desorption of the polymer coating. They termed CNTs coated with C₁₈-terminated GalNAc-conjugated polymers “C₁₈-MMCNTs,” where “MM” denotes “mucin mimic.” To interface these functionalized CNTs with cells, they took advantage of the *Helix pomatia* agglutinin (HPA), a hexavalent lectin that is specific for R-GalNAc residues and is capable of cross-linking cells and glycoproteins. The authors reasoned that the complex of HPA with C₁₈-MM-coated CNTs would possess sufficient available HPA binding sites for further complex formation with cell-surface bound glycoproteins. Alternatively, HPA bound to cell surface glycans would present binding sites for GalNAc residues on C₁₈-MM-coated CNTs. In either situation, binding of HPA to GalNAc residues will allow specific interaction of the cells and

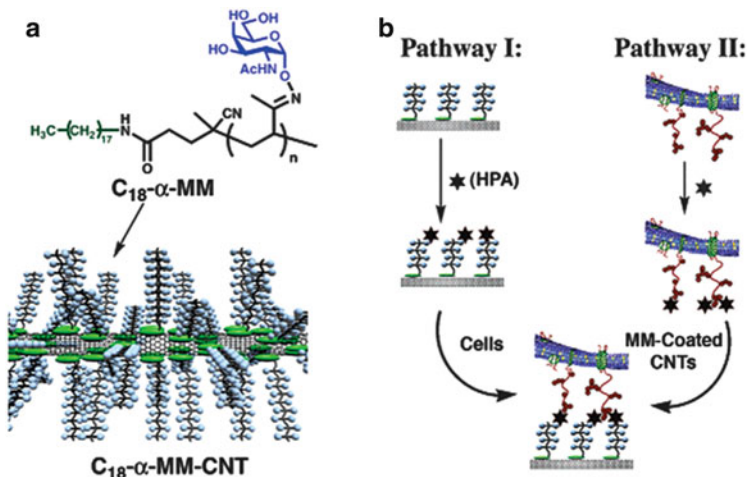


Fig. 9 (a) Structural representation of C₁₈-terminated, R-GalNAc-conjugated mucin mimic (C₁₈-R-MM), which assemble on CNT surface through hydrophobic interaction in aqueous media, imparting CNTs water dispersability. (b) CNTs interaction with cell surfaces via carbohydrate-receptor binding. In pathway I, C₁₈-R-MM-coated CNTs were first bound to HPA, a hexavalent R-GalNAc binding lectin. The complex was then interfaced with cell surface glycoconjugates using the available HPA binding sites. In pathway II, HPA was first bound to cell surfaces and then the remaining available HPA binding sites were then bound to R-GalNAc residues on C₁₈-R-MM-coated CNTs. Reprinted with permission of [121] Copyright 2006, American Chemical Society

CNTs. They then complexed C₁₈-MM-coated CNTs with HPA-FITC, and the protein-modified CNTs were then incubated with Chinese hamster ovary (CHO) cells. The labeling observed by fluorescence microscopy and flow cytometry analysis suggested the formation of GalNAc-HPA complexes at both the CNT and cell surfaces. To evaluate pathway II (Fig. 9b), the authors required a method for the direct detection of C₁₈-MM-coated CNTs independent from HPA. Thus, they synthesized a C₁₈-MM polymer in which about 3% of the GalNAc residues were substituted with the fluorescent dye Texas Red (C₁₈-MM/TR). CHO cells were incubated with unmodified HPA to introduce GalNAc receptors onto the cell surface. The cells were then subjected to different concentrations of C₁₈-MM/TR-coated CNTs and then screened by flow cytometry. Dose-dependent labeling was observed and the labeling was dependent upon precomplexation of the cells with HPA. Therefore, the glycopolymer coating imparts biocompatibility to the CNTs and also generates a way for specific cell surface interaction. Other examples of carbohydrate-modified CNTs have been recently reviewed by Zhao and Stoddart [30].

Other elegant examples of supramolecular CNT derivatization to elicit important biological properties were reported by Dai and coworkers. They found that the molecule 2-distearoyl-*sn*-glycero-3-phosphoethanolamine-*N*-amino(PEG)₂₀₀₀ (PL-PEG-NH₂) irreversibly adsorbs onto the outer sidewalls of SWNTs, by the interaction of the aliphatic portion of the phospholipidic moiety. This molecule is therefore very useful because the polyethylene core imparts water solubility and

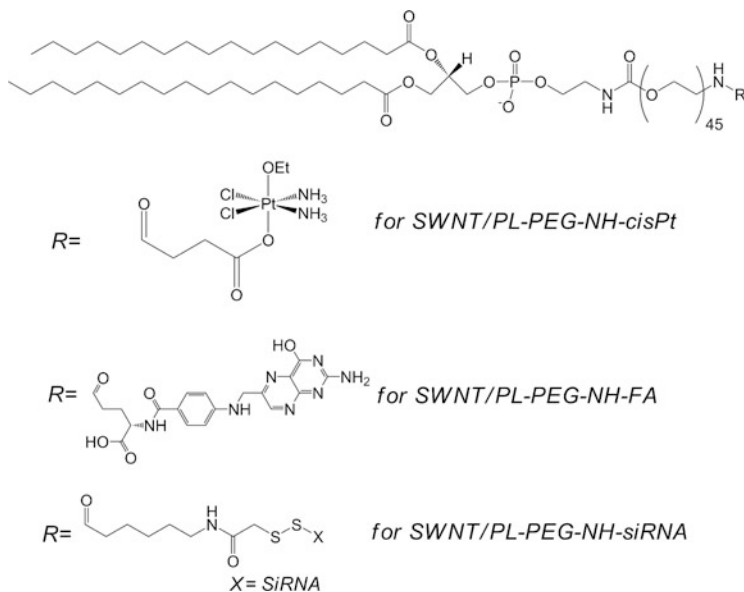


Fig. 10 Structural representation of the phospholipid-based universal functionalizing agent used by Dai and coworkers for the production of functional moieties useful toward different bioapplications, from drug-delivery to genetic expression interference

moreover offers a terminal amino group suitable for the further attachment of several biomolecules (Fig. 10).

For instance, PL-PEG-NH₂ was functionalized by carbodiimides chemistry with the folic acid (FA), a naturally occurring product that can be easily internalized in several cell lines that express the membrane-bound folate receptors (FR) [122]. FR are overexpressed in several kinds of cancerous cells and for this reason the SWNT/PL-PEG-NH-FA bioconjugate (Fig. 10) was used to target and selectively internalize SWNTs in to FR overexpressing cancerous cells. The goal of such study was to exploit the SWNTs property of adsorb light in the visible and near-infrared (Vis–NIR) regions and to convert it into heat, in order to selectively kill the cancerous cells through the photothermal effect. To exploit this system, FR-positive HeLa cells (FR + cells) with overexpressed FR on the cell surfaces were obtained by culturing cells in FA-depleted cell medium. Both FR + cells and normal cells without abundant FRs were exposed to SWNT/PL-PEG-NH-FA for 12–18 h, washed, and then radiated with 808-nm laser (1.4 W cm^{-2}) continuously for 2 min. After the NIR radiation, the authors observed extensive cell death for the FR + cells, evidenced by drastic cell morphology changes, whereas the normal cells remained unaffected and exhibited normal proliferation behavior over 2 weeks. In another study, the same authors anchored the cisplatin derivative [Pt(NH₃)₂Cl₂(OEt)(O₂CCH₂CH₂CO₂H)] onto the PL-PEG-NH₂ moiety adsorbed onto SWNTs to use them as longboat prodrug delivery systems for platinum (IV) (Fig. 10) [123]. Also in this case, as a way to anchor this carboxyl group bearing cisplatin derivative to the PL-PEG-NH₂ moiety,

carbodiimides chemistry was used, allowing to obtain a SWNT longboat (SWNT/PL-PEG-NH-cisPt) with an average loading of 65 platinum (IV) centers per nanotube, as evaluated by atomic absorption spectroscopy (AAS). In order to evaluate the feasibility of this method for delivering a toxic dose of platinum, the authors conducted cytotoxicity assays of SWNT/PL-PEG-NH-cisPt using the testicular carcinoma cell line Ntera-2. MTT assay was employed to assess cell viability, on a time lapse of 4 days, with either the free platinum (IV) complex or the SWNT/PL-PEG-NH-cisPt. Compared to *cis*-[Pt(NH₃)₂Cl₂] (IC₅₀ 0.05 μM), the cytotoxicity of the asymmetrically substituted [Pt(NH₃)₂Cl₂(OEt)(O₂CCH₂CH₂CO₂H)] was one order of magnitude less effective (IC₅₀ = 0.5 μM) and also the amine-functionalized SWNTs/PL-PEG-NH₂ showed negligible cytotoxicity. The SWNT/PL-PEG-NH-cisPt conjugate, however, showed a substantial increase in toxic character with respect to that of the free complex (IC₅₀ = 0.02 μM) and surpasses that of *cis*-[Pt(NH₃)₂Cl₂] if compared on a per platinum basis. In another example by the same group, by employing the heterobifunctional cross-linker sulfosuccinimidyl 6-(3'-[2-pyridyldithio]propionamido) hexanoate (Fig. 10) the authors obtained SWNT/PL-PEG-NH-linker able to anchor thiolated DNA and short interfering RNA (siRNA). By immobilizing these derivatives onto pristine SWNTs, they were able to obtain bioconjugates that showed enhanced activity as carriers for the nucleic acid derivatives inside cancerous HeLa cells [113] and human T lymphocytes [115]. In the former work with the HeLa cells, the ability to release the nucleic acids inside the cells, through the lysosomal-confined cleavage of the disulfidic bonds was assessed [113]. They used lamin A/C (a protein present inside the nuclear lamina of cells) gene silencing mediated by a particular siRNA sequence and compared the results obtained with SWNTs (acting as carriers) with existing transfection agents. HeLa cells were incubated with SWNT/PL-PEG-NH-siRNA for up to 24 h, fixed 48–72 h later and stained with antilamin and a fluorescently-tagged secondary antibody. For comparison, they also employed a commercial transfecting agent (lipofectamine) for siRNA delivery. Confocal imaging revealed significant reduction in lamin A/C protein expression by SWNT/PL-PEG-NH-siRNA relative to untreated control cells. Furthermore, flow cytometry data showed that for a given siRNA concentration, the percentage of silencing with SWNT/PL-PEG-NH-siRNA was greater than the one obtained with lipofectamine-siRNA. When they interfaced SWNT/PL-PEG-NH-siRNA with lymphatic T cells they investigated SWNT delivery of siRNA against CXCR4, a cell-surface coreceptor required for HIV entry into human T cells and infection. 50–60% knockdown of CXCR4 receptors on H9, Sup-T1, and CEM cells incubated in a solution of SWNT/PL-PEG-NH-siRNA ([siRNA] about 50 nM) for 24 h and approximately 90% silencing efficiency was observed upon incubation for 3 days [115]. Also Prato and coworkers reported elegant supramolecular strategies to functionalize CNTs with nucleic acids to alter the expression of selected genes. In fact, after 1,3 dipolar cycloaddition of azomethyne ylides, it was possible to introduce a significant amount of amino functionalities to CNTs, which are positively charged in the biological context [96, 108–111, 124]. Since nucleic acids possess the negative charges arising from the phosphate backbone, electrostatic interaction between the ammonium CNTs and plasmidic DNA was at first studied [114, 125].

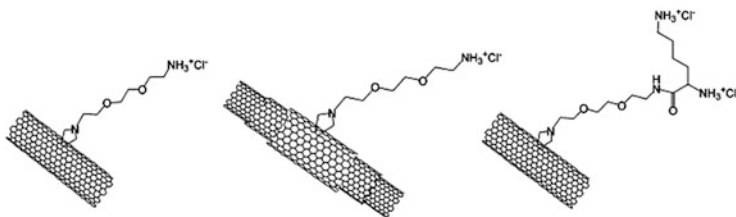


Fig. 11 Structural representation of ammonium-functionalized CNTs used by Prato and coworkers for the supramolecular immobilization of DNA. Reprinted with permission of [114] Copyright 2005, American Chemical Society

The ammonium-functionalized CNTs employed in this study were SWNT-NH₃⁺, MWNT-NH₃⁺, and lysine-functionalized SWNT (SWNT-Lys-NH₃⁺) (Fig. 11). As a plasmidic DNA the authors employed pCMV-Bgal, a 7.2-kb eukaryotic expression vector which brings the genetic information for the synthesis of β -galactoxidase. CNT-DNA complexes were analyzed by several analytical techniques, such as surface plasmon resonance, scanning electron microscopy, PicoGreen dye exclusion, and agarose gel shift assay. The results indicate that all three types of ammonium CNTs were able to complex the plasmidic DNA (with different degrees of affinity) and suggested that both CNT charge density and surface area are important parameters that determine the interaction between ammonium CNTs and DNA. The authors then focalized on the gene-transfer efficiency of the various CNT/DNA complexes by transfecting model cell lines (A549 cells). SWNT-NH₃⁺ appears to be most efficient in gene transfer when complexed to DNA at an 8:1 charge ratio, while SWNT-Lys-NH₃⁺ appears most efficient at a 1:1 charge ratio. Interestingly, the PicoGreen data indicate that, at these charge ratios, approximately 30% of DNA is free to interact with the dye in the case of SWNT-NH₃⁺ and a noticeably similar 25% of DNA is free in the case of SWNT-Lys-NH₃⁺. In the case of MWNT-NH₃⁺, since DNA is fully condensed even at very low charge ratios, there was not much difference in their transfection efficiency across all charge ratios and DNA dose studied.

The same research group has also demonstrated that also siRNA payloads can be efficiently delivered in to mammalian cells by using a dendron-functionalized MWNT series, where the dendron is an alkylated poly-amidoamine (PAMAM) specie bearing 2 (for generation 1, G1 MWNTs) or 4 (for generation 2, G2 MWNTs) net positive charges per dendron unit [116]. Human cervical carcinoma (HeLa) cells were then incubated with the dendron-MWNTs complexed with a noncoding siRNA sequence, which was fluorescently labelled at the 3' end with Atto 655 that emits light in the far-red region ($\lambda_{em} = 690$ nm). Each conjugate of the synthesized dendron-MWNT series was then complexed with the fluorescently labelled siRNA, by using previously optimized conditions (16:1 mass ratio) [117]. By this way, the cellular uptake of the different dendron-MWNT/siRNA was observed using confocal microscopy under identical analytical conditions. The confocal imaging results showed that the dendron-MWNTs with increased degrees

of branching (G2 MWNTs) exhibited more effective intracellular siRNA delivery than did zeroth-generation MWNTs and its alkylated derivative, while almost no uptake of siRNA alone was detected. Both the siRNA and the dendron-MWNTs were internalized within the cell cytoplasm, but it was not clear whether the siRNA was detached from the dendron-MWNTs intracellularly. The fluorescent signal from the Atto 655-labelled siRNA was found to be diffused throughout the cytoplasm of cells treated with the dendron-MWNT:siRNA complexes, without any indication of localization in intracellular compartments such as vesicles (usually evidenced by highly fluorescent pockets within the cell). The cellular morphology did not seem to be affected by the dendron-MWNTs used in these studies, suggesting that the siRNA uptake was not a consequence of cellular damage but most probably due to translocation of the dendron-MWNTs through the plasma membrane.

3 Conclusions

In the past years a great scientific effort has been done toward the production supramolecularly functionalized CNT derivatives with peculiar properties at both physical and biological interfaces. Many of the examples proposed in this text are proof of principles of the enormous technological impacts that CNT derivatives might bring in the next future. Nevertheless, despite the production of pristine fullerenes and CNTs has reached industrial large-scale production, most of the aforementioned examples suffer from the feasibility of scale-up conditions, mostly due to expensive experimental procedures and low yielding processes. Samples' inhomogeneity, due to the dissimilar material properties as a consequence of different production methods and purification strategies, determines a further limitation for their current employment in real applications. However, the supramolecular approach has proven to hold great promises in both development and production of new functional materials with defined structural organization of these novel carbonaceous nanostructures. Probably, most of the current limitations will, one day, be overtaken [126].

References

1. Ruhle M, Recnik A, Ceh M (1997) Chemistry and structure of internal interfaces in inorganic materials. In: Davies PK, Jacobson AJ, Torardi CC, Vanderah TA (eds) Solid-state chemistry of inorganic materials. Symposium of the Materials Research Society. Baldwin City, KS, U.S.A., pp 673–684
2. Filler MA, Bent SF (2003) The surface as molecular reagent: organic chemistry at the semiconductor interface. *Prog Surf Sci* 73:1–56
3. Lehn JM (1988) Supramolecular chemistry—scope and perspectives molecules, supermolecules, and molecular devices. *Angew Chem Int Ed* 27:89–112
4. Bonifazi D, Mohnani S, Llanes-Pallas A (2009) Supramolecular chemistry at interfaces: molecular recognition on nanopatterned porous surfaces. *Chem Eur J* 15:7004–7025

5. Iijima S (1991) Helical microtubules of graphitic carbon. *Nature* 354:56–58
6. Hirsch A (2010) The era of carbon allotropes. *Nat Mater* 9:868–871
7. Kostarelos K, Bianco A, Prato M (2009) Promises, facts and challenges for carbon nanotubes in imaging and therapeutics. *Nat Nanotechnol* 4:627–633
8. Saito R, Dresselhaus G, Dresselhaus MS (1998) Physical properties of carbon nanotubes. World Scientific Publishing Company, London
9. Martel R, Schmidt T, Shea HR, Hertel T, Avouris P (1998) Single- and multi-wall carbon nanotube field-effect transistors. *Appl Phys Lett* 73:2447–2449
10. Bachtold A, Hadley P, Nakanishi T, Dekker C (2001) Logic circuits with carbon nanotube transistors. *Science* 294:1317–1320
11. Avouris P (2002) Molecular electronics with carbon nanotubes. *Acc Chem Res* 35:1026–1034
12. Dillon AC (2010) Carbon nanotubes for photoconversion and electrical energy storage. *Chem Rev* 110:6856–6872
13. Diez-Tascón JM, Bottani EJ (2009) Carbon nanotubes: gas adsorption properties. In: Schwarz JA, Contescu CI, Putyera K (eds) Dekker encyclopedia of nanoscience and nanotechnology. Taylor and Francis, London
14. Antonucci V, Hsiao KT, Advani SG (2003) Review of polymer composites with carbon nanotubes. In: Shonaike GO, Advani SG (eds) Advanced polymeric materials: structure property relationships. Taylor and Francis, London, pp 397–437
15. Li C, Thostenson ET, Chou TW (2008) Sensors and actuators based on carbon nanotubes and their composites: a review. *Compos Sci Technol* 68:1227–1249
16. Shokrieh MM, Rafiee R (2010) A review of the mechanical properties of isolated carbon nanotubes and carbon nanotube composites. *Mech Compos Mater* 46:155–172
17. Balasubramanian K, Burghard M (2006) Biosensors based on carbon nanotubes. *Anal Bioanal Chem* 385:452–468
18. Lei J, Ju H (2010) Nanotubes in biosensing. *Wiley Interdiscip Rev Nanomed Nanobiotechnol* 2:496–509
19. Chichak KS, Star A, Altoè MVR, Stoddart JF (2005) Single-walled carbon nanotubes under the influence of dynamic coordination and supramolecular chemistry. *Small* 1:452–461
20. Guldi DM, Rahman GM, Jux N, Balbinot D, Hartnagel U, Tagmatarchis N, Prato M (2005) Functional single-wall carbon nanotube nanohybrids-associating SWNTs with water-soluble enzyme model systems. *J Am Chem Soc* 127:9830–9838
21. Sgobba V, Rahman GM, Guldi DM, Jux N, Campidelli S, Prato M (2006) Supramolecular assemblies of different carbon nanotubes for photoconversion processes. *Adv Mater* 18:2264–2269
22. Geng J, Ko YK, Youn SC, Kim YH, Kim SA, Jung DH, Jung HT (2008) Synthesis of SWNT rings by noncovalent hybridization of porphyrins and single-walled carbon nanotubes. *J Phys Chem C* 112:12264–12271
23. Tu X, Zheng M (2008) A DNA-based approach to the carbon nanotube sorting problem. *Nano Res* 1:185–194
24. D'Souza F, Ito O (2009) Supramolecular donor-acceptor hybrids of porphyrins/phthalocyanines with fullerenes/carbon nanotubes: electron transfer, sensing, switching, and catalytic applications. *Chem Commun* 33:4913–4928
25. Ehli C, Guldi DM, Herranz MA, Martin N, Campidelli S, Prato M (2008) Pyrene-tetrathiafulvalene supramolecular assembly with different types of carbon nanotubes. *J Mater Chem* 18:1498–1503
26. Yang R, Tang Z, Yan J, Kang H, Kim Y, Zhu Z, Tan W (2008) Noncovalent assembly of carbon nanotubes and single-stranded DNA: an effective sensing platform for probing biomolecular interactions. *Anal Chem* 80:7408–7413
27. Sudibya HG, Ma J, Dong X, Ng S, Li LJ, Liu XW, Chen P (2009) Interfacing glycosylated carbon-nanotube-network devices with living cells to detect dynamic secretion of biomolecules. *Angew Chem Int Ed* 48:2723–2726

28. Tasis D, Tagmatarchis N, Bianco A, Prato M (2006) Chemistry of carbon nanotubes. *Chem Rev* 106:1105–1136
29. Singh P, Campidelli S, Giordani S, Bonifazi D, Bianco A, Prato M (2009) Organic functionalisation and characterisation of single-walled carbon nanotubes. *Chem Soc Rev* 38:2214–2230
30. Zhao YL, Stoddart JF (2009) Noncovalent functionalization of single-walled carbon nanotubes. *Acc Chem Res* 42:1161–1171
31. Chen RJ, Zhang Y, Wang D, Dai H (2001) Noncovalent sidewall functionalization of single-walled carbon nanotubes for protein immobilization. *J Am Chem Soc* 123:3838–3839
32. Liu Z, Tabakman SM, Chen Z, Dai H (2009) Preparation of carbon nanotube bioconjugates for biomedical applications. *Nat Protoc* 4:1372–1382
33. Kauffman DR, Star A (2008) Electronically monitoring biological interactions with carbon nanotube field-effect transistors. *Chem Soc Rev* 37:1197–1206
34. Goldoni A, Petaccia L, Lizzit S, Larciprete R (2010) Sensing gases with carbon nanotubes: a review of the actual situation. *J Phys Condes Matter* 22:013001–013008
35. Hecht DS, Ramirez RJ, Briman M, Artukovic E, Chichak KS, Stoddart JF, Grüner G (2006) Bioinspired detection of light using a porphyrin-sensitized single-wall nanotube field effect transistor. *Nano Lett* 6:2031–2036
36. Guldi DM, Rahman GM, Jux N, Tagmatarchis N, Prato M (2004) Integrating single-wall carbon nanotubes into donor-acceptor nanohybrids. *Angew Chem Int Ed* 43:5526–5530
37. Zhao YL, Hu LB, Stoddart JF, Gruner G (2008) Pyrenecyclodextrin-decorated single-walled carbon nanotube field-effect transistors as chemical sensors. *Adv Mater* 20:1910–1915
38. Collins PG, Bradley K, Ishigami M, Zettl A (2000) Extreme oxygen sensitivity of electronic properties of carbon nanotubes. *Science* 287:1801–1804
39. Stan G, Bojan MJ, Curtarolo S, Gatica SM, Cole MW (2000) Uptake of gases in bundles of carbon nanotubes. *Phys Rev B* 62:2173–2180
40. Kim C, Choi YS, Lee SM, Park JT, Kim B, Lee YH (2002) The effect of gas adsorption on the field emission mechanism of carbon nanotubes. *J Am Chem Soc* 124:9906–9911
41. Krungleviciute V, Heroux L, Talapatra S, Migone AD (2004) Gas adsorption on HiPco nanotubes: surface area determinations, and neon second layer data. *Nano Lett* 4:1133–1137
42. Feng X, Irle S, Witek H, Morokuma K, Vidic R, Borguet E (2005) Sensitivity of ammonia interaction with single-walled carbon nanotube bundles to the presence of defect sites and functionalities. *J Am Chem Soc* 127:10533–10538
43. Saridara C, Brukh R, Iqbal Z, Mitra S (2005) Preconcentration of volatile organics on self-assembled, carbon nanotubes in a microtrap. *Anal Chem* 77:1183–1187
44. Snow ES, Perkins FK, Houser EJ, Badescu SC, Reinecke TL (2005) Chemical detection with a single-walled carbon nanotube capacitor. *Science* 307:1942–1945
45. Kingrey D, Khatib O, Collins PG (2006) Electronic fluctuations in nanotube circuits and their sensitivity to gases and liquids. *Nano Lett* 6:1564–1568
46. Chiashi S, Watanabe S, Hanashima T, Homma Y (2008) Influence of gas adsorption on optical transition energies of single-walled carbon nanotubes. *Nano Lett* 8:3097–3101
47. Liang CW, Sahakalkan S, Roth S (2008) Electrical characterization of the mutual influences between gas molecules and single-walled carbon nanotubes. *Small* 4:432–436
48. Lee CY, Strano MS (2008) Amine basicity (pK(b)) controls the analyte binding energy on single walled carbon nanotube electronic sensor arrays. *J Am Chem Soc* 130:1766–1773
49. Ravelo-Pérez LM, Herrera-Herrera AV, Hernández-Borges J, Rodríguez-Delgado MA (2010) Carbon nanotubes: solid-phase extraction. *J Chromatogr A* 1217:2618–2641
50. Cai Y, Jiang G, Liu J, Zhou Q (2003) Multiwalled carbon nanotubes as a solid-phase extraction adsorbent for the determination of bisphenol a, 4-n-nonylphenol, and 4-tert-octylphenol. *Anal Chem* 75:2517–2521
51. Liu G, Wang J, Zhu Y, Zhang X (2004) Application of multiwalled carbon nanotubes as a solid-phase extraction sorbent for chlorobenzenes. *Anal Lett* 37:3085–3104

52. Cai YQ, Cai YE, Mou SF, Lu YQ (2005) Multi-walled carbon nanotubes as a solid-phase extraction adsorbent for the determination of chlorophenols in environmental water samples. *J Chromatogr A* 1081:245–247
53. Fang GZ, He JX, Wang S (2006) Multiwalled carbon nanotubes as sorbent for on-line coupling of solid-phase extraction to high-performance liquid chromatography for simultaneous determination of 10 sulfonamides in eggs and pork. *J Chromatogr A* 1127:12–17
54. Zhou Q, Ding Y, Xiao J (2006) Sensitive determination of thiamethoxam, imidacloprid and acetamiprid in environmental water samples with solid-phase extraction packed with multiwalled carbon nanotubes prior to high-performance liquid chromatography. *Anal Bioanal Chem* 385:1520–1525
55. Zhou Q, Xiao J, Wang W (2006) Using multi-walled carbon nanotubes as solid phase extraction adsorbents to determine dichlorodiphenyltrichloroethane and its metabolites at trace level in water samples by high performance liquid chromatography with UV detection. *J Chromatogr A* 1125:152–158
56. El-Sheikh AH, Insisi AA, Sweileh JA (2007) Effect of oxidation and dimensions of multi-walled carbon nanotubes on solid phase extraction and enrichment of some pesticides from environmental waters prior to their simultaneous determination by high performance liquid chromatography. *J Chromatogr A* 1164:25–32
57. Suárez B, Santos B, Simonet BM, Cárdenas S, Valcárcel M (2007) Solid-phase extraction-capillary electrophoresis-mass spectrometry for the determination of tetracyclines residues in surface water by using carbon nanotubes as sorbent material. *J Chromatogr A* 1175:127–132
58. Wang S, Zhao P, Min G, Fang G (2007) Multi-residue determination of pesticides in water using multi-walled carbon nanotubes solid-phase extraction and gas chromatography–mass spectrometry. *J Chromatogr A* 1165:166–171
59. Wang WD, Huang YM, Shu WQ, Cao H (2007) Multiwalled carbon nanotubes as adsorbents of solid-phase extraction for determination of polycyclic aromatic hydrocarbons in environmental waters coupled with high-performance liquid chromatography. *J Chromatogr A* 1173: 27–36
60. Yu JC, Hrdina A, Mancini C, Lai EP (2007) Molecularly imprinted polypyrrole encapsulated carbon nanotubes in stainless steel frit for micro solid phase extraction of estrogenic compounds. *J Nanosci Nanotechnol* 7:3095–3103
61. Du D, Wang M, Zhang J, Cai H, Tu H, Zhang A (2008) Application of multiwalled carbon nanotubes for solid-phase extraction of organophosphate pesticide. *Electrochem Commun* 10:85–89
62. Pyrzynska K (2008) Carbon nanotubes as a new solid-phase extraction material for removal and enrichment of organic pollutants in water. *Sep Purif Rev* 37:372–389
63. Ravelo-Peréz LM, Hernández-Borges J, Rodríguez-Delgado MA (2008) Multi-walled carbon nanotubes as efficient solid-phase extraction materials of organophosphorus pesticides from apple, grape, orange and pineapple fruit juices. *J Chromatogr A* 1211:33–42
64. Ravelo-Peréz LM, Hernández-Borges J, Rodríguez-Delgado MA (2008) Multiwalled carbon nanotubes as solid-phase extraction materials for the gas chromatographic determination of organophosphorus pesticides in waters. *J Sep Sci* 31:3612–3619
65. Salam MA, Burk R (2008) Novel application of modified multiwalled carbon nanotubes as a solid phase extraction adsorbent for the determination of polyhalogenated organic pollutants in aqueous solution. *Anal Bioanal Chem* 390:2159–2170
66. Asensio-Ramos M, Hernández-Borges J, Borges-Miquel TM, Rodríguez-Delgado MA (2009) Evaluation of multi-walled carbon nanotubes as solid-phase extraction adsorbents of pesticides from agricultural, ornamental and forestal soils. *Anal Chim Acta* 647:167–176
67. Chen W, Zeng J, Chen J, Huang X, Jiang Y, Wang Y, Chen X (2009) High extraction efficiency for polar aromatic compounds in natural water samples using multiwalled carbon nanotubes/Nafion solid-phase microextraction coating. *J Chromatogr A* 1216:9143–9148

68. Fang G, Min G, He J, Zhang C, Qian K, Wang S (2009) Multiwalled carbon nanotubes as matrix solid-phase dispersion extraction absorbents to determine 31 pesticides in agriculture samples by gas chromatography–mass spectrometry. *J Agric Food Chem* 57:3040–3045
69. López-Feria S, Cárdenas S, Valcárcel M (2009) One step carbon nanotubes-based solid-phase extraction for the gas chromatographic-mass spectrometric multiclass pesticide control in virgin olive oils. *J Chromatogr A* 1216:7346–7350
70. Salam MA, Burk R (2009) Solid phase extraction of polyhalogenated pollutants from freshwater using chemically modified multi-walled carbon nanotubes and their determination by gas chromatography. *J Sep Sci* 32:1060–1068
71. Zhang W, Sun Y, Wu C, Xing J, Li J (2009) Polymer-functionalized single-walled carbon nanotubes as a novel sol–gel solid-phase micro-extraction coated fiber for determination of polybrominated diphenyl ethers in water samples with gas chromatography-electron capture detection. *Anal Chem* 81:2912–2920
72. Hadjmohammadi MR, Peyrovi M, Biparva P (2010) Comparison of C₁₈ silica and multi-walled carbon nanotubes as the adsorbents for the solid-phase extraction of chlorpyrifos and phosalone in water samples using HPLC. *J Sep Sci* 33:1044–1051
73. Márquez-Sillero I, Aguilera-Herrador E, Cárdenas S, Valcárcel M (2010) Determination of parabens in cosmetic products using multi-walled carbon nanotubes as solid phase extraction sorbent and corona-charged aerosol detection system. *J Chromatogr A* 1217:1–6
74. See HH, Sanagi M, Ibrahim WA, Naim AA (2010) Determination of triazine herbicides using membrane-protected carbon nanotubes solid phase membrane tip extraction prior to micro-liquid chromatography. *J Chromatogr A* 1217:1767–1772
75. Wu H, Wang X, Liu B, Lu J, Du B, Zhang L, Ji J, Yue Q, Han B (2010) Flow injection solid-phase extraction using multi-walled carbon nanotubes packed micro-column for the determination of polycyclic aromatic hydrocarbons in water by gas chromatography–mass spectrometry. *J Chromatogr A* 1217:2911–2917
76. Liang P, Liu Y, Guo L, Zeng J, Lu H (2004) Multiwalled carbon nanotubes as solid-phase extraction adsorbent for the preconcentration of trace metal ions and their determination by inductively coupled plasma atomic emission spectrometry. *J Anal At Spectrom* 19:1489–1492
77. Liang P, Ding Q, Song F (2005) Application of multiwalled carbon nanotubes as solid phase extraction sorbent for preconcentration of trace copper in water samples. *J Sep Sci* 28:2339–2343
78. Ding Q, Liang P, Song F, Xiang A (2006) Separation and preconcentration of silver ion using multiwalled carbon nanotubes as solid phase extraction sorbent. *Sep Sci Technol* 41:2723–2732
79. Du Z, Yu YL, Chen XW, Wang JH (2007) The isolation of basic proteins by solid-phase extraction with multiwalled carbon nanotubes. *Chem Eur J* 13:9679–9685
80. Wang RK, Park HO, Chen WC, Silvera-Batista C, Reeves RD, Butler JE, Ziegler KJ (2008) Improving the effectiveness of interfacial trapping in removing single-walled carbon nanotube bundles. *J Am Chem Soc* 130:14721–14728
81. Ziegler KJ, Schmidt DJ, Rauwald U, Shah KN, Flor EL, Hauge RH, Smalley RE (2005) Length-dependent extraction of single-walled carbon nanotubes. *Nano Lett* 5:2355–2359
82. Hudson JL, Casavant MJ, Tour JM (2004) Water-soluble, exfoliated, nonroping single-wall carbon nanotubes. *J Am Chem Soc* 126:11158–11159
83. Mayya KS, Caruso F (2003) Phase transfer of surface-modified gold nanoparticles by hydrophobization with alkylamines. *Langmuir* 19:6987–6993
84. Zhang Y, Shen Y, Kuehner D, Wu S, Su Z, Ye S, Niu L (2008) Directing single-walled carbon nanotubes to self-assemble at water/oil interfaces and facilitate electron transfer. *Chem Commun* 36:4273–4275
85. Karajanagi SS, Vertegel AA, Kane RS, Dordick JS (2004) Structure and function of enzymes adsorbed onto single-walled carbon nanotubes. *Langmuir* 20:11594–11599
86. Asuri P, Karajanagi SS, Dordick JS, Kane RS (2006) Directed assembly of carbon nanotubes at liquid-liquid interfaces: nanoscale conveyors for interfacial biocatalysis. *J Am Chem Soc* 128:1046–1047

87. Edgerton SA, Holdren MW, Smith DL, Shah JJ (1989) Inter-urban comparison of ambient volatile organic compound concentration in U.S. cities. *J Air Pollut Contr* 39:729–732
88. Carrillo-Carrón C, Lucena R, Cárdenas S, Valcárcel M (2007) Liquid-liquid extraction/headspace/gas chromatographic/mass spectrometric determination of benzene, toluene, ethylbenzene, (o-, m- and p-)xylene and styrene in olive oil using surfactant-coated carbon nanotubes as extractant. *J Chromatogr A* 1171:1–7
89. Kim S, Lee HR, Yun YJ, Ji S, Yoo K, Yun WS, Koo JY, Ha DH (2007) Effects of polymer coating on the adsorption of gas molecules on carbon nanotube networks. *Appl Phys Lett* 91:093126–093126-3
90. Pengfei QF, Vermesh O, Grecu M, Javey A, Wang O, Dai HJ, Peng S, Cho KJ (2003) Toward large arrays of multiplex functionalized carbon nanotube sensors for highly sensitive and selective molecular detection. *Nano Lett* 3:347–351
91. Kauffman DR, Shade CM, Uh H, Petoud S, Star A (2009) Decorated carbon nanotubes with unique oxygen sensitivity. *Nat Chem* 1:500–506
92. Lee CY, Sharma R, Radadia AD, Masel RI, Strano MS (2008) On-chip micro gas chromatograph enabled by a noncovalently functionalized single-walled carbon nanotube sensor array. *Angew Chem Int Ed* 47:5018–5021
93. O'Connell MJ, Bachilo SM, Huffman CB, Moore VC, Strano MS, Haroz EH, Rialon KL, Boul PJ, Noon WH, Kittrell C, Ma J, Hauge RH, Weisman RB, Smalley RE (2002) Band gap fluorescence from individual single-walled carbon nanotubes. *Science* 297:593–596
94. Bryning MB, Islam MF, Kikkawa JM, Yodh AG (2005) Very low conductivity threshold in bulk isotropic single-walled carbon nanotube-epoxy composites. *Adv Mater* 17:1186–1191
95. Banerjee S, Hemraj-Benny T, Wong SS (2005) Covalent surface chemistry of single-walled carbon nanotubes. *Adv Mater* 17:17–29
96. Bianco A, Kostarelos K, Partidos CD, Prato M (2005) Biomedical applications of functionalised carbon nanotubes. *Chem Commun* 5:571–577
97. Yang WR, Thordarson P, Gooding JJ, Ringer SP, Braet F (2007) Carbon nanotubes for biological and biomedical applications. *Nanotechnology* 18:412001
98. Liang F, Chen B (2010) A review on biomedical applications of single-walled carbon nanotubes. *Curr Med Chem* 17:10–24
99. Mattson MP, Haddon RC, Rao AM (2000) Molecular functionalization of carbon nanotubes and use as substrates for neuronal growth. *J Mol Neurosci* 14:175–182
100. Hu H, Ni YC, Montana V, Haddon RC, Parpura V (2004) Chemically functionalized carbon nanotubes as substrates for neuronal growth. *Nano Lett* 4:507–511
101. Hu H, Ni YC, Mandal SK, Montana V, Zhao N, Haddon RC, Parpura V (2005) Polyethyleneimine functionalized single-walled carbon nanotubes as a substrate for neuronal growth. *J Phys Chem B* 109:4285–4289
102. Lovat V, Pantarotto D, Lagostena L, Spalluto G, Prato M, Ballerini L, Cacciari B, Grandolfo M, Righi M (2005) Carbon nanotube substrates boost neuronal electrical signaling. *Nano Lett* 5:1107–1110
103. Gheith MK, Pappas TC, Liopo AV, Sinani VA, Shim BS, Motamedi M, Wicksted JR, Kotov NA (2006) Stimulation of neural cells by lateral layer-by-layer films of single-walled currents in conductive carbon nanotubes. *Adv Mater* 18:2975–2979
104. Zanello LP, Zhao B, Hu H, Haddon RC (2006) Bone cell proliferation on carbon nanotubes. *Nano Lett* 6:562–567
105. Jan E, Kotov NA (2007) Successful differentiation of mouse neural stem cells on layer-by-layer assembled single-walled carbon nanotube composite. *Nano Lett* 7:1123–1128
106. Jan E, Hendricks JL, Husaini V, Richardson-Burns SM, Sereno A, Martin DC, Kotov NA (2009) Layered carbon nanotube-polyelectrolyte electrodes outperform traditional neural interface materials. *Nano Lett* 9:4012–4018
107. Namgung S, Kim T, Baik KY, Lee M, Nam J-M, Hong S (2010) Fibronectin-carbon-nanotube hybrid nanostructures for controlled cell growth. *Small* 7:56–61

108. Bianco A, Hoebeke J, Partidos CD, Kostarelos K, Prato M (2005) Carbon nanotubes: on the road to deliver. *Curr Drug Deliv* 2:253–259
109. Pastorin G, Kostarelos K, Prato M, Bianco A (2005) Functionalized carbon nanotubes: towards the delivery of therapeutic molecules. *J Biomed Nanotechnol* 1:133–142
110. Bianco A, Kostarelos K, Prato M (2008) Opportunities and challenges of carbon-based nanomaterials for cancer therapy. *Expert Opin Drug Deliv* 5:331–342
111. Prato M, Kostarelos K, Bianco A (2008) Functionalized carbon nanotubes in drug design and discovery. *Acc Chem Res* 41:60–68
112. Pantarotto D, Singh R, McCarthy D, Erhardt M, Briand JP, Prato M, Kostarelos K, Bianco A (2004) Functionalized carbon nanotubes for plasmid DNA gene delivery. *Angew Chem Int Ed* 43:5242–5246
113. Kam NW, Liu Z, Dai H (2005) Functionalization of carbon nanotubes via cleavable disulfide bonds for efficient intracellular delivery of siRNA and potent gene silencing. *J Am Chem Soc* 127:12492–12493
114. Singh R, Pantarotto D, McCarthy D, Chaloin O, Hoebeke J, Partidos CD, Briand JP, Prato M, Bianco A, Kostarelos K (2005) Binding and condensation of plasmid DNA onto functionalized carbon nanotubes: toward the construction of nanotube-based gene delivery vectors. *J Am Chem Soc* 127:4388–4396
115. Liu Z, Winters M, Holodniy M, Dai HJ (2007) siRNA delivery into human T cells and primary cells with carbon-nanotube transporters. *Angew Chem Int Ed* 46:2023–2027
116. Herrero MA, Toma FM, Al-Jamal KT, Kostarelos K, Bianco A, Da Ros T, Bano F, Casalis L, Scoles G, Prato M (2009) Synthesis and characterization of a carbon nanotube-dendron series for efficient siRNA delivery. *J Am Chem Soc* 131:9843–9848
117. Podesta JE, Al-Jamal KT, Herrero MA, Tian BW, Ali-Boucetta H, Hegde V, Bianco A, Prato M, Kostarelos K (2009) Antitumor activity and prolonged survival by carbon-nanotube-mediated therapeutic siRNA silencing in a human lung xenograft model. *Small* 5:1176–1185
118. Georgakilas V, Kordatos K, Prato M, Guldi DM, Holzinger M, Hirsch A (2002) Organic functionalization of carbon nanotubes. *J Am Chem Soc* 124:760–761
119. Vigmond EJ, Velazquez JLP, Valiante TA, Bardakjian BL, Carlen PL (1997) Mechanisms of electrical coupling between pyramidal cells. *J Neurophysiol* 78:3107–3116
120. Cellot G, Cilia E, Cipollone S, Rancic V, Sucapane A, Giordani S, Gambazzi L, Markram H, Grandolfo M, Scaini D, Gelain F, Casalis L, Prato M, Giugliano M, Ballerini L (2009) Carbon nanotubes might improve neuronal performance by favouring electrical shortcuts. *Nat Nanotechnol* 4:126–133
121. Chen X, Tam UC, Czlapiński JL, Lee GS, Rabuka D, Zettl A, Bertozzi CR (2006) Interfacing carbon nanotubes with living cells. *J Am Chem Soc* 128:6292–6293
122. Kam NW, O'Connell M, Wisdom JA, Dai H (2005) Carbon nanotubes as multifunctional biological transporters and near-infrared agents for selective cancer cell destruction. *Proc Natl Acad Sci U S A* 102:11600–11605
123. Feazell RP, Nakayama-Ratchford N, Dai H, Lippard SJ (2007) Soluble single-walled carbon nanotubes as longboat delivery systems for platinum(IV) anticancer drug design. *J Am Chem Soc* 129:8438–8439
124. Georgakilas V, Tagmatarchis N, Pantarotto D, Bianco A, Briand JP, Prato M (2002) Amino acid functionalisation of water soluble carbon nanotubes. *Chem Commun* 24:3050–3051
125. Pantarotto D, Singh R, McCarthy D, Erhardt M, Briand JP, Prato M, Kostarelos K, Bianco A (2004) Functionalized carbon nanotubes for plasmid DNA gene delivery. *Angew Chem Int Ed* 43:5242–5246
126. Zubritsky, E (2010) A Stellar, Metal-Free Way to Make Carbon Nanotubes. <http://www.nasa.gov/topics/technology/features/metal-free-nanotubules.html>

Oligomers from sp -Hybridized Carbon: Cumulenes and Polyynes

Stephanie Frankenberger, Johanna A. Januszewski, and Rik R. Tykwinski

Abstract Carbon-rich organic compounds are candidates for use in a wide range of new technologies. Particularly interesting are materials with a framework of pure carbon, namely the allotropes. Much is known about the most common allotropes, diamond (sp^3 -carbon) and graphite (sp^2 -carbon), as well as the newer allotropes, fullerenes, nanotubes, and graphene. On the other hand, little is known about the allotrope constructed from sp -hybridized carbon atoms, a material commonly called carbyne. Without a defined sample of carbyne to study, synthetic chemists have attempted to model the properties of carbyne through the formation of defined length oligomers based on a cumulene or polyynes skeleton. Spectroscopic analysis of these series of oligomers by vibrational (IR and Raman), NMR, and UV/Vis spectroscopy has outlined some of the potential properties of carbyne. Likewise, X-ray crystallographic analyses give further clues as to the structure of carbyne. This review will highlight selected synthetic methods for cumulenes and polyynes, and it then summarizes characterization data related to structure and bonding in these molecules.

Keywords Bond length alternation · Carbon allotropes · Cumulenes · Polyynes

Contents

1	Introduction	220
2	Synthesis	222
	2.1 Cumulene Synthesis	222
	2.2 Polyynes Synthesis	225

S. Frankenberger, J.A. Januszewski, and R.R. Tykwinski (✉)
Department für Chemie und Pharmazie and Interdisciplinary Center for Molecular Material (ICMM), Friedrich-Alexander-Universität Erlangen-Nürnberg, Henkestraße 42,
91054 Erlangen, Germany
e-mail: rik.tykwinski@chemie.uni-erlangen.de

3	Structure and Bonding	230
3.1	Vibrational Spectroscopy	230
3.2	¹³ C NMR Spectroscopy	234
3.3	UV/Vis Spectroscopy	237
3.4	X-ray Crystallography	243
4	Conclusions	250
	References	250

1 Introduction

Carbon-rich compounds and materials have become commonplace as candidates for technological advances ranging from molecular wires to solar cells [1–8]. Leading the way in many cases are materials composed entirely, or almost nearly so, of carbon, including fullerenes, nanotubes, and graphene [9]. To an organic chemist, the connection between these materials is quite obvious, they are all carbon allotropes derived from sp²-hybridized carbon atoms. What is, perhaps, surprising is that the properties of each allotrope differ so broadly in spite of their common building block, the trigonal planar sp²-hybridized carbon atom. Unlike the properties of the sp²-carbon allotropes, those derived from tetrahedral sp³-hybridized carbon atoms, i.e., diamond, center about its hardness, heat capacity, and insulating behavior. Like graphite, however, diamond has a long history of technological importance [10, 11].

In considering allotropes based on carbon atom hybridization, the next logical allotrope would be comprised of linear sp-hybridized carbon atoms [12–15]. This would give the compound commonly called carbyne (Fig. 1). Carbyne is the most elusive of the basic carbon allotropes, and its existence, structure, and properties have been a controversial topic for decades [16–21]. One of the most interesting questions surrounding carbyne has been the nature of its bonding: does it resemble a cumulene or a polyene?

In the absence of an authentic and well-defined sample of carbyne, organic chemists have attempted to approximate the properties of this material through the synthesis and study of defined length oligomers. Early work by Kuhn and coworkers [22–27], and later by Bohlmann and coworkers [28–31], targeted the cumulenes, but these efforts were hampered by the rather frustrating instability shown by these compounds. Nevertheless, a number of remarkable synthetic efforts provided several series of cumulenes, including the [n]Ph and [n]Cy series (where *n* is the number of cumulated double bonds), which were extended to the point of [9]cumulenes (Fig. 2). At around the same time, a number of groups also took an interest in the formation of the other structural form for sp-hybridized carbon, the polyynes. This included early independent efforts by the groups of Jones [32–34] and Bohlmann [31, 35], as well as several others [36–38], who already in the early 1950s had realized a number of polyene series. Exploration of the polyynes continued to expand slowly [32, 39, 40] through to Walton's seminal work in the 1970s [41–43].



Fig. 1 The schematic structure of a cumulene and polyne form of carbyne

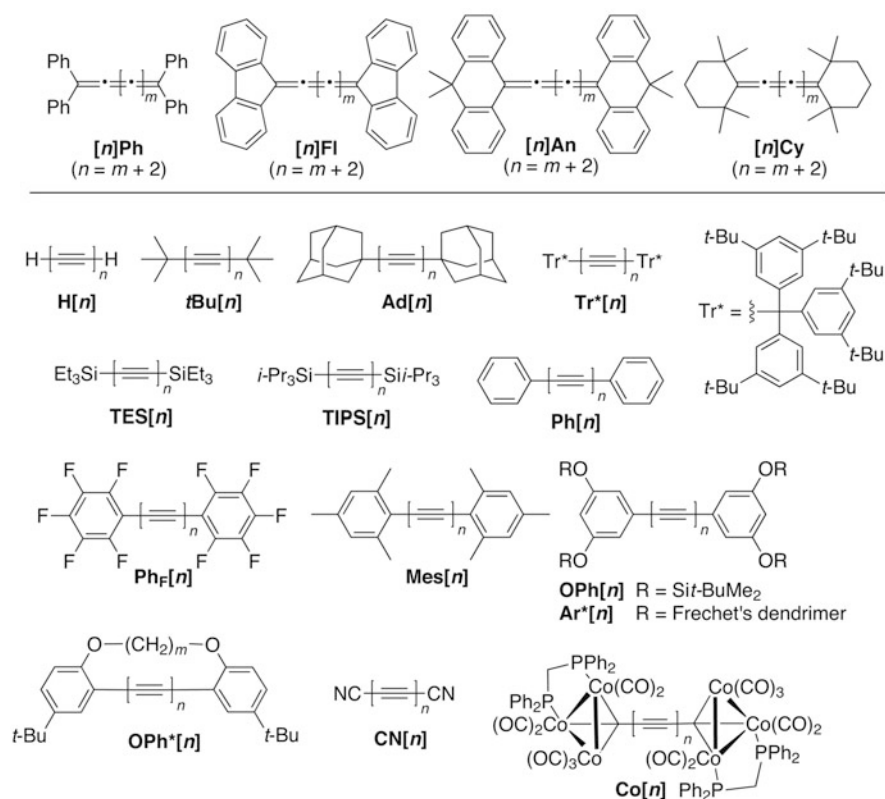


Fig. 2 Cumulene and polyne series discussed in this review

Following the early work on cumulenes, little has been published over the past 50 years to improve our understanding of molecular structure in this class of molecules. For polyynes, on the other hand, synthetic efforts over the past two decades have made substantial progress toward helping to predict the properties of carbyne. This review will attempt to summarize our current understanding of structure and bonding for both cumulenes and polyynes, relying on spectroscopic and crystallographic analyses. While quite narrowly focused on molecules constructed of sp-hybridized carbon, there are still far too many reports to summarize all works in the space of this review. Thus, several important criteria have been used to make this review both manageable and informative. First, only polyynes and cumulenes with carbon or silyl endgroups have been included. While the

chemistry of organometallic polyynes [44–49] and cumulenes [50–57] is certainly quite interesting, bonding between the sp-carbon chain and the terminal metal(s) complicates comparisons to organic systems. Second, only polyynes series that include members beyond the length of a hexayne have been considered, while for cumulenes only series that containing members longer than a [5]cumulene are included. Finally, predominantly odd numbered cumulenes have been included, i.e., [*n*]cumulenes with *n* = odd and thus an odd number of cumulated double bonds (since conjugation between endgroups is only possible via the cumulene chain in odd numbered cumulenes).

2 Synthesis

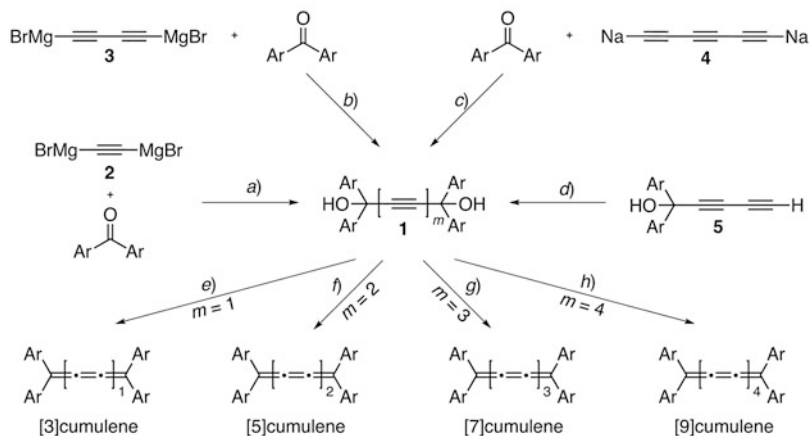
2.1 Cumulene Synthesis

Since the end of the 1930s, many efforts have been made to synthesize compounds with cumulated double bonds, and various synthetic approaches have been developed [58]. In the case of shorter [*n*]cumulenes (*n* = 3, 5), a rather substantial number of synthetic routes have been reported, and a comprehensive overview is not possible but this work has been recently reviewed [59]. Herein, general synthetic steps are outlined for [*n*]cumulenes series [**n**]Ph, [**n**]Fl, [**n**]An, and [**n**]Cy with *n* = 3, 5, 7, or 9. The synthesis of [*n*]cumulenes with *n* = 3, 5, and 7 with dibenzosuberenylidene endgroups has been reported, but few details are available, see: [60]. The synthetic routes described for cumulenes are divided into two general classes of reactions: (1) reduction reactions to achieve aryl-substituted cumulenes and (2) elimination reactions to build up alkyl-substituted cumulenes.

2.1.1 Synthesis of Aryl-Substituted Series of [*n*]cumulenes

An important common synthetic method for [*n*]cumulenes is the formation of [*n*]oligoyne- α,ω -diols **1** followed by a final reduction step (Scheme 1). In the case of formation of aryl-substituted [3]cumulenes, the diol precursor (**1**, *m* = 1) was synthesized using BrMg–C \equiv C–MgBr (**2**) in either Et₂O (Ar = Ph) [22, 61] or benzene (Ar = Fl) [62]. The Ph-substituted diol was then reduced with HI in glacial acid to give [**3**]Ph in 80–85% yield [63]; reduction by P₂I₄ in Et₂O gave 30% yield [22]. In analogous fashion, [**3**]Fl was formed in quantitative yield from the precursor diol via reduction with HI in H₂O in the presence of iodine [62].

The synthesis of the diol precursor for [5]cumulenes (**1**, *m* = 2) follows the analogous procedure using BrMg–[C \equiv C]₂–MgBr (**3**) in a reaction with a diarylketone in either Et₂O (Ar = Ph) [22] or Et₂O/benzene (Ar = Fl) [22] with yields of 68% and 29%, respectively. Subsequent reduction of the diol was then affected with P₂I₄ in either pyridine ([**5**]Ph, 0.2% yield) or Et₂O ([**5**]Fl, 1.6% yield)



Scheme 1 Synthesis of aryl-substituted series of $[n]$ cumulenes. Reactions and conditions. (a) For Ar = Ph: Et₂O, rt (no yield given). For Ar~Ar = Fl: PhH, Δ, 2 h (28%). (b) For Ar = Ph: Et₂O (68%). For Ar~Ar = Fl: Et₂O/PhH 12.5:1 (29%). (c) For Ar = Ph: Et₂O (30–50%). For Ar~Ar = Fl: Et₂O (20%). (d) For Ar = Ph: CuCl in H₂O, O₂, MeOH, 8 h (no yield given). (e) For **[3]Ph**: HI in CH₃CO₂H, 0°C, 2–3 h (80–85%) or P₂I₄, Et₂O, 20 min (30%). For **[3]Fl**: HI in H₂O, I₂, Δ, 3 h (quantitative yield). (f) For **[5]Ph**: P₂I₄, pyr, 0°C (<1%) [Using CrCl₂ as a reductant, the yield of **[5]Ph** and **[5]Fl** (94% and 89%, respectively) improved substantially, see [23]]. For **[5]Fl**: P₂I₄, Et₂O (1.6%). (g) For **[7]Ph** and **[7]Fl**: PhH, Et₃N, P₂I₄. (h) For **[9]Ph**: SnCl₂, HCl (10%), PhH

[22]. The yields of **[5]Ph** and **[5]Fl** were very poor with these reaction conditions, and the reduction was subsequently optimized through the use of Cr(II) chloride and HCl in dry Et₂O. This improved the yields for **[5]Ph** and **[5]Fl** to 94% and 89%, respectively [23].

It is interesting to note that, by providing access to the necessary diols, it was the advances in polyne synthesis during the early 1950s [29, 31, 33] that propelled forward the synthesis of cumulenes beyond the length of the [5]cumulene. For the synthesis of the diol precursor for [7]cumulene (**1**, $m = 3$), the disodium acetylide **4** was reacted with benzophenone or fluorenone [25]. The resulting diols were then reduced in the presence of P₂I₄ and Et₃N in benzene to give **[7]Ph** and **[7]Fl** [25]. Unfortunately, neither **[7]Ph** nor **[7]Fl** was sufficiently stable for isolation as a pure solid, and yields were thus not reported.

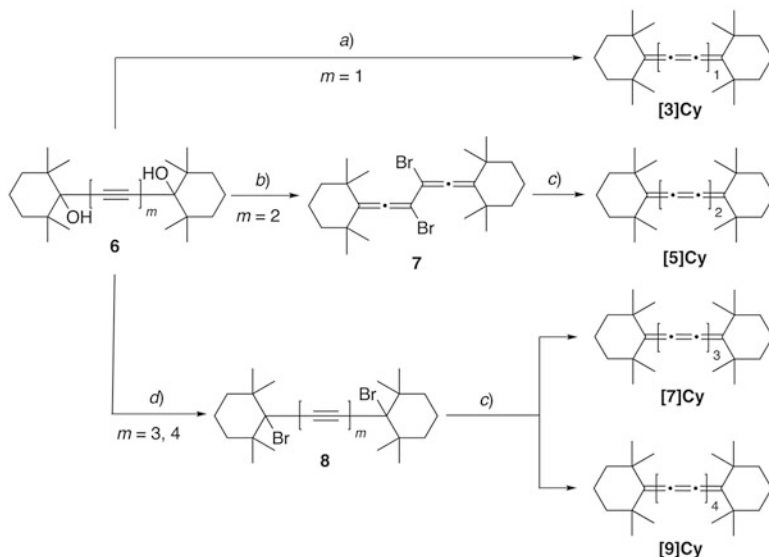
The formation of the [9]cumulene, **[9]Ph**, required first the formation of the diynol **5**, which was conveniently synthesized from the reaction of Na–[C≡C]₂–H and benzophenone [30]. The tetrayne linked diol precursor (**1**, $m = 4$) was then obtained by a homocoupling reaction of **5**, using CuCl catalyst in H₂O and MeOH in the presence of oxygen. The reduction to **[9]Ph** was then carried out in benzene with SnCl₂ and aqueous 10% HCl [30]. As in the case of **[7]Ph**, **[9]Ph** could not be obtained as a pure solid due to a lack of stability. The $[n]$ An series of cumulenes has also been described ($n = 3, 5, 7$), but no specific synthetic details have been reported, and no yields were available [64].

2.1.2 Synthesis of an Alkyl-Substituted Series of $[n]$ cumulenes

The second general synthetic route to $[n]$ cumulenes was used to assemble the alkyl cumulenes, such as the tetramethylcyclohexylidenyl terminated derivatives $[n]$ Cy. Unlike the aryl endcapped cumulenes, the reduction process to the $[n]$ Cy derivatives passed through a dibromide intermediate, rather than occurring directly from the diol (Scheme 2) [29]. The synthesis of the oligoene- α,ω -diol precursors **6** mirrored the routes discussed in Sect. 2.1.1. With these diols in hand, the [3]cumulene, [3]Cy, was formed directly from the diol **6** ($m = 1$) via reaction with PBr_3 in pyridine, giving 16% yield of the desired product [29].

Reaction of diynediol **6** ($m = 2$) with PBr_3 in benzene gave the diallene intermediate **7** in 71% yield. This dibromide was then subjected to Zn powder (activated by H_2SO_4 and I_2) in Et_2O to afford the [5]Cy in an excellent yield of 92% [29]. The synthesis of [5]Cy could also be accomplished directly from **6** ($m = 2$) via reduction with PI_3 in Et_3N , although this reaction gave a very poor yield (<2%) [29].

The formation of both [7]Cy and [9]Cy followed similar procedures. Bromination of **6** ($m = 3$ or 4) was performed with PBr_3 in benzene with heating. Although no yield was provided in the case of the triyne (**8**, $m = 3$), a reasonable yield (53%) was obtained in the case of the tetrayne (**8**, $m = 4$). Finally, reduction with Zn in Et_2O gave the desired products [7]Cy and [9]Cy, but yields of these cumulenes were not reported due to instability of the products [29].



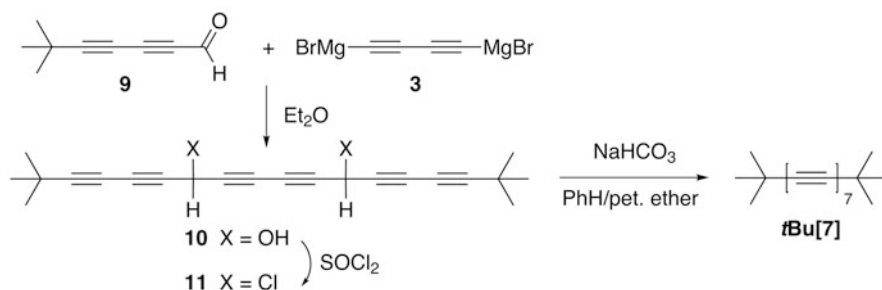
Scheme 2 Synthesis of alkyl-substituted series of $[n]$ cumulenes, $[n]$ Cy. (a) PBr_3 , pyr, (16%). (b) PBr_3 , PhH (71%). (c) Zn (activated by H_2SO_4 and I_2), Et_2O (92% for [5]Cy, no yield given for [7]- and [9]Cy). (d) PBr_3 , PhH, 4 h Δ then 12 h rt, 60–70°C ($m = 3$, no yield given); 75–80°C ($m = 4$, 53%)

2.2 Polyne Synthesis

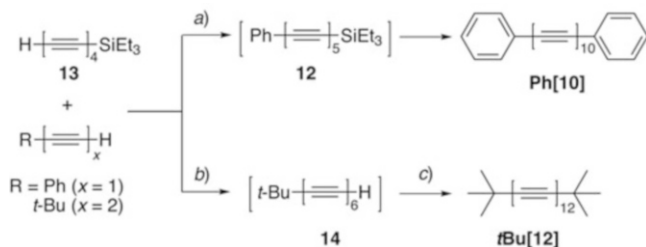
In comparison with the cumulenes, there have been far more synthetic methods explored during the last half century for building up polyynes. Many are based on hetero- and homocoupling of acetylenic precursors, while others rely on an elimination process or the extrusion of a molecular subunit to form the polyne chain [14, 65]. Not all of these various methods, many of which have been reviewed, can be discussed completely in this section. Thus, selected examples of synthetic methods are presented, especially those that relate to longer members of polyne series that will be discussed later in this chapter.

Early synthetic routes to polyynes mimicked, to some extent, the formation of cumulene precursors, as described earlier. This approach typically involved the addition of an acetylide to an aldehyde, conversion of the alcohol to a halide, followed by an elimination reaction. In 1953, Bohlmann used this general approach for the first synthesis and characterization of a heptyne (Scheme 3), as part of his study of *t*Bu[*n*] polyynes (where *n* is the number of triple bonds) [66]. Reaction of diynal **9** with Grignard **3** gave the desired diol **10**, which was then converted to dichloride **11** with thionyl chloride. Subjecting this dichloride to NaHCO₃ in benzene and petroleum ether gave heptyne *t*Bu[7] via elimination of two equivalents of HCl. *t*Bu[7] was isolated as a yellow solid that was stable to 150°C. A similar route was used in 1960 by Jones and coworkers for the synthesis of *t*Bu[10] [67].

Johnson and Walton reported the formation of several polyne series via mixed oxidative coupling reactions using triethylsilyl terminated alkynes as building blocks [41]. For example, the synthesis of the decayne **Ph[10]** started with the attempted formation of pentayne **12** via mixed Hay coupling of triethylsilyl terminated tetrayne **13** and phenylacetylene (Scheme 4) [41]. Rather than desired product **12**, however, the product isolated from this reaction was decayne **Ph[10]**. It was supposed that the desilylation of **12** occurred in situ to give the terminal pentayne, which then underwent homocoupling to give **Ph[10]**. Attempts to isolate pure **Ph[10]** were, however, futile: concentration of a chloroform solution of



Scheme 3 Bohlmann's synthesis of *t*Bu[7]



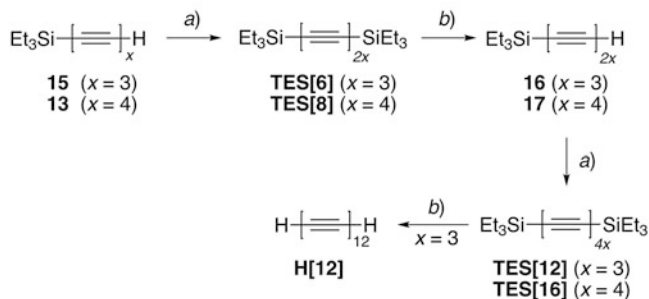
Scheme 4 Synthesis of decayne **Ph[10]** and dodecayne **tBu[12]** by Johnson and Walton. (a) CuCl, TMEDA, acetone/petrol, air, 3 h. (b) 1. CuCl, TMEDA, acetone, O₂, 90 min; 2. 0.1 N NaOH, MeOH, 20°C. (c) Cu(OAc)₂, pyr, MeOH, H₂O, 72 h

Ph[10] from the reaction medium gave dark red needles that rapidly decomposed exothermically.

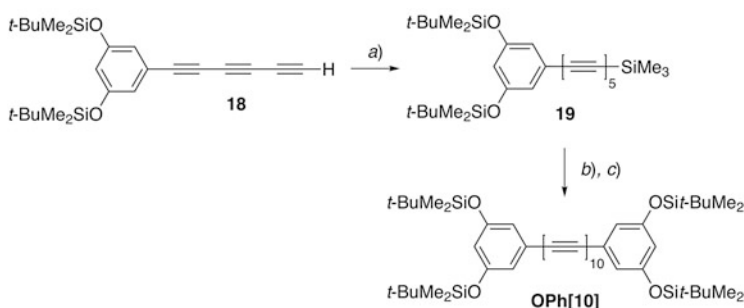
A similar procedure was used to form one of the first known dodecaynes, **tBu[12]**, which was also reported by Johnson and Walton [41]. Mixed Hay coupling using an excess *t*-butyl-1,3-butadiyne (5,5-dimethylhexa-1,3-diyne) and tetrayne **13** resulted in the triethylsilyl endcapped hexayne, which was neither isolated nor characterized (Scheme 4). Rather, immediate removal of the triethylsilyl group with NaOH gave the terminal hexayne **14**. The subsequent coupling reaction of terminal hexayne **14** under Eglinton–Galbraith conditions gave the dodecayne **tBu[12]** as reddish-brown needles. The sample decomposed in less than 10 minutes at room temperature under nitrogen.

Complementing the oxidative cross-coupling employed to form **12** and **14** was the use of oxidative homocoupling reaction for chain extension. This method has been used for, e.g., the synthesis of **TES[12]**, **H[12]**, and **TES[16]**, as reported by Walton and coworkers (Scheme 5) [43]. The triethylsilyl endcapped tri- or tetrayne (**15** or **13**, respectively) was used in homocoupling reactions under Hay conditions to give **TES[6]** or **TES[8]**, respectively. Carefully controlled desilylation in the presence of NaOH allowed for removal of one of the triethylsilyl groups and gave **16** and **17**, which were carried on to homocoupling reactions under Hay conditions to give **TES[12]** and **TES[16]**. While **TES[12]** could be isolated pure in solution via column chromatography, samples of hexadecayne **TES[16]** were reportedly characterized as mixtures that could not be purified. The dodecayne **TES[12]** could be desilylated with NaOH to give **H[12]**, which was purified chromatographically and characterized in a solution of hexane.

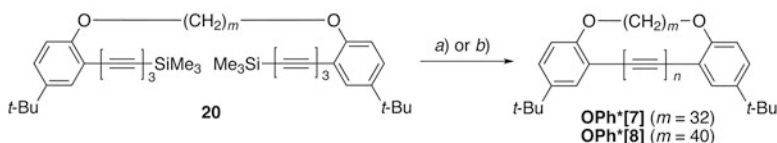
In an attempt to circumvent selectivity issues associated with oxidative coupling of terminal acetylenes, Hirsch and coworkers explored a cross-coupling route to aryl endcapped polyynes [68]. In this reaction, the terminal acetylene **18** was treated with *n*-BuLi in THF at low temperature, followed by addition of CuCl, pyridine, and Br–[C≡C]₂–SiMe₃ (Scheme 6). This gave pentayne **19**, which was then desilylated and subjected to homocoupling under Hay conditions to give decayne **OPh[10]**. Interestingly, this homocoupling reaction also reportedly resulted in the formation of octayne **OPh[8]** and nonayne **OPh[9]**, which could



Scheme 5 Synthesis of **TES[12]**, **TES[16]**, and **H[12]** by Walton and coworkers. (a) CuCl, TMEDA, acetone/petrol, air/O₂. (b) aqueous NaOH, MeOH/petrol



Scheme 6 Synthesis of decayne **OPh[10]** by Hirsch and coworkers. (a) 1. *n*-BuLi, THF, 0°C; 2. CuCl; 3. pyr, Br-[C≡C]₂-SiMe₃. (b) K₂CO₃, MeOH/THF (1:1). (c) CuCl, TMEDA, acetone, O₂, 20°C. Yield could not be determined, **OPh[10]** obtained only as mixture with **OPh[8]** and **OPh[9]**

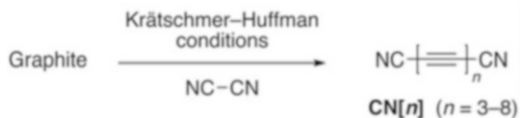


Scheme 7 Synthesis of insulated wire by Hirsch and coworkers. (a) For **OPh*[7]**: 1. K₂CO₃, MeOH/THF (1:1); 2. Pd(PPh₃)₂Cl₂, CuI, I-C≡C-I, Et₃N, CH₂Cl₂, rt (11%). (b) For **OPh*[8]**: 1. K₂CO₃, MeOH/THF (1:1); 2. Pd(PPh₃)₂Cl₂, CuI, Br-[C≡C]₂-SiMe₃, Et₃N, CH₂Cl₂, 0°C (1.1%)

not be separated. This same general procedure was also exploited for the synthesis of the dendrimer endcapped polyynes series **Ar*[n]** [68].

As a part of their effort to encase polyynes within an insulating, protective sheath of an alkyl group, Hirsch and coworkers reported a rather unique mode of hepta- and octayne formation (Scheme 7) [69]. Subjecting a tethered triyne **20** to a Pd-catalyzed coupling reaction in the presence of diiodoacetylene provided the desired heptayne **OPh*[7]** in 11% yield as an orange solid. Conversely, reaction of **20** with Br-[C≡C]₂-SiMe₃ under similar conditions gave **OPh*[8]**.

Scheme 8 Synthesis of dicyanopolyynes **CN[n]**



A homologous series of cyano-endcapped polyynes has been synthesized by vaporization of graphite under Krätschmer–Huffman conditions [70] in the presence of cyanogen (Scheme 8) [71, 72]. The process conveniently provided gram quantities, and the mixture of dicyanopolyynes resulting from the reaction could be separated from the accompanying soot by preparative HPLC, yielding **CN[3]** (55%), **CN[4]** (35%), **CN[5]** (7%), **CN[6]** (2%), **CN[7]** (0.7%), and **CN[8]** (0.3%). The **CN[n]** polyynes were sufficiently stable in solution under ambient conditions to allow for spectroscopic characterization, and dilute solutions were indefinitely stable at low temperature in the dark. In the solid state, however, the **CN[n]** polyynes were only stable at low temperature in the dark.

An efficient method for the synthesis of polyynes made use of the Fritsch–Buttenberg–Wiechell (FBW) rearrangement [73–75]. The formation of polyynes series **TIPS[n]** [76], **tBu[n]** [77], **Ad[n]** [78], **Ph[n]** [79], and **Ph_F[n]** [80, 81] has been accomplished via FBW rearrangement, using several variations on a common theme that typically targets dibromoolefins as stable and readily available precursors to polyynes [12, 82–84]. Two examples have been outlined in Scheme 9. Starting with either tetrabromoolefin **21** or dibromoolefin **22**, FBW rearrangement in hexanes at low temperature using *n*-BuLi or HexLi afforded the unsymmetrical pentaynes **23** and **24**. Desilylation of **23** with K₂CO₃ in a mixture of THF/MeOH (1:1), followed by homocoupling in the presence of CuCl and TMEDA in CH₂Cl₂ resulted in **TIPS[10]** [76]. In the case of pentayne **24**, no desilylation step was required, and the trimethylsilyl group was effectively removed under the conditions of the homocoupling reaction, which was performed in a mixture of pyr/THF/MeOH (1:1:1) with Cu(OAc)₂•H₂O as catalyst [77].

A newly designed synthesis of polyynes with Co₃C-containing endgroups was introduced by Bruce and coworkers using gold acetylides in cross-coupling reactions with alkynyl iodides [85–88]. The longest member of this series to be synthesized, **Co[12]**, was formed from the Pd-catalyzed reaction of the gold-acetylide **25** and the diiodo-tetrayne **26** (Scheme 10) [87]. Dodecayne **Co[12]** was isolated in 39% yield as a dark purple microcrystalline solid that slowly decomposed in solution. The octayne **Co[8]** was also obtained in the reaction, as a result of the homocoupling reaction of the gold-acetylide **25**.

The most recent and successful synthesis of polyynes relied on the use of a sterically demanding triarylmethyl endcapping moiety, the “super trityl” group, Tr* (see Fig. 2) [89]. One of the main benefits of this general synthetic protocol was the stability observed for terminal alkyne precursors, such as the heptayne **27** (Scheme 11), which allowed for chromatographic purification prior to the chain elongation step, thus reducing the number of by-products produced. For example, the reaction of pure **27** with **28** in the presence of excess Cu(OAc)₂•H₂O, K₂CO₃,

and 2,6-lutidine, gave **29** in 35% isolated yield. Two aspects of this transformation were noteworthy. First, the removal of the trimethylsilyl groups of **28** was effected in situ under the Eglinton–Galbraith reaction conditions, and this eliminated the need for an independent desilylation step. Second, 2,6-lutidine was used in place of the typical base, pyridine, and this was essential to the success of the reaction. Removal of the terminal *i*-Pr₃Si-group of **29** was achieved using CsF in a mixture of THF/H₂O (5:1), and the product was taken on directly, following workup, to the formation of **Tr***[**22**], which was isolated as a reasonably stable orange–red solid.

3 Structure and Bonding

Following the oligomer approach [90, 91], individual members of the cumulene and polyynes series have typically been characterized by a variety of physical and spectroscopic methods, often with an eye toward identifying saturation of a particular effect. For a set of oligomers, convergence of spectroscopic data versus length to constant value (saturation) can shed light on the expected properties of the polymeric form, carbyne. Alternatively, when saturation is not yet reached, extrapolation of the data versus length to an asymptotic limit can also be a useful predictive tool. These modes of evaluating cumulenes and polyynes also depend, quite obviously, on the presence or absence of endgroup effects. While the electronic impact of the terminal groups might be minimized by the use of potentially benign alkyl or silyl groups, it should be noted that effects of the endcapping group cannot be entirely eliminated. Below is a survey of common characterization efforts that have provided insight into the structure and bonding of cumulenes and polyynes.

3.1 Vibrational Spectroscopy

3.1.1 Cumulenes

In considering characterization of [*n*]cumulenes by vibrational spectroscopy, it is noted that for [3]cumulenes, only ν_1 is expected in a diagnostic range (ca. 2000 cm⁻¹) [58, 92] that is not obscured by other vibrations (Fig. 3). For centrosymmetric molecules, however, ν_1 is IR inactive because the transition is forbidden. For [5]cumulenes, ν_1 is also forbidden by symmetry, whereas ν_2 is expected in the range of 1900–2125 cm⁻¹ [58, 93, 94]. While IR spectroscopic data for surprisingly few cumulenes have been reported, those available seem to confirm these theoretical predictions. A weak absorption is observed at 1997 cm⁻¹ for [**5**]Ph, as well as at 2000 and 2003 cm⁻¹ for the tetra(4-tolyl)- and tetra(4-*t*-BuC₆H₄)-substituted [5]cumulenes, respectively [95]. No IR data have been published for longer cumulenes.

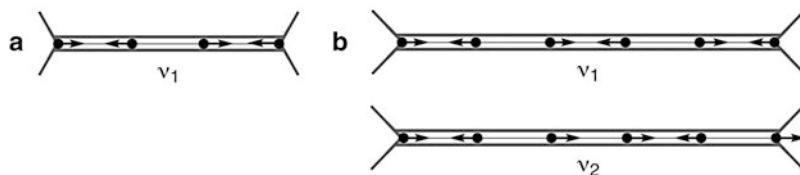


Fig. 3 Schematic illustrations of vibrations for (a) [3]cumulenes and (b) [5]cumulenes

3.1.2 Polyynes

To our knowledge, no recent attempt has been made to compile vibrational data for polyynes, and available data for series discussed in this review have thus been tabulated in Table 1 for polyynes up to $n = 14$ (A comprehensive study of the series $\mathbf{H}[n]$ has not been reported and only selected values are available: [99–102]). While in many cases IR and Raman data have been reported as only routine characterization, there are a couple of studies that have delved deeper into the results of vibrational spectroscopy, including the study of the $\mathbf{Ad}[n]$ polyynes [78]. Following is a summary of some of the salient observations from IR and Raman spectroscopic analysis of polyynes.

1. The IR data for many series initially show a single absorption for shorter derivatives, while multiple absorptions are found as the chain length increases. For $n \geq 3$, the highest energy absorption typically appears at around 2200 cm^{-1} (except for $\mathbf{TIPS}[n]$ and $\mathbf{Co}[n]$). This highest energy absorption frequency remains relatively constant as n increases, and computational results attribute this signal to the ν_1 vibration shown in Fig. 4a, as determined for the $\mathbf{Ad}[n]$ series [78].
2. At a length of between $n = 6$ and $n = 8$, two additional bands typically appear in the IR spectra; a strong signal (ν_2) and a weak signal at lower energy (ν_3). For example, in the spectrum of $\mathbf{Ad}[6]$ these two signals appear at 2170 and 2078 cm^{-1} , respectively (these vibrations are shown schematically in Fig. 4b, c for $\mathbf{Ad}[10]$). The energy of both bands decreases as polyyne length is increased. This dispersion is shown graphically in Fig. 5 for the strongest band (ν_2) in the IR spectra of the $\mathbf{Tr}^*[n]$ and $\mathbf{Ad}[n]$ series. While the decrease in energy is nearly linear in both cases through $n = 10$, a leveling of the vibrational frequency becomes apparent for the $\mathbf{Tr}^*[n]$ series for ca. $n > 12$.
3. Comparison of IR and Raman data for polyynes with $n \geq 6$ shows that the weak low energy signal in the IR spectra consistently corresponds to the energy of the strongest Raman signal. This phenomenon has been explained by bending of the polyyne chain in solution, which results in a non-centrosymmetric structure and a concurrent activation of the Raman band in the IR spectrum [78].

Table 1 IR data for series of $[n]$ polyyynes ($\nu_{\text{C}\equiv\text{C}}$ [cm^{-1}])

$n =$	2	3	4	5	6	7	8	10	11	12	14	Reference
tBu $[n]^a$	IR	2160 ^b 2212	2221 ^c	2206 2119	2195 2076	–	2208 2127 2020	2204 2115 2080 2009	–	–	–	[77, 96]
Ad $[n]^d$	IR	2166 s 2141 s	2208 s	2220 s	2204 s 2170 s 2078 vw	2191 s –	2203 s 2124 s 2024 vw 2024 s	2195 s 2081 s 1985 vw 1985 s	–	–	–	[78]
	Raman	2246 s	2211 s	2177 m 2158 s	2115 s 2078 s	–	–	–	–	–	–	
Tr $^*[n]^a$	IR	–	–	2216 m	–	2201 m 2178 m	2206 m 2124 m 2018 w	2201 m 2080 s 1981 vw	–	2201 m 2156 m 2042 s 1956 w	2201 w 2128 m 2015 m 1939 vw	[89] ^e
TIPS $[n]^c$	IR	2061	2154	2042	2178 2030	2158 2030	2119 2021 1958	2072	–	–	–	[76]
Ph $[n]$	IR	2220 ^f	2200 ^f	2205 ^f	2175 ^g 2075	2174 ^c 2159	2184 ^h 2105	2185 w ^g 2070 m 2020 w	–	–	–	[41, 79, 97, 98]
Ph_F $[n]^a$	IR	–	–	2218 w	–	2192 w 2165 w	2200 w ^j 2114 w 2012 w	–	–	–	–	[80]
Mes $[n]^f$	IR	–	–	2193 w 2190 s 2075 w	–	2175 m 2100 m 2065 w	2180 w ^g 2100 m	–	–	–	–	[41]
Ar $^*[n]$	Raman	–	–	–	–	2057 m ^j	2013 m ^k	1982 w ^k	–	–	–	[68]

(continued)

Table 1 (continued)

$n =$	2	3	4	5	6	7	8	10	11	12	14	Reference
OPh[n]	IR ⁱ	2148 vw	–	2201 m 2136 vw	–	2183 m 2160 m 2058 vw	–	2194 m 2112 s 2009 vw	–	–	–	[68]
	Raman ^j	2232 w	–	2171 w 2135 s	–	2060 m	–	2012 s	–	–	–	
CN[n]^j	IR	–	2187	2186 2120	2187 2118	2170 2154	2172 2128 2092	2172 2126 2092	–	–	–	[72]
Co[n]	IR	2128 vw ^m	2089 vw ^m 2104 vw	2112 vw ^m 2104 vw	–	–	2172 w ^c 2157 vw 2127 vw	2154 vw ^c 2123 vw	–	2170 w ^a 2122 w	2168 vw ^c 2129 vw	– – [85, 87, 88]

^aSolid state^bCCl₄ (cast)^cCH₂Cl₂ (cast)^dTHF (solution)^eFor the sake of convenience, values of the longer members of the **Tr^{*}[n]** series are given here: **Tr^{*}[16]** 2201 m, 2166 w, 2106 m, 2055 w, 1991 s, 1925 w; **Tr^{*}[18]** 2201 m, 2151 m, 2082 m, 2053 w, 2033 w, 1974 m, 1917 vw; **Tr^{*}[20]** 2200 m, 2134 m, 2101 w, 2061 m, 2013 w, 1956 m, 1905 w; **Tr^{*}[22]** 2199 m, 2159 w, 2116 m, 2083 vw, 2042 m, 1997 vw, 1942 m, 1897 vw; see also [89].^fCCl₄ (solution)^gCHCl₃ (solution)^hTHF (cast)ⁱCHCl₃ (cast)^jCH₂Cl₂ (solution)^kEtOAc (solution)^lKBr^mNujol

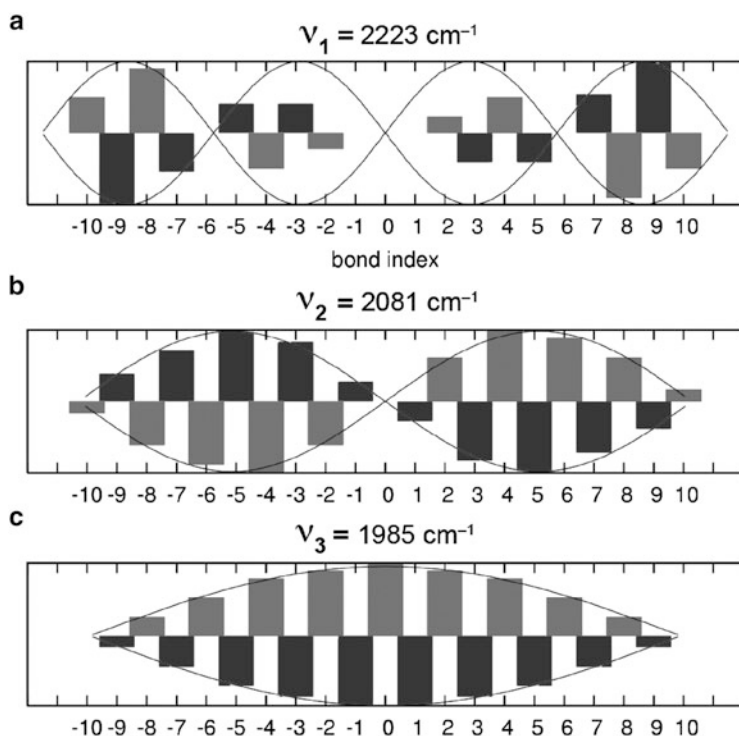


Fig. 4 Theoretical vibrational displacements (bond length changes) and frequencies for Ad[10] associated with the three observed vibrations ν_1 , ν_2 , and ν_3 (from PBEPBE/cc-pVDZ calculations). The central bond of the chain is indicated by the bond index of zero. Dark bars denote C≡C bonds and light bars C-C bonds. Sinusoidal lines are superimposed onto the stick plots to facilitate recognition of the number of nodes [78]

3.2 ^{13}C NMR Spectroscopy

With a rigid framework of sp-hybridized carbons that can be unstable for longer derivatives, ^{13}C NMR spectroscopy of both cumulenes and polyynes can be challenging due to long T1 relaxation times, insolubility of the sample, and decomposition of the material during acquisition. This is particularly true for the analysis of cumulenes, whereas several very recent studies have provided more details for polyynes.

3.2.1 Cumulenes

Unfortunately, no ^{13}C NMR spectroscopic data have been reported for cumulenes beyond the length of a [5]cumulene, and even data describing [5]cumulenes are scarce. Iyoda has described the characterization of several derivatives by ^{13}C NMR

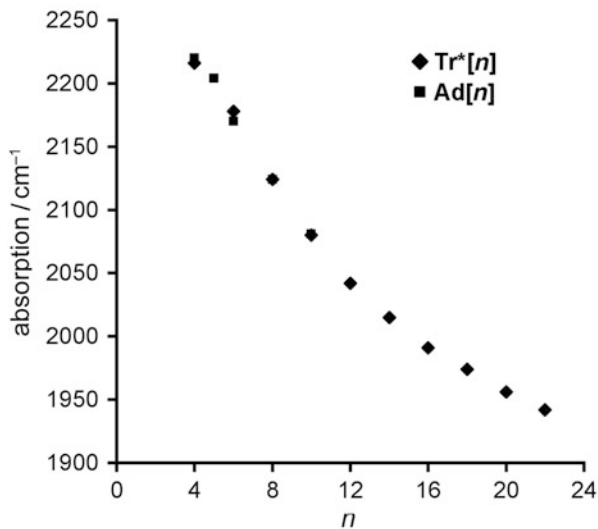
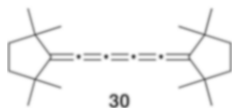


Fig. 5 IR absorptions for **Ad**[*n*] (squares) and **Tr***[*n*] (diamonds) as THF solutions and CH₂Cl₂ cast films, respectively (values for **Tr***[*n*] are listed in Table 1; see also [89])

spectroscopy, including [5]Cy, which shows resonances at δ 154.3, 138.9, and 132.1 for the three unique carbons of the cumulene chain. While comparisons are not available to longer or shorter derivatives, the effect of ring strain introduced to the endgroup by moving to a tetramethylcyclopentylidene endgroup can be observed, where signals are observed at δ 149.7, 144.7, 132.1 for compound **30** [95].



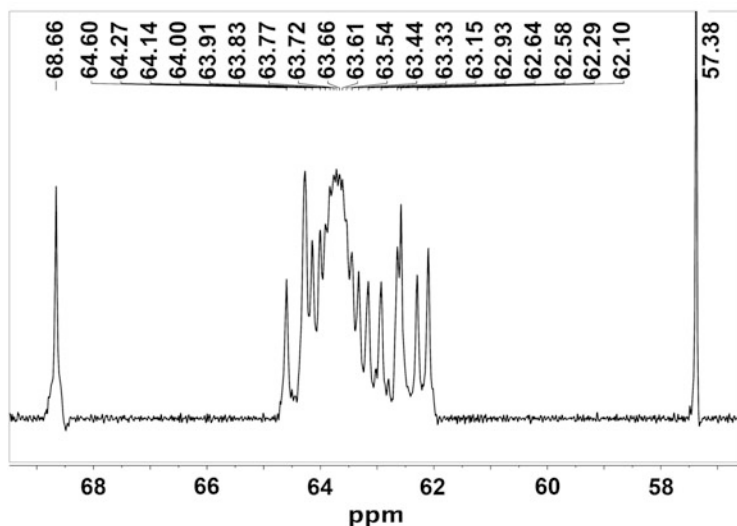
3.2.2 Polyynes

¹³C NMR spectroscopic analysis of a number of polyyne series has been reported over the past decade, as summarized in Table 2 and Fig. 6, for the longest derivative in each series. Several trends are observed that shed light on polyyne structure.

1. There appears to be an endgroup effect, as would be expected. The longest derivative in the alkyl series (**tBu**[*n*], **Tr***[*n*], **Ad**[*n*]) shows one downfield resonance in the range of 69–90 ppm, while silyl and aryl endcapped derivatives show two downfield signals over approximately the same spectral window (70–89 ppm). In each case, the remaining resonance fall into a rather narrow

Table 2 ^{13}C NMR alkyne carbon resonances for $[n]$ polyynes^a

	Alkyne carbon chemical shift in CDCl_3 (ppm)	Reference
<i>t</i>Bu[10]	89.6, 64.3, 63.8, <i>63.5(2x)</i> , <i>63.0</i> , 62.6, 62.1, 61.6, 61.4	[77]
Ad[10]	89.2, 64.7, 63.9, 63.7, <i>63.5</i> , <i>63.1</i> , 62.6, 62.1, 61.6, 61.5	[78]
Tr*[22]	68.66, 64.60, 64.27(2x), 64.14, 64.00, 63.91, 63.83, 63.77, 63.72, <i>63.66</i> , <i>63.61</i> , 63.54, 63.44, 63.33, 63.15, 62.93, 62.64, 62.58, 62.29, 62.10, 57.38	[89]
TIPS[10]^b	89.3, 88.8, 63.8, 63.6, <i>63.5</i> , <i>63.2</i> , 62.9, 62.5, 62.2, 61.0	[76]
Ph[8]^c	79.1, 74.1, 67.9, <i>64.6</i> , <i>63.8</i> , 63.75, 63.72, 63.4	[79]
Ph_F[8]	85.0, 70.3, 66.2, <i>64.4</i> , <i>63.6</i> , 62.8, 61.0, 60.8	[80]
Ar*[10]^d	78.36, 73.64, 67.24, 64.71, <i>64.09</i> , <i>63.97(2x)</i> , 63.84(2x), 63.79	[68]
OPh[8]	77.53, 73.73, 67.04, <i>64.45</i> , <i>63.61</i> , 63.39, 63.30, 62.57	[68]

^aMedian values shown in italics^bIn CD_2Cl_2 ^cIn THF- d_8 ^dIn acetone- d_6 **Fig. 6** ^{13}C NMR spectrum of **Tr*[22]** in CDCl_3 showing sp-carbon resonances (outlying signals at 68.66 and 57.38 ppm arise from the endmost acetylenic carbons)

range of ca. 61–67 ppm (except for **Tr*[22]** which also shows an upfield signal at δ 57.38).

2. Aside from the most downfield signals, the endgroup effect is rather minimal: In all cases, the sp-carbon resonances converge toward a median value of ca. 63–64 ppm. For alkyl and silyl derivatives (***t*Bu[10]**, **Tr*[22]**, **Ad[10]**, and **TIPS[10]**), this range is slightly upfield (63.0–63.7 ppm) in comparison with the aryl derivatives (63.6–64.6 ppm).

3. A unique resonance is observed for each sp-hybridized carbon in all cases except for **Tr***[22], in which case 21 of the 22 expected resonances are found (Fig. 6). Thus, these remain molecular species – i.e., degeneracy of chemical shifts of the acetylenic carbons has not yet been achieved.
4. Extrapolating from these data suggests that a ^{13}C NMR spectrum of the allotrope carbyne would likely consist of a broadened signal that is centered at a chemical shift of about 63.7 ppm (see Fig. 6). This estimate is consistent with that expected from a polyynic framework composed of alternating single and triple bonds.

3.3 UV/Vis Spectroscopy

A semi-empirical evaluation of the electronic landscape of polyynes and cumulenes can be obtained by UV/Vis spectroscopic characterization. Historically, this has been the primary means of comparison of members within a homologous series of conjugated molecules, particularly with respect to analysis of electronic effects (e.g., band gap) as a function of length and substitution pattern. In particular, evidence of saturation is sought, which might lead to a prediction of the band gap of carbyne.

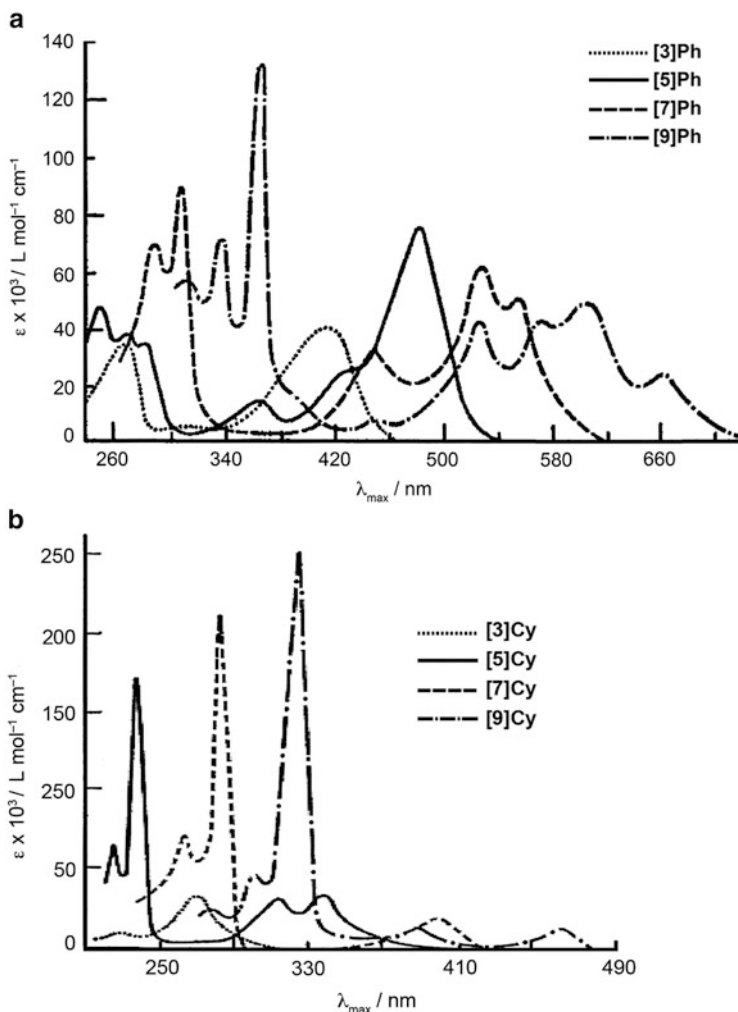
3.3.1 Cumulenes

The UV/Vis spectroscopic data for four series of $[n]$ cumulenes that contain members with $n \geq 7$ are available: three with aryl endcapping groups ($[n]\text{Ph}$, $[n]\text{Fl}$, $[n]\text{An}$) and one endcapped with alkyl groups ($[n]\text{Cy}$). A summary of λ_{max} values is listed in Table 3, while spectra for the $[n]\text{Ph}$ and $[n]\text{Cy}$ series are shown in Fig. 7a, b, respectively. Several defining features can be observed, giving insight into trends in the absorption energy (band gap) as a function of length and substitution pattern.

1. Solution-state measurements show two regions of absorption bands for each cumulene (except for $[3]\text{Cy}$), one at high energy and the other at lower energy (Fig. 7a, b). In aryl endcapped derivatives, fine structure increases as a function of length.
2. λ_{max} values for absorptions in both the high and low energy regions are red-shifted with increasing the chain length, as expected when conjugation is extended.
3. Coplanarity of the endgroups with the cumulene skeleton plays an important role in establishing the absorption energy (band gap). Specifically, λ_{max} values of $[n]\text{Fl}$ and $[n]\text{An}$ cumulenes, with coplanar aryl endgroups, are found at lower energy than λ_{max} values of the analogous $[n]\text{Ph}$ cumulenes in which the phenyl groups are not coplanar with respect to the cumulene skeleton.

Table 3 λ_{\max} values for $[n]$ cumulenes in nm (E_g in eV)

$n =$	3	5	7	9	Reference
$[n]\text{Ph}^{\text{a}}$	420 (2.95)	489 (2.54)	557 (2.23)	663 (1.87)	[22, 25, 30, 103]
$[n]\text{Fl}^{\text{a}}$	484 (2.56)	543 (2.28)	597 (2.08)	–	[22, 24, 25]
$[n]\text{An}^{\text{b}}$	481 (2.58)	555 (2.24)	610 (2.03)	–	[64]
$[n]\text{Cy}^{\text{c}}$	272 (4.56)	339 (3.66)	401 (3.09)	465 (2.67)	[29]

^aMeasured in PhH^bMeasured in CHCl_3 ^cMeasured in Et_2O **Fig. 7** UV/Vis spectra of $[n]$ cumulenes. (a) $[n]\text{Ph}$ measured in PhH (adapted with permission from [58]. Copyright 1964 John Wiley & Sons) and (b) $[n]\text{Cy}$ cumulenes measured in Et_2O (adapted with permission from [58]. Copyright 1964 John Wiley & Sons)

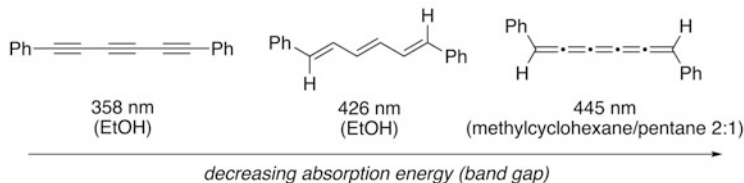


Fig. 8 Comparison of λ_{\max} values of a polyynes, polyene, and cumulene (solvent for each measurement is given in parentheses)

- Changes in λ_{\max} values of $[n]\mathbf{FI}$ and $[n]\mathbf{An}$ series are similar as a function of length, suggesting that the planar framework of the endcapping group (common to both series) dominates over the prospect of increased conjugated resulting from the zero linked bridge of the $[n]\mathbf{FI}$ molecules versus the saturated CH_2 linker found in the $[n]\mathbf{An}$ series.
- The disparity in absorption energy gap (E_g) between the two classes of cumulenes with aromatic endgroups (i.e., planar and nonplanar endgroups) decreases as a function of length, from 0.39 eV ($E_{g([3]\mathbf{Ph})} - E_{g([3]\mathbf{FI})}$) to 0.15 eV ($E_{g([7]\mathbf{Ph})} - E_{g([7]\mathbf{FI})}$), confirming the reduced influence of endgroups in the longer derivatives.
- λ_{\max} values of $[n]\mathbf{Cy}$ are substantially higher energy than those of all series containing aromatic endgroups. The difference in absorption energy gap between the $[n]\mathbf{Cy}$ and $[n]\mathbf{FI}$ series decreases substantially as a function of length, from 1.61 eV ($E_{g([3]\mathbf{Cy})} - E_{g([3]\mathbf{Ph})}$) to 0.86 eV ($E_{g([7]\mathbf{Cy})} - E_{g([7]\mathbf{Ph})}$).
- It is interesting to note the effect on electronic behavior between polyynes, polyenes, and cumulenes of identical length (e.g., six sp- or sp²-hybridized carbons) and analogous substitution (Fig. 8). The λ_{\max} value of diphenylhexatriyne (358 nm in EtOH) [97] is significantly higher energy than λ_{\max} of the corresponding sp²-hybridized framework diphenylhexatriene of 426 nm (in EtOH) [104]. Finally, λ_{\max} for the 1,6-diphenylcumulene lies at longer wavelength (445 nm in methylcyclohexane/pentane 2:1) than either the polyene or the polyene [64].

3.3.2 Polyynes

λ_{\max} values for the polyynes series are summarized in Table 4. Several general points are worthy of comment with respect to length and the nature of the endcapping group.

- There is a clear decrease in the absorption energy versus polyene length, and this is illustrated in Fig. 9 for the $\mathbf{Tr}^*[n]$ series. Furthermore, the lowest energy absorption transition dominates each spectrum, with vibronic structure unmistakably showing as a series of narrow absorption peaks with steadily increasing intensity toward the visible region.

Table 4 UV/Vis data for series of [n]polyyynes containing lowest energy wavelength λ_{max} in nm

n =	2	3	4	5	6	7	8	9	10	12	14	16	18	20	22	Reference
H[n]^a	-	-	-	225.5 ^b	250.5	273.5	295	315	331.5	348	375	-	-	-	-	[43]
H[n]^c	-	-	-	226	251.5	275	297	316	331.5	349	-	-	-	-	-	-
tBu[n]^c	-	213	240	266	289	310.5 ^{b,d}	330	-	362	387	-	-	-	-	-	[41, 66, 77]
Ad[n]^c	-	-	246	272	295	-	335	-	367	-	-	-	-	-	-	[105]
Tr[*][n]^c	-	-	268	-	310	-	347	-	376	400	419	432	443	451	458	[89]
TIPS[n]^c	-	234	260	284	304	-	339	-	369	-	-	-	-	-	-	[76]
TES[n]^a	263.5 ^b	230 ^b	256 ^b	278	298.5	317.5	335	349	365	388	-	426 ^e	-	-	-	[43]
TES[n]^c	264	231.5	256.5	279	299.5	319	336	350.5	367	390	-	-	-	-	-	[43]
CN[n]^f	-	232	259	282	303	322	339	-	-	-	-	-	-	-	-	[72]
Ph[n]^g	328	358 ^h	399	-	465	-	512	-	549 ⁱ	-	-	-	-	-	-	[41, 79, 97]
Ph_F[n]^g	325 ^a	-	399	-	461	-	507	-	-	-	-	-	-	-	-	[81, 106]
Mes[n]^c	341.5	-	407	-	469 ^a	-	522 ⁱ	-	-	-	-	-	-	-	-	[41]
Ar[*][n]^j	-	-	-	-	469	-	514	532	546	-	-	-	-	-	-	[68]
OPh[n]^j	336	-	403	-	467	-	514	-	-	-	-	-	-	-	-	[68]
OPh[*][n]^j	355	385	416	448	477	496	515	-	-	-	-	-	-	-	-	[69]

^aIn MeOH

^bAbsorptions with lower energy are observed in some cases, but with very low intensity

^cIn hexane(s)

^dIn Et₂O

^eIn petrol solution contaminated with starting material

^fIn NCCH₃

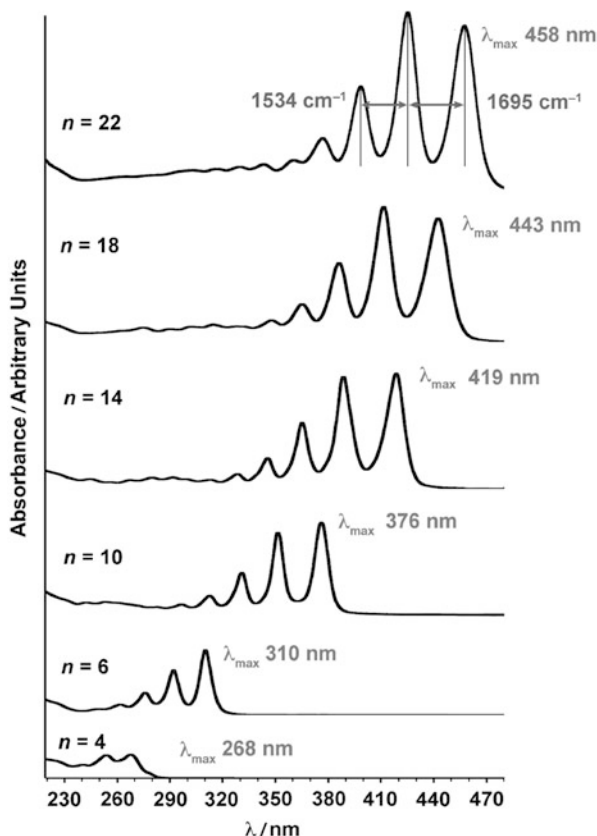
^gIn THF

^hIn EtOH

ⁱIn CHCl₃

^jIn CH₂Cl₂

Fig. 9 UV/Vis spectra of selected $\text{Tr}^*[n]$ polyynes as measured in hexanes; wavelength of λ_{max} is shown for each compound and vibrational separation of lowest energy absorptions for $\text{Tr}^*[22]$ is also shown



2. Closer examination of the spectra in Fig. 9 shows that the high-energy region of the UV/Vis spectra (230–300 nm) of the longer polyynes is nearly transparent, a feature that stands out against most other conjugated organic oligomers.
3. The choice of endgroup clearly has noticeable effect on λ_{max} values, and this is particularly evident through comparison of the $\mathbf{H}[n]$ series with all others. λ_{max} values for the $\mathbf{H}[n]$ are at higher energy than all other polyynes of comparable length.
4. For shorter polyynes, the endgroup effect on the absorption energy gap (E_g) is also rather pronounced, e.g., the difference in E_g between the two tetraynes $t\text{Bu}[4]$ to $\text{Tr}^*[4]$ is ca. 0.54 eV (as calculated from $\lambda_{\text{max}} = 240$ nm and 268 nm, respectively). The effect diminishes substantially for longer polyynes, e.g., the difference in E_g for decaynes $t\text{Bu}[10]$ and $\text{Tr}^*[10]$ is only 0.13 eV (as calculated from $\lambda_{\text{max}} = 362$ nm and 376 nm, respectively).
5. It is interesting to note that the electronic influence of the terminal cyano groups on λ_{max} is approximately equal to that of an alkyl or silyl group, despite the prospect of conjugation of the cyano group to the polyyne chain.

6. As expected, extension of the π -system through the incorporation of terminal aryl rings results in a dramatic red shift in λ_{\max} in comparison with polyynes terminated with non-aryl groups.

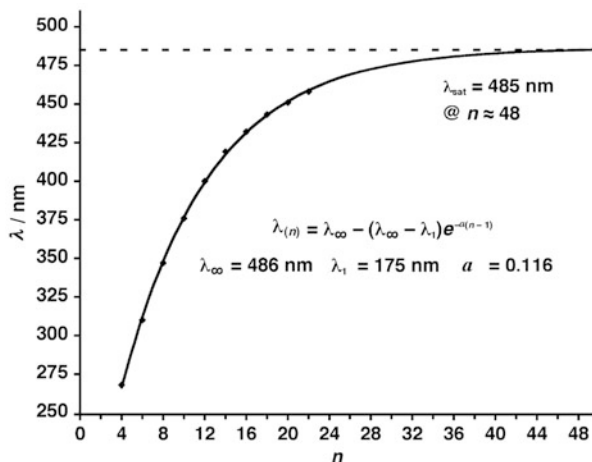
Many studies have used λ_{\max} values for polyyne series as a predictive tool for the bandgap of carbyne based on the premise that the absorption energy should eventually reach an asymptotic limit, and this should be a reasonable estimate of λ_{\max} (E_g) for carbyne. Often, a plot of E_g versus $1/n$ has been used (where n , as usual, is the number of acetylene units), and extrapolation to the y-intercept then provides an estimate of λ_{\max} for an infinite polyyne chain. Using this analysis for the series **TIPS**[n] ($n = 2$ – 10), a limiting value of $\lambda_{\max} = 570$ nm [76] is predicted, and this value is nearly identical to that predicted for **Ar***[n] polyynes of the same lengths ($\lambda_{\max} = 569$ nm) [68]. There is, however, a possible problem with this estimation, which is discussed by Meier and coworkers for other conjugated oligo- and polymers [107]. Using a plot of E_g versus $1/n$ assumes that any trend in E_g will continue monotonically through to an infinite length molecule. It is well known, however, that π -conjugated organic oligomers reach an effective conjugation length (ECL, also referred to as a confinement length, convergence length, delocalization length, and saturation length) with frameworks that contain a relatively small number of repeat units [91]. Thus, the ECL and saturation of properties such as λ_{\max} or E_g occurs at a finite oligomer length. Looking at a plot of E_g versus $1/n$ for the series **Tr***[n] does indeed show a noticeable deviation from linearity for the longest members of the series [89]. Meier has suggested an alternative protocol [107], in which the λ_{\max} or E_g values are analyzed using an exponential function of the form:

$$\lambda_{(n)} = \lambda_{\infty} - (\lambda_{\infty} - \lambda_1)e^{-a(n-1)} \quad (1)$$

where n is the number of acetylene units, $\lambda_{(n)}$ is λ_{\max} for a polyyne of length n (λ_1 is thus λ_{\max} of the monomer with $n = 1$, calculated according to (1)), and λ_{∞} is the limiting value as $n \rightarrow \infty$. The parameter a offers an estimate of how fast saturation is approached. Using λ_{\max} data for **Tr***[n] provides $\lambda_{\infty} = 486 \pm 5$ nm, $\lambda_1 = 175 \pm 13$ nm, and $a = 0.116 \pm 0.008$ (Fig. 10). Thus, the convergence of λ_{\max} values for **Tr***[n] based on (1) predicts λ_{\max} for carbyne of ca. 485 nm (2.56 eV) and a convergence length of ca. $n = 48$.¹ Clearly, this λ_{\max} value is considerably higher in energy than that predicted by extrapolating to the asymptotic of E_g at $n = \infty$ ($\lambda_{\max} \approx 564$ nm, 2.20 eV) [89]. Also of note is the value $a = 0.116$ that shows saturation for polyynes is reached quite gradually in comparison with other series of conjugated oligomers [107]. Finally, the analysis for **Tr***[n] series suggests quite

¹ A practical definition is required to relate the approach of λ_{\max} to λ_{∞} , i.e., when one consider the two quantities to be equal. Meier's suggestion has been adopted here [107]: considering the accuracy of the typical UV/Vis spectrometer (± 1 nm), λ_{\max} for carbyne is defined by fulfillment of the relationship $\lambda_{\infty} - \lambda_{(n)} \leq 1$ nm. Thus, in the present case, this is true at 485 nm (i.e., 486–485 nm ≤ 1 nm).

Fig. 10 Analysis of the absorption maxima in the series of $\text{Tr}^*[n]$ showing convergence of values according to (1)



strongly that a polyyne structure of alternating single and triple bonds will be maintained for carbyne, i.e., Peierls distortion will be upheld [77, 108].

3.4 X-ray Crystallography

Experimentally, as the electronic characteristics of cumulenes and polyynes are probed by UV/Vis spectroscopy, these analyses document a predictable lowering of the optical band gap as a function of increasing length, as described in the last section. These analyses also have shown that saturation of this trend has not yet been reached over the length of polyynes that is synthetically available. Given that cumulenes and polyynes are essentially 1D conjugated systems, changes in the band gap versus length should also be tied to structural changes of the molecules, and manifested in bond length alternation values (BLA = the difference in the bond length between the central-most bonds) [109, 110]. Recent theoretical studies predict that neither the band gap nor the BLA for polyynes should reach a value of zero [111–114], a phenomena commonly referred to as Peierls distortion [108]. The situation is less clear for cumulenes, where calculations point to a minimal BLA value already at the length of a [9]cumulene [94].

3.4.1 Cumulenes

To date, X-ray data have been obtained for approximately 22 [3]cumulenes, but only five structures longer than this are reported, including [4]Ph, [5]Ph, [4]Cy, [5]Cy, and [5]EtPh (Fig. 11) [115]. For the present comparison, the X-ray data for these structures are described, including that of [3]Ph and [3]Cy. Bond lengths and

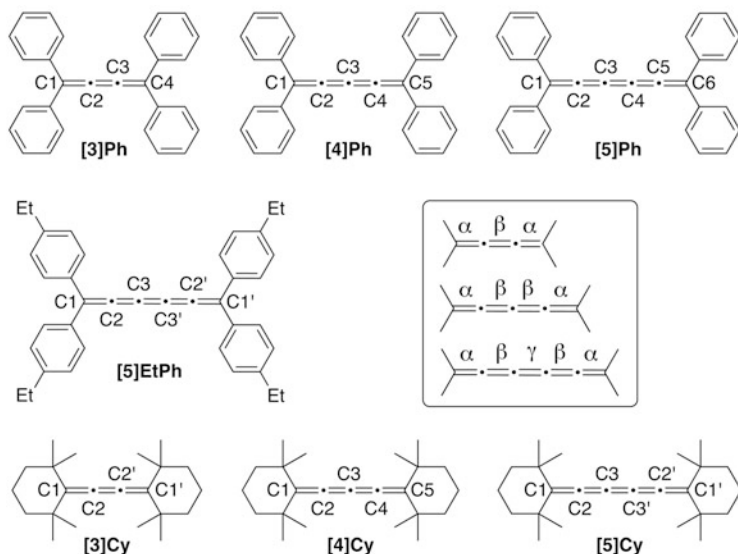


Fig. 11 Chemical structures and atomic numbering of $[n]\text{Ph}$, $[n]\text{Cy}$, and $[5]\text{EtPh}$ with X-ray structures reported in the literature. *Inset*: schematic description of α -, β -, and γ -bonds of generic cumulene structures

angles of the cumulenic chains are listed in Tables 5 and 6, respectively, following the atomic numbering system found in Fig. 11.

Several general trends are found from these data.

1. The terminal double bonds (α) of the cumulenic chain are always the longest within a particular cumulene structure, at 1.31–1.35 Å. In the “odd” $[n]$ cumulenes (i.e., $n = \text{odd}$), these values are similar to that of a typical conjugated double bond. For the “even” cumulene, [4]Ph, as well as the $[n]\text{Cy}$ series terminated with nonconjugating alkyl groups, the α -bonds are shorter, in a range of 1.313–1.332 Å. Thus, the presence or lack of conjugation through both endgroups has a marked effect on this bond length. This is nicely described schematically with simple resonance structures as in Fig. 12, where the α -double bonds in [4]cumulenes maintain more double bond character in the ionic resonance structures. Conversely, odd numbered $[n]$ cumulenes show that the α -double bond has more single bond character, a situation that would be augmented with aromatic substituents.
2. In all cases, the β -double bond is the shortest in the cumulenic chain, with values that lie between ca. 1.25 and 1.28 Å, i.e., they begin to resemble acetylenic bonds. The values of the central bonds in [5]cumulenes, γ , at 1.30–1.31 Å, are intermediate to those of α and β . Thus, bond length alternation remains strong for cumulenes with either aryl or alkyl endgroups.
3. The BLA values for $[n]\text{Ph}$ and $[n]\text{Cy}$ cumulenes decrease as a function of length although data are limited. Interesting is the fact that BLA values for the [4]- and [5]cumulenes in both series are approximately identical.

Table 5 Selected bond lengths (Å) for series of $[n]$ cumulenes^a

	C1–C2	C2–C3	C3–C4	C4–C5	C5–C6	BLA ^b	Reference
[3]Ph	1.344 (3) ^c	1.246 (3) ^c	1.345 (3) ^c	–	–	0.099	[116]
	1.346 (2) ^d	1.260 (2) ^d	1.349 (2) ^d	–	–	0.088	[116]
[4]Ph^e	1.327	1.270	1.271	1.326	–	0.056	[117]
[5]Ph	1.3453 (17)	1.2503 (18)	1.3091 (19)	1.2515 (18)	1.3456 (17)	0.058	[118] ^f
[5]EtPh	1.349 (2)	1.251 (2)	1.310 (3) ^g	–	–	0.059	[119]
[3]Cy^e	1.328 ^h	1.256 ^{h,i}	–	–	–	0.072	[117]
	1.332	1.261 ⁱ	–	–	–	0.071	[120]
[4]Cy^e	1.317	1.273	1.279	1.313	–	0.039	[117]
[5]Cy^e	1.329 ^j	1.260 ^j	1.300 ^{g,j}	–	–	0.040	[120]
	1.332 ^d	1.267 ^d	1.295 ^{d,g}	–	–	–	[120]

^aSee Fig. 11 for atomic numbering scheme^bCalculated as difference in bond length between the two central-most bonds. For non-centrosymmetric structures, BLA was calculated using the average of positionally equivalent bonds^cStructure determination at 20°C^dStructure determination at –160°C^eESDs not reported in [117, 120]^fThe structure of **[5]Ph** was reported without values for bond lengths and angles, see [118]; Bond lengths and angles from Januszewski et al. unpublished^gC3–C3'^hAveraged in case of multiple determination (see [117])ⁱC2–C2'^jStructure determination at 22°C

Table 6 Selected angles ($^{\circ}$) for series of $[n]$ cumulenes^a

	C1–C2–C3	C2–C3–C4	C3–C4–C5	C4–C5–C6	Reference
[3]Ph	176.3 (2) ^b	176.3 (2) ^b	–	–	[116]
	176.1 (1) ^c	176.0 (1) ^c			[116]
[4]Ph ^d	178.5	178.9	177.9	–	[117]
[5]Ph	178.83 (15)	179.81 (19)	179.04 (17)	179.31 (16)	[118] ^e
[5]EtPh	177.96 (17)	177.9 (3) ^f	–	–	[119]
[3]Cy ^d	179.0 ^g	–	–	–	[120]
[4]Cy ^d	179.1	178.9	178.1	–	[117]
[5]Cy ^d	179.0	179.7 ^f	–	–	[120]

^aSee Fig. 11 for atomic numbering scheme

^bStructure determination at 20 $^{\circ}$ C

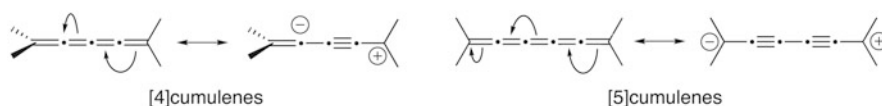
^cStructure determination at –160 $^{\circ}$ C

^dESDs not reported in [117, 120]

^eThe structure of [5]Ph was reported without values for bond lengths and angles, see [118]; Bond lengths and angles from Januszewski et al. unpublished

^fC2–C3–C3'

^gC1–C2–C2'

**Fig. 12** Canonical structures for [4]- and [5]cumulenes

4. BLA values for the longest derivatives, [5]Ph, [5]EtPh, and [5]Cy at 0.058 Å, 0.059 Å, and 0.040 Å, respectively, reflect endgroup effects, as described in point 1.

The bond angles of the $[n]$ cumulenes approach 180 $^{\circ}$ as expected for linear molecules, and deviations are negligible for all derivatives ($<2^{\circ}$), except for [3]Ph which shows angles of 176.3(2) $^{\circ}$. While only a small number of structures are available, the linearity of the $[n]$ cumulenes stands in stark contrast to that observed for polyynes (vide infra), where bending of the sp-carbon polyne chain is often observed, even in short derivatives [45, 76, 78, 85, 121].

3.4.2 Polyynes

As outlined in several of the previous sections, NMR, UV/Vis, and IR spectroscopic analyses for polyynes have become almost routine in recent years. In spite of these efforts, one particular question has remained unanswered until recently: Do extended polyynes show experimental evidence of reduced bond length alternation (BLA) as molecular length is increased? Unfortunately, like the analysis of cumulenes, X-ray crystallographic data for polyynes that could provide a definitive answer to this question are quite rare. A recent review by Szafert and Gladysz

beautifully tabulated crystallographic data for known polyynes with $n \geq 4$, and they estimated a BLA of ca. 0.07–0.08 Å for an infinite polyyne system [44, 45]. Computational chemists have also addressed the issue of BLA in polyynes [111–114], and from these theoretical studies it is clear that several factors can have a dramatic effect on results, including the choice of basis set and electron correlation [111–114, 122–125]. Nonetheless, the trend that emerges from recent investigations suggests that the BLA value for **H**[n] polyynes should converge to a value of ca. 0.13 Å at the infinite limit of carbyne [111, 112, 114]. A comparison of these predictions to experiment will be, quite clearly, complicated by “endgroup effects,” since crystallographic analysis will be limited to derivatives that are terminated with endgroups other than H. The presence of endgroups will perturb the polyyne framework, to some extent, but this is unavoidable in the absence of stable, crystalline **H**[n]. When excluding polyynes endcapped with metals, four series offer a sufficient number of crystallographic analyses for consideration of BLA trends: **tBu**[n], **TIPS**[n], **Ph**[n], and **Co**[n]. A summary of bond lengths is found in Table 7, using the bond labeling scheme shown in Fig. 13, which classifies each bond based on its position in the polyyne chain.

The analysis of BLA from these X-ray data has been conducted as reported for computed structures: BLA equals the bond length difference between the central single and triple bonds in each structure (Table 7).² The most complete set of data exists for **tBu**[n] polyynes and shows a consistent decrease in BLA values from a maximum of 0.183 Å for dimer **tBu**[2] to a minimum of 0.139 Å (averaged BLA of two crystallographically independent molecules of **tBu**[10]). A plot of BLA versus n for **tBu**[n] polyynes is shown in Fig. 14 and suggests that BLA will reach a constant value at around 0.135 Å, consistent with theoretical predictions [77].

Both **TIPS**[n] and **Ph**[n] polyynes also show a general overall reduction in both BLA values as a function of length, although **Ph**[5] and **TIPS**[8] present a rather dramatic divergence from the trend. It is not known whether these apparent deviations result from variances from the individual experimental values or from, perhaps, endgroup effects. Crystallographic data for the **Co**[n] polyynes, interestingly, show an increase in BLA, from 0.121 Å for **Co**[2] to values of 0.15 and 0.132 Å for **Co**[6] and **Co**[7], respectively. It seems plausible that this would result from electronic interactions between the Co_3 -carbonyl clusters that terminate the polyynes.

An analysis of bond angles for **tBu**[n], **TIPS**[n], **Ph**[n], and **Co**[n] series of polyynes would undoubtedly yield interesting observations, but would not provide any discernable trends beyond those elegantly presented in the review from Szafert and Gladysz [44, 45]. Thus, only several comments are provided here regarding bond angles observed for polyynes in the solid state. Of the molecules discussed in this review, **TIPS**[8] shows the most dramatic deviations from linearity (Fig. 15a). Each individual acetylene unit bears only a slight deviation from linearity, ranging

²For non-centrosymmetric structures, the BLA was calculated using the average of positionally equivalent bonds.

Table 7 Selected bond length (Å) and BLA values of *t*Bu[n], TIPS[n], Ph[n], and Co[n] polyynes.^a

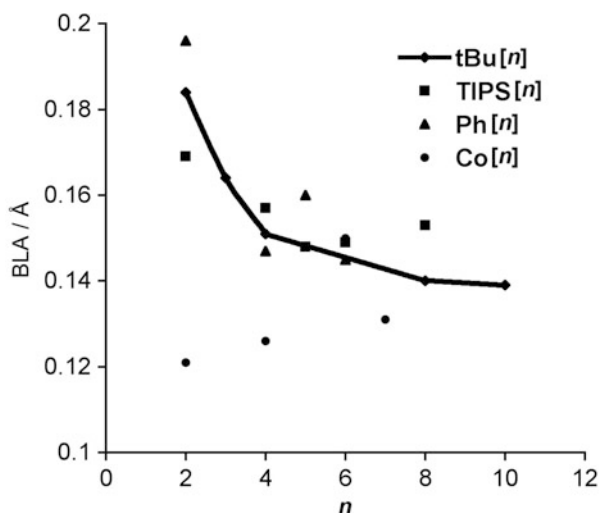
	α	β	γ	δ	ε	ζ	η	θ	ι	κ	BLA	Reference
<i>t</i> Bu[2]	1.200 (3)	1.382 (3)	–	–	–	–	–	–	–	–	0.183	[77]
1.198 (3)												
<i>t</i> Bu[3] ^b	1.201 (4)	1.368 (3)	1.204 (5)	–	–	–	–	–	–	–	0.164	
<i>t</i> Bu[4]	1.1989 (18)	1.3683 (19)	1.2095 (18)	1.3597 (19)	–	–	–	–	–	–	0.151	
1.1993 (19)	1.3679 (19)	1.2083 (19)										
<i>t</i> Bu[8]	1.201 (2)	1.367 (2)	1.210 (2)	1.352 (2)	1.218 (2)	1.349 (2)	1.213 (2)	1.353 (2)	–	–	0.140	
1.196 (2)	1.366 (2)	1.207 (2)	1.355 (2)	1.214 (2)	1.352 (2)	1.352 (2)	1.213 (2)					
<i>t</i> Bu[10] ^c	1.198 (6)	1.360 (6)	1.213 (6)	1.354 (6)	1.211 (6)	1.340 (6)	1.218 (6)	1.342 (6)	1.207 (6)	1.351 (6)	0.144	
1.194 (6)	1.354 (6)	1.206 (6)	1.356 (6)	1.204 (6)	1.352 (7)	1.208 (6)	1.340 (6)	1.340 (6)	1.208 (6)			
<i>t</i> Bu[10] ^{b,d}	1.192 (8)	1.365 (8)	1.200 (8)	1.354 (9)	1.216 (8)	1.356 (9)	1.210 (9)	1.347 (9)	1.212 (8)	1.346 (13)	0.134	
TIPS[2] ^b	1.204 (2)	1.373 (3)	–	–	–	–	–	–	–	–	0.169	[126]
TIPS[4] ^b	1.2122 (18)	1.3682 (18)	1.2061 (18)	1.363 (3)	–	–	–	–	–	–	0.157	[76]
TIPS[5] ^b	1.209 (2)	1.3673 (19)	1.208 (2)	1.357 (2)	1.209 (3)	–	–	–	–	–	0.148	
TIPS[6] ^b	1.206 (2)	1.368 (2)	1.208 (2)	1.356 (2)	1.2090 (19)	1.358 (3)	–	–	–	–	0.149	
TIPS[8]	1.199 (5)	1.367 (5)	1.195 (4)	1.373 (5)	1.199 (4)	1.354 (5)	1.197 (4)	1.356 (5)	–	–	0.153	
1.197 (4)	1.380 (5)	1.199 (4)	1.348 (5)	1.207 (4)	1.352 (5)	1.209 (5)						
Ph[2] ^b	1.197 (9)	1.393 (12)	–	–	–	–	–	–	–	–	0.196	[127]
Ph[4] ^{b,e}	1.202 (3)	1.361 (3)	1.209 (3)	1.356 (4)	–	–	–	–	–	–	0.147	[80]
Ph[5] ^b	1.192	1.369	1.206	1.368	1.208	–	–	–	–	–	0.160	[98]
Ph[6]	1.199 (3)	1.365 (3)	1.206 (3)	1.360 (3)	1.209 (3)	1.355 (3)	–	–	–	–	0.145	[79]
1.201 (3)	1.365 (3)	1.209 (3)	1.358 (3)	1.211 (3)								
Co[2] ^b	1.225 (3)	1.346 (3)	–	–	–	–	–	–	–	–	0.121	[85]
Co[4] ^b	1.226 (3)	1.345 (3)	1.221 (3)	1.347 (3)	–	–	–	–	–	–	0.126	[85]
Co[6] ^b	1.25 (3)	1.38 (2)	1.24 (3)	1.32 (3)	1.18 (3)	1.33 (4)	–	–	–	–	0.15	[87]
Co[7] ^b	1.221 (8)	1.336 (8)	1.228 (8)	1.339 (8)	1.221 (8)	1.343 (9)	1.211 (9)	–	–	–	0.132	[86]

^aSee Fig. 13 for a description of bond labeling^bCentrosymmetric structure^cTwo crystallographically independent molecules in unit cell; data for Molecule A^dTwo crystallographically independent molecules in unit cell; data for Molecule B^eAs a cocrystal with Ph₂[4]

Fig. 13 Chemical structures and bond labeling scheme of polyynes with X-ray structures described in this review



Fig. 14 Bond length alternation values for $t\text{Bu}[n]$, $\text{TIPS}[n]$, $\text{Ph}[n]$, and $\text{Co}[n]$ polyynes



from $179.3(4)$ to $173.7(4)^\circ$ with an average $\text{C}\equiv\text{C}-\text{X}$ ($\text{X}=\text{C}$ or Si) bond angle of 176.9° . Overall, however, the cumulative effect of these deviations results in a rather dramatic curvature in an unsymmetrical bow shape. The shape of $\text{TIPS}[8]$ most closely resembles that of a platinum endcapped hexayne reported by Gladysz and coworkers [128] that assumes a symmetric bow conformation in the solid state with a slightly lower average $\text{C}\equiv\text{C}-\text{X}$ angle of 174.6° .

There are two crystallographically independent molecules in the unit cell of the structure of $t\text{Bu}[10]$ and both deviate somewhat from linearity. The unsymmetrical molecule $t\text{Bu}[10]\text{A}$ adopts a sort of helical conformation with $\text{C}\equiv\text{C}-\text{C}$ bond angles that range from $174.4(6)$ to $179.3(5)^\circ$ (Fig. 15b, d). The centrosymmetric molecule $t\text{Bu}[10]\text{B}$ adopts a gentle S shape, with a slightly smaller deviation from linearity and $\text{C}\equiv\text{C}-\text{C}$ bond angles that range from $176.1(6)$ to $179.5(8)^\circ$ (Fig. 15c, e).

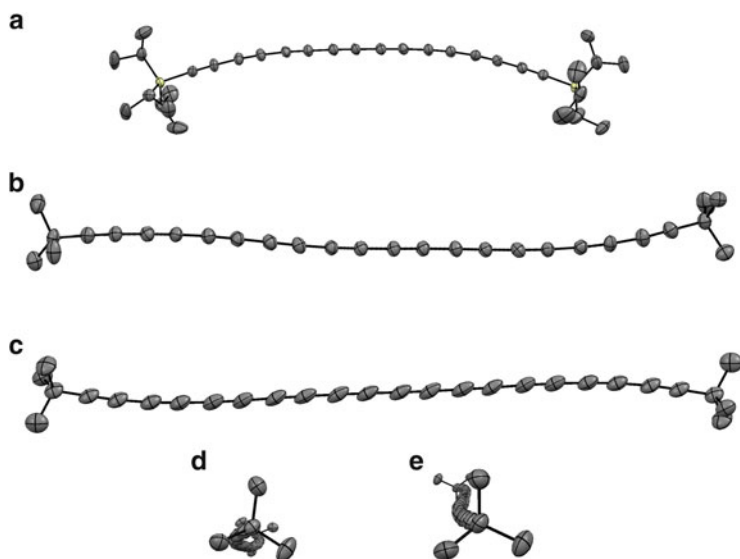


Fig. 15 Bond angles for (a) TIPS[8], (b) *t*Bu[10]A, and (c) *t*Bu[10]B; end on view of (d) *t*Bu[10]A and (e) *t*Bu[10]B

4 Conclusions

The studies outlined in this review offer a description of the current knowledge of the properties and structure of cumulene and polyynes oligomers. Furthermore, studies of polyynes provide some insight as to the possible properties of carbyne, which is currently predicted to maintain a polyynes structure with significant bond length alternation. Unlike the study of polyynes, the investigation of cumulenes remains in its infancy, with instability of the longer cumulenes thwarting most synthetic efforts to date. As a result, trends for most physical and spectroscopic characteristics of the cumulenes remain to be discovered. Undoubtedly, this synthetic challenge will be undertaken by chemists in the near future. Indeed, during the course of production for this chapter, the structural characteristics of cumulenes have been described [129].

Acknowledgments Funding from the University of Erlangen-Nuremberg and the Deutsche Forschungsgemeinschaft (DFG SFB 953, *Synthetic Carbon Allotropes*) is gratefully acknowledged.

References

1. Diederich F, Rubin Y (1992) Synthetic approaches toward molecular and polymeric carbon allotropes. *Angew Chem Int Ed* 31(9):1101–1123. doi:10.1002/anie.199211013

2. He GS, Tan L-S, Zheng Q, Prasad PN (2008) Multiphoton absorbing materials: molecular designs, characterizations, and applications. *Chem Rev* 108(4):1245–1330. doi:[10.1021/cr050054x](https://doi.org/10.1021/cr050054x)
3. Murphy AR, Frechet JMJ (2007) Organic semiconducting oligomers for use in thin film transistors. *Chem Rev* 107(4):1066–1096. doi:[10.1021/cr0501386](https://doi.org/10.1021/cr0501386)
4. Hoeben FJM, Jonkheijm P, Meijer EW, Schenning APHJ (2005) About supramolecular assemblies of π -conjugated systems. *Chem Rev* 105(4):1491–1546. doi:[10.1021/cr030070z](https://doi.org/10.1021/cr030070z)
5. Anthony JE (2006) Functionalized acenes and heteroacenes for organic electronics. *Chem Rev* 106(12):5028–5048. doi:[10.1021/cr050966z](https://doi.org/10.1021/cr050966z)
6. Diederich F, Stang PJ, Tykwinski RR (eds) (2005) Acetylene chemistry: chemistry, biology, and material science. Wiley-VCH, Weinheim
7. Haley MM, Tykwinski RR (eds) (2006) Carbon-rich compounds: molecules to materials. Wiley-VCH, Weinheim
8. Hoheisel TN, Schrettl S, Szilluweit R, Frauenrath H (2010) Nanostructured carbonaceous materials from molecular precursors. *Angew Chem Int Ed* 49(37):6496–6515. doi:[10.1002/anie.200907180](https://doi.org/10.1002/anie.200907180)
9. Falcao EHL, Wudl F (2007) Carbon allotropes: beyond graphite and diamond. *J Chem Technol Biotechnol* 82(6):524–531. doi:[10.1002/jctb.1693](https://doi.org/10.1002/jctb.1693)
10. Kelly B (1981) Physics of graphite. Applied Science Publishers, London
11. Kirk R, Othmer D, Grayson M, Eckroth D (eds) (1978) Kirk-Othmer encyclopedia of chemical technology, vol 4. Wiley, New York
12. Chalifoux WA, Tykwinski RR (2006) Polyynes synthesis using carbene/carbenoid rearrangements. *Chem Rec* 6(4):169–182. doi:[10.1002/tcr.20081](https://doi.org/10.1002/tcr.20081)
13. Tobe Y, Wakabayashi T (2005) Carbon-rich compounds: acetylene-based carbon allotropes. In: Diederich F, Stang PJ, Tykwinski RR (eds) Acetylene chemistry: chemistry, biology, and material science. Wiley-VCH, Weinheim. doi:[10.1002/3527605487.ch9](https://doi.org/10.1002/3527605487.ch9)
14. Chalifoux WA, Tykwinski RR (2009) Synthesis of extended polyynes: toward carbyne. *CR Chim* 12(3–4):341–358. doi:[10.1016/j.crci.2008.10.004](https://doi.org/10.1016/j.crci.2008.10.004)
15. Haley MM (2010) Carbon allotropes on the road to carbyne. *Nature Chem* 2(11):912–913. doi:[10.1038/nchem.884](https://doi.org/10.1038/nchem.884)
16. Cataldo F (1997) A study on the structure and electrical properties of the fourth carbon allotrope: carbyne. *Polym Int* 44(2):191–200. doi:[10.1002/\(sici\)1097-0126\(199710\)44:2<191::aid-pi842>3.0.co;2-y](https://doi.org/10.1002/(sici)1097-0126(199710)44:2<191::aid-pi842>3.0.co;2-y)
17. Cataldo F (ed) (2006) Polyynes: synthesis, properties, and applications. Taylor and Francis, Boca Raton
18. Kudryavtsev YP, Evsyukov SE, Gusevca M, Babaev C, Khvistov C (1997). In: Thrower PA (ed) Chemistry and physics of carbon, vol 25. Marcel Dekker, New York, pp 1–99
19. Smith PPK, Buseck PR (1982) Carbyne forms of carbon: do they exist? *Science* (Washington) 216(4549):984–986. doi:[10.1126/science.216.4549.984](https://doi.org/10.1126/science.216.4549.984)
20. Bunz UHF (1996) Organometallic “carbon chains”: they just keep getting longer! *Angew Chem Int Ed* 35(9):969–971. doi:[10.1002/anie.199609691](https://doi.org/10.1002/anie.199609691)
21. Kudryavtsev YP, Heimann RB, Evsyukov SE (1996) Carbynes: advances in the field of linear carbon chain compounds. *J Mater Sci* 31(21):5557–5571. doi:[10.1007/BF01160799](https://doi.org/10.1007/BF01160799)
22. Kuhn R, Wallenfels K (1938) Über Kumulene I. Synthese von Tetraphenyl-hexapentaen und Di-biphenyl-hexapentaen. *Chem Ber* 71(4):783–790. doi:[10.1002/cber.19380710416](https://doi.org/10.1002/cber.19380710416)
23. Kuhn R, Wallenfels K (1938) Über Kumulene II. Eine wesentliche Verbesserung des Darstellungs-Verfahrens. *Chem Ber* 71(7):1510–1512. doi:[10.1002/cber.19380710725](https://doi.org/10.1002/cber.19380710725)
24. Kuhn R, Platzer G (1940) Über Kumulene III. *Chem Ber* 73(12):1410–1417
25. Kuhn R, Zahn H (1951) Über Kumulene IV. Oktaheptaene. *Chem Ber* 84(5–6):566–570. doi:[10.1002/cber.19510840526](https://doi.org/10.1002/cber.19510840526)
26. Kuhn R, Krauch H (1955) Über Kumulene VIII. Reduktion von Acetylen-, Diacetylen- und Triacetylen-glykolen mit Zinn-(II)-chlorid; Kumulene mit nur zwei aromatischen Substituenten. *Chem Ber* 88(3):309–315. doi:[10.1002/cber.19550880302](https://doi.org/10.1002/cber.19550880302)
27. Kuhn R, Blum D (1959) Über Kumulene X. *cis-trans*-Isomerie bei Dinitro-tetraphenyl-kumulenen. *Chem Ber* 92(7):1483–1500. doi:[10.1002/cber.19590920702](https://doi.org/10.1002/cber.19590920702)

28. Bohlmann F, Kieslich K (1955) Konstitution und Lichtabsorption, VII. Mitteil.: Über den Einfluß der Phenylchromophore auf die Lichtabsorption der Kumulene. *Chem Ber* 88(8):1211–1218. doi:[10.1002/cber.19550880811](https://doi.org/10.1002/cber.19550880811)
29. Bohlmann F, Kieslich K (1954) Polyacetylene, VI. Mitteil.: Umwandlung von Polyinen in Kumulene. *Chem Ber* 87(9):1363–1372. doi:[10.1002/cber.19540870926](https://doi.org/10.1002/cber.19540870926)
30. Bohlmann F, Kieslich K (1957) Untersuchungen in der Kumulen-Reihe. *Abh braunschweig wiss Ges* 9:147–166
31. Bohlmann F (1953) Die Polyine. *Angew Chem* 65(15):385–389. doi:[10.1002/ange.19530651502](https://doi.org/10.1002/ange.19530651502)
32. Jones ERH (1960) Pedler lecture. Polyacetylenes. *Proc Chem Soc* 6:199–210
33. Jones ERH, Whiting MC, Armitage JB, Cook CL, Entwistle N (1951) Synthesis of polyacetylenic compounds. *Nature (London)* 168(4282):900–903. doi:[10.1038/168900a0](https://doi.org/10.1038/168900a0)
34. Cook CL, Jones ERH, Whiting MC (1952) Researches on acetylenic compounds. Part XXXIX. General routes to aliphatic polyacetylenic hydrocarbons and glycols. *J Chem Soc* 2883–2891. doi:[10.1039/JR9520002883](https://doi.org/10.1039/JR9520002883)
35. Bohlmann F (1951) Konstitution und Lichtabsorption, III. Mitteil.: Polyacetylenverbindungen. *Chem Ber* 84(9):785–794. doi:[10.1002/cber.19510840902](https://doi.org/10.1002/cber.19510840902)
36. Hunsmann W (1950) Nachweis und Synthese des Triacetylen. *Chem Ber* 83(3):213–217. doi:[10.1002/cber.19500830302](https://doi.org/10.1002/cber.19500830302)
37. Schlubach HH, Franzen V (1951) Über Polyacetylene III: Über das Diphenyl-pentaacetylen und das Monophenyl-diacetylen. *Justus Liebigs Ann Chem* 573(1):105–109. doi:[10.1002/jlac.19515730111](https://doi.org/10.1002/jlac.19515730111)
38. Schlubach HH, Wolf V (1950) Über Polyacetylene. *Justus Liebigs Ann Chem* 568(2):141–159. doi:[10.1002/jlac.19505680206](https://doi.org/10.1002/jlac.19505680206)
39. Nakagawa M, Akiyama S, Nakasuji K, Nishimoto K (1971) Novel linear relation in the electronic spectra of α , ω -diarylpolyyenes. *Tetrahedron* 27(22):5401–5418. doi:[10.1016/S0040-4020\(01\)91706-5](https://doi.org/10.1016/S0040-4020(01)91706-5)
40. Viehe HG (ed) (1969) *Chemistry of acetylenes*. Marcel Dekker, New York
41. Johnson TR, Walton DRM (1972) Silylation as a protective method in acetylene chemistry. *Tetrahedron* 28(20):5221–5236. doi:[10.1016/S0040-4020\(01\)88941-9](https://doi.org/10.1016/S0040-4020(01)88941-9)
42. Eastmond R, Johnson TR, Walton DRM (1973) Base-catalyzed cleavage of silyl-substituted polyyenes. Attenuation of hydrocarbon acidity and transmission of substituent electrical effects in long-chain conjugated polyacetylenes. *J Organomet Chem* 50(1):87–92. doi:[10.1016/S0022-328X\(00\)95093-9](https://doi.org/10.1016/S0022-328X(00)95093-9)
43. Eastmond R, Johnson TR, Walton DRM (1972) Silylation as a protective method for terminal alkynes. *Tetrahedron* 28(17):4601–4616. doi:[10.1016/0040-4020\(72\)80041-3](https://doi.org/10.1016/0040-4020(72)80041-3)
44. Szafert S, Gladysz JA (2003) Carbon in one dimension: structural analysis of the higher conjugated polyyenes. *Chem Rev* 103(11):4175–4205. doi:[10.1021/cr030041o](https://doi.org/10.1021/cr030041o)
45. Szafert S, Gladysz JA (2006) Update I of: carbon in one dimension: structural analysis of the higher conjugated polyyenes. *Chem Rev* 106(11):PR1–PR33. doi:[10.1021/cr068016g](https://doi.org/10.1021/cr068016g)
46. Zheng Q, Bohling JC, Peters TB, Frisch AC, Hampel F, Gladysz JA (2006) A synthetic breakthrough into an unanticipated stability regime: a series of isolable complexes in which C₆, C₈, C₁₀, C₁₂, C₁₆, C₂₀, C₂₄, and C₂₈ polyyne-diyl chains span two platinum atoms. *Chem Eur J* 12(25):6486–6505. doi:[10.1002/chem.200600615](https://doi.org/10.1002/chem.200600615)
47. Long NJ, Williams CK (2003) Metal alkynyl σ complexes: synthesis and materials. *Angew Chem Int Ed* 42(23):2586–2617. doi:[10.1002/anie.200200537](https://doi.org/10.1002/anie.200200537)
48. Stahl J, Mohr W, de Quadras L, Peters TB, Bohling JC, Martin-Alvarez JM, Owen GR, Hampel F, Gladysz JA (2007) sp Carbon chains surrounded by sp³ carbon double helices: coordination-driven self-assembly of wirelike Pt(C \equiv C)_nPt moieties that are spanned by two P(CH₂)_mP linkages. *J Am Chem Soc* 129(26):8282–8295. doi:[10.1021/ja0716103](https://doi.org/10.1021/ja0716103)
49. de Quadras L, Bauer EB, Mohr W, Bohling JC, Peters TB, Martin-Alvarez JM, Hampel F, Gladysz JA (2007) sp Carbon chains surrounded by sp³ carbon double helices: directed syntheses of wirelike Pt(C \equiv C)_nPt moieties that are spanned by two P(CH₂)_mP linkages via alkene metathesis. *J Am Chem Soc* 129(26):8296–8309. doi:[10.1021/ja071612n](https://doi.org/10.1021/ja071612n)

50. Suzuki N, Hashizume D, Yoshida H, Tezuka M, Ida K, Nagashima S, Chihara T (2009) Reversible haptotropic shift in zirconocene-hexapentaene complexes. *J Am Chem Soc* 131(6):2050–2051. doi:[10.1021/ja8077472](https://doi.org/10.1021/ja8077472)
51. King RB, Harmon CA (1975) Organometallic chemistry of transition metals XXX. Reactions of tetraalkylhexapentaenes with iron carbonyls. *J Organomet Chem* 88(1):93–100. doi:[10.1016/S0022-328X\(00\)89333-X](https://doi.org/10.1016/S0022-328X(00)89333-X)
52. Bildstein B (2000) Cationic and neutral cumulene sp-carbon chains with ferrocenyl termini. *Coord Chem Rev* 206–207:369–394. doi:[10.1016/S0010-8545\(00\)00248-4](https://doi.org/10.1016/S0010-8545(00)00248-4)
53. Skibar W, Kopacka H, Wurst K, Salzmann C, Ongania KH, de Biani FF, Zanella P, Bildstein B (2004) α , ω -Diferrocenyl cumulene molecular wires. Synthesis, spectroscopy, structure, and electrochemistry. *Organometallics* 23(5):1024–1041. doi:[10.1021/om0342331](https://doi.org/10.1021/om0342331)
54. Bildstein B, Skibar W, Schweiger M, Kopacka H, Wurst K (2001) In situ synthesis of the first C₇ cumulene (Fc)₂C=C=C=C=C=C=C(Fc)₂ via deprotonation of its conjugate acid [(Fc)₂C₇H(Fc)₂]⁺BF₄⁻ (Fc = ferrocenyl). *J Organomet Chem* 622(1–2):135–142. doi:[10.1016/S0022-328X\(00\)00882-2](https://doi.org/10.1016/S0022-328X(00)00882-2)
55. Nakamura A (1965) The interaction of cumulene systems with organometallic π -complexes. III. Iron carbonyl complexes of hexapentaene and of tetra- and dimethylbutatriene. *Bull Chem Soc Jpn* 38(11):1868–1873. doi:[10.1246/bcsj.38.1868](https://doi.org/10.1246/bcsj.38.1868)
56. Werner H, Wiedemann R, Mahr N, Steinert P, Wolf J (1996) Coordination and coupling of OH-functionalized C₂ units at a single metal center: the synthesis of alkynyl(vinylidene), alkynyl(enyne), bis(alkynyl)hydrido, enynyl, and hexapentaene rhodium complexes from propargylic alcohols as precursors. *Chem Eur J* 2(5):561–569. doi:[10.1002/chem.19960020516](https://doi.org/10.1002/chem.19960020516)
57. Song LS, Arif AM, Stang PJ (1990) Cumulenes as ligands. IV. Rhodium and platinum complexes of tetraphenylhexapentaene. X-ray crystal structure of bis(triphenylphosphine) chloro(tetraphenylhexapentaene)rhodium. *J Organomet Chem* 395(2):219–226. doi:[10.1016/0022-328X\(90\)85279-8](https://doi.org/10.1016/0022-328X(90)85279-8)
58. Fischer H (1964) Cumulenes. In: Patai S (ed) *The chemistry of alkenes*. Wiley, New York, pp 1025–1159
59. Ogasawara M (2008) Cumulenes and allenes. In: Krause N (ed) *Science of synthesis*, vol 44. Georg Thieme Verlag, Stuttgart, pp 9–70
60. Ried W, Schlegelmilch W, Piesch S (1963) Äthinierungsreaktionen, XX. Über Alkindiole und Kumulene. *Chem Ber* 96(5):1221–1228. doi:[10.1002/cber.19630960508](https://doi.org/10.1002/cber.19630960508)
61. Dupont G (1913) Recherches sur les γ -glycols acétyléniques et sur les cétohydrofuranes qui en dérivent. *Ann Chim Phys* 8:485–587
62. Bergmann E, Hoffmann H, Winter D (1933) Beobachtungen auf dem Gebiet des Fluorens. *Chem Ber* 66(1):46–54. doi:[10.1002/cber.19330660110](https://doi.org/10.1002/cber.19330660110)
63. Salkind J, Kruglow A (1928) Einwirkung von Jodwasserstoff auf Tetraphenyl-butindiol. *Chem Ber* 61(10):2306–2312. doi:[10.1002/cber.19280611014](https://doi.org/10.1002/cber.19280611014)
64. Fischer H, Hell WD (1967) UV-Absorption von α , α , ω -Tetraphenylkumulenen mit coplanaren Phenylringen. *Angew Chem* 79(21):931–932. doi:[10.1002/ange.19670792104](https://doi.org/10.1002/ange.19670792104)
65. Siemsen P, Livingston RC, Diederich F (2000) Acetylenic coupling: a powerful tool in molecular construction. *Angew Chem Int Ed* 39(15):2632–2657. doi:[10.1002/1521-3773\(20000804\)39:15<2632::AID-ANIE2632>3.0.CO;2-F](https://doi.org/10.1002/1521-3773(20000804)39:15<2632::AID-ANIE2632>3.0.CO;2-F)
66. Bohlmann F (1953) Polyacetylene, IV. Mitteil.: Darstellung Von Di-*tert.*-butylpolyacetylenen. *Chem Ber* 86(5):657–667. doi:[10.1002/cber.19530860519](https://doi.org/10.1002/cber.19530860519)
67. Jones ERH, Lee HH, Whiting MC (1960) Researches on acetylenic compounds. Part LXIV. The preparation of conjugated octa- and deca-acetylenic compounds. *J Chem Soc* 3483–3489. doi:[10.1039/JR9600003483](https://doi.org/10.1039/JR9600003483)
68. Gibtner T, Hampel F, Gisselbrecht JP, Hirsch A (2002) End-cap stabilized oligoynes: model compounds for the linear sp carbon allotrope carbyne. *Chem Eur J* 8(2):408–432. doi:[10.1002/1521-3765\(20020118\)8:2<408::AID-CHEM408>3.0.CO;2-L](https://doi.org/10.1002/1521-3765(20020118)8:2<408::AID-CHEM408>3.0.CO;2-L)
69. Klinger C, Vostrowsky O, Hirsch A (2006) Synthesis of alkylene-bridged diphenyl-oligoynes. *Eur J Org Chem* 6:1508–1524. doi:[10.1002/ejoc.200500851](https://doi.org/10.1002/ejoc.200500851)
70. Krättschmer W, Lamb LD, Fostiropoulos K, Huffman DR (1990) Solid C₆₀: a new form of carbon. *Nature (London)* 347(6291):354–358. doi:[10.1038/347354a0](https://doi.org/10.1038/347354a0)

71. Grösser T, Hirsch A (1993) Dicyanopolyynes: formation of new rod-shaped molecules in a carbon plasma. *Angew Chem Int Ed Engl* 32(9):1340–1342. doi:[10.1002/anie.199313401](https://doi.org/10.1002/anie.199313401)
72. Schermann G, Grösser T, Hampel F, Hirsch A (1997) Dicyanopolyynes: a homologous series of end-capped linear sp carbon. *Chem Eur J* 3(7):1105–1112. doi:[10.1002/chem.19970030718](https://doi.org/10.1002/chem.19970030718)
73. Fritsch P (1894) Ueber die Darstellung von Diphenylacetaldehyd und eine neue Synthese von Tolanderivaten. *Justus Liebigs Ann Chem* 279(3):319–323. doi:[10.1002/jlac.18942790310](https://doi.org/10.1002/jlac.18942790310)
74. Buttenberg WP (1894) Kondensation des Dichloracetals mit Phenol und Toluol. *Justus Liebigs Ann Chem* 279(3):324–337. doi:[10.1002/jlac.18942790311](https://doi.org/10.1002/jlac.18942790311)
75. Wiechell H (1894) Kondensation des Dichloracetals mit Anisol und Phenetol. *Justus Liebigs Ann Chem* 279(3):337–344. doi:[10.1002/jlac.18942790312](https://doi.org/10.1002/jlac.18942790312)
76. Eisler S, Slepov AD, Elliott E, Luu T, McDonald R, Hegmann FA, Tykwinski RR (2005) Polyynes as a model for carbyne: synthesis, physical properties, and nonlinear optical response. *J Am Chem Soc* 127(8):2666–2676. doi:[10.1021/ja0445261](https://doi.org/10.1021/ja0445261)
77. Chalifoux WA, McDonald R, Ferguson MJ, Tykwinski RR (2009) *tert*-Butyl-end-capped polyynes: crystallographic evidence of reduced bond-length alternation. *Angew Chem Int Ed* 48(42):7915–7919. doi:[10.1002/anie.200902760](https://doi.org/10.1002/anie.200902760)
78. Lucotti A, Tommasini M, Fazzi D, Del Zoppo M, Chalifoux WA, Ferguson MJ, Zerbi G, Tykwinski RR (2009) Evidence for solution-state nonlinearity of sp-carbon chains based on IR and Raman spectroscopy: violation of mutual exclusion. *J Am Chem Soc* 131(12):4239–4244. doi:[10.1021/ja078198b](https://doi.org/10.1021/ja078198b)
79. Luu T, Elliott E, Slepov AD, Eisler S, McDonald R, Hegmann FA, Tykwinski RR (2005) Synthesis, structure, and nonlinear optical properties of diarylpolyynes. *Org Lett* 7(1):51–54. doi:[10.1021/ol047931q](https://doi.org/10.1021/ol047931q)
80. Kendall J, McDonald R, Ferguson MJ, Tykwinski RR (2008) Synthesis and solid-state structure of perfluorophenyl end-capped polyynes. *Org Lett* 10(11):2163–2166
81. Tykwinski RR, Kendall J, McDonald R (2009) Pentafluorophenyl end-capped polyynes as supramolecular building blocks. *Synlett* 13:2068–2075. doi:[10.1055/s-0029-1217706](https://doi.org/10.1055/s-0029-1217706)
82. Eisler S, Tykwinski RR (2000) Migrating alkynes in vinylidene carbenoids: an unprecedented route to polyynes. *J Am Chem Soc* 122(43):10736–10737. doi:[10.1021/ja005557t](https://doi.org/10.1021/ja005557t)
83. Jahnke E, Tykwinski RR (2010) The Fritsch-Buttenberg-Wiechell rearrangement: modern applications for an old reaction. *Chem Commun* 46(19):3235–3249. doi:[10.1039/c003170d](https://doi.org/10.1039/c003170d)
84. Eisler S, Tykwinski RR (2005) Polyynes via alkylidene carbenes and carbenoids. In: Diederich F, Stang PJ, Tykwinski RR (eds) *Acetylene chemistry*. Wiley-VCH Weinheim, pp 259–302. doi:[10.1002/3527605487.ch7](https://doi.org/10.1002/3527605487.ch7)
85. Bruce MI, Smith ME, Zaitseva NN, Skelton BW, White AH (2003) A new approach to the synthesis of carbon chains capped by metal clusters. *J Organomet Chem* 670(1–2):170–177. doi:[10.1016/s0022-328x\(02\)02186-1](https://doi.org/10.1016/s0022-328x(02)02186-1)
86. Antonova AB, Bruce MI, Ellis BG, Gaudio M, Humphrey PA, Jevric M, Melino G, Nicholson BK, Perkins GJ, Skelton BW, Stapleton B, White AH, Zaitseva NN (2004) A novel methodology for the synthesis of complexes containing long carbon chains linking metal centres: molecular structures of $\{\text{Ru}(\text{dppe})\text{Cp}^*\}_2(\mu\text{-C}_{14})$ and $\{\text{Co}_3(\mu\text{-dppm})(\text{CO})_7\}_2(\mu_3\text{-C}_{16})$. *Chem Commun* 8:960–961. doi:[10.1039/b315854n](https://doi.org/10.1039/b315854n)
87. Bruce MI, Zaitseva NN, Nicholson BK, Skelton BW, White AH (2008) Syntheses and molecular structures of some compounds containing many-atom chains end-capped by tricobalt carbonyl clusters. *J Organomet Chem* 693(17):2887–2897. doi:[10.1016/j.jorganchem.2008.06.007](https://doi.org/10.1016/j.jorganchem.2008.06.007); erratum (2009) *J Organomet Chem* 694(3):478. doi:[10.1016/j.jorganchem.2008.11.007](https://doi.org/10.1016/j.jorganchem.2008.11.007)
88. Bruce MI, Nicholson BK, Zaitseva NN (2009) Two complexes containing 19-atom chains linking metal centres. *CR Chim* 12(12):1280–1286. doi:[10.1016/j.crci.2009.06.002](https://doi.org/10.1016/j.crci.2009.06.002)
89. Chalifoux WA, Tykwinski RR (2010) Synthesis of polyynes to model the sp-carbon allotrope carbyne. *Nature Chem* 2(11):967–971. doi:[10.1038/nchem.828](https://doi.org/10.1038/nchem.828)
90. Müllen K, Wegner G (eds) (1998) *Electronic materials – the oligomer approach*. Wiley-VCH, Weinheim

91. Martin RE, Diederich F (1999) Linear monodisperse π -conjugated oligomers: model compounds for polymers and more. *Angew Chem Int Ed* 38(10):1350–1377. doi:[10.1002/\(SICI\)1521-3773\(19990517\)38:10<1350::AID-ANIE1350>3.0.CO;2-6](https://doi.org/10.1002/(SICI)1521-3773(19990517)38:10<1350::AID-ANIE1350>3.0.CO;2-6)
92. Kuhn R, Fischer H (1959) Über Kumulene. XI. Bis-butatriene und unsymmetrische Butatriene. *Chem Ber* 92(8):1849–1857. doi:[10.1002/cber.19590920817](https://doi.org/10.1002/cber.19590920817)
93. Otting W (1954) Über Kumulene VII: Die Ultrarotspektren einiger Kumulene und Acetylenlykole. *Chem Ber* 87(4):611–624. doi:[10.1002/cber.19540870427](https://doi.org/10.1002/cber.19540870427)
94. Innocenti F, Milani A, Castiglioni C (2010) Can Raman spectroscopy detect cumulen structures of linear carbon chains? *J Raman Spectrosc* 41(2):226–236. doi:[10.1002/jrs.2413](https://doi.org/10.1002/jrs.2413)
95. Kuwatani Y, Yamamoto G, Oda M, Iyoda M (2005) Nickel-catalyzed dimerization of [5] cumulenes (hexapentaenes). *Bull Chem Soc Jpn* 78(12):2188–2208. doi:[10.1246/bcsj.78.2188](https://doi.org/10.1246/bcsj.78.2188)
96. House HO, Umen MJ (1973) The chemistry of carbanions. XXV. The reaction of various organocopper reagents with α , β -unsaturated carbonyl compounds. *J Org Chem* 38(22):3893–3901. doi:[10.1021/jo00962a016](https://doi.org/10.1021/jo00962a016)
97. Armitage JB, Entwistle N, Jones ERH, Whiting MC (1954) Researches on acetylenic compounds. Part XXI. The synthesis of diphenylpolyacetylenes. *J Chem Soc* 147–154. doi:[10.1039/JR9540000147](https://doi.org/10.1039/JR9540000147)
98. Rubin Y, Lin SS, Knobler CB, Anthony J, Boldi AM, Diederich F (1991) Solution-spray flash vacuum pyrolysis: a new method for synthesis of linear polyynes with odd numbers of CC bonds from substituted 3,4-dialkynyl-3-cyclobutene-1,2-diones. *J Am Chem Soc* 113(18):6943–6949. doi:[10.1021/ja00018a035](https://doi.org/10.1021/ja00018a035)
99. Jones AV (1952) Infra-Red and Raman spectra of diacetylene. *P Roy Soc Lond A Mat* 211 (1105):285–295. doi:[10.1098/rspa.1952.0040](https://doi.org/10.1098/rspa.1952.0040)
100. Kloster-Jensen E (1972) Preparation of pure triacetylene, tetraacetylene, and pentaacetylene and investigation of their electronic spectra. *Angew Chem Int Ed* 11(5):438–439. doi:[10.1002/anie.197204381](https://doi.org/10.1002/anie.197204381)
101. Shindo F, Benilan Y, Chaquin P, Guillemin JC, Jolly A, Raulin F (2001) IR spectrum of C_8H_2 : integrated band intensities and some observational implications. *J Mol Spectrosc* 210(2):191–195. doi:[10.1006/jmsp.2001.8459](https://doi.org/10.1006/jmsp.2001.8459)
102. Wakabayashi T, Tabata H, Doi T, Nagayama H, Okuda K, Umeda R, Hisaki I, Sonoda M, Tobo Y, Minematsu T, Hashimoto K, Hayashi S (2007) Resonance Raman spectra of polyyne molecules $C_{10}H_2$ and $C_{12}H_2$ in solution. *Chem Phys Lett* 433(4–6):296–300. doi:[10.1016/j.cplett.2006.11.077](https://doi.org/10.1016/j.cplett.2006.11.077)
103. Brand K, Busse-Sundermann A (1950) Tetra- [2,4-xylyl]-butatrien und 1.1.4.4-Tetra-[2,4-xylyl]-butin-(2); XVI. Mitteil. über Reduktion organischer Halogenverbindungen und Verbindungen der Tetraarylbutanreihe. *Chem Ber* 83(1):119–128. doi:[10.1002/cber.19500830122](https://doi.org/10.1002/cber.19500830122)
104. Jousset B, Blanchard P, Frere P, Roncali J (2000) Enhancement of the π -electron delocalization and fluorescence efficiency of 1,6-diphenyl-1,3,5-hexatriene by covalent rigidification. *Tetrahedron Lett* 41(26):5057–5061. doi:[10.1016/S0040-4039\(00\)00792-9](https://doi.org/10.1016/S0040-4039(00)00792-9)
105. Tykwinski RR, Chalifoux W, Eisler S, Lucotti A, Tommasini M, Fazzi D, Del Zoppo M, Zerbi G (2010) Toward carbyne: synthesis and stability of really long polyynes. *Pure Appl Chem* 82(4):891–904. doi:[10.1351/pac-con-09-09-04](https://doi.org/10.1351/pac-con-09-09-04)
106. Waugh F, Walton DRM (1972) Silylation as a protective method for terminal alkynes in organometallic synthesis. Preparation of 1,4-diethynyltetrafluorobenzene and (pentafluorophenyl)acetylene. *J Organomet Chem* 39(2):275–278. doi:[10.1016/S0022-328X\(00\)80451-9](https://doi.org/10.1016/S0022-328X(00)80451-9)
107. Meier H, Stalmach U, Kolshorn H (1997) Effective conjugation length and UV/Vis spectra of oligomers. *Acta Polymer* 48(9):379–384. doi:[10.1002/actp.1997.010480905](https://doi.org/10.1002/actp.1997.010480905)
108. Hoffmann R (1987) How chemistry and physics meet in the solid state. *Angew Chem Int Ed Engl* 26(9):846–878. doi:[10.1002/anie.198708461](https://doi.org/10.1002/anie.198708461)
109. Kertesz M, Choi CH, Yang S (2005) Conjugated polymers and aromaticity. *Chem Rev* 105(10):3448–3481. doi:[10.1021/cr990357p](https://doi.org/10.1021/cr990357p)
110. Milani A, Tommasini M, Zerbi G (2009) Connection among Raman wavenumbers, bond length alternation and energy gap in polyynes. *J Raman Spectrosc* 40(12):1931–1934. doi:[10.1002/jrs.2342](https://doi.org/10.1002/jrs.2342)

111. Zeinalipour-Yazdi CD, Pullman DP (2008) Quantitative structure–property relationships for longitudinal, transverse, and molecular static polarizabilities in polyynes. *J Phys Chem B* 112(25):7377–7386. doi:[10.1021/jp800302s](https://doi.org/10.1021/jp800302s)
112. Yang S, Kertesz M (2006) Bond length alternation and energy band gap of polyynes. *J Phys Chem A* 110(31):9771–9774. doi:[10.1021/jp062701+](https://doi.org/10.1021/jp062701+)
113. Yang S, Kertesz M, Zolyomi V, Kürti J (2007) Application of a novel linear/exponential hybrid force field scaling scheme to the longitudinal Raman active mode of polyynes. *J Phys Chem A* 111(12):2434–2441. doi:[10.1021/jp067866x](https://doi.org/10.1021/jp067866x)
114. Peach MJG, Tellgren EI, Salek P, Helgaker T, Tozer DJ (2007) Structural and electronic properties of polyacetylene and polyynes from hybrid and coulomb-attenuated density functionals. *J Phys Chem A* 111(46):11930–11935. doi:[10.1021/jp0754839](https://doi.org/10.1021/jp0754839)
115. Based on a search of the CCDC, 18 September 2012 (CSD version 5.33, November 11)
116. Berkovitch-Yellin Z, Leiserowitz L (1977) Electron density distribution in cumulenes: an X-ray study of tetraphenylbutatriene at 20°C and –160°C. *Acta Crystallogr Sect B* 33(12):3657–3669. doi:[10.1107/S0567740877011819](https://doi.org/10.1107/S0567740877011819)
117. Irgartinger H, Götzmann W (1986) Structure determinations of pentatetraenes—comparison of the structures of cumulenes. *Angew Chem Int Ed Engl* 25(4):340–342. doi:[10.1002/anie.198603401](https://doi.org/10.1002/anie.198603401)
118. Woolfson MM (1953) The structure of 1:1:6:6 tetraphenylhexapentaene. *Acta Cryst* 6(11–12):838–841. doi:[10.1107/S0365110X53002465](https://doi.org/10.1107/S0365110X53002465)
119. Suzuki N, Hashizume D, Chihara T (2007) 1,1,6,6-Tetrakis(4-ethylphenyl)-1,2,3,4,5-hexapentaene. *Acta Crystallogr Sect E* 63(8):o3436. doi:[10.1107/s1600536807032576](https://doi.org/10.1107/s1600536807032576)
120. Irgartinger H, Jager HU (1976) Structure and density distribution of bonding electrons of cumulenes. *Angew Chem Int Ed Engl* 15(9):562–563. doi:[10.1002/anie.197605621](https://doi.org/10.1002/anie.197605621)
121. Qi H, Gupta A, Noll BC, Snider GL, Lu Y, Lent C, Fehlner TP (2005) Dependence of field switched ordered arrays of dinuclear mixed-valence complexes on the distance between the redox centers and the size of the counterions. *J Am Chem Soc* 127(43):15218–15227. doi:[10.1021/ja054508j](https://doi.org/10.1021/ja054508j)
122. Zhang C, Cao Z, Wu H, Zhang Q (2004) Linear and nonlinear feature of electronic excitation energy in carbon chains $HC_{2n+1}H$ and $HC_{2n}H$. *Int J Quant Chem* 98(3):299–308. doi:[10.1002/qua.20023](https://doi.org/10.1002/qua.20023)
123. Weimer M, Hieringer W, Della Sala F, Görling A (2005) Electronic and optical properties of functionalized carbon chains with the localized Hartree–Fock and conventional Kohn–Sham methods. *Chem Phys* 309(1):77–87. doi:[10.1016/j.chemphys.2004.05.026](https://doi.org/10.1016/j.chemphys.2004.05.026)
124. Scemama A, Chaquin P, Gazeau MC, Benilan Y (2002) Theoretical study of the structure and properties of polyynes and monocyno- and dicyanopolyynes: predictions for long chain compounds. *J Phys Chem A* 106(15):3828–3837. doi:[10.1021/jp013043q](https://doi.org/10.1021/jp013043q)
125. Horny L, Petraco NDK, Pak C, Schaefer HF (2002) What is the nature of polyacetylene neutral and anionic chains $HC_{2n}H$ and $HC_{2n}H^-$ ($n = 6–12$) that have recently been observed? *J Am Chem Soc* 124(20):5861–5864. doi:[10.1021/ja012014q](https://doi.org/10.1021/ja012014q)
126. Constable EC, Gusmeroli D, Housecroft CE, Neuburger M, Schaffner S (2006) 1,4-Bis(triisopropylsilyl)buta-1,3-diyne and 1,4-bis(biphenyl-4-yl)buta-1,3-diyne. *Acta Crystallogr Sect C* 62:o505–o509. doi:[10.1107/S0108270106025157](https://doi.org/10.1107/S0108270106025157)
127. Surette JKD, Macdonald MA, Zaworotko MJ, Singer RD (1994) X-ray crystal structure of 1,4-diphenylbutadiyne. *J Chem Cryst* 24(10):715–717. doi:[10.1007/BF01668237](https://doi.org/10.1007/BF01668237)
128. Mohr W, Stahl J, Hampel F, Gladysz JA (2003) Synthesis, structure, and reactivity of sp carbon chains with bis(phosphine) pentafluorophenylplatinum endgroups: butadiynediyl (C_4) through hexadecaoctaynediyl (C_{16}) bridges, and beyond. *Chem Eur J* 9(14):3324–3340. doi:[10.1002/chem.200204741](https://doi.org/10.1002/chem.200204741)
129. Januszewski JA, Wendinger D, Methfessel CD, Hampel F, Tykwinski RR (2013) Synthesis and structure of tetraarylcumulenes: characterization of bond-length alternation versus molecule length. *Angew Chem Int Ed* 52(6):1817–1821. doi:[10.1002/anie.201208058](https://doi.org/10.1002/anie.201208058)

Index

A

Acetylcarnitine, 6
Adamantanol, 197
Aerosol-OT, 201
Allotropes, 70, 193, 219
Amphiphiles, 23–42, 45–48, 58, 77, 81, 108, 117, 136, 166
 molecular packing, 25
Amphiphilicity, 1, 16, 39
 hydrophobic, 1
Ascorbic acid, 82

B

Back electron transfer (BET), 160
Bathocuproine (BCP), 166
Biom mineralization, 4
Bionanocomposites, 77
Biotinyl-3,6-dioxaoctanediamine, 195
N,N'-Bis(2,5-di-*tert*-butylphenyl)-3,4:9,10-perylenebis(dicarboximide), 84
16,17-Bis(octyloxy)anthra[9,1,2-*cde*-]benzo[*rst*]pentaphene-5,10-dione, 84
Bis(phthalocyaninato) terbium, 174
Bola-amphiphiles, 31
Bolaphiles, 31
Bond length alternation (BLA), 219, 243, 246, 250
Brewster angle microscopy (BAM), 109
BTEX-S, 202
Buckysomes, 101
Bulk heterojunction (BHJ), 148, 156, 166, 170
 organic solar cells, 24
t-Butyl-1,3-butadiyne (5,5-dimethylhexa-1,3-diyne), 226

C

C₆₀, 1, 23, 55, 145
C₆₀-*N,N*-dimethylpyrrolidinium iodide, 28
C₆₀-Ru[bpy]₃²⁺ hybrid, 33
Carbon allotropes, 70, 193, 205, 219
Carbon nanotubes (CNT), 55, 74, 84, 90, 145, 193
 biological interface, 205
 DNA, 211
 gas/solid interface, 202
Carbosilazane, 123
Carbyne, 247, 250
CdTe nanoparticles, 89, 92
Cell surface mucin glycoproteins
Charge-transfer (CT) interactions, 60
Cholesterol, 34, 108, 120
Cisplatinum, 209
Co-evaporated devices, 168
Critical packing parameter (CPC), 26
Critical reaggregation concentration (CRC), 45
Cumulenes, 219
CuPc tetrasulfonic acid (TsCuPc), 176
CXCR4, 210
Cyanobiphenyl, 122
Cyclodextrin, 38
Cyclotrimeratrylene, 118

D

Decayne, 225
Dendrimers, 5, 37, 60, 71, 103, 136, 156, 203, 227
Dendrofullerenes, 38
Dendrons, 37, 46, 135, 156, 211
Deposition, 66

- Dibenzo-24-crown-8, 160
 Diiodo-tetrayne, 228
 Dimethyl methylphosphonate (DMMP), 204
 Dimethylviologen, 82
 Dipalmitoylphosphatidylcholine (DPPC), 131
 DNA, 211
 Dodecaynes, 226
 Dodecyltrimethylammonium bromide (DTAB), 201
 Drop drying, 3
- E**
- Electron acceptors, 150
 Eu₈-G3-PAMAM-(1,8-naphthalimide) dendrimer, 203
- F**
- Field emission transistors (FET), 3
 Flowerlike assemblies, 10
 Folate receptors, 209
 Folic acid, 209
 Fréchet-type dendrons, 39
 Fritsch–Buttenberg–Wiechell (FBW) rearrangement, 228
 Fullerenes, 1, 23, 55, 145
 hexakisadducts, 101
 room temperature liquid, 16
 Fulleropyrrolidines, 7, 9, 16, 83, 118, 161, 176
 Fulleropyrrolidinium–androstane–ferrocene, 88
- G**
- Gas adsorption, 204
 Gas sensors, 202
- H**
- Heptayne, 227
 Hexakisadducts, 45, 101
 thermotropic liquid-crystalline, 118
 Hexakis(4-nonylphenyl)dipyrazino [2,3-f:2',3'-h]quinoxalene, 118
 Highly oriented pyrolytic graphite (HOPG), 7
 Homooxacalix[3]arenes, 62
 2-Hydroxypropyl- β -cyclodextrin, 38
- I**
- Imidazole ligand, 82
 Imidazolium-modified SWNTs (SWNTs-Im), 200
- Incident photon-to-current efficiency (IPCE), 174
 Interfaces, 193
- L**
- Lamin A/C, 210
 Langmuir–Blodgett (LB) thin films, 45, 55, 58, 70, 102
 Langmuir–Schaefer method, 55, 71
 Layer by layer (LBL), 33, 55, 59, 68, 78, 84
 Lipofectamine, 210
 Lipofullerenes, 131
 Liposomal vesicles, 129
 Liquid crystals (LC), 15, 101
 Liquid–liquid interfacial precipitation (LLIP), 3
 Lutidine, 229
- M**
- 3-Mercaptoethanesulfonate, 62
 Metallization, 13
N-Methyl fulleropyrrolidines, 7
 Micelles, 7, 26, 63, 101, 129, 138
 Molecular dynamics (MD), 26
 Molecular packing, 23
 Mucin glycoproteins, 207
 Multilayer, 63
 Multiwalled carbon nanotubes (MWNT), 77, 172
- N**
- Nano-containers, 47
 Nanomaterials, 23
 Nanorods, 4, 27–31
 Nanospheres, 37–44, 102, 129, 134
 Nanotubes, carboxylic acids, 172
 Nematic phase, 123
 Neural stem cells (NSCs), 206
 Neurons, cell growth/differentiation, 205
 Neurospheres, 207
 Nickel porphyrin/C₆₀ conjugate, 82
 NN4A, 6
 Nonayne, 226
 Nucleic acids, 210
- O**
- Octadecylamin (ODA), 74, 81
 Octadecyltrichlorosilane, 71
 Octakis(propylsulfonyl)PdPc, 161
 Octayne, 226

- Octyloxybiphenyl derivatives, 122
Organic light-emitting diodes (OLED), 3
Organic solar cells, 145
- P**
Pentaphenyl fullerene anion, 44
Perylene bisimide (PBI), 146
2-(Phenylimidazolyl)fulleropyrrolidine, 83
Phospholipids, 129
Photoenergy conversion, 55
Photoinduced electron transfer (PET), 145, 151
Photovoltaics, organic, 80, 145
Phthalocyanines, 32, 81, 145, 149
Phytochlorin/C₆₀ conjugate, 81
Planar heterojunction (PHJ), 148
Plasticization, 13
Polyanions–polycations, 68
Polyelectrolytes, 59, 60, 63, 68, 89, 206
Polythiophene, 177
 carboxyl, 92
Polynes, 219
Poly(diallyldimethylammonium chloride), 68
Poly(2,5-dioctyloxy-1,4-phenylene-alt-2,5-thienylene) (POPT), 84, 85
Poly(ethylene oxide) (PEO), 6
Poly(3-hexylthiophene), 81, 84
Poly-L-ornithine (PLO), 207
Poly(m-phenylenevinylene-co-2,5-dioctyloxy-p-phenylenevinylene) (PmPV), 77
Poly(sodium 4-styrene sulfonate), 68
Poly(styrene-b-acrylic acid), 63
Poly[(vinylbenzyl)trimethylammonium chloride], 91
Porphyrin–fullerene hybrids, 38, 74
6-*O*-Porphyrin-2,3-di-*O*-stearoylcellulose, 83
Postsynaptic currents (PSCs), 205
Pyrene, 195
Pyrenecyclodextrin, 197
Pyridine-dithiol-derivative-MWNT-hydrogenase, 77
Pyrrolidinofullerenes, amphiphiles, 28
 trialkoxylbenzene-appended, 37
- S**
Self-assembled monolayers (SAMs), 102
Self-assembly, 1, 23, 55
- Self-organized bilayers, 102
Semiconductors, 15, 57, 60, 80, 146, 177
Siloxane, 123
Silsequioxane, 123
Single-molecule magnets (SMMs), 175
Single-wall carbon nanotubes (SWNT), 12, 75, 91, 172, 195
siRNA, 210
Smectic A phase, 119
Solar cells, 55, 80, 148
 Langmuir–Blodgett/Langmuir–Schaefer film-based, 81
 layer-by-layer film-based, 84
Solvophobic effect, 25
Steroids, 108
Subphthalocyanines (SubPcs), 147
Succinimidyl-1-pyrenebutanoate, 195
Sulfosuccinimidyl 6-(3'-[2-pyridyldithio]propionamido)hexanoate, 210
Superconductivity, 3, 70
Superhydrophobicity, 10, 37
Supramolecular materials/chemistry, 1, 193
Supramolecular organization/coassembly, 4, 145
Surface-enhanced Raman scattering (SERS), 14
Syndiotactic-poly(methyl methacrylate) (st-PMMA), 6
- T**
Tetramethylcyclopentylidene, 235
Tetraphenylporphyrin/C₆₀, 88
Tetra(4-sulfonatophenyl)porphyrin, 83
Tetrayne, 223–226, 241
Tetrathiafulvalene, 39
Thin films, 101
Transfer ratio, 66
Truncated cones, 26, 39, 41
- Z**
Zinc porphyrin, 82
Zinc tetrakis(N-methylpyridinium) porphyrin tetrachloride, 83
Zinc tetra-tert-butylphthalocyanine (ZnNc), 174
Zirconium 1,10-decanebisphosphonate, 60